

The Russian River Estuary: Inlet Morphology, Management, and Estuarine Scalar Field
Response

By

DANE KRISTOPHER BEHRENS

B.S. (University of California, Davis) 2006

M.S. (University of California, Davis) 2008

DISSERTATION

Submitted in partial satisfaction of the requirements for the degree of

DOCTOR OF PHILOSOPHY

in

Civil and Environmental Engineering

in the

OFFICE OF GRADUATE STUDIES

of the

UNIVERSITY OF CALIFORNIA

DAVIS

Approved:

Fabián Bombardelli, Co-Chair

John Largier, Co-Chair

David Schoellhamer

Gregory Pasternack

Committee in Charge

2012

i

© 2012 by Dane Kristopher Behrens. All Rights Reserved.

Dane Kristopher Behrens

December 2012

Civil and Environmental Engineering

The Russian River Estuary: Inlet morphology, Management, and Estuarine Scalar Field Response

Abstract

Bar-built estuaries with unstable tidal inlets are widespread in Mediterranean climates and along wave-exposed coasts. While similarly important to coastal sediment balances and estuarine ecosystems, and more numerous than larger inlet systems, they suffer from a relative lack of understanding. This is a result of the setting: bar-built estuaries lie at a nexus of coastal and fluvial environments, often behaving like lakes with extreme variability in boundary conditions. At the ocean-side boundary, inlet channel blockage from wave-driven sedimentation is common, leading to water levels in the lagoon that are consistently higher than ocean levels (perched conditions) or to complete disconnection between the lagoon and the ocean (inlet closure). During times when the inlet channel allows tidal conveyance, flood tides provide saline, nutrient-rich water and vigorous turbulent mixing. Inlet closure traps seawater in the estuary and transforms these systems into salt-stratified coastal lakes. The amount of habitat space provided by the closed system is then constrained by the extent of the salt field, since it has marked effects on temperature and dissolved oxygen. Although closed and perched conditions are

natural, encroachment from agriculture, roads and development has led to a host of fundamental changes to the way the inlet and estuary function. Combined with the present lack of understanding of how these systems behave in response to natural processes, this will be a growing concern as long-term shifts in climate continually alter the landscape and forcing conditions.

This dissertation explores three areas in need of better understanding: (1) Variability of inlet closure frequency, (2) response of the estuarine salt field to inlet closure, and (3) the influence of inlet management on stratification in the estuary. These questions are addressed by examining the Russian River Estuary (RRE), a prototypical bar-built estuary in Northern California. This work builds from existing studies of the site by the author, leveraging a uniquely extensive set of *in situ* observations of daily inlet behavior with additional field and numerical modeling work. The aim is to use these tools to provide a more complete picture of the combined function of the inlet and estuary than is currently present in the literature.

Inlet closure frequency is examined using over 60 years of daily closure records detailing the behavior of the Russian River mouth. Inlet morphological behavior is shown to be a response to processes which act to scour the inlet (driven by tides and river flows) and processes that act to deposit sand in the inlet (driven by waves). The observed time-dependent closure pattern is shown to be well-described as a response to tidal, weather-related, seasonal and interannual processes. A parametric model is developed to predict closure events in the short- and seasonal-term scales, and is shown to improve on existing models. Lastly, closure records from the nineteenth and twentieth centuries are compared,

showing that inlet closures have become shorter and more sporadic over time at this site. Long term shifts such as this are examined within the context of management practices and climate variability.

The evolution of the salt field is tracked during several inlet closure events in 2009 and 2010 using repeated boat-based conductivity temperature depth (CTD) surveys, stationary sondes and upward facing acoustic doppler current profilers (ADCPs). The motion of the intruding salt front is in general well-studied in relatively deep estuaries with gradually varying bathymetry. However, in bar-built estuaries such as the RRE, the mechanisms of upstream salt transport are more obscure, since these systems are often associated with sharply-varying bathymetry resulting from extensive meandering and high stream gradients. The field data are used to show that the salt front movement persists in the estuary despite these characteristics. Empirical orthogonal functions and a horizontal Richardson Number are employed to link the salt transport into the inner estuary to buoyancy-driven currents which move epilimnetic salt water upstream along the top of the pycnocline when diurnal winds are not active. Internal waves are also present, but are limited by the bathymetry in the extent to which they transport salt upstream. Volumetric capacity of the pools upstream of the front and turbulence caused by diurnal winds are shown to be the main impediment to the salt front advance.

The impacts of inlet management on stratification in the estuary are assessed by examining two practices: (1) Allowing the inlet to remain closed and (2) enforcing perched conditions by cutting a one-way supratidal outflow channel over the beach. The ramifications of the latter are presently unknown. A numerical model is used to examine

the different outcomes achieved during hypothetical two-week closure and overflow events at the RRE. The model uses a two-dimensional (x - z plane) representation that emphasizes the vertical salt stratification in the estuary. The modeling results show that having an overflow channel only several meters above the pycnocline results in strengthened stratification when winds are applied, while inlet closure leaves stratification mostly intact. Long-term changes in estuary salt mass are well-described as a function of the hydraulic gradient through the beach during closure, and as a function of vertical diffusion of salt during perched overflow. A ratio of the magnitudes of seepage flow out of the beach and vertical diffusive flow of salt across the pycnocline is a good descriptor of which process will dominate the long-term evolution of salt in the estuary. Boat-based field data confirm the model results, suggesting that the two management states present divergent outcomes in the estuary.

Acknowledgments

This dissertation is the product of six challenging but very fulfilling years. I can attribute the fact that I pulled this together to many family members, friends, and colleagues, who have collectively made this work possible.

First, I would like to thank my advisors, Fabián Bombardelli and John Largier. Fabián was a constant source of support and a diligent ambassador of my research and of my young career. What I appreciated most was the fact that he always made time to answer my unrelenting and probably inconvenient onslaught of questions, many of which at late hours of the night. Much of the technical backbone of my work evolved from dozens of late-night conversations in his office, as he always made it clear that his door was always open. My work would not have made it far off the ground if not for his help along the way. John played an equally important role, teaching me how to see complex environmental problems in simple and solvable ways. Because of his mentorship, I like to consider myself not only as an engineer but also as a scientist. Most importantly, he taught me that I could learn the most about a subject by simply being at the site to observe how it behaves. Now, despite destroying multiple cell phones, falling overboard into freezing cold water and having multiple lunches stolen by seagulls, I feel like I understand the Russian River Estuary much better than I would otherwise have!

In addition to my advisors, I also want to express gratitude to professors David Schoellhamer and Greg Pasternack, for all of their guidance (and patience) throughout this process. I chose you to be part of my committee because the courses you taught and the discussions we had had a profound effect on my development as a researcher. I am also thankful to Professor Jeanny Darby, who deserves credit for convincing me to stay at Davis for graduate school, and who put me in a position to take on this research.

I also want to acknowledge that my work was funded and made possible almost entirely by the Sonoma County Water Agency and Philip Williams and Associates. My research was possible because of the Agency's appreciation for the importance of scientific research as a tool for advancing restoration efforts. I am proud to have been a part of a broad group of scientists who have pushed and continue to push for greater understanding of the Russian River Estuary. In particular, I would like to thank Chris Delaney and Jessica Martini-Lamb for being a consistent source of support and guidance. I also want to thank Jeff Church for helping to push forward my field work in the estuary, and Dave Cook, Dave Manning, Justin Smith, Erin Sighesio, and many others in the agency for collaboration.

I would also like to thank my colleagues at Philip Williams and Associates, who have played an invaluable role in my work from the beginning. Their restoration of Crissy Field, in San Francisco Bay, was a template for my research on inlet stability. In addition, their ongoing role in the estuary management made my numerical modeling studies possible. The people I have interacted with the most over the years have been Don Danmeier, Matt Brennan, Michelle Orr, Dave Revell, and Bob Battalio, all of whom were very important to this work in various aspects.

The single greatest contributor to my work was Elinor Twohy. Her stewardship of the Russian River for the last five decades provided the backbone of the inlet morphology work in this study, and will be essential in future studies of the effects of human impacts and changing climate in small estuaries. Although she does not refer to herself as a scientist, she has contributed something with her records from 1973 to the present that most scientists in their respective fields are never lucky enough to have or to create. The fact that our society today is beginning to have a conscience about its interaction with the natural environment is because people like her exist.

I am also thankful to the many people who made my field work in the estuary possible. Special thanks go to Dave Dann, who took my safety and the safety of my equipment as a top

priority. I am also thankful to Jamie O'Bryan and his family for letting me keep my boat in Bridgehaven. I did my best not to step on Valentina's flowers! I would also like to thank Prof. Steven Morgan for letting me borrow his boat and CTD for both field seasons. Finally, many divers from the Bodega Marine Laboratory helped me deploy, recover, check on, and occasionally rescue devices in the field. These included Megan Sheridan, Henry Fastenau, Dave Dann, Matt Robart, Tammer Barkouki, and Gabrielle Miller-Messner.

Of course, the support I have received extends well past the academic and professional community. The support of my family has been essential. Although this was a long process, I never doubted that I could complete it because of the example of my parents, Dave and Vikki, who I have never known to give up on anyone or anything. I owe my work ethic to my dad, and my creativity to my mom, and this dissertation is as much for them as it is for me. I also owe a great deal to my brother Max and sister Karin, who really restored my spirits when I made the time to see them. The biggest thing I look forward to after having reached this goal is to make up for lost time with you two! I want to thank John for keeping my car running, which was my main mode of transport to and from the river. I also want to thank Hayden and Leah for all of their innocent trouble-making. If I someday have back problems from all the times I ran around with you on my shoulders, it will have been well worth it.

I also want to thank my many friends both in the department and out, for ideas and collaboration throughout these six years. My colleagues at the Bodega Marine Laboratory and in the Civil and Environmental Department at Davis were a great source of ideas and inspiration. These included Carlos Cabrera, Akshay Vichare, Marisol Garcia Reyes, Kaveh Zamani, Kate Hewett, Shreya Hegde, Lauren Garske, and many others.

I also want to thank the people of Jenner for accommodating this study, as well as the many seal watch volunteers and concerned citizens who made this a very exciting and scientific-minded community to work in.

Lastly, I want to acknowledge my partner, Tony, whose support has been unwavering since the beginning. He saved me from the brink of catastrophe on more occasions than I can count. Whether this involved helping me make a figure at the last minute, or driving four hours in the middle of the night to bring me something I left at home, his support was an absolute certainty. He was even there to jump in the river and grab submerged devices when I could not. More than anything, he was a calming force that I could rely on every day, which made it easier to put my best work into this.

Table of Contents

Abstract	iii
Acknowledgments.....	vii
Table of Contents	xi
List of Tables.....	xv
List of Figures	xvi
Chapter 1. Introduction.....	1
1.1. Occurrence, behavior and classification of bar-built estuaries.....	2
1.2. Management aspects	3
1.3. Motivation of the present study	4
Chapter 2. Review of Literature.....	7
2.1. Morphology and Stability	7
2.1.1 Analytical Approaches	11
2.1.2. Empirical Approaches.....	13
2.1.3. Statistical Approaches.....	14
2.1.4. Numerical Approaches.....	14
2.2. Estuarine Response to Inlet Configuration	15
2.3. Function and Management	17
Chapter 3. Field Site and Experimental Methods	21
3.1. Setting	21
3.2. Data Sources.....	26
3.2.1. Inlet Condition and External Data Sources.....	26
3.2.2. Field Measurements.....	28
3.2.3. Beach Spatial Data	31
3.2.3. Nearshore Wave Height Estimates	34
Chapter 4. Episodic Closure of the Tidal Inlet at the Mouth of the Russian River – a Small Bar-Built Estuary in California	37
4.1. Introduction	37

4.2. Study site: Present behavior and historical changes	41
4.3. Methods.....	46
4.3.1 <i>Data collection</i>	46
4.3.2 <i>Model description</i>	47
4.4. Results	55
4.4.1 <i>Temporal characteristics</i>	55
4.4.2 <i>High-frequency variability</i>	57
4.4.3 <i>Seasonal variability</i>	63
4.4.4 <i>Interannual variability</i>	67
4.5. Discussion	71
4.5.1 <i>Stability parameter and prediction skill</i>	71
4.5.2 <i>Seasonality</i>	73
4.5.3 <i>Influences of local human activity and estuary management</i>	74
4.5.4 <i>Climate variability</i>	77
4.6. Conclusions.....	79
4.7. Uncertainty Analysis.....	81
4.7.1 <i>Measurements</i>	81
4.7.2 <i>Calculations</i>	84
5. Salt Field Mechanics in a Shallow Bar-Built Estuary After Inlet Closure	86
5.1. Introduction	86
5.2. Methods.....	91
5.2.1 <i>Field Observations</i>	91
5.2.2 <i>Analysis methods</i>	92
5.3. Results	96
5.3.1 <i>Salt field evolution</i>	96
5.3.2 <i>Flow structure</i>	105
5.3.3 <i>EOF analysis</i>	109
5.3.4 <i>Salt front advance in the inner estuary</i>	115
5.4. Discussion	122
5.4.1 <i>Processes driving salt front excursion</i>	122
5.4.2 <i>Limiting factors</i>	124

5.4.3. <i>The Ri approach and future considerations</i>	126
5.5. Uncertainty Analysis.....	127
5.5.1. <i>Measurements</i>	127
5.5.2. <i>Calculations</i>	128
6. The Effects of Several Inlet Management Practices on Water Column Stability in an Intermittently Closed Bar-Built Estuary.....	134
6.1. Introduction	134
6.2. Methods.....	137
6.2.1. <i>Field Observations</i>	137
6.2.2. <i>Theoretical Model</i>	139
6.2.3. <i>Numerical Model</i>	142
6.2.4. <i>Grid and Boundary Conditions</i>	143
6.2.5. <i>Validation</i>	146
6.2.6. <i>Model Simulations</i>	147
6.3. Results	148
6.3.1. <i>Current structure and residual circulation</i>	148
6.3.2. <i>Salt field evolution</i>	152
6.3.3. <i>Water Column Stability</i>	156
6.3.4. <i>Total Salt Mass</i>	159
6.4. Discussion	162
6.4.1. <i>Short-Term Water Column Stability</i>	162
6.4.2. <i>Salt Export and Long-Term Stability</i>	164
6.4.3. <i>Comparison With Observations</i>	171
6.5. Conclusions.....	177
7. Conclusions and Future Work	179
7.1. Inlet Morphology.....	179
7.2. Salt Field Mechanics after closure	184
7.3. Effects of Inlet Management Practices on Water Column stability	188
References	194
Appendix A. Estuary Water Balance and Berm Seepage	210
A.1. Importance of Flow Losses.....	210

A.2. Methods	211
A.2.1. Mass Balance Components	213
A.2.2. Application.....	219
A.3. Results	221
A.4. Uncertainty.....	224
Appendix B. Numerical Model Validation.....	225
B.1. Basis for Validation Tests.....	225
B.2. Model Domain and Mesh	226
<i>Grid Resolution</i>	231
B.3. Canonical Tests.....	234
<i>B.3.1. Effect of rigid boundary on flows</i>	234
<i>B.3.2. Wind Stress</i>	239
<i>B.3.3. Density interface displacement</i>	243
B.4. Comparison Against Observations	248
<i>B.4.1. Approximating Surface Wind Stress</i>	248
<i>B.4.2. Flow Structure Comparison</i>	250
<i>B.4.3. Comparison with Observed Density Field Evolution</i>	254
Appendix C. Boat-Based Field Data	258
C.1. Lagoon Scalar Fields in 2009	267
C.2. Lagoon Scalar Fields in 2010	291

List of Tables

Table 3.1. Summary of sources of data used for modeling and analysis.	28
Table 3.2. Closure dates and data collection	29
Table 4.1. History of closure and human-induced changes within the Russian River estuary and watershed.	45
Table 4.2. Statistical characteristics and uncertainty of key forcing parameters	82
Table 6.1. Summary of model runs.....	148
Table B.1. Agreement between modeled wind-driven profile and empirical solutions.	242
Table B.2. Agreement between modeled interface displacement and analytical solution	246
Table B.3. Correlation between modeled and observed wind speeds at Station A4	252
Table B.4. RMSE (kg m^{-3}) of modeled density profiles during the 2009 closure event.	257

List of Figures

Figure 3.1. Plan view of the Russian River inlet emphasizing its limited migration range between the rock jetty and the northern extent of Goat Rock State Beach. Goat Rock (not shown) forms the southern extent of the beach and is located roughly 1 km south of the jetty. Waves are predominantly from the northwest, although southerly swell conditions also occur.	23
Figure 3.2. Plan view of RRE with measurement stations. Darker shading represents higher altitude. The estuary is divided qualitatively into wind-exposed downstream and relatively wind-shield upstream segments.	24
Figure 3.3. RRE on 1 Oct 2009, after 23 days of inlet closure. Normal inlet position is left (north) of jetty visible in center. Copyright © 2002-2010 Kenneth & Gabrielle Adelman, California Coastal Records Project, www.californiacoastline.org	26
Figure 3.4. CTD setup (left) used for boat-based profiles.	30
Figure 3.5. Illustration of Goat Rock State Beach with extents of beach surveys used in this study. SCWA surveys were obtained on a monthly basis. Study surveys were taken on an irregular basis between December 2009 and August 2010. Beach coloration represents elevation (red colors are higher elevation) given by the LiDAR map of the site. Background image is an aerial photograph provided by BingMaps, ©Microsoft.	33
Figure 4.1. (top) An inlet closure event in October 2009 and (bottom) an example of the range of inlet migration. The dark object at the left is the rock jetty, indicated in Figure 3.1. Northward inlet migration is common after flood events, but also sometimes occurs directly after inlet breach events, as is shown here from 27-29 September 2003.....	43
Figure 4.2. Closure record from 1973 to 2009. White (grey) spaces indicates periods when the inlet was open (closed). Extreme drought (1977) and flood (1975, 1982) years are apparent. Nearly 80 percent of closure events during this period were ended manually when heavy equipment was used to dig a trench across the beach.	46
Figure 4.3. Schematic of an inlet indicating processes leading to sediment import to the inlet (black text) and sediment export (grey text) and (bottom) illustration of inlet conditions discussed in this study. We consider inlet stability in the context of sedimentation/erosion within the inlet channel. We assume that riverborne sediments must be reworked by waves to cause sedimentation.	49
Figure 4.4. FFT visualization of the 1973-2009 daily inlet condition. Data are smoothed in the frequency domain to improve confidence and the 95 percent confidence interval is indicated. The peaks at 365 and 182 days are statistically significant at this level.....	56
Figure 4.5. Proportion of days within one day of a closure event, based on the nearshore wave height (H_s) and peak daily inlet flow ($Q_{inlet, max}$). This reflects data from the years 1999-2008, when a tide gage was operated within the estuary. Except during winter, the majority of $Q_{inlet, max}$ is associated with tides.	59

Figure 4.6. Probability distribution functions of wave parameters (upper row) and inlet hydraulic parameters (bottom row). Solid line represents all data from the years 1999-2008. For the same period, dashed line only includes datapoints within five days prior to a closure event.60

Figure 4.7. Comparison of five-day closure risk based on (a) wave height (b) inlet hydraulic parameters and (c,d) the closure parameters ϕ_1 and ϕ_2 . Parameters are normalized based on percentile to allow direct comparison.62

Figure 4.8. Comparison of (top) inlet position, (middle) river discharge and (bottom) nearshore significant wave height between the years 1997 and 2008. Vertical grey bars in top plot represent inlet closure events. Inlet position is defined by the centerline of the inlet. Although all parameters appear to have similar seasonal fluctuations, their phases occasionally differ. For instance, this is visible for waves and river flow during the 2000-2001 wet season.64

Figure 4.9. Seasonal cycles determined from Julian day averages of (top) river discharge, wave height and estuary tide range, (middle) wave steepness and Dean Number, and (bottom) the proportion of days closed and parameter ϕ_1 using only Q_r in the denominator. Each data point represents the average across its Julian day for the period that the data were available. Wave, river flow and inlet condition data are averaged using the period from 1981-2008, while tide range data reflect the period 1999-2008.66

Figure 4.10. Multi-year records of (top) closure anomaly, (second) median annual river discharge, (third) NOI signal and (bottom) PDO signal. NOI and PDO values represent October-March averages. Error bars in top plot reflect periods of recorder malfunction. Grey areas are observed values and solid black line is a three-year moving average.69

Figure 4.11. Duration of closure periods based on median flow during closure. Dashed line illustrates the potential for an envelope of limiting conditions following the expectation that $t_{over} \sim (Q_r - Q_{bar})^{-1}$. The envelope is intended to illustrate a possible limiting condition and is not validated. It is based on the assumption that barrier seepage is nonzero, which will be tested in a subsequent study.71

Figure 4.12. Jenner jetty during construction and at the time of the present study. A second jetty was planned, to allow permanent navigability of the inlet, but was never built. Upper photograph courtesy of Russian River Historical Society.77

Figure 5.1. Salinity, temperature and dissolved oxygen observed at the onset of inlet closure on 4 October 2010.88

Figure 5.2. Salinity, temperature and dissolved oxygen observed after 8 days of closure, on 12 October 2010.89

Figure 5.3. Longitudinal salinity map of the RRE during representative (top) tidal and (bottom) closed conditions. Measurement station locations from Figure 3.2 are indicated. Bottom edge represents the along-estuary thalweg profile.97

Figure 5.4. Sequential salinity maps of RRE during closure E5. The approximate boundary between the inner and outer estuary (Fig. 3.2) is at 5 km from the inlet. The first stage of salt redistribution is clearly visible for distances less than 8 km from the inlet. The second stage is visible 8 km and farther upstream. 102

Figure 5.5. Image subtraction of RRE salinity field between the last day of closure E5 (12 October 2010) and the day prior to closure (3 October 2010). 103

Figure 5.6. Along-estuary salinity gradient in the epilimnion during E5. Salinity values represent averages from the centerline of the metalimnion to the water surface. 104

Figure 5.7. (top) Difference in water level between stations B3 and A1 and **(bottom)** time-series of along-stream component of velocities measured from upward-facing ADCP at site B3 during closure E1. 107

Figure 5.8. (top) Difference in water level between stations B3 and A1 and time-series of along-stream component of velocities measured from upward-facing ADCP at site B3 during closures **(middle)** E4 and **(bottom)** E5. 108

Figure 5.9. Response of along-stream velocities at sites A4 (lower left) and B3 (lower right) to wind (upper) on 28 September 2010, during closure event E4. Difference in water levels between sites B3 and A1 are used as a proxy for wind. Horizontal gray band represents the pycnocline location. Velocities are positive in the upstream direction. The increase in wind during the middle of the day, shown in the upper plot, was a typical daily occurrence during the measurement period. 109

Figure 5.10. Eigenvectors of along-stream velocity from EOF analysis at sites A4 and B3 (left) and time series of first two variance modes (right). Horizontal gray band represents the pycnocline location. 110

Figure 5.11. Comparison of EOF modes against predicted flow structures. Upper plot compares along-stream velocity vector given for predicted seiche modes against EOF mode 2 at site A4. Lower plot compares gravitational current profile against EOF mode 1 at site B3. Horizontal gray band represents the pycnocline location. At the outer estuary site (A4), the predicted V3H1 seiche is strongly correlated with the second EOF mode (shown). At the inner estuary site (B3), the first EOF mode more closely matches a gravitational current, but there are too few available data points to provide statistical certainty. 114

Figure 5.12. Conceptual drawing of the first (1a,b) and second (2a,b) phases of salt field redistribution after closure. H and C are a representative depth of the epilimnion and the dimensionless inundation capacity, respectively. Darker shading represents higher salinity water. The Wedderburn number is sometimes supercritical in the first phase (leading to strong upwelling) and subcritical afterwards, due to change in depth, H 119

Figure 5.13. (a) Estuary water level from 25 September – 12 October 2010, compared with time series of **(b)** reduced gravity and TKE production, **(c)** horizontal Richardson Number (brackets denote vertical average in the epilimnion), **(d)** the primary variance

mode at site B3 and **(e)** total salt mass and inundation capacity from sites B3-B6. The first variance mode at site B3 is most likely tied to gravitational circulation. 121

Figure 5.14. The percentage of the total variance captured by the first 8 variance modes for **(left)** Station A4 and **(right)** Station B3. In both plots the 95 percent significance level obtained from a Monte Carlo (Rule N) simulation (Preisendorfer, 1988) are given. 130

Figure 6.1. Summary of the typical inlet states observed at the Russian River Estuary. From left to right, the states are **(left)** the inlet after closure, **(middle)** the inlet during perched overflow and **(right)** the inlet during open, fully tidal conditions. The modeling effort herein focuses on the closed and perched overflow states. Photographs are courtesy of Elinor Twohy. 136

Figure 6.2. (top) Arial view of Russian River Estuary, showing boat-based CTD measurements sites and **(bottom)** side view using the estuary thalweg profile to mark the channel bottom. The approximate boundary between the inner and outer estuary (pictured) represents the departure between the relative deep and wind exposed outer estuary and the relatively shallow and wind shielded inner estuary. 139

Figure 6.3. Summary of **(top)** wind forcing conditions used in the model runs and **(bottom)** the initial salinity profile enforced at the initial time step. The wind signal is repeated diurnally for the two-week model duration. The initial density field mirrors the salt field. 146

Figure 6.4. (top) Vertical density profiles after 12 days at site A4 during the closed and overflow cases with high-wind and a porous beach, compared with the initial density profile. Along-stream current velocities are also shown at site A4 for the high-wind and porous beach simulations with (middle) a closed beach and (bottom) a porous overflow channel. Positive values are directed upstream. The dashed line represents the vertical location of the mean density, which is the center of the pycnocline. 150

Figure 6.5. Residual current profiles at site A4 for simulations with a porous beach and (top) full inlet closure and (middle) a perched overflow channel. Elevations are normalized by the total depth to account for the change in depth during closure. The grey band represents the pycnocline elevation. (bottom) The residual profile of the product of x-velocity and local salinity, representing the net along-stream salt transport at site A4. 151

Figure 6.6. Image subtraction of the salt field in the outer estuary between the initial and final time steps, representing a two-week net change in the salinity field. (a-c) Image subtraction for closure with a nonporous beach. (d-f) Image subtraction for closure with a porous beach. 154

Figure 6.7. Image subtraction of the salt field in the outer estuary between the initial and final time steps, representing a two-week net change in the salinity field. **(a-c)** Image subtraction for perched overflow with a nonporous beach. **(d-f)** Image subtraction for perched overflow with a porous beach. 155

Figure 6.8. Time series of peak N2 values (a-d) 0.3 km from the inlet and (e-h) 2.4 km from the inlet. Line weights correspond to the (-) high-wind, (--) low wind and (:) no wind cases. Peak N2 values were generally located at the center of the pycnocline. Values shown here represent a low-pass filter of the raw N2 time series at each site, using a rectangular filter width of approximately two days. This was used to extract the diurnal variability. 158

Figure 6.9. Time series of potential energy anomaly (Simpson et al. 1990) measured (a-d) 0.3 km from the inlet and (e-h) 2.4 km from the inlet. Line weights correspond to the (-) high-wind, (--) low wind and (:) no wind cases. Values shown here represent a low-pass filter of the raw ϕ time series at each site, using a rectangular filter width of approximately two days. This was used to extract the diurnal variability. 159

Figure 6.10. Comparison of normalized estuary salt mass during the two-week simulation period for (top) inlet closure with a porous beach, (middle) perched overflow with a nonporous beach and (bottom) perched overflow with a porous beach. 161

Figure 6.11. Schematic of the inlet during (top) inlet closure and (bottom) perched overflow, indicating the main components of the salt mass balance. Δh is the head difference between the estuary and mean ocean level adjacent to the beach. η is the displacement of the pycnocline at the upwind (left) boundary. All terms are based on unit widths, corresponding to the x-z planar modeling approach. 165

Figure 6.12. Time series of normalized estuary salt mass compared with integrated measures of (a-b) the hourly head difference measured between the estuary and ocean and (c-d) vertical salt diffusion per unit area of the unbroken pycnocline. The data indicate that (a) seepage dominates export during inlet closure and (d) vertical diffusion dominates export during perched overflow, for the conditions used in this study. Linear fits used in (a) and (d) represent least-square fits of the data. 170

Figure 6.13. Time series of (top) peak N², (middle) potential energy anomaly and (bottom) normalized estuary salt mass during a perched overflow event from 1-7 July 2010 and a closure event from 7 September to 5 October 2009. Values were taken at various times during the days within the field campaign, so that diurnal variability is included in the trends shown here. 174

Figure 6.14. Comparison of modeled and observed examples of the estuary salinity field, with using field data from closed-inlet and perched overflow conditions. 175

Figure 6.15. Illustration of upwelling for modeled closure and overflow cases. As time advances from 4 to 12 hours, the landward wind increases from 0 to 8 m s⁻¹. 176

Figure A.1. Estuary schematic detailing processes relevant to changes in water volume during closure. 213

Figure A.2. Estuary stage-volume relation comparing methods of estimating upstream surface area. 214

Figure A.3. Salinity measured at the bottom of the pools near the mouth (Station A1) and 2.3 km upstream (Station A4) during closure event E1.....	218
Figure A.4. Q_{loss} compared against Δh for the period from 1999 and 2009. Data were taken out when certain conditions were met (Section A.2.2) which would have invalidated the simplifying assumptions needed for this estimate. Q_{loss} represents the combination of Q_{seep} and $Q_{aquifer}$	222
Figure A.5. Q_{loss} vs time during several individual closure events. Plots at left show estuary water surface elevation (-) and 25-hr average Pt. Reyes tide level (--).	223
Figure B.1. Cross channel density plots at (top) site A4 and (bottom) site A5, on 29 September, 2010, during a closure event. At the time of data collection, winds were below 3 ms^{-1}	229
Figure B.2. Comparison of modeled density profiles at the mouth for different vertical grid resolutions.	233
Figure B.3. Model domain for boundary-effect test, with expected result.	236
Figure B.4. Comparison of FLOW3D results (o) and the analytical solution (-) for the velocity profile in fully turbulent channel flow. Velocities are normalized by the constant incoming velocity (u_i), and sampled at the center of a 4 km-long basin.	238
Figure B.5. Model domain for test of wind-driven velocity profile in a freshwater basin.	240
Figure B.6. Modeled velocity profiles (o) compared with solutions of Mathieu et al. (-) and Tsuruya et al. (--), for wind blowing over a 4 km - long basin with water of uniform density. Vertical cell resolution is 10 cm.	243
Figure B.7. Model domain for test of interface tilt during winds.	244
Figure B.8. Modeled (o) and analytical (-) solution for the displacement of the density	247
Figure B.9. Modeled (thick grey line) and observed (narrow black line) water surface elevation near the mouth (Station A1) of the RRE during closure event E1.....	250
Figure B.10. Modeled (--) and observed (-) streamwise velocity profile at Station A4 (Fig. 3.2) resulting from winds on 28 September 2010. Velocities are normalized by the mean magnitude of velocity in the water column.	253
Figure B.11. Model domain, showing wind-induced upwelling of the interface at the mouth (left). The porous beach is at left, shown by the drop in water surface elevation indicating the sloping water table from the estuary to the ocean. Higher density water is indicated by warmer colors. Blue represents $\rho = 998 \text{ kg m}^{-3}$	255
Figure B.12. Modeled (--) and observed (-) density profiles at the Mouth in the final 10 days of the 2009 closure event.	256
Figure C.1. Time series of water surface elevation measured near the RRE mouth during the 2009 field season. Vertical dashed lines represent times when CTD transects were	

taken in the estuary. The horizontal grey bar represents the period of the ADCP deployment.....	259
Figure C.2. (top) Time series of water surface elevation measured near the RRE mouth during the 2010 field season. Bottom panels are close-ups of the closure events E3-E6 (see Table 3.x). Vertical dashed lines represent times when CTD transects were taken in the estuary. The horizontal grey bar represents the periods of ADCP deployments.....	260
Figure C.4. Summary of (a) water levels, (b) offshore and nearshore waves, (c) freshwater inflows and (d) BML wind speed during closure event E2. Vertical dashed lines represent times when CTD transects were taken in the estuary. The horizontal grey bar represents periods of ADCP deployment.....	262
Figure C.5. Summary of (a) water levels, (b) offshore and nearshore waves, (c) freshwater inflows and (d) BML wind speed during closure event E3. Vertical dashed lines represent times when CTD transects were taken in the estuary.....	263
Figure C.6. Summary of (a) water levels, (b) offshore and nearshore waves, (c) freshwater inflows and (d) BML wind speed during closure event E4. Vertical dashed lines represent times when CTD transects were taken in the estuary. The horizontal grey bar represents periods of ADCP deployment.....	264
Figure C.7. Summary of (a) water levels, (b) offshore and nearshore waves, (c) freshwater inflows and (d) BML wind speed during closure event E5. Vertical dashed lines represent times when CTD transects were taken in the estuary. The horizontal grey bar represents periods of ADCP deployment.....	265
Figure C.8. Summary of (a) water levels, (b) offshore and nearshore waves, (c) freshwater inflows and (d) BML wind speed during closure event E6. Vertical dashed lines represent times when CTD transects were taken in the estuary.....	266
Figure C.9. 2D planar view of the estuary salinity interpolated from CTD transects from 20 July to 11 Aug 2009.....	268
Figure C.10. 2D planar view of the estuary salinity interpolated from CTD transects from 14 Aug 2009 to 7 September 2009.....	269
Figure C.11. 2D planar view of the estuary salinity interpolated from CTD transects from 7 September 2009 to 13 September 2009.....	270
Figure C.12. 2D planar view of the estuary salinity interpolated from CTD transects from 15 September 2009 to 28 September 2009.....	271
Figure C.13. 2D planar view of the estuary salinity interpolated from CTD transects from 30 September 2009 to 5 October 2009.....	272
Figure C.14. 2D planar view of the estuary salinity interpolated from CTD transects from 6 October to 7 October 2009.	273
Figure C.15. 2D planar view of the estuary salinity interpolated from CTD transects from 7 October to 15 October 2009.....	274

Figure C.16. 2D planar view of the estuary salinity interpolated from CTD transects from 16 October to 25 October 2009.....	275
Figure C.17. 2D planar view of the estuary temperature interpolated from CTD transects from 20 July to 11 August 2009.....	276
Figure C.18. 2D planar view of the estuary temperature interpolated from CTD transects from 14 August to 7 September 2009.....	277
Figure C.19. 2D planar view of the estuary temperature interpolated from CTD transects from 7 September to 13 September 2009.	278
Figure C.20. 2D planar view of the estuary temperature interpolated from CTD transects from 15 September to 28 September 2009.	279
Figure C.21. 2D planar view of the estuary temperature interpolated from CTD transects from 30 September to 5 October 2009.	280
Figure C.22. 2D planar view of the estuary temperature interpolated from CTD transects from 6 October to 7 October 2009.	281
Figure C.23. 2D planar view of the estuary temperature interpolated from CTD transects from 7 October to 15 October 2009.	282
Figure C.24. 2D planar view of the estuary temperature interpolated from CTD transects from 16 October to 25 October 2009.....	283
Figure C.25. 2D planar view of the estuary dissolved oxygen interpolated from CTD transects from 20 July to 11 August 2009.	284
Figure C.26. 2D planar view of the estuary dissolved oxygen interpolated from CTD transects from 14 August to 7 September 2009.	285
Figure C.27. 2D planar view of the estuary dissolved oxygen interpolated from CTD transects from 15 September to 28 September 2009.	286
Figure C.28. 2D planar view of the estuary dissolved oxygen interpolated from CTD transects from 30 September to 5 October 2009.....	287
Figure C.29. 2D planar view of the estuary dissolved oxygen interpolated from CTD transects from 6 October to 7 October 2009.....	288
Figure C.30. 2D planar view of the estuary dissolved oxygen interpolated from CTD transects from 7 October to 15 October 2009.....	289
Figure C.31. 2D planar view of the estuary dissolved oxygen interpolated from CTD transects from 16 October to 25 October 2009.....	290
Figure C.32. 2D planar view of the estuary salinity interpolated from CTD transects from 1 July to 8 July 2009.	292
Figure C.33. 2D planar view of the estuary salinity interpolated from CTD transects from 16 July to 19 July 2009.....	293
Figure C.34. 2D planar view of the estuary salinity interpolated from CTD transects from 24 July to 28 July 2009.....	294

Figure C.35. 2D planar view of the estuary salinity interpolated from CTD transects from 28 July to 6 August 2009.....	295
Figure C.36. 2D planar view of the estuary salinity interpolated from CTD transects from 6 August to 10 August 2009.	296
Figure C.37. 2D planar view of the estuary salinity interpolated from CTD transects from 27 September to 29 September 2009.	297
Figure C.38. 2D planar view of the estuary salinity interpolated from CTD transects from 30 September to 6 October 2009.	298
Figure C.39. 2D planar view of the estuary salinity interpolated from CTD transects from 7 October to 25 October 2010.	299
Figure C.40. 2D planar view of the estuary temperature interpolated from CTD transects from 1 July to 8 July 2010.	300
Figure C.41. 2D planar view of the estuary temperature interpolated from CTD transects from 16 July to 19 July 2010.....	301
Figure C.42. 2D planar view of the estuary temperature interpolated from CTD transects from 24 July to 28 July 2010.....	302
Figure C.43. 2D planar view of the estuary temperature interpolated from CTD transects from 28 July to 6 August 2010.....	303
Figure C.44. 2D planar view of the estuary temperature interpolated from CTD transects from 6 August to 10 August 2010.	304
Figure C.45. 2D planar view of the estuary temperature interpolated from CTD transects from 27 August to 29 September 2010.....	305
Figure C.46. 2D planar view of the estuary temperature interpolated from CTD transects from 30 September to 6 October 2010.	306
Figure C.47. 2D planar view of the estuary temperature interpolated from CTD transects from 7 October to 25 October 2010.	307
Figure C.48. 2D planar view of the estuary temperature interpolated from CTD transects from 1 July to 8 July 2010.	308
Figure C.49. 2D planar view of the estuary temperature interpolated from CTD transects from 16 July to 19 July 2010.....	309
Figure C.50. 2D planar view of the estuary temperature interpolated from CTD transects from 24 July to 28 July 2010.....	310
Figure C.51. 2D planar view of the estuary temperature interpolated from CTD transects from 28 July to 6 August 2010.....	311
Figure C.52. 2D planar view of the estuary temperature interpolated from CTD transects from 6 August to 10 August 2010.	312
Figure C.53. 2D planar view of the estuary temperature interpolated from CTD transects from 27 August to 29 September 2010.....	313

Figure C.54. 2D planar view of the estuary temperature interpolated from CTD transects from 30 September to 6 October 2010.314

Figure C.55. 2D planar view of the estuary temperature interpolated from CTD transects from 7 October to 25 October 2010.315

Chapter 1. Introduction

Bar-built estuaries are small coastal basins fed by freshwater and fronted by barrier beaches (bars) that separate the basin from the ocean. An opening (inlet) through the beach acts both as a conduit for tides and as a terminus of river flows. While inlets and the back-barrier estuary they connect to are often treated separately in the literature, they are parts of a single coherent system which exists within both the coastal and fluvial realms. The separation of the inlet/beach and estuary systems in the literature is a detriment to both, because these two connected parts are interrelated in terms of morphology (Morris and Turner, 2010), hydrodynamics (Gale et al., 2007) and ecology (Hayes et al., 2008). In arid or semiarid climates, the inlet is often an intermittent feature, as wave-driven sediment transport into the inlet bed sometimes overwhelms the flushing capacity of tidal and riverine currents, causing the beach to block the inlet and isolate the estuary from the ocean. Despite this periodic isolation, bar-built estuaries provide invaluable habitat for myriad endemic aquatic species, many of which have adapted to and take advantage of the variability caused by the intermittent connection with the ocean. However, since the fringing adjacent floodplain is also ideal for agriculture and urban use, management of these systems reflects a competition between natural resource preservation and socioeconomic pressures. The latter will intensify in the near future as the continued increase in the world population leads to additional development in coastal

regions. Ongoing management is complicated by these pressures and by a pervasive lack of understanding of many of the processes associated with these systems.

1.1. Occurrence, behavior and classification of bar-built estuaries

Bar-built estuaries are widespread throughout the world's temperate and tropical coastlines. Most were formed during the Holocene sea level transgression, as river valleys and coastal plains were flooded by rising sea levels (e.g. Cooper, 2001). Influent streams carry sediment eroded from hillslopes within the watershed to the coastal zone, where it is arrested by waves, which act to build the beach barrier and supply sediment to adjacent beaches within the local littoral cell. Since the inlet substrate usually consists of sand or gravel, the channel varies in size, shape and location, as it responds to (1) sediment supply from waves and (2) sediment erosion from tide- or fluvial-driven currents (see Chapter 4). In systems with substantial riverflow or expansive back-barrier basins, the inlet allows full conveyance of the tides, whereas small systems with intermittent flows tend to have small inlets that actively migrate and close, truncating or blocking the tides.

This morphologic variability has consequences within the estuary, where the distribution of the salt field is of primary importance to benthic and pelagic organisms (Jassby et al., 1995), and imposes a strong influence on the temperature and dissolved oxygen fields (Cousins et al., 2010; Borsuk et al., 2001). The entry of tidal saltwater into the estuary is controlled by the ability of the inlet channel to convey the tidal flows.

During flood tide, negatively buoyant intruding saltwater moves through the inlet and plunges on the estuary side, moving upstream along the bottom (Largier and Taljaard, 1991). When the inlet channel thalweg is higher than the lowest tide levels, the salt field is periodically immobilized when tide levels are low. When the inlet is completely closed, the beach traps tidal saltwater in the estuary, and the estuary is best-described as a vertically salt-stratified coastal lagoon, with a freshwater layer overlying a saltwater layer at depth (see Chapter 5).

Many classification systems exist for both inlets (Davis and Hayes, 1984) and estuaries (Valle-Levinson, 2010), but these often oversimplify the dynamic nature of bar-built estuaries, or simply neglect the interplay between the estuary and inlet. The inlet is often classified as being dominated by tides, waves or riverflow. However, each of these primary forcing mechanisms vary independently in magnitude in both short- and long-term time scales at most sites, so a single inlet system can fit within multiple classifications throughout a year (Behrens et al., 2009). Estuaries are usually classified by the magnitude of the river or tidal forcing, or by morphology, geologic history or the strength of vertical stratification in the water column (Valle-Levinson, 2010). Except for geologic history, all of these factors are variable in bar-built estuaries, making it especially difficult to apply any one classification in a meaningful way.

1.2. Management aspects

Management practices in bar-built estuaries are variable, reflecting a large number of constraints among sites. Inlet closure prevents navigation between the ocean and estuary, increases the risk of flooding of low-lying properties, and extends the residence time of trapped tidal saltwater, which can prolong hypoxia at depth (Ranasinghe and Pattiaratchi, 2003). In watersheds with substantial agricultural or urban development, closure can also cause trapping of nutrients from runoff (Roy et al., 2001). Despite these concerns, closure is a natural process, and for species that have adapted to take advantage of the unstable inlet conditions, it is known to improve habitat conditions and survival (Hayes et al., 2008).

1.3. Motivation of the present study

Bar-built estuaries are poorly understood (Mehta, 1996), despite a wealth of focused study efforts in the United States, Australia and South Africa that have occurred within the past century. The present lack of understanding stems from several factors:

- Bar-built estuaries differ dramatically in form and behavior among sites
- Most existing research is biased toward navigable systems
- Field data are lacking both in the vicinity of the inlet and within the backbarrier estuary after closure.

The first point is true not only for bar-built estuaries in separate geologic and climate settings, but also for systems within the same littoral cell, sometimes even several miles apart (e.g. Cooper, 2001; Perissinotto et al., 2010; Roy et al., 2001). As discussed above,

their variability has made it difficult to apply the existing classification systems meaningfully. The second point reflects socioeconomic pressures: sheltered coastal basins with permanently-open connections to the ocean have tremendous economic value. Despite this, small systems far outnumber navigable systems in many regions, such as in California (e.g. Griggs, 2005). While interest in smaller, unstable systems has grown within the past several decades, much more research is needed. The third point is a reflection of the difficulty in obtaining sediment transport rates within an inlet, and (until recently) difficulties in assessing turbulence and salt field mechanics in estuaries. These and other factors are discussed in more detail in Chapter 5 and by Behrens (2008).

The motivation of this dissertation is the scarcity of comprehensive studies in the literature that examine both inlet and estuarine processes at sites, considering the interplay between the two. The objective here is to provide an example of such a coherent approach, by performing the following tasks:

- Examining inlet closure at a bar-built estuary site using extensive existing observations,
- Studying the mechanics of the salt field within this site after closure, and
- Comparing the effects of several management practices on the estuarine salt field.

These tasks are performed by gathering existing records, collecting boat-based field data and by testing, applying, and improving (when practicable) existing models. This work does not provide a framework of classifying either estuaries or inlets, but instead shows how these systems are interconnected, through several case studies of the Russian River Estuary (RRE), a prototypical bar-built estuary in California.

Chapter 2 examines the existing research pertaining to inlet closure, estuarine physics, and inlet management. Chapter 3 discusses the field site and data collection methods. Inlet closure at the Russian River is examined in detail in Chapter 4, which is the body of a manuscript that is tentatively accepted in the journal of Geomorphology, and Chapter 5 examines the mechanics of the salt field in the estuary. Chapter 6 looks at the consequences of two separate inlet management practices on stratification within the estuary, using a numerical model and field data as a means of comparison. Finally, Chapter 7 summarizes the main conclusions of the study and suggests areas where further work is needed. Separate appendices provided at the end discuss berm seepage and numerical model validation. The last appendix summarizes the boat-based field data used in chapters 5 and 6.

Chapter 2. Review of Literature

Focused research efforts in the post-war 1950s-1960s in Europe and the United States led to breakthroughs in our understanding of inlet and estuarine processes. Pritchard (1954), Hansen and Rattray (1965) and later Fischer et al. (1979) provided most of the framework for the present-day knowledge of estuarine physics. During the same period, the General Investigation of Tidal Inlets (GITI) led by the U.S. Army Corps of Engineers (USACE) and the Hydraulic Engineering Laboratory (HEL) at the University of California, Berkeley consolidated early findings from Brown (1928), O'Brien (1931) and Escoffier (1941), with several decades of publically-funded research that led to key findings in inlet/bay hydrodynamics (Keulegan, 1967) and inlet mouth geometry (Jarrett, 1976). This work, along with concurrent advances in the study of oceanic waves and beaches, culminated in the 1984 Shore Protection Manual (USACE, 1984).

These parallel efforts largely focused on large bay or estuary systems, but provided context and an understanding of the underlying physics. However, there is extensive evidence to show that the form and function of large inlet-bay systems do not scale to smaller systems (e.g. Byrne et al., 1980). In this section, I describe some of the most relevant existing literature for inlet/estuary studies, including frameworks developed for large systems for context. I emphasize three areas in need of ongoing research in bar-built estuary systems: inlet morphology and stability, the response of estuarine scalar fields to the condition of the inlet, and inlet function and management.

2.1. Morphology and Stability

Inlets in equilibrium maintain a balance between the input of beach-building (constructive) processes and erosive output (destructive) processes of channel bed sediments (FitzGerald, 1996). Constructive processes are usually driven by waves, which transport sediment toward the shoreline in bars (cross-shore transport: CST) or in a shore-parallel direction (longshore transport: LST). LST is more commonly associated with closure, usually from trapping within the inlet (Rosati and Kraus, 1999) or from causing a shore-parallel bar to form across the mouth (Castelle et al., 2005). Destructive processes are normally associated with inlet currents, which result from tidal fluctuations within the lagoon and river flows. Inlet currents generate shear stress at the inlet channel boundary, bringing sediment in suspension (and thus eroding the channel) when this stress surpasses a threshold for incipient motion of the sediment grains (Julien, 1998). During storm events, waves can also act as a destructive force, and have been shown to cause breaching of previously-closed lagoons by eroding the beach and filling the lagoon to breaching heights (Kraus et al., 2008).

While equilibrium between sediment inputs and outputs is a simple concept, its application is difficult in practice because of the stochastic nature of sediment transport in the vicinity of inlets. The inlet forms a continuum between the marine and fluvial/estuarine environments, so relations derived for sediment transport in these separate regimes are difficult to apply with any confidence. Additionally, changes in the channel depth are rapid for small inlets, and accurate assessment of changes requires repeated surveys, which are difficult to achieve in the inlet (Webb et al., 1991).

Since wave energy, fluvial inputs, sediment availability and local geology (affecting basin size) vary among sites, different degrees of inlet equilibrium exist. Systems that always maintain an equilibrium balance of sediment inputs and outputs have stable cross-sections and tend to also to have large basins, high, consistent freshwater inputs, or artificial stabilization of the mouth. When perturbed from equilibrium by a storm or other large change, these may take decades (Van de Kreeke, 2004) or centuries (Cayocca, 2003) to return to a new equilibrium. For systems with low freshwater inputs and small tidal basins, the equilibrium channel cross section is smaller, and adjustments are more rapid (Van de Kreeke, 2004). In the latter case, departure from equilibrium may cause the inlet to remain unstable long enough for constructive processes to completely fill the channel with sediment, temporarily ending tidal interaction between the ocean and lagoon. This is termed “inlet closure”, and is a common trait on the majority of the world coastlines (Cooper, 2001). In semiarid climates, annual fluctuations in precipitation allow winter floods to overtop the beach and re-form the inlet (“inlet breaching”), creating a recurrent seasonal closure-breaching pattern. In arid climates, coastal lagoons often remain closed for many years at a time (e.g. Roy et al., 2001).

Large, stable inlets, tend to occupy passive continental margins, where coastal plains with low topographic relief were flooded during the Holocene sea level transgression (FitzGerald et al., 2002), providing expansive areas for tides to traverse. These sites are common and well-studied along the eastern US coast (FitzGerald, 1996) and Northern and Western Europe (Van de Kreeke, 2004). Active continental margins tend to have higher relief, leading to steep gradients and narrow, deeply-cut river valleys

(Syvitski et al., 2003). When these flooded during the Holocene transgression, generally smaller tidal basins were formed owing to the confinement created by the topography. Since the space for flooding tides is smaller in these smaller systems, tidal conveyance is weaker through the inlet in systems on passive continental margins, so destructive processes are not always strong enough to balance constructive beach-building from waves. These sites are common along the US Pacific Coast, Chile, South Africa, and Australia, and experience closure more frequently (see Chapter 4).

Unstable systems are usually classified as “closed” or “open”, but this oversimplifies the dynamic nature of the inlet bed. Many examples exist of systems which maintain “perched” conditions, having lagoon water levels that are consistently above mean sea level. This results when sediment deposition in the channel bed prevents full tidal exchange. If this accretion elevates the channel above high tide levels, a one-way, supra-tidal spillover channel may exist. This persists if the overflowing currents are too weak to cause incipient motion of the beach sediments (i.e. allowing erosion of a tidal inlet), and if wave runup on the beachface cannot reach the elevation of the channel. Coastal lagoons with this behavior are rarely studied, but appear to be common in arid or semiarid climates such as South Africa (Stretch and Parkinson, 2006; Perissinoto et al., 2010). Further, there is evidence that these systems support anadromous salmonid species despite the weak connection between the lagoon and ocean (Perissinoto et al., 2010).

Although accurate measures of waves and current speeds are now possible, many existing inlet studies occurred when little or no data were available, and many features of inlet behavior were described from surveys and visual observations alone (Mehta, 1996).

In addition, most of the existing framework for assessing inlet stability was developed with systems that are rarely closed. These approaches tend to be analytical, relying on assumptions that are valid for sites with deep channels (channel depth \gg tide range), no freshwater input and simple tides (e.g. Keulegan, 1967). These have proven their usefulness where these assumptions are valid (e.g. navigable or stabilized inlets), especially in predicting inlet currents and basin tides (Keulegan, 1967). In the majority of inlets, these models provide little benefit since most of the above assumptions are violated. Some researchers avoid this shortcoming by employing empirical or parametric approaches (Johnson, 1973; O'Brien, 1976). More recently, numerical approaches have also become more common (Ranasinghe et al., 1999). I summarize these approaches in the following subsections.

2.1.1 Analytical Approaches

Analytical inlet-bay models largely rely on solving conservation equations for mass and momentum in either one- or two-dimensions. One-dimensional (1D) approaches solve for cross-sectionally averaged flows in the inlet by lumping many of the important parameters into several dimensionless numbers (Van de Kreeke, 1988). The most common is Keulegan's repletion coefficient (Keulegan, 1967; SPM, 1984) which relates measures of the tide, inlet and bay dimensions to the filling potential of the bay. Two-dimensional (2D) approaches provide depth-averaged flows by solving the depth-averaged conservation of mass and momentum equations, but can only provide analytical solutions when many simplifying assumptions are used. The most common is to obtain

the ocean-side depth-averaged velocity in the inlet by using the theory of the turbulent plane jet (Van de Kreeke, 1988). Both approaches contain friction and momentum exchange coefficients that need to be determined through calibration.

Another common approach was developed by Escoffier (1940) who compared a 1D solution of the conservation equations (Brown, 1928) to the depth-averaged velocity required to scour sand. This indicates a nonlinear relation between peak inlet flows and cross-sectional area: As the inlet cross section enlarges, the peak velocity initially increases, but peaks and begins to decline for the largest cross sections as a result of energy loss to friction. As long as the peak velocity on this curve is above the empirical threshold for eroding sand ($\sim 1 \text{ m s}^{-1}$), then there are two points on the curve at which velocities are at this threshold (see Fig. 2 in Van de Kreeke, 2004). The channel cross sections that correspond to these points are the equilibria for the inlet. If a wave event perturbs the inlet channel by depositing sediment, the inlet adjusts and returns to equilibrium if it started at the larger (stable) of the two characteristic cross-sectional areas, whereas it will close if it has the smaller (unstable) configuration.

The majority of the existing analytical approaches were developed between 1960 and 1980, and were applied to or calibrated with stable inlets on the US Atlantic Coast (e.g. Keulegan, 1967; Mehta and Özsoy, 1978; Van de Kreeke, 1988;). 2D approaches have mostly been replaced with numerical models, but 1D models are still applied in field studies. Rustomji (2007) and (Shuttleworth et al., 2005) used the 1D method of Van de Kreeke (1967) to examine the process of inlet closure in Australian sites.

2.1.2. Empirical Approaches

The most commonly used models for predicting inlet stability are empirical. These typically relate lagoon traits to inlet shape. The most prominent relation exists between the lagoon intertidal volume (tidal prism) and the inlet cross sectional area (O'Brien, 1969):

$$A = CP^n \quad \text{Eq. (2.1)}$$

Where A is the cross sectional area, P is the tidal prism and C and n are empirical coefficients. This was initially calibrated for a small number of US Pacific Coast inlets before Jarrett (1976) widened the dataset to include sites from the US Atlantic and Gulf Coasts. The tidal prism is a surrogate for shear stress generated by inlet currents – for larger tidal prisms, more water moves through the inlet within a tidal period, increasing the velocity and thus the shear acting at the inlet boundary.

A and CP^n are strongly correlated, but there are discrepancies based on wave energy, sediment size and inlet size. Pacific Coast inlets have smaller cross-sectional areas than predicted by the universal calibration of Eq. (2.1) which is attributed to the higher wave energy compared with East Coast and Gulf Coast sites (Jarrett, 1976). Similar relations have been found for New Zealand (Hume and Herdendorf, 1992) and the United Kingdom (Townend, 2005), but these found that the relation worked best when calibrated separately for sites with different geologic history. Lastly, laboratory (Mayor-Mora, 1977) and field (Byrne et al., 1980) studies of small inlets show that sites having cross sections below 100 m² have larger cross-sections than predicted by the universal calibration of Eq. (2.1). Kraus (1998) and Hughes (1999) accounted for this by

replacing the coefficients C and n with dimensionless parameters combining traits such as the inlet width and median sediment grain size.

Johnson (1973) used Pacific Coast inlets to demonstrate that the risk of inlet closure can be quantified by relating constructive and destructive properties explicitly. For several sites he estimated wave power (see USACE, 1984) and distinguished them by their frequency of closure. This comparison formed the basis of the later model presented by O'Brien (1976) which is modified and discussed further in Chapter 4. Both the Johnson (1973) and O'Brien (1976) methods are also discussed by Behrens (2008).

2.1.3. Statistical Approaches

Statistical models are less common in the literature. Walker (2003) presented a statistical model that relates closure of the Murray River to river flow, showing generally good results. The Murray River is the largest river in Australia, and its inlet responds strongly to river flooding. Elwany et al. (1998) presented a similar Bayesian statistical model of closure at a Southern California site based solely on river flow, successfully explaining the seasonal closure pattern, in which the site was open during the winter and generally closed during the dry season. These models were applied at monthly time steps, limiting their predictive ability to seasonal or long-term patterns. It remains to be seen whether a similar model would provide meaningful predictive ability at daily or hourly time scales, when tidal variability is not averaged out.

2.1.4. Numerical Approaches

Numerical models have assimilated many of the analytical models presented before 1980. Some focus strictly on inlet flows (Amein and Kraus, 1991), while others resolve the entire coastal or upstream estuarine or fluvial environment (Castelle et al. 2005). Ranasinghe et al. (1999) demonstrated that CST and LST can be isolated by numerical modeling and associated with inlet closure. They simulated the closure of an Australian inlet by testing its response to scenarios involving LST and a combination of LST and CST. Castelle et al. (2005) simulated the lateral migration of another Australian inlet in response to LST and shielding from a breakwater. Numerical models are consistently improving, with the most robust models linking continental shelf models and wave transformation models with models of inlet hydrodynamics and nearshore coastal zone mechanics (Castelle et al., 2005). Despite these advances, the usefulness of numerical models has a limit, since our present understanding of inlet processes is severely limited by a pervasive lack of field data (Mehta, 1996).

2.2. Estuarine Response to Inlet Configuration

In large estuaries and deltaic systems with strong fluvial input, the inlet functions as a relatively constant conduit for tidal intrusion into the estuary. The incoming seawater intrusion is typically constrained by strong inflows rather than bathymetry in these systems (Vijith et al., 2009). These are often only partially stratified, and the position of the salt front with time can be correlated with riverflow (Ford et al., 1990; Stacey et al., 2001) or the spring-neap phase of the tide (O'Callaghan et al., 2007). Since tidal interaction is uninterrupted, saline flood waters reach a quasi-steady balance with

seaward-bound ebb flows at the surface (Ford et al., 1990). While at the scale of multiple days, the salt front may occupy a nearly consistent position in the estuary, the diurnal ebb-flood cycle leads to strong variations in the strength of stratification within a day. This is caused by the interaction between the vertically sheared flow and the local density field during ebb tide (Simpson et al., 1990; Stacey et al., 2001), and is normally dissipated by the subsequent flood tide, which generates high amounts of turbulence.

In well-mixed and partially-stratified estuaries, estuarine circulation is driven by a background baroclinic pressure gradient (Hansen and Rattray, 1965; Geyer, 2010) and exhibits an asymmetry in the velocities and turbulent mixing between flood and ebb tides (MacCready and Geyer, 2010). In systems with stronger stratification, the role of mixing decreases and intruding seawater propagates along coherent density interfaces (Vaz et al., 1989). The horizontal transfer can be tied to the Richardson number (Geyer, 2010). As stratification increases, the Richardson number decreases, and the overall along-stream circulation increases (Linden and Simpson, 1988).

In systems where the inlet is subject to intermittent perching or closure, the inlet's role as a conduit for tides is diminished by the buildup of a sandbar in the mouth. The top of this sill is the thalweg of the inlet channel. If it rests above mean lower low water (MLLW) levels, it has the effect of altering tides as they propagate into the estuary. Harmonic overtides begin to dominate the diurnal tides as they pass through the constricted inlet, resulting in rapid flood tides and prolonged ebb tides. When large areas of mudflat or saltmarsh are present, this pattern is also accentuated as flood tides fill the marginal areas faster than they can be drained (Friedrichs and Aubrey, 1988).

The presence of a bar also heavily influences the salt front entering the estuary. When the inlet is relatively deep and when currents are sufficiently slow (meeting a critical internal Froude Number criterion), flows are bi-directional, with fresh surface flows leaving the estuary at the surface and salty oceanic flows entering the estuary underneath (Largier, 1992). When a bar is present, this alters the depth and the flow speeds up, making it more common for outflows to prevent seawater from entering the estuary (critical Froude Number exceeded more frequently). When seawater does enter, it plunges on the estuary side of the inlet and propagates upstream along the bottom, generating turbulence and mixing as it moves (Largier and Taljaard, 1991).

When inlet currents are insufficient to achieve the critical shear stress to cause erosion in the inlet bed, wave-driven constructive processes can lead to inlet closure (see Section 2.1). At this time, prior seawater intrusions are trapped within the estuary. Without the regular turbulence generated by tides, the estuary becomes sharply salt stratified in the vertical, with the trapped salt layer separated from the upper freshwater flows by a narrow transitional band (“metalimnion/ pycnocline”). Circulation in a closed estuary is in response to wind and river forcing (Largier and Taljaard, 1991). If the estuary bathymetry is deep and simple, a contiguous, large salty lower layer is formed, a condition that is analogous to lake stratification and is ideal for the generation of internal waves (Vidal and Casamitjana, 2008). If the bathymetry is irregular, the salt layer is compartmentalized within pools and separated by shallow areas (“sills”).

2.3. Function and Management

Inlet management strategies reflect a range of drivers, including economics, municipal and industrial needs, environmental preservation, recreation and other factors. Management options range from invasive (stabilization with jetties or rock armor) to non-invasive (altering development practices to minimize anthropogenic impact to the beach). Shifts have occurred in management practices in developed countries within the past century, reflecting several long-term changes:

- More focus has been given to conserving species that use inlet-lagoon systems, and
- Understanding of coastal zone processes has improved

These shifts are explained here in the context of documented management practices in the United States from different parts of the past century.

Prior to 1980, inlet management favored invasive options for maintaining an open channel. These included rock armoring and jetty construction to prevent the inlet from moving laterally and to maintain a permanent opening, and dredging within the inlet and lagoon to maintain navigable depths and to increase the tidal prism. Much of the research conducted at this time was publicly funded and concerned issues of inlet stability. In the US, many studies were funded by GITI program led by the USACE.

Jetty construction was a common approach during this time, which is visible from the remaining jetties that exist at many of the inlets in heavily populated areas along the US coasts (Griggs, 2005). These were effective in maintaining permanently open inlets, but resulted in significant changes to the nearby beach environments. In areas with strong annual LST rates, downdrift beaches were heavily depleted while the updrift beach grew

extensively (Griggs, 2005). While dual jetty systems became the standard, single-jetty systems were attempted at the Russian and Navarro Rivers in California, which both failed to maintain an open inlet (Rice, 1974).

During the same time period, sites without jetties were often breached manually after closure. Breaching was performed for a number of reasons, including:

- To allow fish passage,
- To prevent flooding of low-lying property, and
- To prevent dissolved oxygen depletion in bottom waters.

This was (and still is) performed on an irregular basis by beachgoers with shovels (pers. comm. J. Smith). In areas where lagoons border development, public agencies were often given responsibility to open the mouth with heavy equipment such as bulldozers, so that breaching could be performed more reliably (e.g. Goodwin and Cuffe, 1994).

After 1980, shifts in attitude which began during the 1960s began to heavily influence management practices. The Endangered Species Act, enacted in 1973, required that resources be spent to prevent the decline of native species, many of which require estuarine habitat for survival. Especially in the case of salmonids, this federal recognition provided an impetus for studying inlet-lagoon systems within the context of lagoon function and habitat space. Studies within the past several decades have shown that closed lagoons provide beneficial rearing habitat space for salmonids (Hayes et al., 2008). Even systems that are naturally perched show evidence of beneficial use by salmonids (Perissinotto et al., 2010).

Recent observations suggest that breaching can have a negative impact on water quality in stratified coastal lagoons by stirring hypoxic bottom waters into the upper layer or by draining out only the relatively-well oxygenated upper fresh layer. These changes can lead to extensive fish kills, negating some of the benefits of an open mouth (Becker et al., 2009). Despite this, manual breaching is still a common practice in some areas (e.g. Goodwin and Cuffe, 1994).

Chapter 3. Field Site and Experimental Methods

3.1. Setting

The Russian River Estuary (RRE) is one of many small bar-built estuaries along California's active continental margin (Johnson, 1973; Goodwin, 1996). The river spans a distance of 175 km within a 3850 km² basin, and discharges into the Pacific Ocean 90 km north of San Francisco, in Northern California (Fig. 3.1). The river and estuary provide extensive spawning and rearing habitat for what used to be a prolific run of Chinook (*Oncorhynchus tshawytscha*) and Coho (*Oncorhynchus kisutch*) salmon as well as Steelhead trout (*Oncorhynchus mykiss*) (SEC, 1996). The Russian River was once the third most productive watershed for wild steelhead in California (Moyle, 2002). The site has an extensive history of occupation from various settler groups, beginning with the first Russian settlers (1820s), and continuing through timber harvest and gravel mining operations in the nineteenth and twentieth centuries. The lagoon is fringed by access roads and housing, and the upstream reaches are heavily impacted by sedimentation and nutrient loading resulting from road construction, agriculture and urbanization in the watershed (Opperman et al., 2005).

Elevations range from sea level to 1325 m and much of the watershed is underlain by a Jurassic-Cretaceous age Franciscan Formation (Blake et al., 2002). The mouth is wave-dominated based on the classification system of Davis and Hayes (1984), has no visible ebb- or flood-tidal deltas for most of the year, and has a reflective beach composed of coarse sand with D_{50} of 1.02 mm (USACE, 1965). The estuary is narrow,

with a mean width of ~200 m and comprises several major bends. The landward half of the estuary is at least partly shielded from winds by topography, while the seaward half is more exposed. The bottom topography is characterized by alternating pools (depths 4-12 m) and sills (depths 1-3 m) with the deeper sections located near the inlet and at the channel bends. The estuary is divided into two reaches by topography: a deeper, wind-exposed outer reach comprising the 5 km upstream of the inlet and an upstream reach extending as far as 11 km upstream from the inlet. For the purpose of this study, these are termed the "outer" and "inner" estuary, respectively (Fig. 3.2).

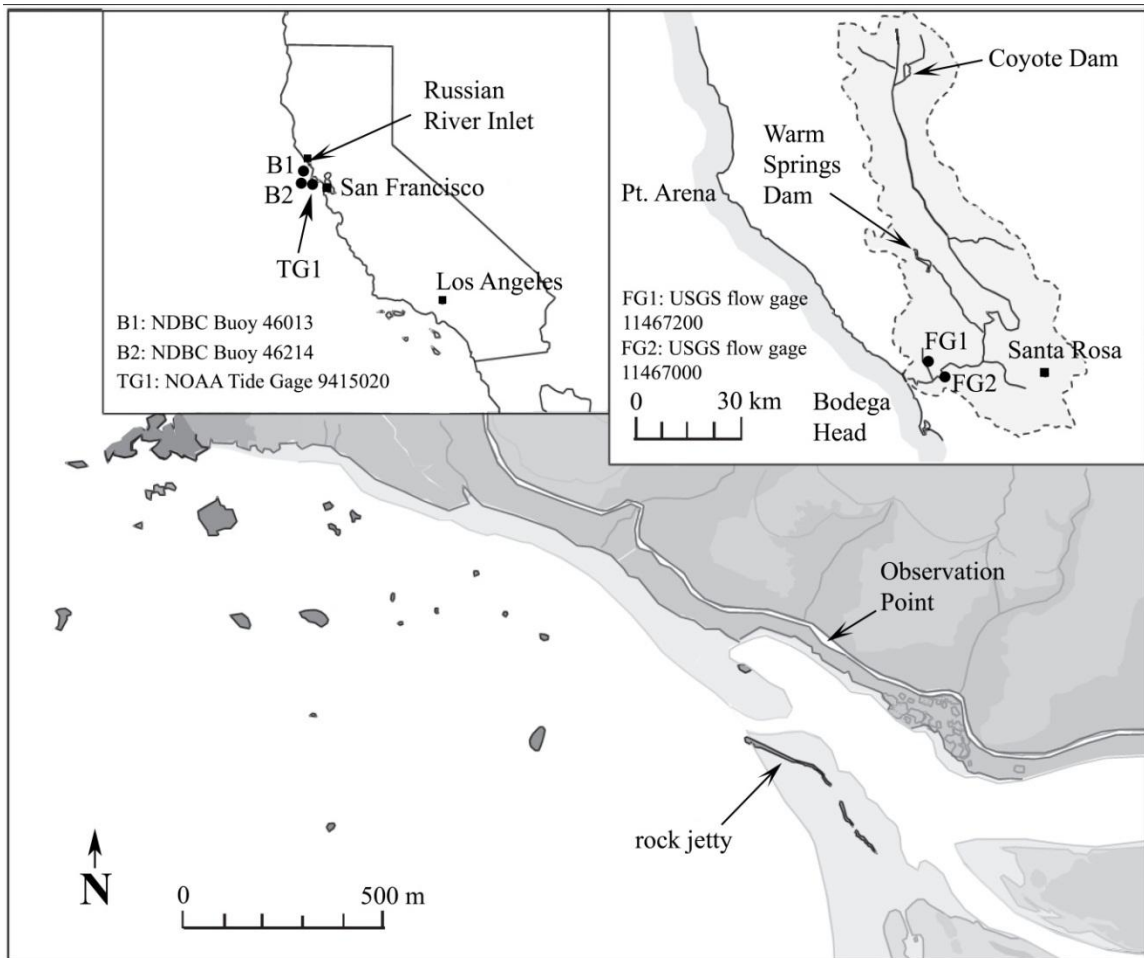


Figure 3.1. Plan view of the Russian River inlet emphasizing its limited migration range between the rock jetty and the northern extent of Goat Rock State Beach. Goat Rock (not shown) forms the southern extent of the beach and is located roughly 1 km south of the jetty. Waves are predominantly from the northwest, although southerly swell conditions also occur.

The regional climate is Mediterranean, and the majority of the precipitation arrives in a small number of storms between the months of November and April. Steep gradients and lack of snowmelt within the basin lead to a flashy hydrograph in winter and generally low flows in summer. Dry-season flows are presently maintained at $2\text{-}4\text{ m}^3\text{s}^{-1}$, while winter floods provide brief periods with flows exceeding $1000\text{ m}^3\text{s}^{-1}$.

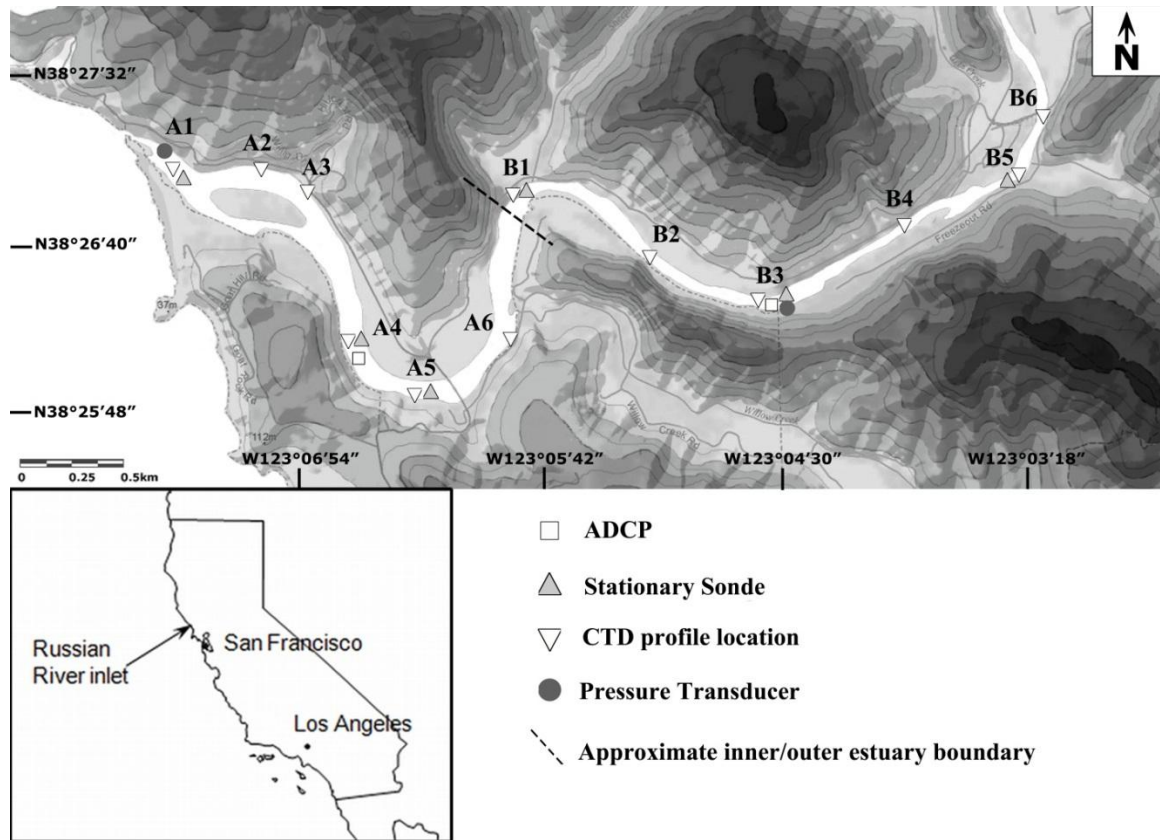


Figure 3.2. Plan view of RRE with measurement stations. Darker shading represents higher altitude. The estuary is divided qualitatively into wind-exposed downstream and relatively wind-shielded upstream segments.

Marine influences are mostly dominated by Northeast Pacific storm events and local winds (Allan and Komar, 2006), but El Niño events have an impact on the local climate as far north as this location (Wingfield and Storlazzi, 2007). Local winds are diurnal and sometimes exceed 15 m s^{-1} during storms. Between the months of September and May, deep-water significant wave heights (H_s) measured at Point Reyes (Fig. 3.1) average 2.6 m, have periods between 12 s and 16 s, and generally arrive from the northwest (270° - 310°), although occasional southerly swell events occur (200° - 240°). Summer conditions are generally dominated by short-period (6-10 s) northwesterly

(270° - 330°) waves with deep-water H_s that average 2 m. Ocean tides are mesotidal (spring tide range ~ 2.7 m), but the tidal prism ($0-2 \times 10^3 \text{ m}^3$) is inadequate to keep the inlet open during periods of low flow and high waves.

Inlet closure events occur during every season of the year. Figure 3.3 illustrates the beach and the ponded estuary during closure. These events typically last less than three weeks and are ended by manual breaching with heavy equipment or by natural breaching resulting from ponding and overflow of the estuary (Kraus et al., 2008; Behrens et al., 2009). Historically, breaches were also performed by local citizens to prevent flooding of property, but this was eventually adopted on a larger scale by various public agencies in the 1960s. Presently, the inlet is breached by SCWA to enhance fish passage, prevent flooding, and prevent long-term degradation of trapped bottom waters (Goodwin and Cuffe, 1994). Closure and its management at the RRE are discussed in more detail in Chapter 4.



Figure 3.3. RRE on 1 Oct 2009, after 23 days of inlet closure. Normal inlet position is left (north) of jetty visible in center. Copyright © 2002-2010 Kenneth & Gabrielle Adelman, California Coastal Records Project, www.californiacoastline.org.

3.2. Data Sources

This section describes the sources of data used in this study and the methods of their collection. Data analyses are described separately in Chapters 4-6 and Appendix A. The sources of data for the present study include long-term sets of site observations, remote measurements of coastal and fluvial processes available online, and field measurements taken at the RRE.

3.2.1. Inlet Condition and External Data Sources

The RRE is unique compared with other bar-built estuarine systems because it has an unusually-long set of *in situ* observations of daily inlet condition. Two multi-year

records are used here: one provided by Rice (1974) from 1931 to 1957 and another recorded by E. Twohy, a resident of Jenner from 1973 to 2009 (Behrens et al., 2009). The latter record includes daily photographs from 1991 to 2009 taken at a distance of 300 m from the inlet (Fig. 3.1; see "Observation point"). As described in Behrens et al. (2009), these were used in conjunction with visible beach landmarks with known earth coordinates to make daily estimates of inlet width, length and position.

Wave, tide and river flow data were collected to evaluate drivers of inlet closure. Wave data are from the National Data Buoy Center (NDBC: <http://ndbc.noaa.gov>) buoys 46013 (Bodega Bay) and 46214 (Pt. Reyes; also see Coastal Data Information Program, CDIP: <http://cdip.ucsd.edu>). Tide data are from the Pt. Reyes tide gage operated by the National Oceanic and Atmospheric Administration (NOAA: <http://tidesandcurrents.noaa.gov>), 48 km south of the inlet, yet representative of the tide in the ocean off the Russian River mouth. Within the estuary, a water-level gage operated by SCWA collected hourly data 1.5 km upstream of the inlet beginning in 1999. Flow measurements are available from the U.S. Geological Survey (USGS: <http://waterdata.usgs.gov/nwis>) stations at Hacienda Bridge (site no. 11467000), 27 km upstream of the inlet, and at Austin Creek (site no. 11467200), the only perennial tributary to the lower river or estuary, 11 km from the ocean inlet. Data sources are summarized, along with periods of measurement, in Table 3.1.

Table 3.1. Summary of sources of data used for modeling and analysis.

Parameter	Source/Location	Position	Measurement Period
Wave Height	NDBC Buoy 46214: Near Pt. Reyes	37.945 N 123.470 W	1996-present
	NDBC Buoy 46013: Bodega Bay	38.242 N 123.301 W	1981-present
River Flow	USGS: Russian River Near Guerneville	38.509 N 122.927 W	1939-present
	USGS: Austin Creek Near Cazadero	38.507 N 123.069 W	1959-present
Tides	NOAA: Pt. Reyes	37.995 N 122.977 W	1990-present
	SCWA: Jenner Visitors Center	38.449 N 123.115 W	1999-present
Inlet	Rice (1974): Russian River Inlet	38.451 N 123.127 W	1931-1957
Condition	E. Twohy ¹ : Russian River Inlet	38.451 N 123.127 W	1973-present
Inlet Shape²	Behrens et al. (2009): Russian River Inlet	38.451 N 123.127 W	1991-2009
Bathymetry	EDS (2009)	--	October 2009

¹Fourth author of Behrens et al. (2009); ²Including inlet width, length and position.

3.2.2. Field Measurements

Field measurements were taken between the months of July and October in 2009 and 2010. The inlet was open for most of this time, but data were collected during six closure events which are summarized in Table 3.2. Fieldwork consisted of:

- Water surface elevation measurements,
- Current measurements using upward-facing acoustic doppler current profilers (ADCPs),
- Repeated boat-based conductivity temperature depth (CTD) profiles supplemented with hourly measurements from stationary sondes operated by SCWA, and
- Beach surveys taken with a standard real-time kinetic global positioning system (RTK GPS) setup.

Locations of measurement stations are given in Figure 3.2. During tidal conditions, boat-based CTD profiles were taken at peak low and high tides and during maximum ebb and flood periods to capture the main features of the salt field during different parts of the mixed semidiurnal tidal regime. Profiles were taken more frequently during closure events to assess the evolution of the salinity field after tidal interaction becomes absent in the estuary. CTD data from all events (provided in Appendix C) are used to broadly characterize the observed salt field evolution pattern, while ADCP currents measured during the final three events are used for additional analysis.

Table 3.2. Closure dates and data collection

Event	Dates	Data¹
E1	7 Sep – 5 Oct 2009	CTD, ADCP
E2	14 – 16 Oct 2009	CTD
E3	4 – 11 Jul 2010	CTD
E4	20 Sep – 1 Oct 2010	CTD, ADCP ²
E5	4 – 12 Oct 2010	CTD, ADCP ²
E6	21 – 24 Oct 2010	CTD

¹ In addition to pressure transducers and sondes

² Operated in mode 12

The boat-based CTD depth-profiles were taken at the 12 locations shown in Figure 3.2 using a SeaBird SBE19plus CTD profiler measuring conductivity, temperature, pressure, dissolved oxygen, fluorescence and photosynthetically active radiation (PAR). Profile locations were arranged in the streamwise direction to provide information about longitudinal changes in scalar distribution. The longitudinal thalweg profile was estimated from an existing bathymetric map of the estuary (EDS, 2009) and used to provide spatial context for CTD profiles. Stationary sondes maintained by SCWA

measured the same parameters as the CTD at hourly intervals at the top and bottom of the water column at several locations shown in Figure 3.2.



Figure 3.4. CTD setup (left) used for boat-based profiles.

Changes in the water surface elevation were tracked at four locations in 2009 and two locations in 2010 (Fig. 3.2) using HOBO pressure-temperature loggers. These were located at 1-3m depths and continuously sampled pressure and temperature at 10-minute intervals. CTD profiles and surface sonde measurements were used to assess surface layer density, which was then used in conjunction with the HOBO logger data to estimate depths via the Equation of State (UNESCO, 1981) by assuming hydrostatic conditions. Depths were then transferred to surface elevation data by surveying both the water surface and a local benchmark with a standard RTK GPS setup.

Bottom-mounted 1200 kHz RDI Workhorse Sentinel ADCPs were placed 2.4 km and 7.4 km upstream of the inlet (Fig. 3.2). The outer site (A4) is located in the center of the deepest portion of the estuary, a continuous basin oriented along a NW-SW axis running from 0-4 km upstream of the inlet (Fig. 3.2). The inner site (B3) is located in a pool isolated by long, shallow sills immediately upstream and downstream, and is partially protected from westerly winds by hills. The ADCPs were deployed in mode 12, sampling 12 subpings per second during 10-minute bursts at the beginning of every hour with 0.5 m vertical bins. These data were used to estimate turbulent velocity fluctuations as well as mean currents, and are primarily used in Chapter 5.

3.2.3. Beach Spatial Data

The shape of the barrier beach is important to the analyses in Chapter 6. In particular, the beach foreshore slope, width and crest height are necessary for

understanding surf zone processes and for approximating seepage flow rates through the beach berm. Spatial data were obtained from three sources (Fig. 3.5):

- RTK GPS surveys of the beach performed as part of this dissertation,
- Monthly monitoring surveys of the beach north of the Jetty performed by SCWA, and
- Light detection and ranging (LiDAR) data obtained in 2010.

RTK surveys were taken on 1 December 2009, 3 January 2010, 22 March 2010 and 4 August 2010. Shore-normal transects were collected at approximately 50 m spacing along the beach. Transects began on the estuary side of the beach spit and progressed over the beach crest to as low an elevation as possible on the ocean side. The presence of harbor seals limited the extent of the surveys. Pacific harbor seals (*Phoca vitulina richarsi*) are protected by the federal Marine Mammal Protection Act (MMPA), and survey profiles were not taken within approximately 300 ft of any seals on the beach, in accordance with beach signage provided by local volunteer agencies. Surveys were tied to the NAD83 and NAVD88 datums by surveying over a benchmark placed by EDS (2009) near the Jenner Visitors Center. Errors in RTK GPS measurements are nominally 3 cm in the vertical and horizontal (e.g. Harley et al., 2010).

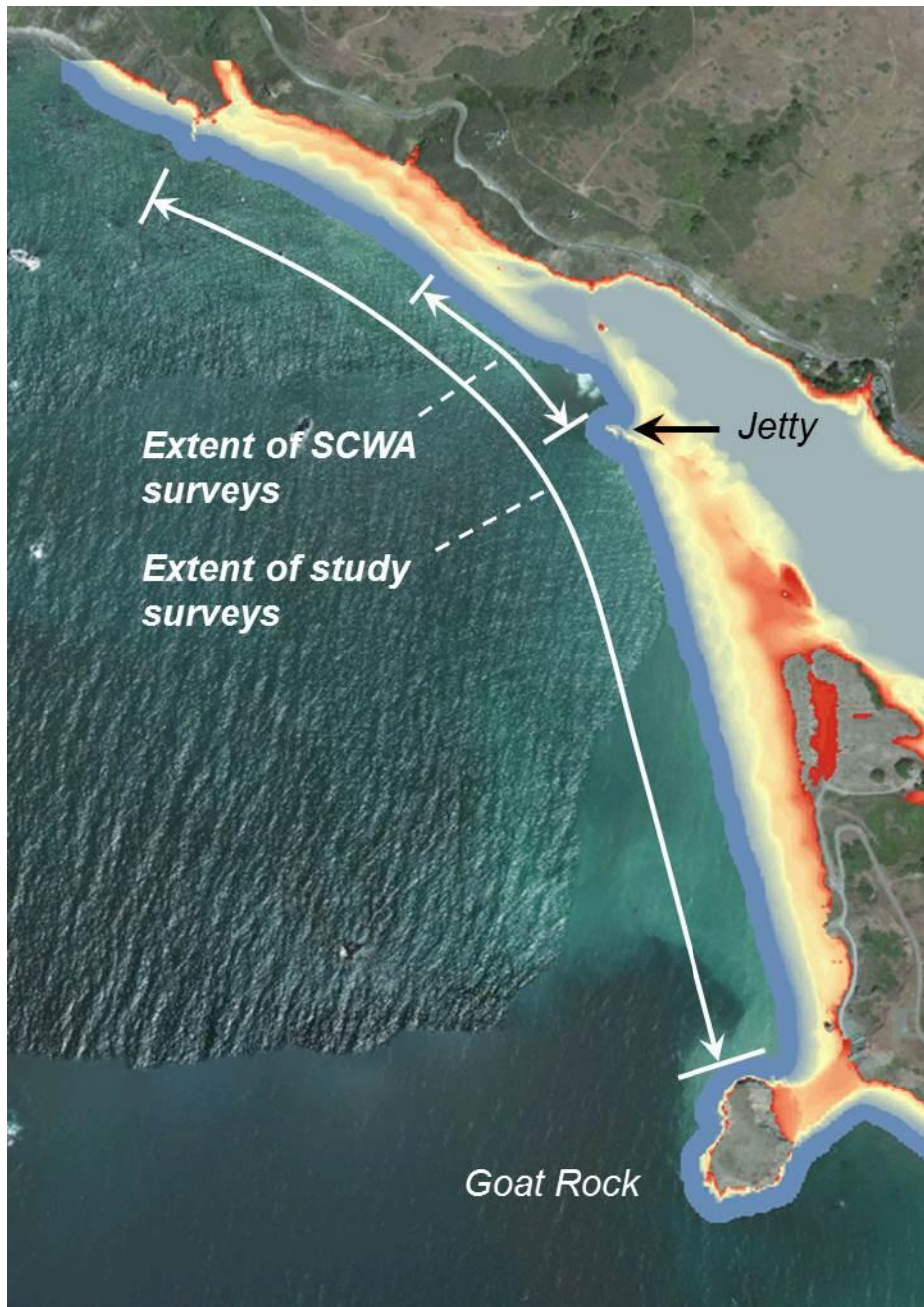


Figure 3.5. Illustration of Goat Rock State Beach with extents of beach surveys used in this study. SCWA surveys were obtained on a monthly basis. Study surveys were taken on an irregular basis between December 2009 and August 2010. Beach coloration represents elevation (red colors are higher elevation) given by the LiDAR map of the site. Background image is an aerial photograph provided by BingMaps, ©Microsoft.

Monthly surveys were taken by SCWA on the segment of Goat Rock State Beach (GRSB) north of the Jetty. These are taken for monitoring purposes as part of a long-term adaptive management plan aimed at improving habitat for salmonids in the estuary during the summer rearing season (NMFS, 2008). These are collected with standard survey equipment, and were also limited by the presence of harbor seal haulouts on the beach.

A digital elevation model (DEM) was constructed from LiDAR data collected as part of the Coastal LiDAR Project led by the California Coastal Conservancy (<http://csc.noaa.gov/dataviewer>). Data were collected from an aircraft using a Leica ALS60 MPiA sensor, which collected multiple return x , y , z and intensity data on the beach. Data were tied into the NAD83 datum and adjusted vertically to the NAD88 vertical datum using ground control points. Orthometric heights were obtained by applying the GEOID09 model to the processed LiDAR data. The DEM is accurate to 50 cm in the horizontal and approximately 18 cm in the vertical (NOAA, 2012).

3.2.3. Nearshore Wave Height Estimates

Nearshore significant wave heights were estimated from deep-water measurements at buoy 46214 using a transformation matrix (personal communication, W. O'Reilly, 2006) to account for the effects of shoaling and refraction between Pt. Reyes and a location at a depth of 10 m adjacent to the inlet (38°26'52" N, 123°8'6" W). This accounts for wave refraction and shoaling using a numerical model which applies linear wave theory (USACE, 2002). Refraction is the lateral spreading or concentration of energy along a wave train, caused by the interaction between the wave train and the local

bathymetry. Because of refraction, waves tend to focus toward headlands and spread out as they approach concave shorelines (Komar, 1998). Shoaling is the change in wave energy caused by the change in wave group velocity (C_g) in shallow water (Komar, 1998). These are represented as follows:

$$K_r = \sqrt{\frac{b_0}{b_{NS}}} \quad (3.1)$$

$$K_s = \sqrt{\frac{C_{g0}}{C_{gNS}}} \quad (3.2)$$

where K_r is the refraction coefficient, K_s is the shoaling coefficient, b is the lateral distance between wave rays, the subscripts “NS” and “O” correspond to nearshore and offshore (deep-water) conditions, respectively, and

$$C_g = \frac{1}{2} \left(1 + \frac{4\pi d / L}{\sinh(4\pi d / L)} \right) \frac{gT}{2\pi} \tanh\left(\frac{2\pi d}{L}\right) \quad (3.3)$$

is the group velocity, where L is the nearshore wave length, d is the local depth and T is the wave period. L is approximated after Fenton and McKee (1990). The numerical model generates a transformation matrix by propagating wave rays from the Pt. Reyes buoy to RRE over a bathymetry composed of 100 m \times 100 m grid cells (pers. comm. W. O’Reilly) and comparing the offshore and resultant nearshore energies.

The resulting transformation matrix consists of a set of $K_r \times K_s$ coefficients, separated by wave frequency (f) and direction (θ). These are used with the wave energy spectra measured at Pt. Reyes to estimate nearshore wave energy with the following relation (USACE, 2002):

$$E(f, \theta) = \sum_f \sum_\theta K_s^2(f, \theta) K_r^2(f, \theta) E_0(f, \theta) \Delta f \Delta \theta \quad (3.3)$$

where E is the wave energy at the 10 m isobath offshore of the RRE. Nearshore wave heights were then obtained from E by assuming Rayleigh-distributed wave conditions (USACE, 2002). Waves generated by winds between Pt. Reyes and the RRE mouth are not considered in the analysis. These are probably most important during the summer, when long-period swell waves are weak, but are less important from November to April, when swell waves dominate much of the California shoreline (Wingfield and Storlazzi, 2007).

This approach was tested against a limited amount of field data collected from 6 June to 5 Aug 2009 at a 10 m depth offshore of the Russian River (38° 26' 32" N, 123° 07' 45" W). Wave data were collected with an upward facing, bottom-mounted Nortek© Acoustic Wave and Current (AWAC) profiler. The AWAC creates a time series of water surface position, from which a Fourier analysis creates an hourly set of H_s and T_p measurements. Although the data are limited, comparison of the predicted and measured nearshore waves show a close agreement, with a root mean square error of 22 cm. The transformation matrix works well for prediction nearshore swell waves ($T_p > 10$ s) but is less accurate for waves with short periods. This is expected to have a small impact on the above analyses, since the majority of waves responsible for closure at the site have periods above 10 s.

Chapter 4. Episodic Closure of the Tidal Inlet at the Mouth of the Russian River – a Small Bar-Built Estuary in California

Dane K. Behrens, Fabián A. Bombardelli, John L. Largier and Elinor Twohy

4.1. Introduction

Tidal inlets exhibit a range of behaviors that depend on their degree of tidal and fluvial influence, as well as their size, shape and stratigraphy. Small inlets ($A < 100 \text{ m}^2$) are commonly associated with bar-built estuaries, especially along active continental margins in Mediterranean climates, such as in California (e.g. Webb et al., 1991; Behrens et al., 2009), Chile (Dussailant et al., 2009), South Africa (Cooper, 2001) and Australia (Rustomji et al., 2007; Ranasinghe and Pattiaratchi 1998, 1999a, 2000; Gale et al. 2006, 2007). A hallmark of these systems is their unstable connectivity with the ocean, as waves periodically block the inlet channel with sediment. Despite this variability, these systems are vital for many species that have adapted to and thus take advantage of the closed inlet conditions (Becker et al., 2009). In western North America, the state of the inlet is increasingly recognized as a critical factor for endangered salmonid populations, which migrate into the estuary and upriver to spawn in seasons when the inlet is typically open, but may also use the lower estuary as a nursery when the inlet is closed during the dry season (Hayes et al., 2008). In addition to preventing navigation between the ocean and the lagoon, inlet closures effectively prevent tides and their associated turbulence from entering the estuary, which can have significant negative impacts on estuarine

mixing, circulation and flushing (e.g. Ranasinghe et al., 1999). Small inlet systems are also important in land-ocean sediment transport as they are typical of the mouths of rivers originating in high-gradient catchments, which are the dominant contributors of sediment to the world oceans (Syvitski et al., 2003).

Inlet morphology is governed by a balance between sediment import through wave-driven transport (constructive processes) and sediment export through tides and river flow (destructive processes) (e.g. FitzGerald, 1996). A state of dynamic equilibrium occurs when these transport rates balance, but this is rarely achieved for inlets with areas less than 100 m^2 because channel-bed friction at this scale constrains the flushing capacity of tides and river flow (e.g. Byrne et al., 1980). The resulting imbalance in sediment imports and exports may lead to changes in cross-sectional area ("constriction/expansion"; O'Brien, 1969), lateral movement of the inlet ("migration"; e.g. Aubrey and Speer, 1984), or loss of connection to the ocean ("closure"; Escoffier, 1977).

This study is focused on full closure of the inlet, which occurs when wave-driven sediment from onshore-migrating bars or longshore drift fully chokes the inlet (Ranasinghe et al., 1999). Although this is a widespread phenomenon, most of the existing literature is focused in a few regions: Australia (e.g. Ranasinghe et al., 1999; Rustomji, 2007), South Africa (Cooper, 2001), and the continental United States (e.g. FitzGerald, 1996; Goodwin, 1996). Most of these studies have addressed closure using analytical solutions to the equation of conservation of momentum (Rustomji, 2007), parametric models (O'Brien, 1976), numerical models (Ranasinghe et al., 1999), or

statistical models linking the state of the inlet solely with river flow (Elwany et al., 1998; Walker, 2003).

Anthropogenic changes to the estuary or watershed have in many cases altered the natural timing and duration of closure events. Dam construction in particular has been a common influence within the last century, altering both the hydrograph and the supply of bedload and suspended sediment to the mouth at many sites (Mount, 1995). Jetty construction is another common practice, used to maintain non-migrating, permanently-open inlet channels. Alternatively, manual opening ("breaching") after inlet closure is common in estuaries near local population centers (e.g. Ranasinghe and Pattiaratchi, 2003; Stretch and Parkinson, 2006). Although breaching may occur naturally as a consequence of ponding in the estuary after closure (Kraus et al., 2008), artificial breaching is often induced before this point to prevent total oxygen depletion in bottom waters (Gale et al., 2006; Becker et al., 2009), and to avoid flooding of low-lying areas (Behrens et al., 2009).

At present, much less is understood about the behavior of small, unstable inlets than that of their larger counterparts. Several factors contribute to this discrepancy:

- Many of the conceptual and analytical frameworks used with large inlets cannot be scaled down for use with smaller inlets (Mayor-Mora, 1977; Mehta, 1996). For example, Byrne et al. (1980) show that inlets with widths below about 100 m depart from Jarrett's (1976) widely used relation between tidal prism and inlet area. Also, the assumption that the inlet depth is much larger than the tide range, used in classical

models for inlet flows (e.g. Keulegan, 1967), is invalid for most small inlets (e.g. Byrne et al., 1980).

- River contributions are sometimes much larger than the tidal prism in small inlet systems. This is especially true for systems with high variability in river flow, where strong river flows can even prevent tidal waters from entering through the inlet (Largier, 1992; Ranasinghe and Pattiaratchi, 1999a). In contrast, large inlets often have a relatively large tidal prism, so that inlet flows can be estimated based on tides alone.
- Small inlets are less static than large inlets. While large inlets often respond to changing environmental conditions over periods of months to years (e.g. Van de Kreeke, 2004), small inlets respond on time scales of hours to days. Behrens et al. (2009) observe large changes within a tidal cycle.

Given the importance of small inlet systems to estuarine biota and regional and global sediment balances, it is important to address the present knowledge gaps. To allow for proper management in the future, it is also important to understand the differences between natural and human-induced influences on the closure pattern at these sites, especially as watershed populations increase and more sensitive estuarine systems and processes are altered by human activities. Further, understanding of the causes and consequences of closure events is increasingly important in projecting estuarine changes as sea level, wave heights and riverflow change as a result of climate change (e.g. Duong et al., 2012).

The objectives of this study are:

1. To document and describe tidal, seasonal and interannual variability in a small tidal inlet.
2. To identify and understand the physical processes leading to closure in this system.
3. To find a suitable model for predicting closure in the Russian River and similar systems.
4. To identify drivers of trends in closure patterns, including anthropogenic drivers.

The Russian River Estuary is representative of many other small inlet systems elsewhere in the world. A unique dataset at this site catalogues the closure conditions across seven decades in the twentieth century (Chapter 3). This study builds on earlier work with this dataset by Behrens et al. (2009), which linked the morphological behavior of the Russian River inlet to processes at separate time scales.

4.2. Study site: Present behavior and historical changes

When open to the ocean, the inlet of the RRE is in a continual state of morphologic adjustment: constricting, expanding, and laterally migrating within a 300 m span at the northern extent of Goat Rock Beach (Fig. 3.1). An illustration of closure and migration at the site is given for separate years in Figure 4.1. In a typical year, flood flows during winter remove much of the beach between the jetty and the rock wall

forming the northern boundary of migration. During peak flows above $1000 \text{ m}^3\text{s}^{-1}$, the inlet width often accounts for most or all of the 300m span, with the strong outflow jet directed northward, possibly as a result of the shape of the outer estuary (Fig. 3.1). When flows recede during spring, the inlet narrows and a bar begins to form at the northern boundary (Rice, 1974). Normally, the bar accretes on its southern edge, forcing the inlet to return to the southern boundary in a period lasting as little as weeks as long as several months. In some years, this southward migration is interrupted by closure events, but these do not appear to influence the direction of movement, and it was common for the inlet to be found adjacent to the jetty by summer (Behrens et al., 2009). Aside from this seasonal pattern, breach events sometimes are followed by short (< 4 week) periods in which the inlet migrates north for 0-100 m and subsequently returns to the south. These patterns are examined further in the results.



Figure 4.1. (top) An inlet closure event in October 2009 and **(bottom)** an example of the range of inlet migration. The dark object at the left is the rock jetty, indicated in Figure 3.1. Northward inlet migration is common after flood events, but also sometimes occurs directly after inlet breach events, as is shown here from 27-29 September 2003.

Early written records indicate that the closure pattern has changed over the course of the nineteenth and twentieth centuries. The records, summarized in Table 4.1, suggest a transition from a seasonal regime with inlet closures lasting several months during the dry season to a regime dominated by a high number of sporadic short-lived events centered in the spring and fall seasons. Journal entries from Russian settlers in Northern California confirm that the inlet closed periodically prior to 1840, but there is no mention of the frequency or duration of the episodes (Khlebnikov, 1990). When American settlers

established a major timber industry within the watershed after 1840, regular newspaper reports and documents of ferry operations indicate that the inlet was closed for the whole summer over a 20-year span between 1846 and 1866 (Finley, 1937). After six decades with no records, a water level gage operated by the California Department of Water Resources (DWR) tracked the inlet condition from 1931 to 1957 (Rice, 1974). During this time, closure events occurred in every month of the year, although they were mostly concentrated in late spring and fall, and lasted from as little as several days to as much as four months. After another absence of records from 1957 to 1973, direct daily observations of inlet condition were recorded by the fourth author of this study from 1973 to the present. Illustrated in Figure 4.2, this later period is dominated by closure events lasting less than two weeks, mostly falling within the spring and fall seasons.

Table 4.1. History of closure and human-induced changes within the Russian River estuary and watershed.

Period	Closure frequency	Breach frequency	Events
Pre 1840	periodic closure (duration and frequency unknown) ¹	Unknown	-Russian settlement at Fort Ross ¹
1840-1870	Seasonal closure during entire summer for 20 years ²	Unknown	-Extensive logging within watershed ²
1870-1931	Unknown	Unknown	-Eel River supplement flows (1908) -Expansion of supplement (1922)
1931-1957	0-6 yearly closure events mostly concentrated in spring and fall. Typical duration 1-4 weeks ³	Occasional breaches by local residents ⁴	-Single Jetty (1941)
1957-1973	Unknown	-Occasional breaches by local residents -Breaches by public agencies after 1960s ⁴	-Coyote Dam (1958) -inlet dredging in 1960s
1973-2009	0-15 yearly closure events. Typical duration < 2 weeks	80 percent of breaches artificially induced by various public agencies	Warm Springs Dam (1982) -minimum flow requirement (1986) -Current breach protocol created (1994)

¹(Khlebnikov, 1990); ²(Finley, 1937); ³(Rice, 1974); ⁴(Schrad, 1992)

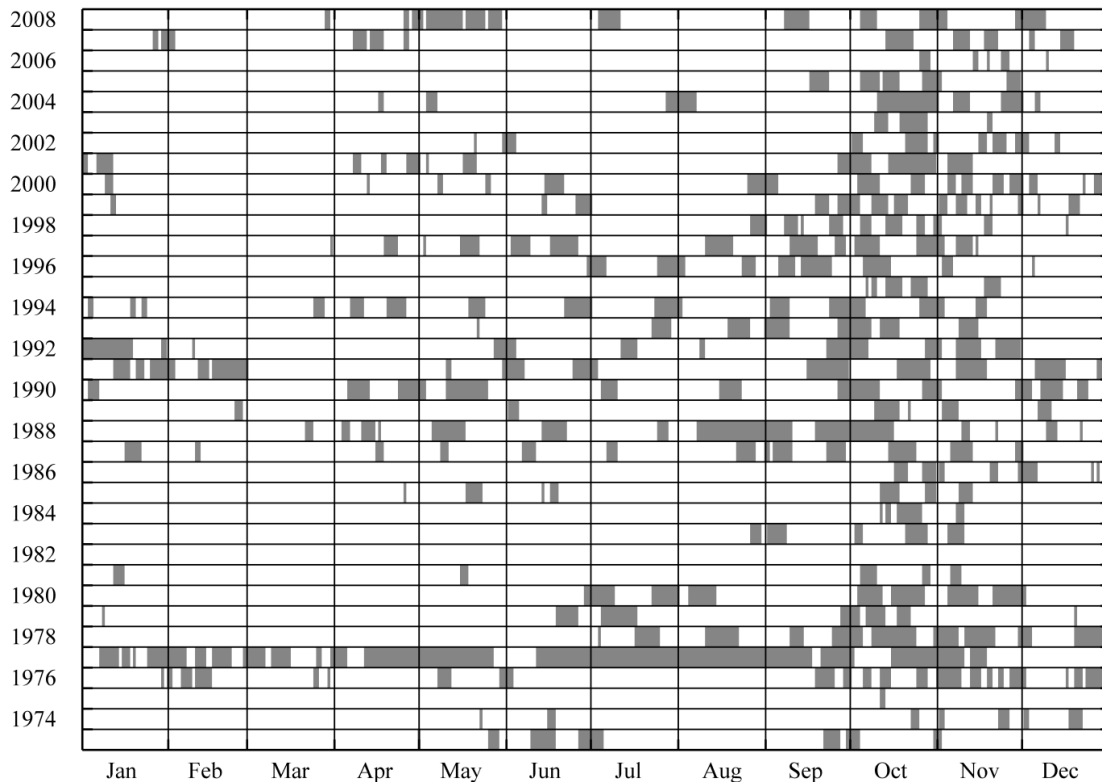


Figure 4.2. Closure record from 1973 to 2009. White (grey) spaces indicates periods when the inlet was open (closed). Extreme drought (1977) and flood (1975, 1982) years are apparent. Nearly 80 percent of closure events during this period were ended manually when heavy equipment was used to dig a trench across the beach.

4.3. Methods

4.3.1 Data collection

The analyses in this chapter primarily rely on the extensive records of daily inlet condition at the site. The records of offshore waves and river flow (Table 3.1) are used to understand forcing from the coastal and fluvial boundaries of the estuary, respectively, and these are compared against the time series of inlet condition to infer relations between external forcing and inlet response. Hourly estimates of total flows through the

inlet (from combined tides and river flow) were found by using estuary tide levels provided by SCWA in conjunction with a stage-storage relation derived from the 2009 estuary bathymetry (EDS, 2009). Together, these provide a time series of the change in estuary volume per hour, which can be added with hourly river discharge rate to give an estimate of the total flow rate through the inlet.

4.3.2 Model description

We use a simple parametric model to predict closure events. It bears some similarity with those of Bruun and Gerritsen (1960) and O'Brien (1976) but differs in its treatment of inlet flows. The model is based on a one-dimensional, along-channel sediment mass balance for the inlet with considerations for the sediment gain (imports) and losses (exports) in the system. Due to the inherent uncertainty in estimates of sediment transport in such a complex environment, this is intended as a scaling approach, with the potential for further refinement when detailed sediment transport data are available. The Exner Equation in one dimension (Julien, 1998; Garcia, 2008) describes the sediment balance:

$$\frac{\partial \eta}{\partial t} = - \frac{1}{(1 - \lambda_p)} \frac{\partial q}{\partial x} \quad (4.1)$$

where η [L] is the bed elevation above a datum, λ_p [L^3/L^3] is the sediment porosity, q [L^2/T] is the along-channel volumetric flow rate of sediment per unit cross-section width and t [T] and x [L] are time and along-channel distance, respectively. In this study, we take q as the total of both bedload and suspended sediment. According to Eq. (4.1),

changes in the bed elevation result when the term $\partial q/\partial x$ is nonzero. If we represent the inlet as a single control volume:

$$\frac{\partial q}{\partial x} \approx \frac{q_{\text{export}} - q_{\text{import}}}{L} \quad (4.2)$$

where L [L] is the length of the inlet, q_{import} is the sum of the sediment imports to the inlet, and q_{export} is the sum of the sediment exports from the inlet (Fig. 4.3).

For an inlet to be stable against sedimentation and eventual closure, the change in the bed elevation must be zero or negative (steady or eroding), which gives the need for $\partial q/\partial x \leq 0$ from Eq. (4.1). From Eq. (4.2) one can then get the following condition for inlet stability:

$$\phi_1 = \frac{q_{\text{import}}}{q_{\text{export}}} \leq 1 \quad (4.3)$$

where ϕ_1 is an index of stability. Below we outline our methods for estimating q_{import} and q_{export} in the model.

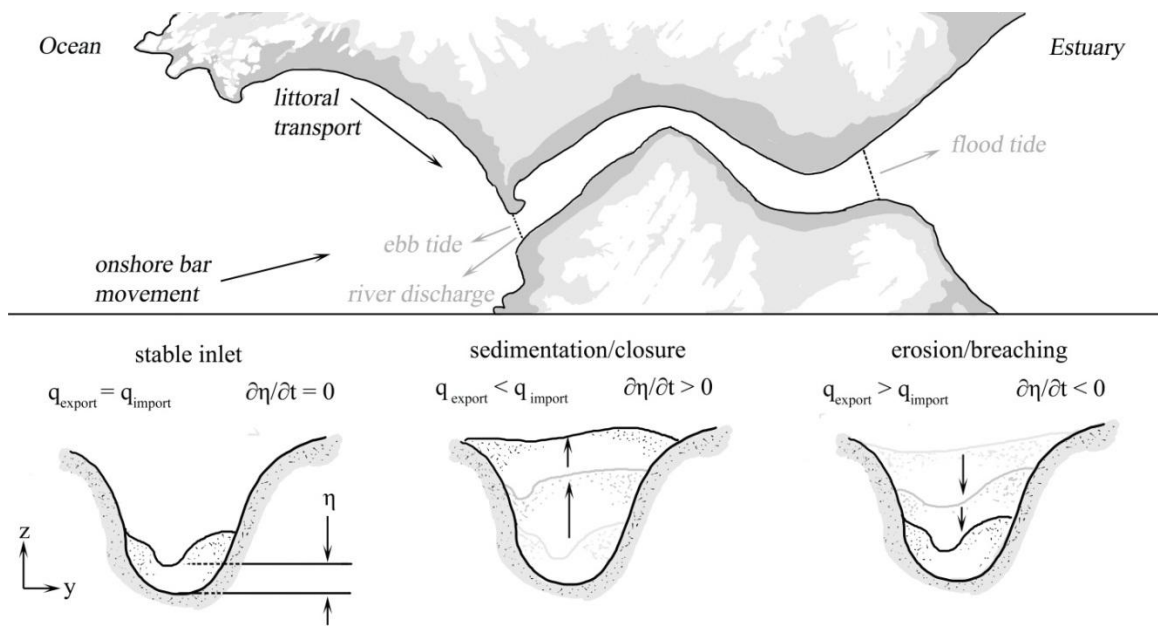


Figure 4.3. Schematic of an inlet indicating processes leading to sediment import to the inlet (black text) and sediment export (grey text) and **(bottom)** illustration of inlet conditions discussed in this study. We consider inlet stability in the context of sedimentation/erosion within the inlet channel. We assume that riverborne sediments must be reworked by waves to cause sedimentation.

4.3.2.1. Sediment import

Following Ranasinghe and Pattiaratchi (2003), sediment import to the inlet results when onshore migrating bars weld onto the beach (cross-shore transport, CST) or when the inlet traps sediment from an alongshore current (longshore transport, LST). Based on Johnson's (1973) assessment of the conditions in the Russian River's littoral cell, we assume that CST is negligible compared with LST for this site (also assume negligible import from estuary side of inlet). While this may be true of time-averaged intervals, Cooper (1990) has shown that CST can be important immediately following breach events. We check the CST assumption in Section 4.3 using the Dean Number (Dean and Dalrymple, 2002). Given the high trapping efficiency of inlets (Dean and Walton, 1973),

we assume that the LST-derived sediment transport into the inlet, q_{LST} is proportional (hereafter we use a tilde to indicate proportionality) to the total volumetric flow rate on the adjoining beach, Q_{LST} . We choose the commonly-used energetics approach to estimate Q_{LST} , which assumes that Q_{LST} is proportional to the shore-parallel component of wave energy flux (US Army Corps of Engineers, 1984):

$$Q_{LST} \sim P_l = \frac{1}{16} \rho_o g H_b^2 C_g \sin 2\theta_b \quad (4.4)$$

where $C_g = (gd_b)^{0.5}$ is the group speed of incident waves, ρ_o [ML^{-3}] is the density of seawater, g [LT^{-2}] is the gravitational acceleration and d_b [L], θ_b [$^\circ$] and H_b [L] are the depth, incident angle and height of the waves at the breaker line, respectively. There are several other models for determining Q_{LST} , with the greatest differences being the level of emphasis on the directional term and the inclusion of additional terms such as sediment size and wave period (e.g. Alegria-Arzaburu and Masselink, 2010). The energetics method is preferable in this case because it requires little data, which is important given that many small inlet systems are located in regions that are not intensively monitored.

Since breaking wave height and direction data are not available at the mouth of the Russian River, we assume that H_b is proportional to H_s estimates at 10 m depth and we assume a constant wave angle of 45 degrees. However, since we have chosen to represent sediment import as a function of LST, directional data are an important component and should be included in future work with similar systems if data are available. We supplement the resulting LST per unit length of the beach by including a beach length scale (L_b):

$$q_{import} \sim \rho_o g H_s^2 C_g L_b \sin 2\theta_b \quad (4.5)$$

We have included L_b merely to differentiate between systems with extensive littoral supply and those with more limited supply, such as inlets within small embayments. It is intended to be a measure of the inlet-affected coastline. For an inlet acting as a sediment sink on a small embayed beach, it would span the distance between the inlet and the nearest updrift headland. For a very long, straight updrift beach, it would reach an upper limit of approximately 25 km (Galgano, 2009). For simplicity, we scale L_b as the distance between the jetty and the northern rock wall (Fig. 3.1), although it clearly may change as wave direction or inlet position change. Even so, we will later show that it provides a better scale than the inlet width (e.g. O'Brien, 1976) in quantifying the sediment supply to the inlet.

4.3.2.2. Sediment export

Inlet throughflow scours sediment from the channel by increasing shear stress at the bed (Van de Kreeke, 1985). Using a mass balance for the inlet, after Keulegan (1967), we define the total throughflow resulting from both river and tidal components:

$$Q_{inlet} = -A_s \frac{d\eta_e}{dt} + Q_r \quad (4.6)$$

where A_s [L^2] is the surface area of the estuary, η_e [L] is the water surface elevation in the estuary, and Q_r [L^3T^{-1}] is the volumetric river discharge. Since it is difficult to measure the shear stress directly, sediment export has been attributed to a number of other parameters, many of which are reviewed by Van de Kreeke (2004). Many of these are based on inlet velocity, which cannot be obtained from Eq. (4.6) without knowledge of

the inlet cross sectional area, a parameter that is difficult to predict for small inlets (Byrne et al., 1980). We instead adopt an energetics approach based on the method of Bagnold (1966) and later applied by O'Brien (1976), and associate sediment export with the rate of change of potential energy in the estuary during tidal fluctuations. The appeal of this approach is that it only requires knowledge of the basin hypsometry and a time series of water levels. Bruun and Gerritsen (1960) and O'Brien (1976) applied this approach using bulk parameters such as the tidal prism and bulk tide range. The change in potential energy in a given measurement interval can be defined as:

$$\Delta PE = \rho_e g \Delta \eta_e \Delta V_e \quad (4.7)$$

where ρ_e [ML^{-3}] is the estuary density, $\Delta \eta_e$ [L] is the change in estuary water level and ΔV_e [L^3] is the change in estuary volume, found by integrating the first term on the right hand side of Eq. (4.6) with respect to time. If taken for the duration of a tidal cycle, ΔV_e is the tidal prism. After O'Brien (1976), the sediment export is associated with the power of the flow, which can be defined as the rate of change of potential energy in the estuary resulting from water level fluctuations:

$$q_{\text{export}} \sim \frac{dPE}{dt} = \rho_e g \Delta \eta_e \left(A_s \frac{d\eta_e}{dt} \right) \quad (4.8)$$

Though q_{export} can be estimated for any data sampling rate, we use representative daily values to match the sampling frequency of our other measurements. We use the maximum hourly value of q_{export} measured in a given day to characterize this, and signify it with the subscript "max".

Although we have chosen to emphasize the influence of tides here, q_{export} can be associated alternatively with Q_r when river flows are more important, as we will later show in Section 4.3. In the results, we represent sediment export as a function of either tidal fluctuations or river flow, but not both. It would be useful in subsequent work to arrive at a single export term that combines both, but this was beyond the scope of the present study.

4.3.2.3. Parameterizing inlet stability

After substituting our approximations for q_{import} and q_{export} into Eq. (4.3) we have:

$$\phi_1 = \frac{\rho_o g H_s^2 C_g L_b \sin 2\theta_b}{(dPE/dt)_{\max}} = \frac{\rho_o H_s^2 C_g L_b \sin 2\theta_b}{\rho_e \Delta \eta_e \left(A_s \frac{d\eta_e}{dt} \right)_{\max}} \quad (4.9)$$

As ϕ_1 increases, we expect the likelihood of inlet closure to increase, with the opposite true for a decrease. O'Brien (1976) reaches a similar result after framing the problem as a power balance:

$$\phi_2 = \frac{\rho_o g H_s^2 C_g W}{(dPE/dt)_{\text{bulk}}} = \frac{\rho_o H_s^2 C_g W}{\rho_e F P \Delta h / T_t} \quad (4.10)$$

Given that
$$\left(\frac{dPE}{dt} \right)_{\text{bulk}} = F \frac{P}{T_t} \Delta h \quad (4.11)$$

where W [L] is the inlet width, P [L³] is the tidal prism, T_t [T] is a representative tidal period, F is the fraction of potential energy used to overcome friction and velocity head in the inlet and Δh [L] is the bulk tide range. and all other terms are the same as defined above. The numerator is a “wave power” term which represents the rate of energy

supplied across the width of the inlet throat by normally-incident waves whereas the denominator is a “tidal power” calculated from bulk tidal parameters. Battalio et al. (2006) used Eq. (4.10) to model stability of a small inlet inside San Francisco Bay with little river inflow, while Goodwin and Cuffe (1994) used Eq. (4.10) with an added Q_r term to characterize stability of the Russian River inlet during the years 1992-1993. The primary difference between ϕ_1 and ϕ_2 is the absence of W in the numerator – while smaller W in larger inlets will lead to faster flow, in smaller frictional inlets this is not the case (more likely the opposite is true with small W indicating additional frictional and slowing of the tidal flow). W is replaced by L_b . Also, the parameter F does not appear in ϕ_1 as small inlets remain in the frictional regime. Otherwise, $P T^1$ is replaced by $A_s d\eta/dt$ and Δh is replaced by $\Delta\eta$.

We compare these stability indices ϕ_1 and ϕ_2 as well as single-parameter indices (like H_s) with the observed closure record in Section 4. Based on the assumptions used in their derivation, these models are not applicable where littoral drift is not the dominant supply of sediment to the inlet. Furthermore, although inclusion of additional parameters (e.g. variable wave direction, sediment size) may improve the skill of similar indices, we lack the data to properly evaluate these additional factors and further complexity in the index formulation is unlikely to improve skill without adequate data resolution and confidence. Here we rather show the ability of a relatively simple model to predict closure events.

4.4. Results

4.4.1. Temporal characteristics

From the closure record of the Russian River for 1973 to 2009, we determine the most important time scales of inlet variability. The record is decomposed into a signal by treating the inlet condition shown in Figure 4.2 as a variable: assigning values of unity to days when the inlet is closed and values of zero when open. This signal is analyzed with a Fast Fourier Transform (FFT), giving the result shown in Figure 4.4. The raw transform is filtered in the frequency domain using a 5-point Daniell filter (Bloomfield, 2000) to improve confidence. Three distinct spectral regions are evident: (i) broad high-frequency peak with maximum at 10-30 days, (ii) narrow seasonal peak at 365 days with additional seasonal harmonic at 182 days, and (iii) interannual variability. The high-frequency peak is not significant at the 95 percent level, but is noticeable because it is bordered by a region of rapid decay in spectral density with higher frequencies. While more confidence is needed to ascertain any potential meaning of a peak in this location, it seemingly matches with spring-neap tidal variations (28 days) and decreasing variability at synoptic time scales associated with winds (Largier et al., 1993) and waves. The seasonal peaks are presumably driven by strong seasonal variability in river flow and waves (Behrens et al., 2009). Both the peaks at 365 days and 182 days are significant at the 95 percent level. Interannual variability is presumably also associated with interannual variability in riverflow and waves. We investigate these assumptions in the remaining sections.

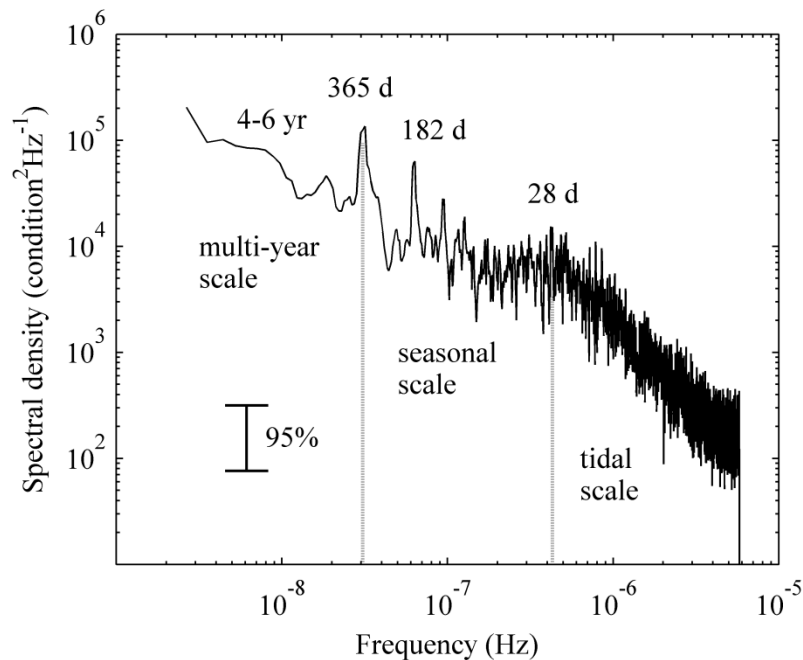


Figure 4.4. FFT visualization of the 1973-2009 daily inlet condition. Data are smoothed in the frequency domain to improve confidence and the 95 percent confidence interval is indicated. The peaks at 365 and 182 days are statistically significant at this level.

Approximately 80 percent of inlet opening events after 1973 were non-natural, so closure periods were almost always brief (Fig. 4.2) and the variability in inlet condition can be assumed to be dominated by the timing of closure events. Thus, the spectral features in Figure 4.4 are interpreted as the time scales of closure dynamics. Although artificial breaches probably alter the duration of closure events heavily (see Section 5.3) and provide offshore sediment deposits which can encourage subsequent closure events (Cooper, 1990), we assume that the closure record still reflects the interplay of the same sediment transport processes that cause closure events in the natural state. Analysis of the influence of breaches on subsequent closures is not within the scope of the present work, but will be addressed in a subsequent study. Sensor malfunctions of the water level gauge

interrupt the closure record from 1931-1957, which prevented the possibility of using an FFT on this period.

4.4.2. High-frequency variability

Mouth conditions vary on time scales of days to weeks in response to changes in tides, waves and river flow. Although the effects of human intervention on mouth conditions are also important at this scale, this is discussed in Section 5. At the highest frequencies (time scales of 28 days or less), we study closure events by examining the association between some of the forcing parameters (e.g. Q_{inlet} , H_s) and closure occurrence. We use the period from 1999-2008, since water level, inlet flow and wave conditions were available for every day in this range. We use the models defined in Section 3 to predict closure likelihood, which we quantify by introducing a parameter called the "five-day closure risk". We define this as the proportion of times that a closure event occurs within five days after a certain condition is observed. For example, the five-day closure risk for a day with H_s at the 20th percentile (0.19 m) is 0.26, which indicates that one in four times that waves of $H_s = 0.19$ m are observed a closure event occurs within five days. We choose a five-day window as the mouth does not close instantaneously – it can take several days for sediment to accumulate. An analysis of closure response shows that when wave and inlet conditions are conducive to closure on any given day within the period 1999-2008, the risk of inlet closure within the next five days is elevated above the average risk. After this time, the risk of closure occurring on each day returns to the long-term average for the period.

We also look at conditions immediately prior to closure (one-day closure risk), although we recognize autocorrelation in tide and wave conditions (conditions may not change much over intervening 4 days). The proportion of times that closure occurred within one day of each combination of wave and inlet-flow parameters is illustrated in Figure 4.5 for 1999-2008. As expected, closures are more common for days with relatively high waves and low inlet currents. For days with $Q_{inlet, max}$ above $40 \text{ m}^3\text{s}^{-1}$ (8th percentile) or H_s below 0.3 m (25th percentile), there is very low probability of closure within a day (less than 20 percent). Although closures occurred during most wave conditions, the proportion of times that the inlet closed within one day increases drastically as wave height increases. A similar increase occurs as $Q_{inlet, max}$ decreases below $40 \text{ m}^3\text{s}^{-1}$ (8th percentile). Conversely, high inlet currents severely limit the potential for closure, evidenced by the fact that no closure events occurred within one day of $Q_{inlet, max}$ exceeding $58 \text{ m}^3/\text{s}$ (25th percentile), irrespective of wave conditions. During the majority of the study period, river flow comprised less than 20 percent of total inlet flows.

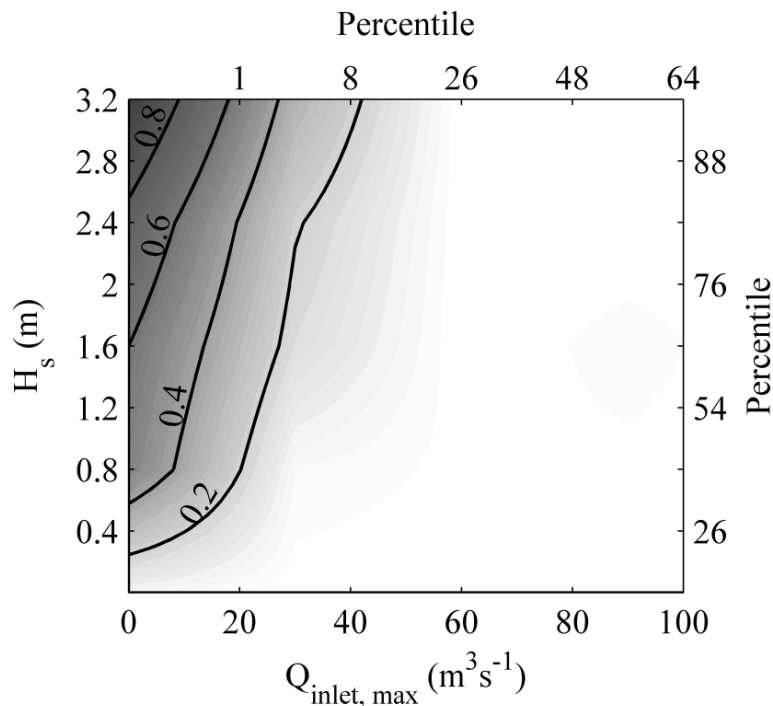


Figure 4.5. Proportion of days within one day of a closure event, based on the nearshore wave height (H_s) and peak daily inlet flow ($Q_{inlet, max}$). This reflects data from the years 1999-2008, when a tide gage was operated within the estuary. Except during winter, the majority of $Q_{inlet, max}$ is associated with tides.

Probability distribution functions (pdfs) are calculated for several variables. Two sets of pdfs were constructed for each variable, one for all datapoints during 1999-2008, and another only for datapoints within five days prior to closure events during 1999-2008. These two sets are compared in Figure 4.6 for nearshore wave height, period and steepness (top row), and also for the tidal prism, inlet aspect ratio and peak daily inlet flow (bottom row). For the three wave parameters tested, conditions prior to closure differ little from overall conditions – indicating that typical wave conditions are likely sufficient to cause closure. In contrast, there are big differences for inlet flow parameters, with the overall mean for each parameter being approximately double the mean prior to

closure (strong flows preclude closure irrespective of wave height). The distribution for the inlet aspect ratio (WL^{-1}) prior to closure is skewed to the left, indicating that the inlet tends to become more sinuous before closure events, as reported by Behrens et al. (2009). This type of shape is less hydraulically efficient, suggesting that frictional losses often play an important role in closure. Overall, these data indicate that hydraulic parameters are the limiting factors for closure at the tidal time scale, rather than sediment delivery from waves.

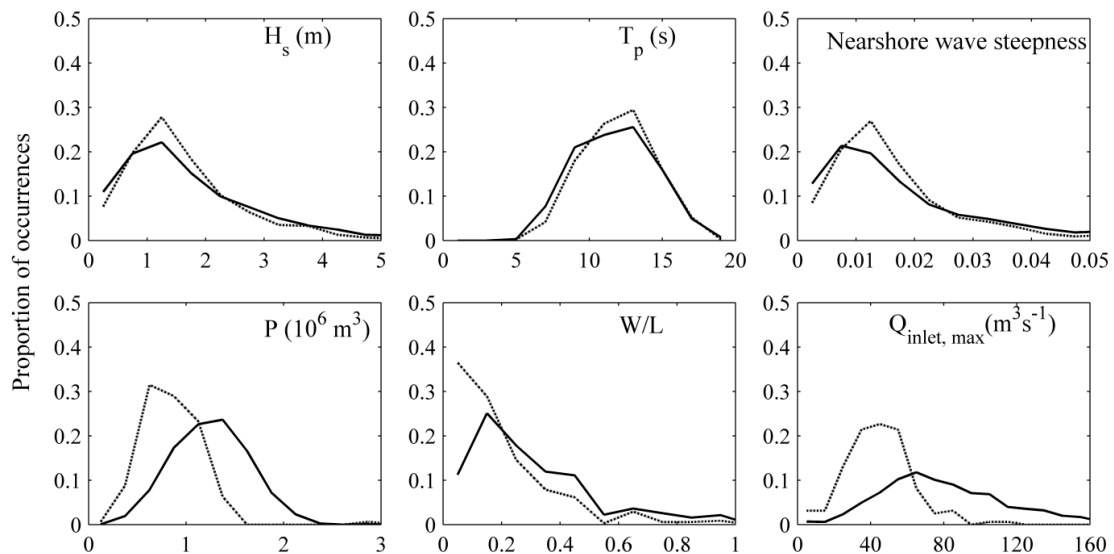


Figure 4.6. Probability distribution functions of wave parameters (upper row) and inlet hydraulic parameters (bottom row). Solid line represents all data from the years 1999–2008. For the same period, dashed line only includes datapoints within five days prior to a closure event.

The predictive ability of ϕ_1 and ϕ_2 and several other parameters are tested using the five-day closure risk. As discussed in Section 4.3, the models produce an index value, which is calculated for each day using the available wave and hydraulic data. To compare the different models directly, we sort their outputs by percentiles and compare this

against the corresponding five-day closure risk. An ideal model would produce a step response: for outputs exceeding a certain threshold percentile on a given day, the risk of closure is 100 percent and below the threshold closure risk is zero. We compare the models based on the extent to which they approach this skill.

Fig. 4.7a shows that for low-flow conditions (typical of summer), the chance of closure occurring within five days increases nonlinearly with increases in H_s – for the largest 20-percentile, closure will happen in 4 out of 5 cases. If days with higher flows are included, the risk of closure decreases for high waves, because high waves are typically associated with high flows during storms. The hydraulic parameters shown in Figure 4.7b, $Q_{inlet, max}$, $W L^{-1}$ and $dPE/dt, max$, all show strong inverse relationships with closure risk. The latter is true because $Q_{inlet, max}$ is often dominated by tidal flows at this site. Our stability parameter (Eq. 4.9) has the best response to the closure risk. It produces a highly nonlinear slope past its 70th percentile, indicating that sedimentation in the inlet increases significantly past this point. Although O’Brien’s parameter ϕ_2 (Eq. 4.10) also appears to have some predictive capacity, it only experiences a weak linear increase in closure risk with higher percentiles (Fig. 4.7c) -- the highest closure risk associated with this model is 0.3, compared with 0.8 for ϕ_1 (Fig. 4.7d). Using bulk parameters (Eq. 4.11) to define the sediment export rather than Eq. (4.8) reduces the predictive ability of the model slightly, from a peak closure risk of 0.8 to 0.6. The ϕ_1 index can be fit against the closure risk with a logarithmic curve to create an empirical closure risk relation for the Russian River.

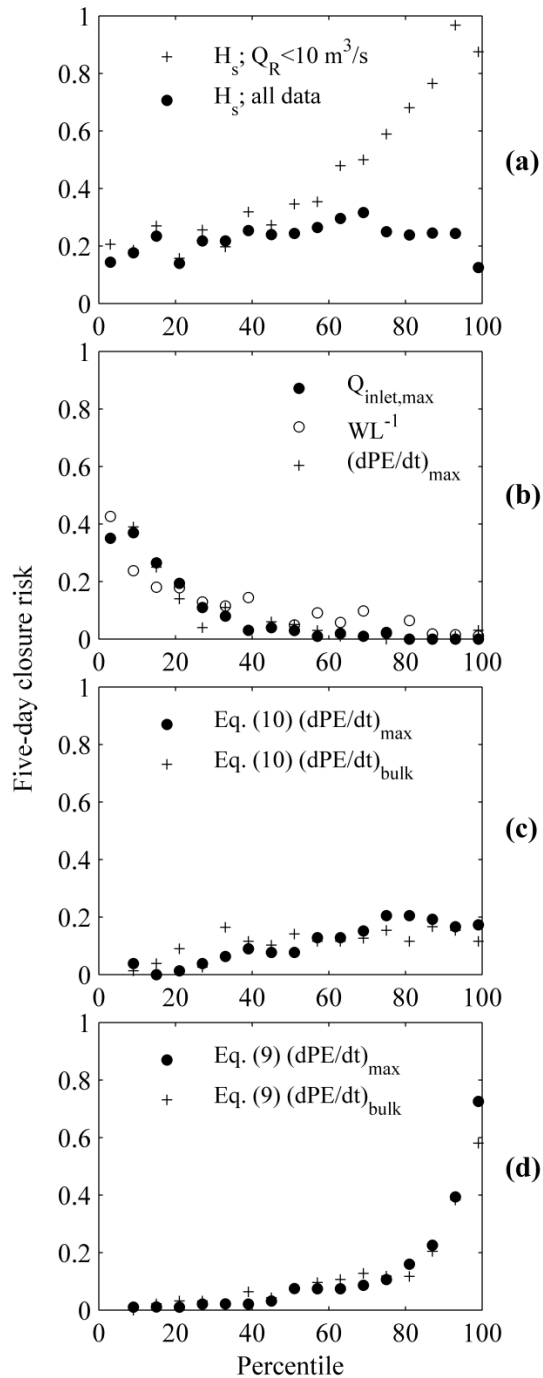


Figure 4.7. Comparison of five-day closure risk based on (a) wave height (b) inlet hydraulic parameters and (c,d) the closure parameters ϕ_1 and ϕ_2 . Parameters are normalized based on percentile to allow direct comparison.

4.4.3. Seasonal variability

Annual variability dominates the spectrum (Fig. 4.4), as can be expected given the marked seasonal cycles observed for rain and river flow, as well as wave energy (Fig. 4.8). But, while wave height, river flow and inlet position exhibit predictable seasonal cycles, the difference in phase of these cycles and the importance of high-frequency variability lead to a seasonal cycle in closures that shifts from year to year. To examine the influence of each of these factors at this scale, we condense the data into a single representative year by averaging conditions across each Julian day (Fig. 4.9a) – this is done for nearshore waves, river flow and the bulk estuary tide range Δh . The key differences apparent in this illustration are: (1) that river flow varies by 2-3 orders of magnitude while waves vary by one and tides vary by less than one, and (2) that waves increase earlier than river flow in early fall. The second point is especially clear from September through November, leading to an imbalance between sediment supplied to the inlet and the ability of the inlet to flush it out, which is seen as a substantial increase in closure likelihood during these months (Fig. 4.9c). The dominant 365-day period in Figure 4.4 is likely caused by the high risk of closure during these months.

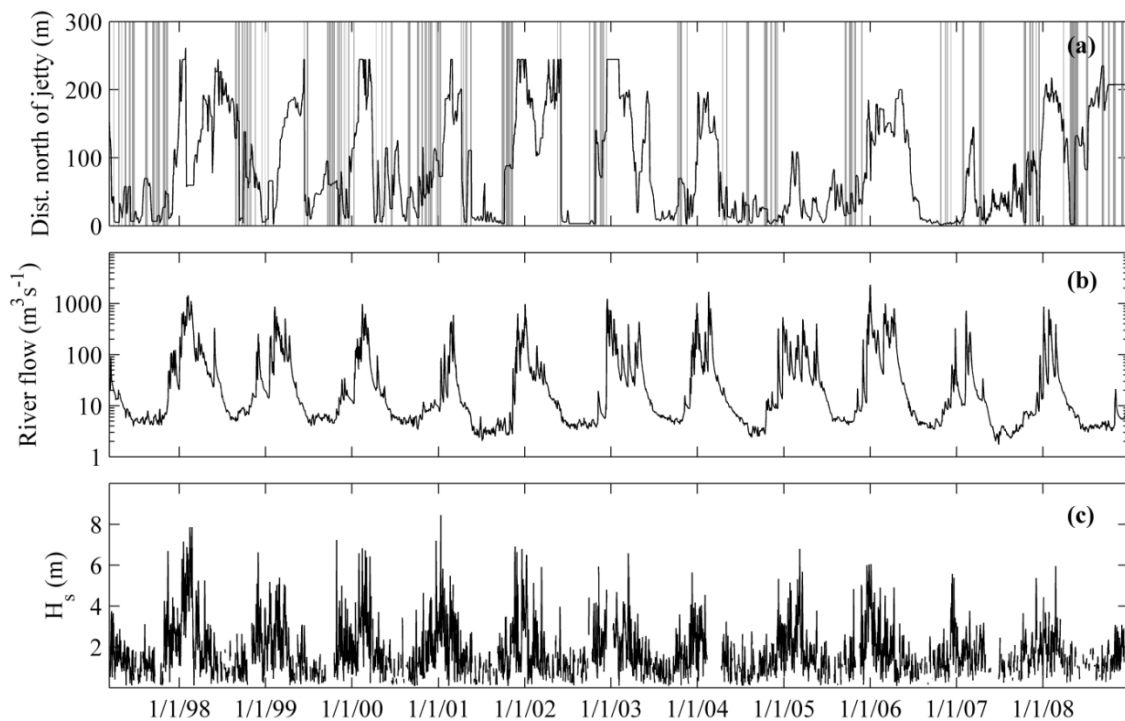


Figure 4.8. Comparison of **(top)** inlet position, **(middle)** river discharge and **(bottom)** nearshore significant wave height between the years 1997 and 2008. Vertical grey bars in top plot represent inlet closure events. Inlet position is defined by the centerline of the inlet. Although all parameters appear to have similar seasonal fluctuations, their phases occasionally differ. For instance, this is visible for waves and river flow during the 2000-2001 wet season.

The seasonal change in wave steepness can help determine whether closure events are caused by onshore bar movement (CST) or shore-parallel littoral drift (LST). Figure 4.9b compares nearshore wave steepness to seasonal values of the Dean Number, as defined by Dean and Dalrymple (2002). The Dean Number is a heuristic model combining wave height and period with the settling velocity of sediment in the nearshore zone. When wave steepness is larger than the Dean Number, sediment is generally not transported onshore, meaning that the most likely source of sediment to the inlet is LST. When the Dean Number is larger, sediment is most likely delivered in the form of bars

approaching the inlet perpendicularly from offshore (Dean and Dalrymple, 2002).

Ranasinghe and Pattiaratchi (1999b) demonstrated the usefulness of this parameter for determining the mode of sediment delivery to Wilson Inlet in Australia. Settling velocity was calculated after Jimenez and Madsen (2003), using the documented D_{50} grain size of 1.02 mm for Goat Rock Beach (US Army Corps of Engineers, 1965). Nearshore wavelength, used to derive wave steepness, was estimated for a 10 m depth offshore of the inlet from deepwater values, after Fenton and McKee (1990). Figure 4.9b indicates that closures in late fall, winter and spring are likely the result of littoral drift, and that both LST and CST are probable causes during summer and early fall.

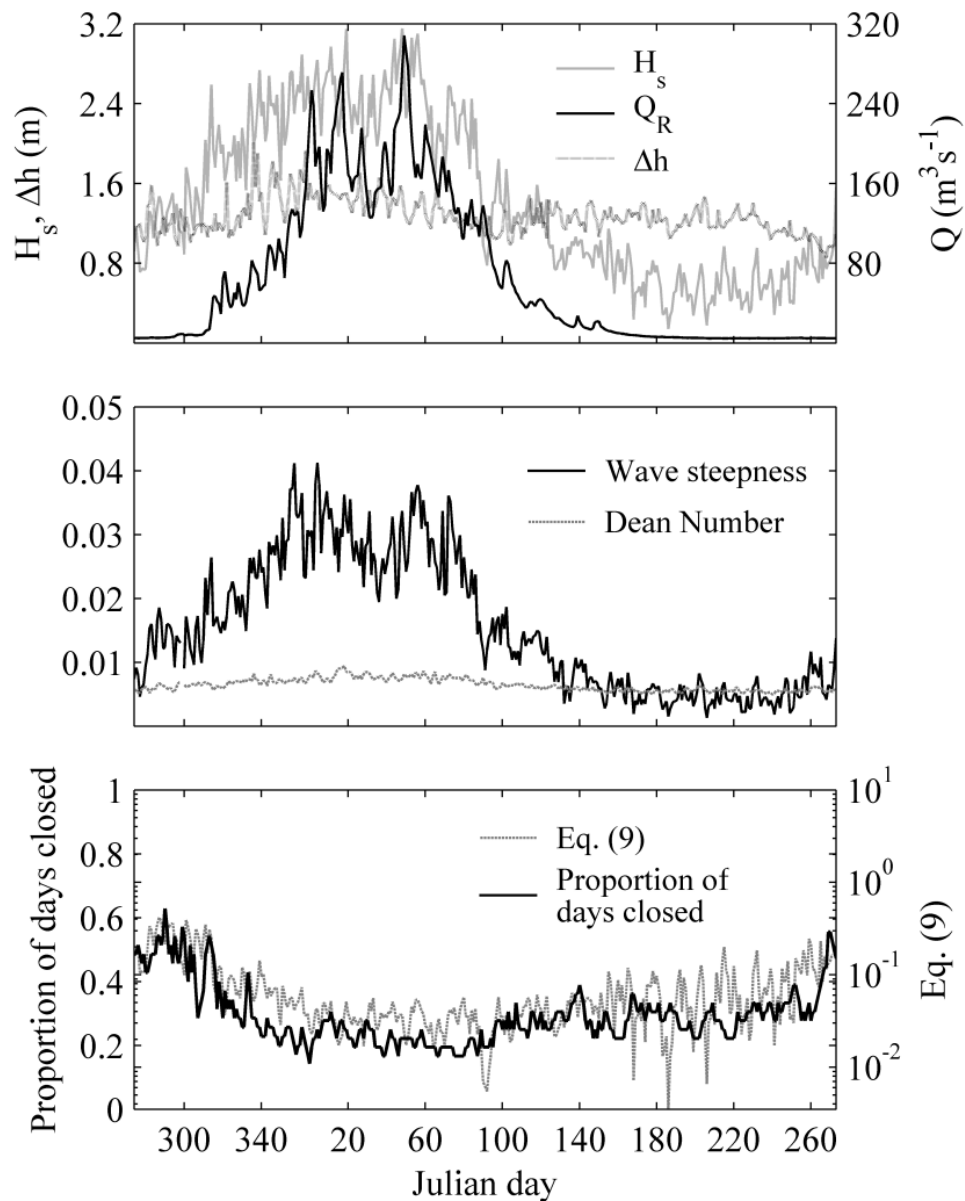


Figure 4.9. Seasonal cycles determined from Julian day averages of **(top)** river discharge, wave height and estuary tide range, **(middle)** wave steepness and Dean Number, and **(bottom)** the proportion of days closed and parameter ϕ_l using only Q_r in the denominator. Each data point represents the average across its Julian day for the period that the data were available. Wave, river flow and inlet condition data are averaged using the period from 1981-2008, while tide range data reflect the period 1999-2008.

Tides vary little through the year, thus in plotting seasonal changes in ϕ_I we replace the tidal terms in the denominator of Eq. (4.9) with Q_r . While it would be more accurate to refer to the inlet velocities resulting from the river flow (as these are closely related to bed shear), this would require estimates of the inlet cross sectional area, which were unavailable. The seasonal variability in Q_r is thus taken as a surrogate for seasonal variation in sediment export, since tides show little variation at this scale. We compare ϕ_I and the annual closure pattern in Figure 4.9c: the two signals have a very strong correlation ($r = 0.64$, $p < 0.001$) indicating that the model is a good descriptor of seasonal variability at the Russian River despite the simplicity of our representation of sediment export.

4.4.4. *Interannual variability*

Year-to-year changes in the frequency of closure of the mouth are shown in Figure 4.10, allowing comparison with year-to-year variability in river flow and climate indices. A closure anomaly is calculated as the number of days closed in a year minus the long-term average of 47 days per year. Notable periods are seen during the drought experienced in the late 1970s (specifically noting the 250 days of closure in 1977) and during the wet years of the early 1980s, which are well known as a major El Niño phase. In general, the inlet is closed more often in drier years than in wetter years, similar to results found for the San Dieguito River in California (Elwany et al., 1998) and the Murray River in Australia (Walker, 2003; Rustomji, 2007). There is no notable relation between annual statistics of waves and the closure anomaly. Consistent with Figures 4.5

and 4.6, wave conditions are less important for closure events than river flow conditions at the Russian River.

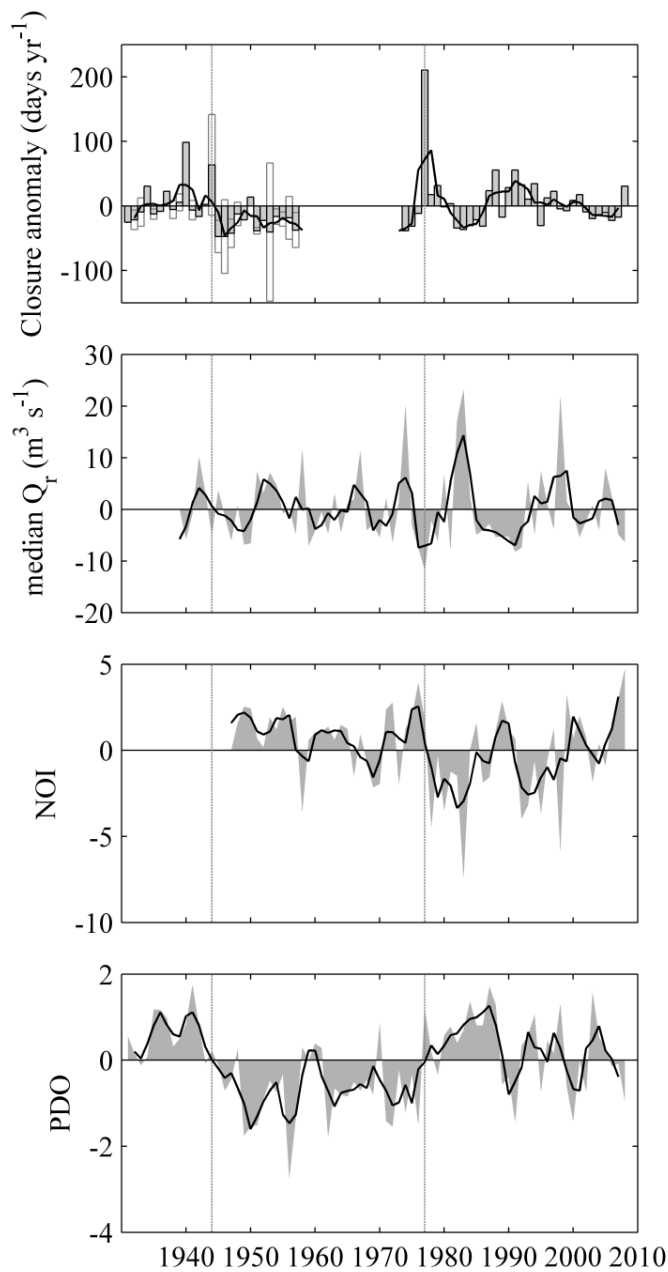


Figure 4.10. Multi-year records of **(top)** closure anomaly, **(second)** median annual river discharge, **(third)** NOI signal and **(bottom)** PDO signal. NOI and PDO values represent October-March averages. Error bars in top plot reflect periods of recorder malfunction. Grey areas are observed values and solid black line is a three-year moving average.

The relationship between river flow and days of closure depends not only on river flows that are low enough to allow wave action to close the mouth but also on river flows that are low enough to allow many days to pass before the estuary fills to the crest of the wave-built sandbar, resulting in overflow and mouth breaching. This second factor is explored through plotting days closed against river flow rate during the closure (Figure 4.11). The qualitative envelope to the right of the data can be explained with a mass balance approach for the estuary after closure. For a given height H of the sandbar crest above estuary water level, the time it takes for the ponding water to overflow over the beach is $t_{over} \sim A_s H Q_r^{-1}$. While the mouth may open for other reasons, such as human intervention, this expression provides an approximate curve that defines the maximum time that the mouth may stay closed under given flow conditions. The expression may be altered to account for seepage through the sandbar or non-breaching overflow Q_{bar} so that $t_{over} \sim A_s H (Q_r - Q_{bar})^{-1}$ and the curve will be shifted to the right by amount Q_{bar} . Not only does Figure 4.11 help to explain the observed relation between the closure anomaly and the river flow, but it exhibits a marked shift in the curve between earlier years (1931-1957) and later years (1973-2009), suggesting a fundamental change in the water balance and mouth management (actions that limit closures to a couple of weeks shift data points down for typical spring and fall flows of 5-10 m^3s^{-1}).

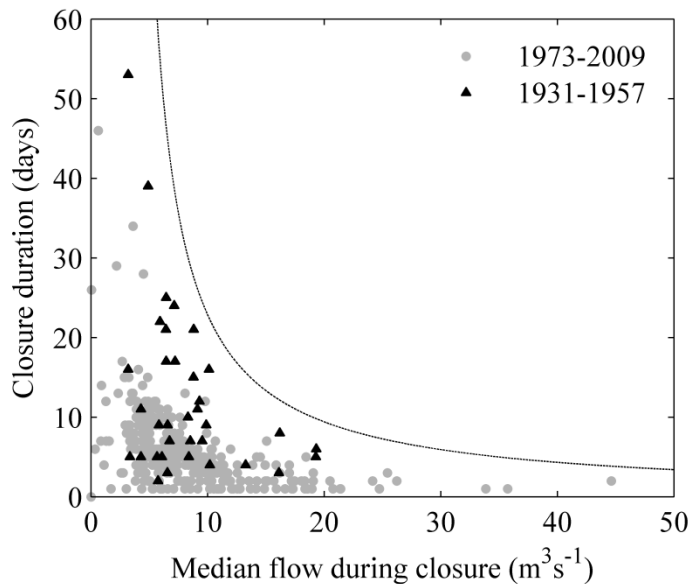


Figure 4.11. Duration of closure periods based on median flow during closure. Dashed line illustrates the potential for an envelope of limiting conditions following the expectation that $t_{over} \sim (Q_r - Q_{bar})^{-1}$. The envelope is intended to illustrate a possible limiting condition and is not validated. It is based on the assumption that barrier seepage is nonzero, which will be tested in a subsequent study.

4.5. Discussion

4.5.1. Stability parameter and prediction skill

The success of our parameter ϕ_I shows the viability of a simple sediment balance approach for predicting closure likelihood in a small inlet system. While this concept is not new, its flexibility allows us to unify some of the existing models which have worked well in special cases. For example, when tides are the dominant source of flow variability (i.e. when Q_r can be neglected) the model resembles those of Bruun and Gerritsen (1960) and O'Brien (1976), whereas when river flow is the dominant source of variability (when

$\Delta\eta$ and $A_s(d\eta_e/dt)$ can be neglected) it resembles those of Elwany et al. (1998) and Walker (2003), although these ignore the influence of waves.

Eq. (4.9) performs better than the O'Brien (1976) model (Eq. 4.10) because the latter uses the assumption that the closure risk is proportional to inlet width (since more wave energy arrives at the inlet throat for greater widths). The results indicate that the opposite is actually true for smaller inlets, like the Russian River – smaller widths lead to substantially greater risk of closure. This is reflected in the inlet aspect ratio ($W L^{-1}$) which is shown to decrease prior to closure (Fig. 4.6). This narrowing is likely a response to the extensive migration often observed prior to closure events (Fig. 4.8), which could be a response to LST (e.g. Behrens et al., 2009). In systems where CST dominates, it may be possible for the inlet width to have a different relation with the short-term closure risk. Although we have included L_b to scale the total volumetric LST flow rate, this parameter may be difficult to estimate, since it may vary by a wide range. This inclusion was intended as a scale value to account for the sediment availability (from adjacent beaches) within an inlet's littoral cell, as well as an alternative to the inlet width as used in the O'Brien (1976) model. However, future models may require a different approach.

The model is well suited for small systems because it emphasizes parameters which are readily obtainable. Offshore wave data and satellite imagery can be used to characterize the sediment import component. Estimating the sediment export requires a water level gage, river flow estimates and some knowledge of the basin hypsometry, which can be estimated via a bathymetric survey or more coarsely using satellite imagery. Since LST is a common form of sediment transport and since small inlet systems are so

widespread, this approach is a useful alternative to more complex models (which cannot be applied in many situations). Furthermore, it can be further refined where enough data are present to better resolve the sediment import and export to the inlet throat.

4.5.2. Seasonality

In their entirety, the more than 60 years comprising the closure record are best defined by a recurring seasonal pattern modified by short- and long-term processes. Closure events in the short-term (< 28 days) appear sporadic but contribute to the seasonal pattern by accumulating during the months of September-November, when differences in the seasonal patterns of waves and river flow (Fig. 4.9) lead to heightened sediment import to the inlet channel. Long-term (> one year) processes have a more visible impact. Examination of the years 1976-77 and 1983-84 in Figure 4.2 show that droughts and floods can essentially amplify or negate the seasonal pattern. For this reason, continued climate change is expected to dramatically alter the shape of the seasonal closure curve over time.

Other factors not discussed in detail here may also play a large role. Comparison of daily values of WL^{-1} and $Q_{inlet, max}$ for the years 1999-2008 shows that the two parameters are closely related ($r = 0.50, p < 0.001$). This demonstrates the importance of inlet migration and channel bending prior to closure. The data from 1999-2008 generally show that WL^{-1} decreases when migration becomes more frequent, and inspection of Figure 4.8a shows that periods of closure are separated by periods of extensive inlet migration. It is expected that this migration contributes to closure by increasing frictional

losses in the inlet channel, thereby decreasing flows. Migration is an expected byproduct of LST and future studies should include it in any analyses of closure in similar systems.

4.5.3. Influences of local human activity and estuary management

Human influences on Russian River hydrology and on the estuary mouth have been significant over the past century. The few data that exist from the late 1800s suggest that a transition away from long, seasonal closures occurred prior to the record that started in 1931 – during 1931-1957 closure events are shorter and concentrated in fall and spring seasons. Even more striking is the change between the 1931-1957 and 1973-2009 records. During the earlier period, closures occurred on average every 134 days and lasted an average of 15 days, while during recent decades, closures occurred every 43 days and lasted 6 days on average. While a steady increase in extreme wave heights in the East Pacific has been observed (Allan and Komar, 2006) in addition to an increase in precipitation variability in California (DWR, 2006), there is no evident change in climate that could explain such a rapid change in closure statistics and attention should be given to the effects of human activities and river/estuary management actions, which include:

1. Sedimentation caused by extensive logging, agriculture and road building,
2. Increase in dry season flows,
3. Attempts to maintain an open inlet through jetty construction and dredging,
4. Management of flood levels through artificial breaching.

The effects of sedimentation are not examined here because the prevalence of nonpoint sources and the lack of repeat bathymetric surveys in the RRE preclude any conclusive analysis. Before dam construction, sediment loading to the estuary probably exceeded export rates as a result of erosion in the watershed associated with extensive timber harvesting, road building and agricultural and urban development within the watershed, all of which have been common practices in northern California watersheds (Mount, 1995; Opperman et al., 2005).

Flows in the Russian River had historically been low or intermittent during the summer months (Florsheim and Goodwin, 1993). Starting in 1908, Eel River flows were diverted into the upper Russian River watershed, delaying the receding limb of the seasonal hydrograph. The expansion of the diversions in 1922 increased typical summer flows in the upper watershed from near zero to $2\text{-}5\text{ m}^3\text{s}^{-1}$ (SEC, 1996). River flow is now maintained above a minimum value of $70\text{ ft}^3\text{s}^{-1}$ ($\sim 2.5\text{ m}^3\text{s}^{-1}$) based on biological constraints, but is typically managed at $110\text{ ft}^3\text{s}^{-1}$ ($\sim 4\text{ m}^3\text{s}^{-1}$) during summer and fall. While the summer flow may not prevent closures during high-wave conditions, larger waves are less common in summer and the lengthening of the receding limb of the seasonal hydrograph results in flows that are high enough to preclude closure during the few high-wave events that are typically observed in late spring (Fig. 4.8). However, the enhanced summer flows do shorten closure duration. When the inlet closes, the estuary fills from continued river inflows until it naturally breaches (Kraus et al., 2008), if not artificially breached sooner. Flows are too high to allow a persistent closure, but as flows decrease below $4\text{ m}^3\text{s}^{-1}$ the duration rapidly tends toward infinity (Fig. 4.11) and closures

may persist. For increasing flows the duration rapidly tends toward zero. The increase in summer base flows in 1922 would lead to shorter closures, partly explaining the shortening of closure events during the twentieth century.

Management of the estuary mouth is also important. A jetty was completed in 1941 to maintain a permanent opening for gravel barges to traverse the river (Fig. 4.12). Although the jetty constrained the inlet to the northern third of the beach, it did not prevent closure events. The inlet was dredged several times during the 1960s, and plans for a second jetty were made but later abandoned over environmental concerns (Magoon et al., 2008). The ad hoc actions of local residents in manually breaching the mouth in the earlier half of the century gave way to management by public agencies in the 1960s. At present the Sonoma County Water Agency is the management authority and approximately 80 percent of breaches occur through digging a trench across the beach with heavy equipment (Schrad, 1992; Behrens et al., 2009). The primary reasons for this practice are to prevent flooding of low-lying residences and to allow passage of anadromous fish species during spawning seasons (Goodwin and Cuffe, 1994). This practice further reduces the duration of closure events as the mouth is opened artificially when the estuary water level reaches 2.1-2.3 m above the NGVD29 datum – well below the height at which breaching would happen naturally. As a result of this disparity, 36 percent of artificial breaches fail to keep the inlet open for more than five days, compared with 17 percent for natural breaches.

The change in inlet closure pattern between 1931-1957 and 1973-2009 amounts to a 67 percent reduction in the average time between closure events and a 60 percent

reduction in the duration of closures. As a result the estuary is in constant flux, with water column conditions shifting rapidly between an open estuary dominated by cold salty ocean waters and a stratified lagoon.



Figure 4.12. Jenner jetty during construction and at the time of the present study. A second jetty was planned, to allow permanent navigability of the inlet, but was never built. Upper photograph courtesy of Russian River Historical Society.

4.5.4. Climate variability

The clear interannual cycles in river flow and mouth closure (Fig. 4.10) can be expected to be related to well-known fluctuations in west coast climate. Specifically, the El Niño/Southern Oscillation (ENSO) phenomenon, with a cycle of 2-7 years, has been shown to have profound effects on precipitation, waves, upwelling, and fisheries resources in the Western U.S. (Trenberth and Hurrell, 1994). ENSO cycles are encompassed by the Pacific Decadal Oscillation (PDO), which has cycles lasting 15-70 years (Mantua and Hare, 2002). "Warm" PDO phases contain high densities of El Niño events while "cool" phases tend to have more La Niña events. Both ENSO and PDO are coupled atmosphere-ocean processes and are thus complex in nature. Their link to inlet behavior is not well established, although it has been suggested before by Allan and Komar (2006) and Behrens et al. (2009).

ENSO-correlated variability in river flow and wave forcing has been reported previously for Northern California (Allen and Komar, 2006, Wingfield and Storlazzi, 2007). El Niño events are associated with exceptionally high winter waves in California, resulting from an intensified Aleutian Low pressure zone and a shift in North Pacific storm tracks that causes storms to approach from a more direct angle (Allan and Komar, 2006). These storms also contribute to generally wetter conditions, while La Niña events produce the opposite effect (Brown and Comrie, 2004). Further, Zoulas and Orme (2007) showed a PDO influence on the net onshore/offshore movement of sediment, with onshore movement associated with cool phases and the opposite occurring during warm phases. Following Schwing et al (2002), we use the Northern Oscillation Index (NOI) to represent ENSO variability adjacent to North America, in contrast to indices such as the

MEI (Wolter and Timlin, 1998) which represents a broader oceanic measure of the signal. For PDO and NOI indices, we obtain annual values by averaging October-March values to account for the lag between initial detection and sensible effects in North America.

Compared without lag, the NOI (Fig. 4.10c) has no statistically significant link to the closure record, even though it was negatively correlated with river flow ($r = -0.65$, $p < 0.01$) after 1977. Qualitatively, the NOI and closure signals appear to parallel each other between 1973 and 1990, but otherwise there is no clear relation. Unfortunately, there are not enough coincident years with available data for these signals to provide any statistical proof of a relation. Comparison of Figures 4.10a and 4.10d show that the PDO regime shifts in 1944-45 and 1976-77 approximately match shifts in the closure record. Inlet closure is more common during the warm phases before 1944 and after 1977 than during the cold phase in between. The resulting correlation between the two signals is small ($r = 0.25$; $p < 0.05$), but may relate to the ties between PDO and northern California precipitation or to the beach accretion/erosion cycle (e.g. Zoulas and Orme, 2007).

4.6. Conclusions

In this study, we showed that a long-term record of inlet closure at a small inlet site can be explained as a combined response to processes acting at the tidal, seasonal and interannual time scales. We also showed that a proposed simple parametric model based on a sediment balance in the inlet is a good indicator of the likelihood of closure in the short-term, and also reproduces the seasonal closure pattern with high accuracy. To our

knowledge, this is the first time this type of model has been tested with an extensive inlet closure dataset. This model combines the strengths of similar models used in more specialized cases. It is expected to work well for small inlets because it does not need to satisfy all of the assumptions used in analytical models, it can be used with or without river discharge, and it is not scaled down from relations intended for larger inlets. This should be tested at similar sites to determine whether it is broadly applicable. Additional testing is also needed in systems where fluvial influence is stronger, possibly with a sediment export term that combines tidal and fluvial influences.

At the tidal scale, closure is best described as the result of an imbalance between short term wave-driven sediment import and export from the scouring flows through the inlet resulting from both tides and river flow. Whereas waves were important for causing closure, the limiting conditions for closure at the tidal scale tend to be the hydraulic characteristics, such as the inlet flow rate, the inlet aspect ratio WL^{-1} and the tidal prism volume.

At the seasonal scale, the closure pattern is defined by a peak likelihood of closure in fall and a lesser peak in spring, while winter and summer have the lowest likelihoods of closure. At this scale, the closure pattern is almost exclusively controlled by interactions between seasonal cycles in wave height and river flow. Analysis of the Dean number showed that longshore transport LST is likely the dominant contributor of sediment during closures at the Russian River, except during the summer, when both LST and CST may be active, but are probably too weak to cause closure.

At the interannual scale, closure is most strongly related to the interannual median river flow, which can be partly explained by climate variability (PDO and NOI). The combined set of inlet closure observations spanning the nineteenth and twentieth centuries suggests a shift from lengthy, dry-season closure events to relatively short (< two weeks) events concentrated in the fall and spring seasons. This shift appears to have largely taken place between 1870 and 1931 and between 1957 and 1973. During the years 1870-1931 a human-induced increase in dry-season base flows occurred while the years 1957-1931 coincided with the adoption of artificial inlet breaching by public agencies, which were shown to be less effective at keeping the inlet open than natural (river-induced) breaches. Further study is needed to better understand how much effect these events have had relative to simultaneous changes in waves and precipitation in California.

4.7. Uncertainty Analysis

4.7.1. Measurements

Values of the important wave and hydraulic parameters used toward understanding and predicting closure events above are approximations limited by the information available at the site. In some cases, a high amount of uncertainty is present because of the difficulty in adequately measuring or approximating the parameters. It is because of this that the models presented in this chapter are intended as scaling approaches, meant for illustrating the physics that lead to, and maintain, closure events.

To provide a scale of the uncertainty in forcing parameters, some of the sample statistics of the parameters presented in Figure 4.7 are given here in Table 4.2.

Table 4.2. Statistical characteristics and uncertainty of key forcing parameters

All Data				
	Mean	Std. Deviation	uncertainty	% of mean
H_s (m)	1.65	0.84	0.24	14.2
T_p (s)	11.75	2.67	0.26	2.2
<i>Wave Steepness</i> ¹	0.017	0.012	0.0028	16.9
<i>Prism</i> (10^6 m^3)	1.26	0.41	0.13	11
WL^{-1}	0.54	0.87	0.05	10.0
$Q_{inlet, max}$ (m^3s^{-1})	112.06	98.77	12.32	11

¹Represents wave steepness at 10m depth

The uncertainty of H_s is a combination of the measurement precision of the Pt. Reyes buoy (1.5 cm; Oceanographic Instruments, 2009) and of the uncertainty associated with the transformation matrix (22 cm). Wave periods are not predicted in the nearshore zone, but typically vary little from offshore to nearshore unless the offshore bathymetry causes swell waves to focus or spread far from the coast (Komar, 1998). The uncertainty of wave steepness includes the uncertainty of H_s and of the nearshore wave length, as predicted by Fenton and McKee (1990), which predicts nearshore wave lengths to within 1.7 percent of the real value.

The tidal prism and $Q_{inlet, max}$ estimates have errors associated with three main sources:

- Errors in water level measurements in the estuary at the Jenner gage,
- The assumption that the estuary water surface is always flat (e.g. Friedrichs and Aubrey, 1988), and

- Errors in the measurement of bathymetry (EDS, 2009).

To estimate the uncertainty, we first determine the uncertainty in the water surface and channel elevations, and then alter the stage-storage curve to see how much this shifts the estimate of the estuary volume (which is directly related to both tidal prism and $Q_{inlet, max}$).

SCWA measurements of water level are limited by the gage height at approximately -0.25 m NGVD, so the lower limb of the tides is sometimes cut off in the water level record. To account for this, a cubic spline interpolation was used in Matlab © to replace the parts of the tidal curve below -0.25 m NGVD. Predictions were compared against water level measurements at Station A1 (~ 1.8 km from the Jenner gage), indicating only small errors (~ 2cm). During periods of high winds or river flow, curvature of the estuary water surface may cause the lone Jenner gage to provide a biased perspective of the estuary water surface. For the majority of the period 1999-2009, this was the only active gage in the estuary. The largest differences in estimated water level between stations A1 and B3 (Fig. 3.2) are ~10 cm, except during floods. Lastly, errors in the estimation of the estuary bathymetry were made by EDS (2009), who compared boat-based depth soundings with direct measurements of the channel elevation in over 30 locations using an RTK GPS setup, indicating errors of ~5 cm. Combining these errors gives a total uncertainty of ~ 17 cm. Shifting the known stage and storage vectors so that they misalign by 17 cm gives changes (i.e. uncertainty) in estuary volume of roughly $1.3 \times 10^5 \text{ m}^3$.

The inlet aspect ratio, represented as WL^{-1} has a high amount of uncertainty owing to the morphologic instability observed at the site and the difficulty in accurately assessing inlet width and length from ground-based photographs. When scaled by a mean value, errors in inlet width and length were both roughly 10 percent (Behrens et al., 2009), so the uncertainty in the aspect ratio is assumed to be $O(0.1 WL^{-1})$.

4.7.2. Calculations

The unfiltered spectrum of the daily closure record had a high amount of noise within the seasonal and tidal frequencies. To remove noise and discern the dominant frequencies more easily, the spectrum was modified with a 7-point Daniell filter, as recommended by Bloomfield (2000). The Daniell window of span m is defined as:

$$g_i = \frac{1}{2(m-1)}, \quad i = 1 \text{ or } i = m$$

$$= \frac{1}{m-1}, \quad \textit{otherwise}$$
(4.12)

where g is the i^{th} weight of the filter. The modified spectrum, $\hat{s}(f)$, has the following variance:

$$\text{var}\{\hat{s}(f)\} = s(f)^2 \sum_i g_i^2$$
(4.13)

where $s(f)$ is the original (unfiltered) spectrum. Confidence intervals are constructed for the modified spectrum by noting that the frequency diagram estimates are independent and exponentially distributed. Because of this, the modified spectral distribution can be

assumed to be approximately χ^2 distributed (Bloomfield, 2000). The degrees of freedom are defined as:

$$v = \frac{2}{\sum_i g_i^2} \quad (4.14)$$

and the 95% confidence interval is then given by:

$$\frac{v\hat{s}(f)}{\chi_v^2(0.975)} \leq s(f) \leq \frac{v\hat{s}(f)}{\chi_v^2(0.025)} \quad (4.15)$$

where the denominators on the left and right side are the 2.5% and 97.5% points of the χ^2 distribution. The confidence interval given on Figure 4.5 is a representative interval for the spectrum shown for reference. Peaks were checked for significance by comparing the spectral density $\hat{s}(f)$ against the confidence limit for each frequency.

5. Salt Field Mechanics in a Shallow Bar-Built Estuary After Inlet Closure

Dane K. Behrens, John L. Largier, Fabián A. Bombardelli

5.1. Introduction

Intruding saltwater fronts constitute an important feature of estuaries which is responsible for introducing nutrient-rich water to the system, but which can also lead to stratification and hypoxia (Cousins et al., 2010). The position of the salt front along the estuary has significant statistical relationships with many measures of marine resources, such as larval fish survival and the abundance of planktivorous, piscivorous and bottom-foraging fish (Jassby et al., 1995). The density difference in the vertical between the intruding saltwater and the ambient brackish or fresh water also inhibits vertical mixing and can lead to extensive oxygen depletion during periods with relatively weak currents, such as neap tides (Nelson et al., 1994). The salt front position is often a result of steady or quasi-steady circulation, which provides a balance of dense seawater intrusions with seaward advection of relatively lighter water at the surface. The bi-directional, vertically sheared flow structure that results from this exchange has been studied extensively in the past (e.g. Fischer et al., 1979) and the understanding of the associated saltwater intrusions have also advanced due to better and more extensive datasets of waterborne constituents and turbulence in the estuarine environment (e.g. Monismith et al., 2002). However, large

estuaries appear to encompass the majority of the existing research. Large estuaries experience consistent tidal influence and often have gradually varying bathymetry and only partial stratification.

A wide array of estuary types exist, many of which do not fit the classifications of large systems. For example, small bar-built estuaries are relatively common throughout the world (e.g. Roy et al., 2001; Cooper, 2001; Ranasinghe and Pattiaratchi, 2003), and their bathymetry and tidal characteristics are less simple. This is a result of two common traits of these systems: (1) The inlet is intermittently closed and (2) the bathymetry is often shallow and characterized by alternating pools and sills. Inlet closure events are common in areas with Mediterranean climates, where river flows are sharply seasonal and wave energy is high (e.g. Ranasinghe and Pattiaratchi, 2003). Many of these systems remain closed from as little as days to as long as several years before the inlet breaches and restores tidal activity (Gale et al., 2006) and trapped tidal saltwater leads to sharp vertical stratification.

An example of salt field evolution in the RRE is given in Figures 5.1 and 5.2, which show the movement of the front from 7.4 km to about 9.5 km upstream of the inlet during event E5, in October 2010. Parallel plots of temperature and dissolved oxygen indicate the effects of this transition on estuarine habitat quality. Compared with Figure 5.1, Figure 5.2 shows a warmer epilimnion throughout the entire estuary length and a marked decrease in bottom water dissolved oxygen near the mouth, where the salt field transitioned from relatively well-mixed to sharply salt-stratified. Examples from other events are given in Appendix C.

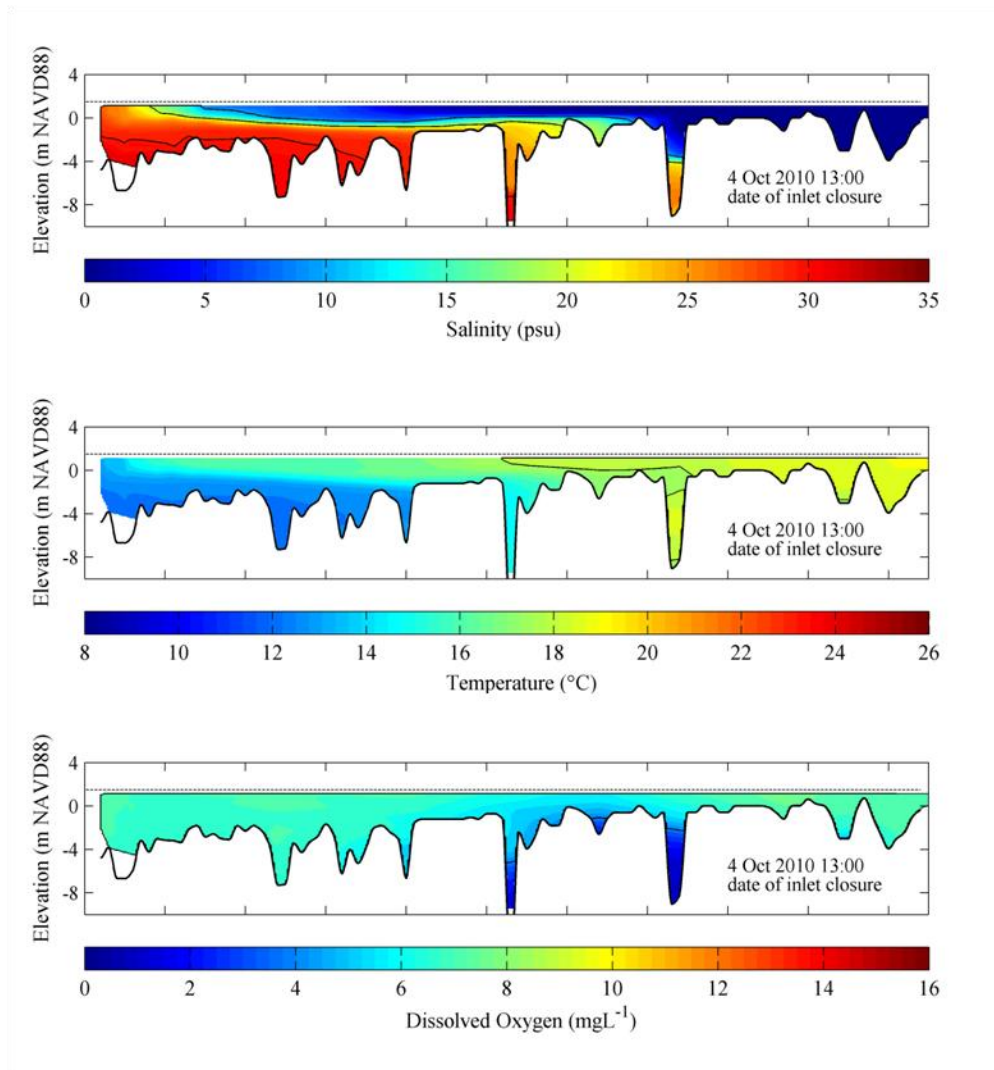


Figure 5.1. Salinity, temperature and dissolved oxygen observed at the onset of inlet closure on 4 October 2010.

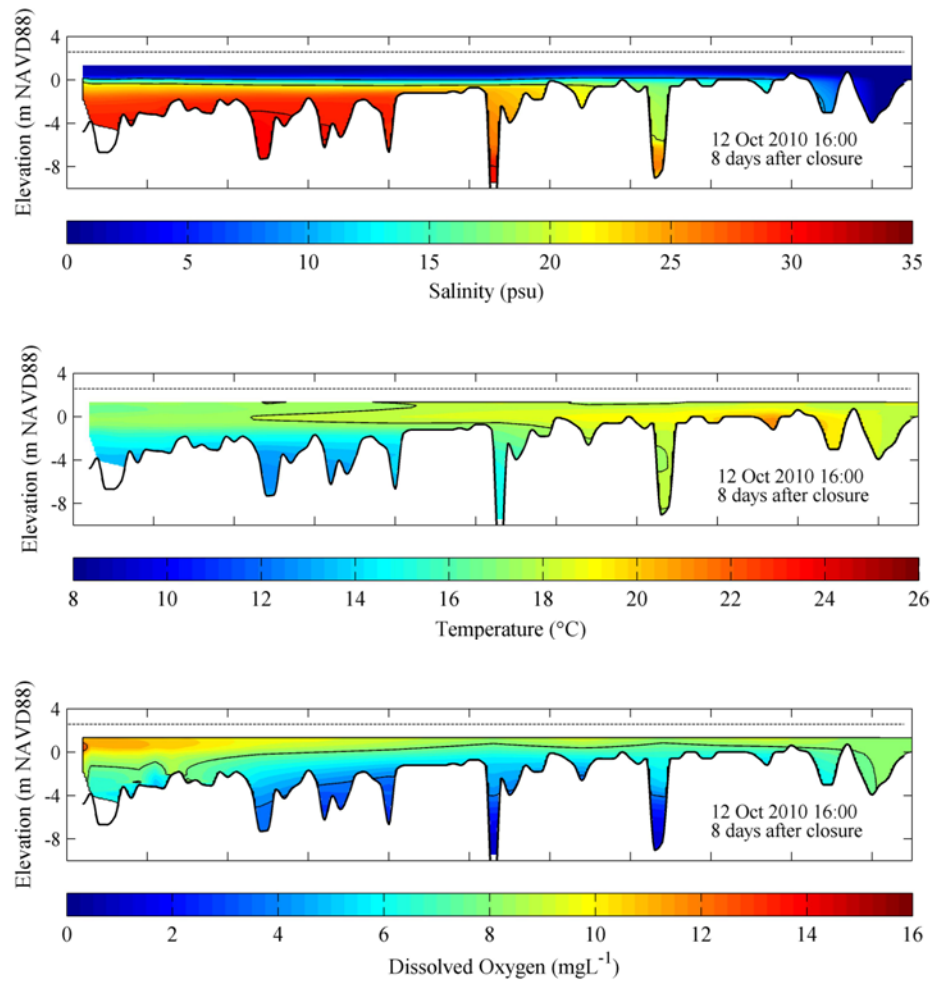


Figure 5.2. Salinity, temperature and dissolved oxygen observed after 8 days of closure, on 12 October 2010.

During inlet closure, wind supplies most of the mixing energy to the estuary (e.g. Gale et al., 2006), either through mixing of the epilimnion or excitation of internal seiche modes which distribute the energy to the metalimnion and hypolimnion. When the extent of this mixing varies along the length of the estuary, it fuels gravity-driven currents which dissipate any ensuing horizontal density gradients caused by diapycnal mixing of

higher density water into the epilimnion (Imberger & Parker, 1985). However, it remains unclear how the pool-sill bathymetry in these systems influences the wind-driven motions and the associated redistribution of the trapped salt field. Although little is known about salt front movement in this scenario, it is clear that the bottom waters tend to become hypoxic for the entire extent of the saltwater intrusion along the estuary (Becker et al., 2009). This is of particular importance in the US Pacific Coast because the populations of salmonids which often occupy the region's closed estuaries have been steadily declining, in part due to habitat constraints (Hayes et al., 2008).

Aside from analogues studies in lakes and reservoirs, little research exists to describe salt front mechanics in small bar-built coastal lagoons after closure. This is partly because much of the existing literature focuses on systems where stratification and scalar fields are often observed or assumed to be spatially uniform (Gale et al., 2006; Cousins et al., 2011). While this may be true of systems with simple bathymetry, many systems along active continental margins have complex bathymetry (Cooper, 2001), which can greatly influence the distribution of scalar fields. Also, while salt intrusion and salt front dynamics have been studied during open-inlet conditions both in stratified (O'Callahan et al., 2007; Largier, 1991) and partially-mixed (Giddings, 2012) systems, the forcing mechanisms are much different in these cases than after inlet closure. Scalar field dynamics have also been studied in small lakes and reservoirs, but stratification in these systems is controlled by temperature rather than salinity (and is thus weaker) and the geometry is often much deeper (Okeley and Imberger, 2007; Vlasenko and Hutter, 2002) than that of small lagoons (Roy et al., 2001).

In combination with the existing complexity of these systems, discrepancies in the available research leave many questions about the mechanics of salt fronts after closure in small coastal lagoons. The purpose of this chapter is to provide an understanding of the conditions in which salt mobilizes upstream in these systems, which is of primary concern for habitat-limited aquatic species which rely on estuaries for much of their life cycle. We also investigate the limiting conditions which prevent this mobilization and draw broad conclusions to link this with other systems.

5.2. Methods

5.2.1. Field Observations

This chapter relies on field observations during three closure events, E1 (September-October 2009), E4 (September 2010) and E5 (October 2010). Special attention is given to the along-estuary set of CTD profiles, which illustrate the evolution of the salt field during both tidal and closed conditions in the estuary. The ADCP data were also used extensively here, to characterize the flow fields and turbulence in the estuary, as described below. The collection of these data is discussed in Chapter 3 and a summary of the boat-based and measurements used herein are illustrated in Appendix B.

Since wind was not measured directly, we used a comparison of water levels throughout the estuary as a qualitative proxy for wind speed and direction. Landward winds are reflected in a landward tilt of the estuary surface, while seaward winds correspond to the opposite. Analysis of the water levels at stations A1 and B3 (Fig. 3.1)

reveal that the periodicity of these fluctuations matches the diurnal frequency of winds measured at the Bodega Marine Laboratory (BML), eight miles away. We chose not to estimate a representative shear velocity for the estuary from these measurements, since it likely varies strongly along the estuary (Imberger and Parker, 1985).

5.2.2. Analysis methods

The majority of the analysis focuses on the period from 25 September to 12 October 2010, when the ADCPs were operated in mode 12. This period includes closure events E4 and E5 (Table 3.1). We isolate the processes that drive the observed salt intrusion during this period by examining the flow structure in detail at moorings A4 and B3 using empirical orthogonal functions (EOFs). EOFs are a tool used to isolate independent sources of variance within a dataset (see Emery and Thomson, 2004 pg. 319-343). They are a purely statistical construct, and thus may not always provide a clear link to the physical processes present in an estuarine setting. However, they often do correlate with physical processes, and have been shown to be useful for isolating oceanographic and estuarine processes in the past (Giddings, 2010; Stacey et al., 2001). We employ this method by condensing the ADCP data at both sites into matrices with columns representing hourly vertical profiles of streamwise velocities. While others have used EOFs with full, directional ADCP data (e.g. Stacey et al., 2001), we only use this approach on the streamwise component of flow, which we obtain by rotating the flow at each mooring site.

The EOF method produces a set of orthogonal eigenvectors (variance modes) which each describe a percentage of the total variance of the dataset. Since we perform the analysis on data that have been rotated into along-stream components, we interpret the flow structures given by the variance modes as separate components of the observed along-stream flow structures at moorings A4 and B3. Using simple analytical models, we then compare the dominant modes against the flow structures typically caused by internal seiches or gravitational currents to determine whether these were important to the observed salt intrusion.

Internal seiche modes are modeled using Long's one-dimensional wave equation (Wiegand and Chamberlain, 1987):

$$\frac{d^2W}{dz^2} + \left(\frac{N^2}{\omega^2} - 1 \right) k^2 \frac{dW}{dz} = 0 \quad (5.1)$$

where W is the amplitude of the vertical velocity of a parcel of water, ω is a characteristic internal wave frequency, k is the horizontal wave number defined as $k = 2\pi/L$ where L is the basin length and N is the Brunt-Vaisälä buoyancy frequency, defined as $N^2 = - (g/\rho)(\partial\rho/\partial z)$. Eq. (5.1) is an ordinary differential equation which we treat as an eigenvalue problem and solve for ω using a finite-differences scheme (LaZerte, 1980). This approach has been used successfully in rotating (Antenucci and Imberger, 2001) and non-rotating (LaZerte, 1980; Wiegand & Chamberlain, 1987; Munnich et al., 1992) systems. Values of N^2 estimated from the CTD casts are used as a constraint, representing the stratification present in the water column. The eigenvectors obtained from solving equation (1) represent the vector of vertical displacement (W) given by each vertical wave mode present in the basin. Using the continuity equation, these are transferred to

vectors of along-stream velocity components given by each wave mode (Munnich et al., 1992). This method also produces a set of eigenvalues, ω , which are characteristic oscillation frequencies associated with each seiche predicted by this method. These are used to find the characteristic internal wave periods (T) using the identity $\omega = 2\pi/T$.

We obtain the flow structure associated with a gravitational current using the relation from Officer (1976):

$$u(\zeta) = \frac{gh^3}{48\rho A_z} \frac{\partial \rho}{\partial x} (1 - 9\zeta^2 - 8\zeta^3); \quad (5.2)$$

where ρ is density, x is the along-stream direction, A_z is the eddy viscosity and ζ is the normalized depth. This method requires the assumption that the pressure gradient and stress divergence (friction) are the only important terms in the momentum budget and that the system is in steady state.

We use the high-frequency ADCP data to estimate Reynolds stresses in the water column using the variance method (Stacey et al., 1999). The along-beam velocity measurements taken at 12 Hz were averaged to give data at 1 s intervals, giving a total of $M = 600$ datapoints for each burst. The choice of a ten-minute interval is based on a compromise between the need for a statistically stationary sample and statistical reliability (Simpson et al., 2005) which increases with $M^{1/2}$ (Williams and Simpson, 2004). Turbulent velocity fluctuations are separated from the mean flow during each burst interval using Reynolds decomposition and the along-beam turbulent velocity fluctuations are then used to calculate the along- and cross-stream Reynolds stresses (Stacey et al., 1999):

$$\frac{\tau_{xx}}{\rho} = -\overline{u'w'} = \frac{\overline{b_2'^2} - \overline{b_1'^2}}{4 \sin \theta \cos \theta},$$

$$\frac{\tau_{yy}}{\rho} = -\overline{v'w'} = \frac{\overline{b_4'^2} - \overline{b_3'^2}}{4 \sin \theta \cos \theta} \quad (5.3)$$

where subscripts denote the beam number and $\theta = 20^\circ$ is the angle that each beam makes with the vertical. The burst-averaged velocity components at each depth bin were also used to provide an hourly record of mean currents at each location. We then use this to obtain the rate of total kinetic energy (TKE) production:

$$P = \tau_{xy} \frac{\partial u}{\partial z} + \tau_{yz} \frac{\partial v}{\partial z} \quad (5.4)$$

Instrument tilt and along-beam velocity variance can be used to estimate the noise floor for estimates after William and Simpson (2004).

Since we will show that the RRE is highly stratified in the vertical, and since winds are variable at the site, upwelling may have an influence on the estuary salt field. We parameterize upwelling with the Wedderburn Number (Shintani et al., 2010):

$$W = \frac{g' h_1^2}{u_*^2 L} \quad (5.5)$$

where g' is the reduced gravity, defined as $g' = g(\Delta\rho\rho^{-1})$, h_1 is the depth of the epilimnion, u_* is the shear velocity in the epilimnion imposed by winds and L is the unbroken length of the pycnocline. We apply the methodology of Shintani et al. (2010), which corrects Eq. (5.5) for the effects of pycnocline curvature. They find that for W values below a critical value of 8/9, the interface at the upwind end of the basin upwells to the water surface.

Water losses through the closed beach berm may also alter the salt field, but direct measurements in the beach are lacking. Setup of ponded flows behind the beach enforces a head difference between the lagoon and the ocean, presumably causing some saline water to advect out of the system via seepage through the porous beach. Estimates from a water mass balance applied to water level and flow data from the RRE during the years 2000-2009 show total water loss rates increasing linearly with head difference, up to values $2\text{-}4\text{ m}^3\text{s}^{-1}$ at head differences of two meters between the lagoon and ocean. The CTD measurements suggest that the total salt mass of the estuary does decrease during closure, which is entirely accounted for in the pool closest to the mouth. However, at the short-term (daily) time scale, salt movement upstream was generally found to be larger than the total losses from the system, so we will not discuss this process further herein. However, future work will incorporate this process in more detail, when in situ measurements in the beach are available.

5.3. Results

5.3.1. Salt field evolution

The inlet at the mouth of the RRE is often morphologically unstable, leading to inconsistent tidal interaction between the ocean and estuary. This in turn leads to extensive amounts of trapped saline water and prolonged periods of sharp stratification throughout much of the estuary. During tidal conditions, the mixing induced by the dense inflows usually left much of the outer estuary salty and unstratified. When tides became

absent from the estuary during closure, all areas with trapped salt became sharply stratified, with peak density gradients on the order of 10 kgm^{-4} across the metalimnion. Figure 5.3 gives a comparison between tidal and closed conditions, using CTD data on 19 July and 28 September 2010. Areas with trapped salt displayed a persistent three-layer stratification, with a 2-3m thick epilimnion, a 1-3m thick pycnocline and a saline lower layer whose thickness depended on the local depth.

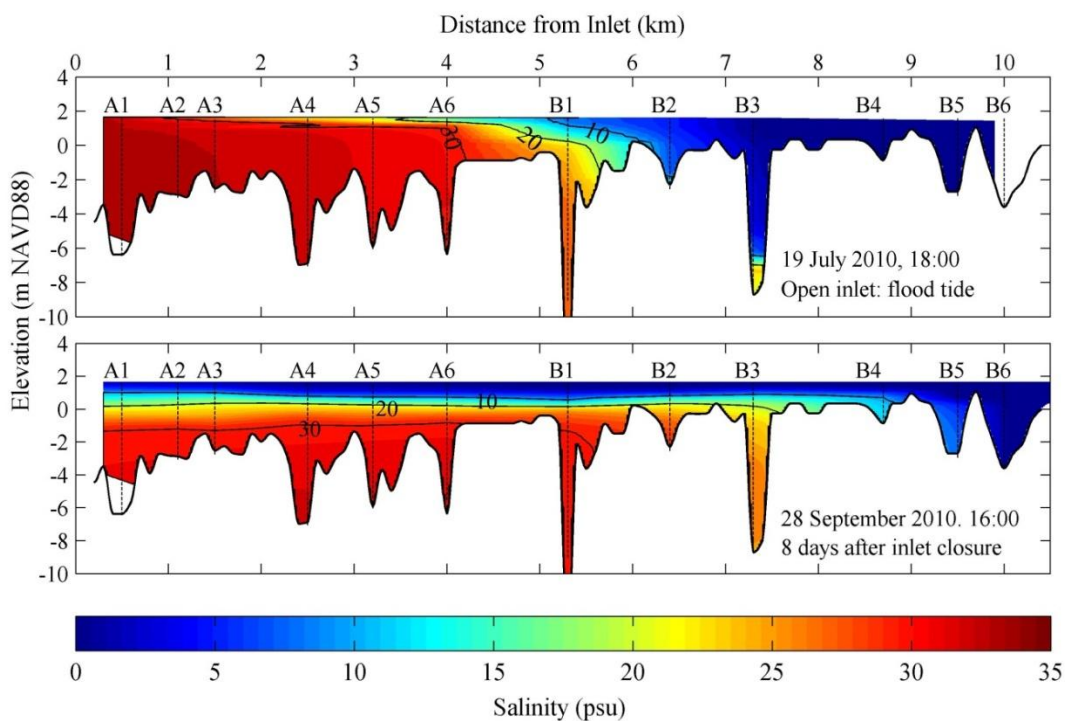


Figure 5.3. Longitudinal salinity map of the RRE during representative **(top)** tidal and **(bottom)** closed conditions. Measurement station locations from Figure 3.2 are indicated. Bottom edge represents the along-estuary thalweg profile.

Field measurements during tidal conditions show that the salt front enters the estuary during flood tide and inundates the deep areas (pools) between sills as it moves upstream. The addition of salt in each pool raises the elevation of the local metalimnion

and the salt wedge advances further upstream when this reaches the elevation of the immediate upstream sill. During ebb, some of this salt is eroded by outgoing currents at the surface, leaving the upper few meters of the water column relatively fresh. However, the jagged bathymetry of the RRE traps much of the incoming salt. Most of the tidal-scale changes in salinity occurred in the upper 1-3m of the water column - the portion above the height of local sills. As shown for similar bar-built estuaries (e.g. O'Callaghan et al., 2007), the excursion length of the intruding saltwater into the RRE depended on the spring-neap cycle. The leading edge of the salt front creates a strong local density gradient that is typically located in the transition zone between the inner and outer estuary (~4-6 km upstream of the inlet; Fig. 5.3). During spring tides, salt was sometimes observed to move as far as 9.5 km upstream of the inlet.

The process of inlet closure is initiated when wave-driven sediment delivery to the inlet throat exceeds the amount of sediment exported by currents. This lasts as little as a single tidal cycle or as long as several weeks at the RRE (Behrens et al., 2009). We found that the inlet channel aggrades in response to the excess sediment delivery, which is analogous to increasing the height of a weir, and results in the inlet blocking part of the incoming tides. During these times the water level records reveal a shortening of the flood tide relative to the ebb, and CTD surveys show an export of salt from the upper water column and an overall sharpening of the pycnocline. For all six closure events that we studied, the final stage of inlet closure (full inlet blockage) culminated with a high tide or high wave event, leaving an ensuing surge of salt water that either remained in the outer estuary or propagated upstream, depending on the elevation of the outer estuary

pycnocline relative to local sills. After the onset of closure, oceanic waves continued to aggrade the beach and occasionally carried additional loads of salt into the estuary.

After the inlet is fully closed, freshwater inflows are trapped behind the beach and contribute to the water mass of the epilimnion. The width of the epilimnion varied in our observations from 1-1.5 m at the onset of closure to as much as 4 m at the end. Each time that the inlet reopened (whether manually or naturally), rapid currents acted to destroy the head difference between the estuary and the ocean set up by the blocked freshwater flows. These currents flushed most of the trapped salt out of the estuary, at which point ensuing tidal motions imported new loads of saline water. Occasionally, remnants of salt water remained in the deepest pools, and some appeared to have residence times of at least a year.

We found that the salt field evolved in two distinct phases after the onset of closure: (1) rapid initial relaxation of the outer estuary pycnocline immediately after full blockage was achieved and (2) slower nightly fluxes of salt above the pycnocline into the inner estuary after the first phase was completed. Both phases are visible in Figure 5.4, during E5. The first phase usually occurred within the first 24 hours of closure and resulted in the outer estuary pycnocline reaching a level resting position. During this time, the epilimnion was usually relatively thin, since freshwater inflows had not had much time to accumulate behind the newly blocked inlet. Winds also tended to be higher during this period, since closure events tend to coincide with storms (Behrens et al., 2009). As a result, this phase was often marked by near-critical values of the Wedderburn Number and upwelling of the density interface at the mouth, which is visible in Figure

5.4b. If the strong winds relaxed at night, the rapid drop of the interface at the mouth caused a surge of salt water to move upstream. Sonde measurements at the surface show that the amplitude of this disturbance diminishes rapidly with distance from the mouth and does not advance farther than station B1 (Fig. 5.3). As time advanced, the deepening epilimnion resulted in higher (less critical) Wedderburn values and fewer observed upwelling-and-releasing events. Despite this, the estuary typically maintained a small longitudinal salt gradient in the epilimnion between the outermost (3-5 psu) and innermost (~ 0 psu) boundaries, which was augmented during winds. During the second phase of salt movement, this upper salt gradient diminished in small bursts during periods when diurnal winds became negligible (typically at night). These loads gradually filled each successive pool in the inner estuary, leading to a slow but substantial redistribution of the salt field for longer events. In most events, the first phase increased the range of salt and stratification in the estuary from about 5.3 to as far as 7.4 km upstream of the inlet while the second phase pushed this range as far as 10.1 km from the inlet.

Image subtraction of the two-dimensional maps used in Figure 5.4 emphasizes the mobility of the salt front and its reliance on the pycnocline as a means for transporting salt upstream. Figure 5.5 shows that the outer estuary lost the majority of its salt within one meter above the interface, while the majority of the gain in the inner estuary was 1-5 m below it. Horizontally, the change is centered around the sill located 4-5 km from the inlet. To better understand this motion we visualize the along-stream salinity in the well-mixed epilimnion. Figure 5.6 shows that this upper salinity varies smoothly along the estuary during E5, which was the case for all closure events. Near the beginning of each

event, the observed decrease in average epilimnion salinity moving upstream was usually nonlinear, sometimes coinciding with the observed upwelling events during strong winds (e.g. Fig. 5.4b). Over time, the epilimnion salinity at the mouth declined and the along-stream shape became linear, as Figure 5.6 shows for 4.5 Oct and 12 Oct 2010. The slope of this line declines over time, but strong wind events and wave overwash occasionally augment it.

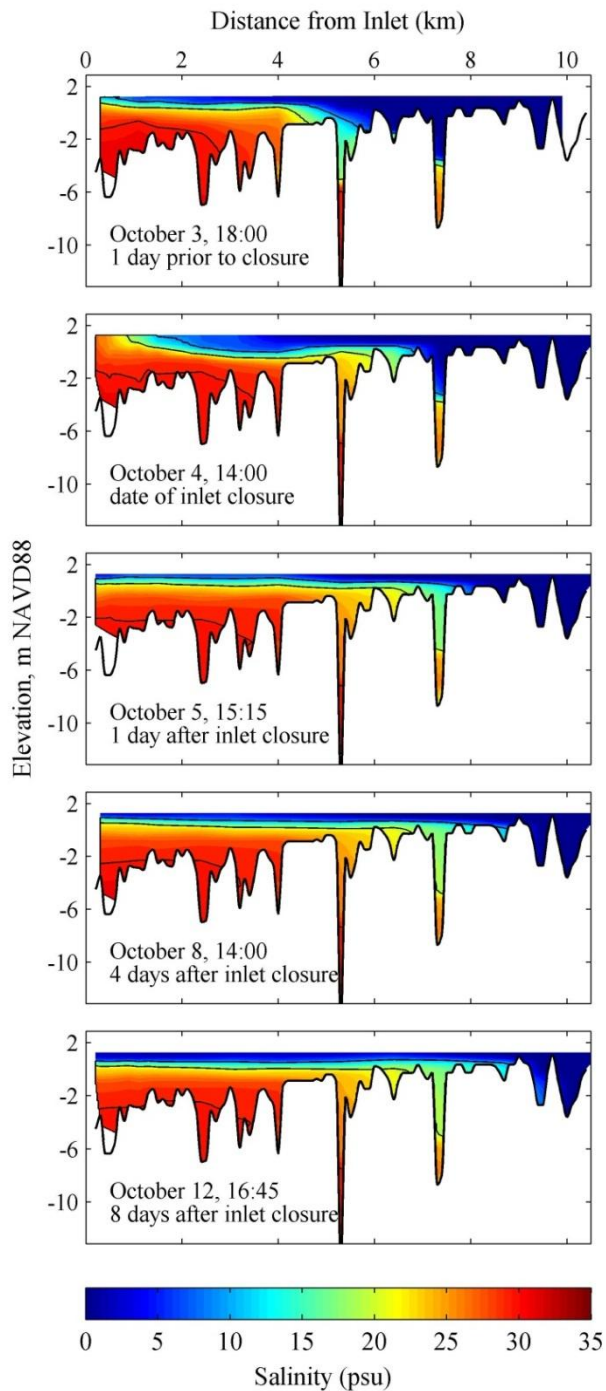


Figure 5.4. Sequential salinity maps of RRE during closure E5. The approximate boundary between the inner and outer estuary (Fig. 3.2) is at 5 km from the inlet. The first stage of salt redistribution is clearly visible for distances less than 8 km from the inlet. The second stage is visible 8 km and farther upstream.

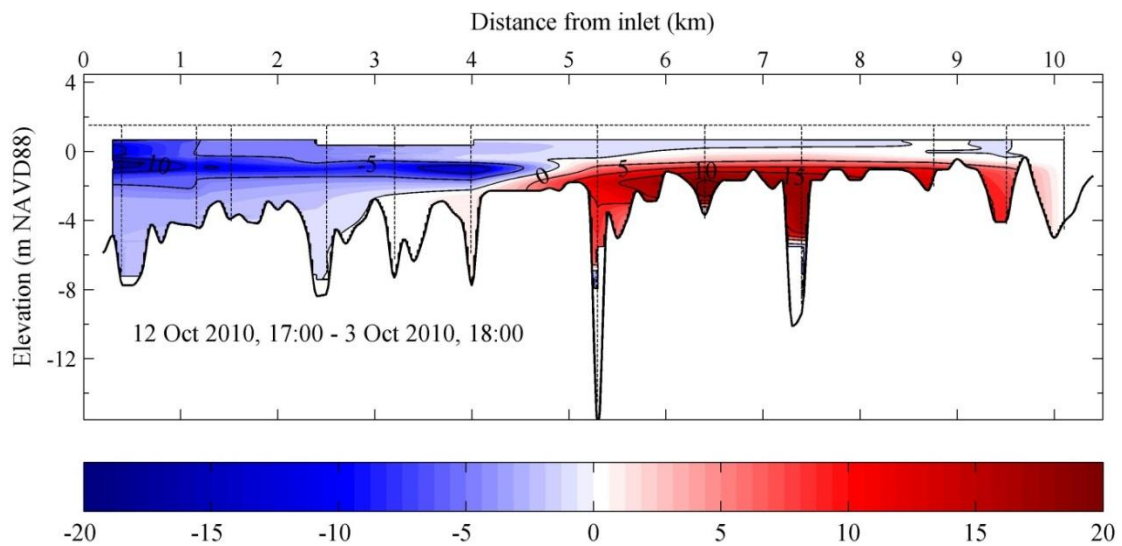


Figure 5.5. Image subtraction of RRE salinity field between the last day of closure E5 (12 October 2010) and the day prior to closure (3 October 2010).

In addition to the measurements described above, vertical salinity profiles were also taken at points across the channel at areas of high and low channel curvature (sites A4, A5, respectively). We found that for typical closure conditions at the site, the cross-channel variations in salinity at each elevation (not shown) were negligible, suggesting that lateral transfer of both salt and momentum are likely minor. However, since cross-channel CTD measurements were taken on an opportunistic (not continuous) basis, there are no observations of cross-channel distribution of salinity structure during the passing of any known flow structures, such as internal seiches or gravitational currents.

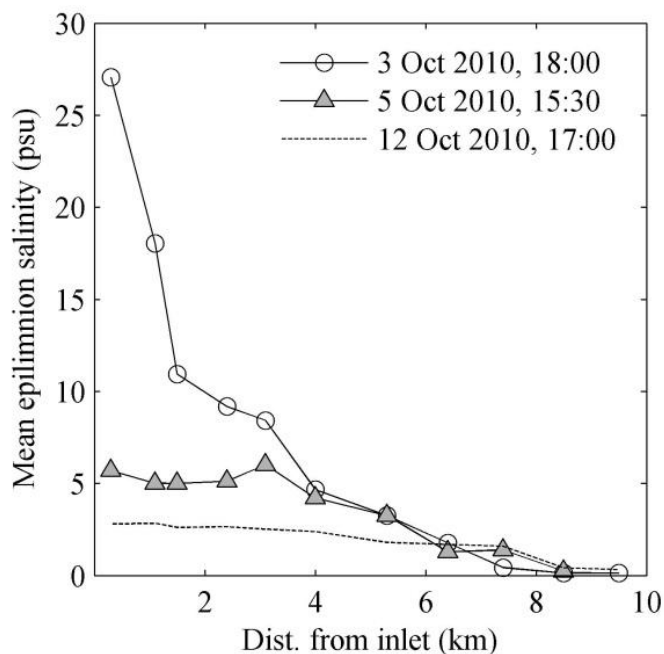


Figure 5.6. Along-estuary salinity gradient in the epilimnion during E5. Salinity values represent averages from the centerline of the metalimnion to the water surface.

The ending salt field is remarkably similar among all events. The only event which ended without stratification present as far as the upstream boundary was E3, but this event was anomalous because it began after several days of perched overflow conditions in which the inlet exported most of the estuary salt without allowing tides to enter. Other than this, all events transitioned to closure directly from a tidal state, and ended with nearly uniform stratification. The dissolved oxygen declined uniformly beneath the pycnocline, with the final amount seemingly depending on the duration of closure. By the end of E1, the longest observed event, most of the hypolimnion had dissolved oxygen levels below 2 mg l^{-1} .

5.3.2. Flow structure

During tidal conditions, the estuary flow structure was dominated by semidiurnal tidal motions. In lieu of these during closure, the flow structure experienced mostly diurnal fluctuations which mirrored those of winds. This is illustrated in Figures 5.7, 5.8 for events E1, E4 and E5. Landward winds during the afternoon and negligible or weak seaward winds at night led to an oscillating flow structure which was isolated within the epilimnion at site B3 and extended to the lower edge of the metalimnion at site A4. Water level observations indicate a diurnal landward tilt of the estuary surface that peaks during the late afternoon. At night the surface is either approximately flat or has a smaller seaward tilt. The fulcrum of the displacement occurs between the inner and outer estuary, at approximately 5 km upstream of the inlet (Fig. 3.2). The highest surface displacements observed between stations A1 and B3 (~8 cm) tend to occur when winds at BML exceed 10 m s^{-1} , although it is unclear to what extent the local topography and diurnal sea/land breezes influence the local wind field.

The shape and location of the pycnocline exerts a strong influence on the magnitude and structure of the observed flows. Figure 5.9 examines this in detail on 28 September 2010, at which time the pycnocline (Fig. 5.3b) created a 4km-long contiguous lower layer in the outer estuary, but isolated the lower water column at each pool upstream by resting at or below the elevation of the local sills. The peak landward surface tilt measured between 14:00 h and 18:00 h was met with a similar wind-sheared velocity profile above the pycnocline at A4 and B3. Flows near the surface were directed

upstream while a weaker return flow was located atop the density interface. As the tilt declined during the evening, the shear at the surface declined at both sites and an upstream-directed flow developed below the pycnocline at A4, while flows at the upstream site were quiescent below this level. By the morning of 29 September, the flow structure at both sites featured an upstream directed current in the upper half of the pycnocline. At site A4, a current with roughly equal magnitude but opposite direction existed in the lower half of the pycnocline, but there were no visible currents at the same elevation at B3. These features were consistent aspects of the flow structure during closure.

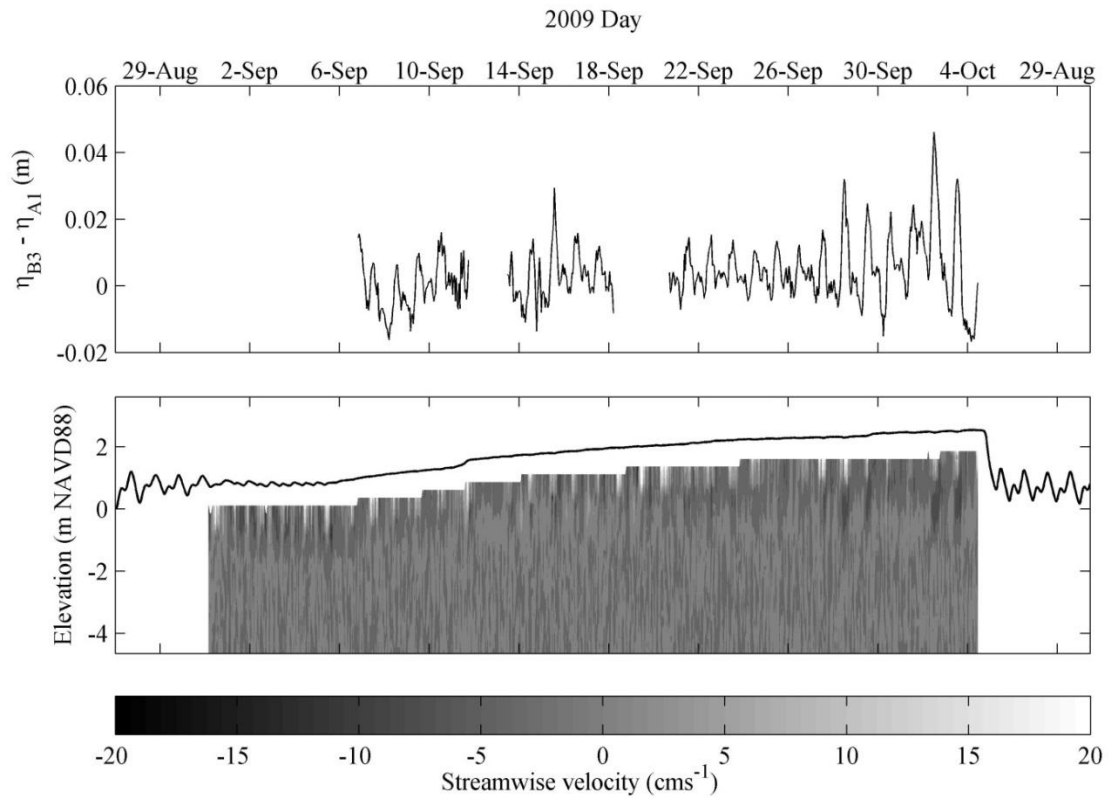


Figure 5.7. (top) Difference in water level between stations B3 and A1 and **(bottom)** time-series of along-stream component of velocities measured from upward-facing ADCP at site B3 during closure E1.

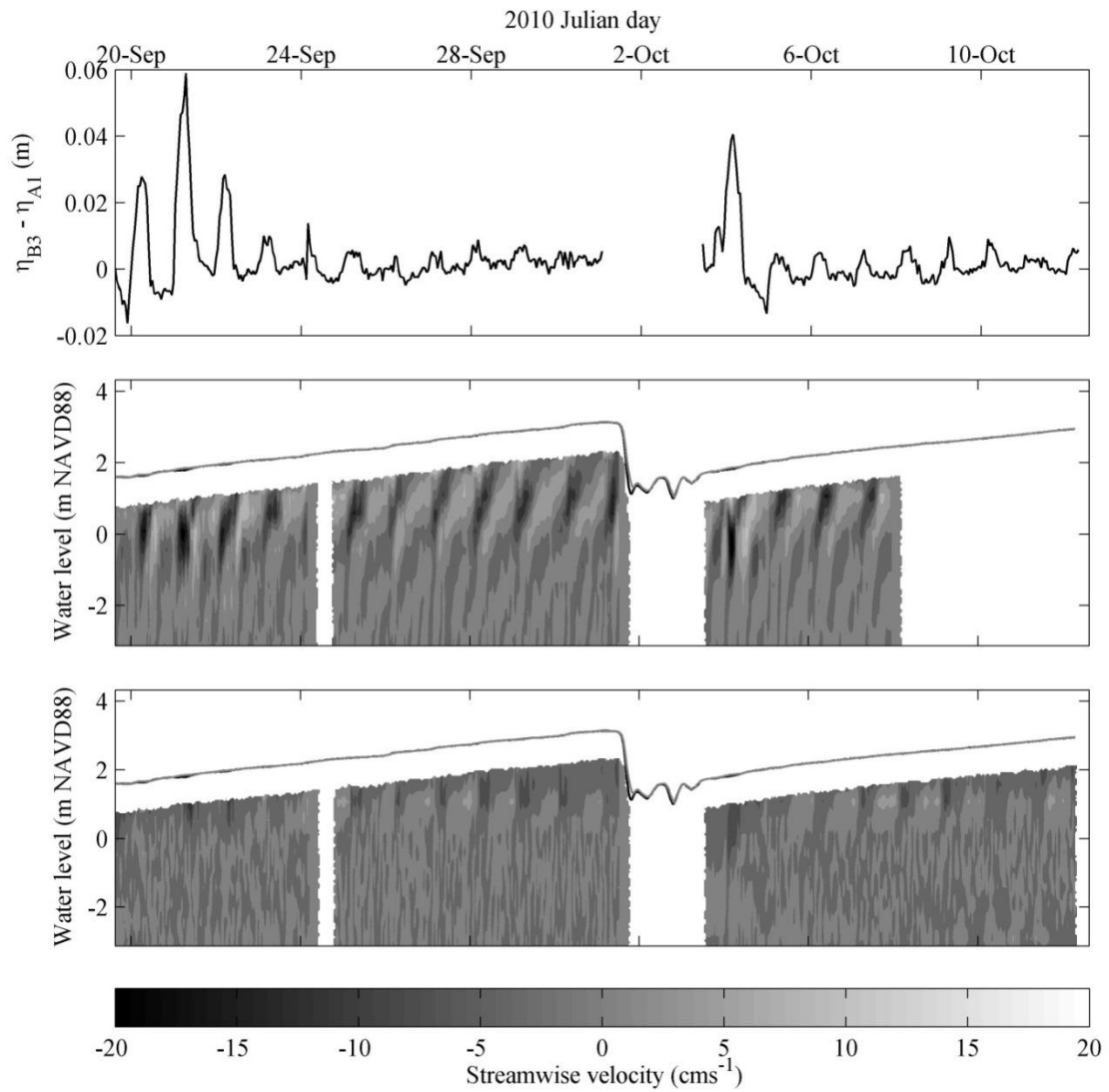


Figure 5.8. (top) Difference in water level between stations B3 and A1 and time-series of along-stream component of velocities measured from upward-facing ADCP at site B3 during closures **(middle)** E4 and **(bottom)** E5.

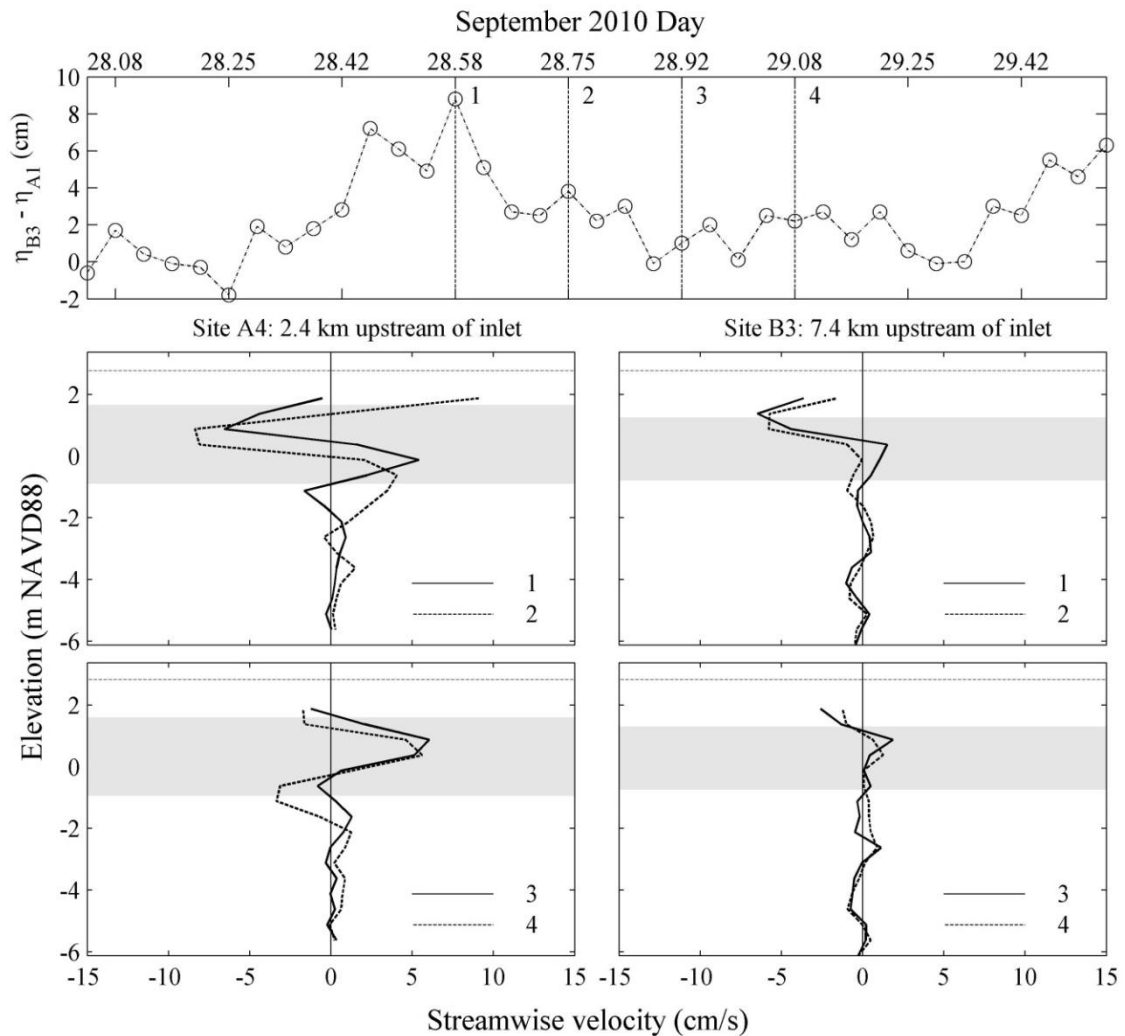


Figure 5.9. Response of along-stream velocities at sites A4 (lower left) and B3 (lower right) to wind (upper) on 28 September 2010, during closure event E4. Difference in water levels between sites B3 and A1 are used as a proxy for wind. Horizontal gray band represents the pycnocline location. Velocities are positive in the upstream direction. The increase in wind during the middle of the day, shown in the upper plot, was a typical daily occurrence during the measurement period.

5.3.3. EOF analysis

Despite the consistent response to afternoon winds, the EOF approach confirms that the flow structure at night is directed by different processes at each site. We applied

the approach discussed in Section 2. Using the set of A4 and B3 velocity profiles during closure events E1, E4 and E5, we found that each site has its own set of major variance modes which were invariant with time. The first two variance modes at each site contain the majority of the total variance and exhibit a dominant 24-hour periodicity which matches that of BML winds and the estuary water level records. Although some of the remaining variance modes (mode 3 and higher) had similar frequencies, none contain more than 20 percent of the variance at either site, and are not discussed here. Figures 5.10a, c illustrate a representative set of results found during E4.

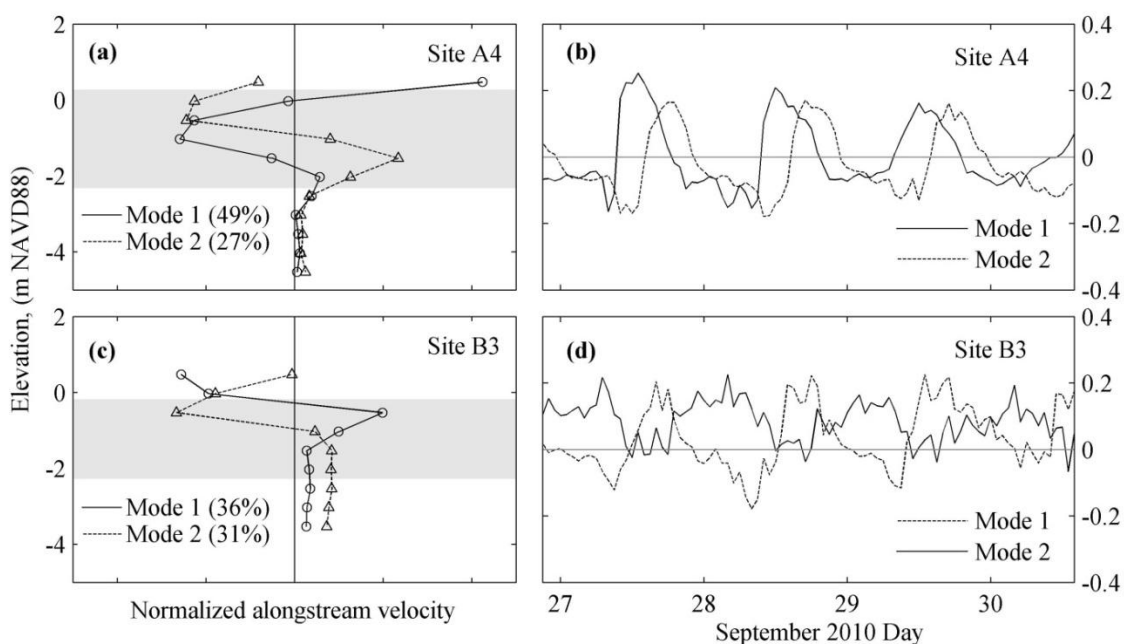


Figure 5.10. Eigenvectors of along-stream velocity from EOF analysis at sites A4 and B3 (left) and time series of first two variance modes (right). Horizontal gray band represents the pycnocline location.

The first variance mode at site A4 and the second at site B3 are associated with surface wind stress. The shapes of their velocity profiles are highly correlated with each

other ($r = 0.97$, $N = 8$, $p < 0.0001$) and both profiles are comprised of a structure with landward flow near the surface and seaward flow at the pycnocline elevation, similar to those calculated analytically by Matheiu et al. (2002). This mode accounts for 48.9 percent of the total variance at A4 and 31.2 percent at B3. The time series of these modes (Figs. 5.10b, d) indicates a diurnal pattern which matches the time series of water level measurements – both modes are strongly positive when strong landward winds are active. The lower fraction of the total variance explained by this mode at B3 suggests that wind stresses are indeed lower in the inner estuary.

The second variance mode at A4 and the first at B3 have different behavior than those described above. In the outer estuary, the second mode accounts for 27.1 percent of the total variance. The dominant feature of this profile is two opposing currents of equal magnitude centered on the middle of the pycnocline. In the inner estuary, the first variance mode accounts for 35.8 percent of the total variance, and its profile is composed of a single upstream-directed flow structure resting on top of the pycnocline and weak seaward flow at the surface. The time series of these modes are quite different from each other: At site A4 the time series has the same shape as for the variance mode tied to winds, but lags by about six hours. At B3 the time series of the first variance mode generally opposes the signal of the second mode (associated with winds), suggesting that it has a strong inverse relation compared with wind speed. It is positive at night, in the small window when winds are negligible or directed towards the ocean (Fig. 5.10).

We tested for signs of internal wave influence at the outer estuary site because of its depth, wind exposure and long uninterrupted metalimnion. Internal waves (seiches)

are standing waves which act to compress, expand or vertically displace isopycnals and can dominate systems with relatively strong stratification or small frictional losses (Antenucci and Imberger, 2001). For simplicity, we only consider seiches having nodes at the basin edges (horizontal mode one, or H1). Horizontal and vertical mode one seiches (hereafter “V1H1” in accordance with the literature) typically form when the metalimnion composes a small fraction of the total depth (e.g. Monismith, 1985). These have the appearance of surface waves, but act on the density interface and have lower celerity, owing to the smaller difference in density across the pycnocline rather than the water surface. In contrast, V2H1 and V3H1 modes act to contract or expand the pycnocline and become relatively important only when the metalimnion is roughly the same size as the upper and lower layers (as is the case in the RRE) (Monismith, 1985). Multiple modes may be present concurrently, so the profile of along-stream currents influenced by seiches can be complex.

We again use data from 28 September 2010, since the density and current structure on this date are prototypical of closure conditions at the RRE. We chose the total uninterrupted distance of the metalimnion in the outer estuary (3.8 km) as the length scale L (after Shintani et al. 2010). N , k and ω are estimated as described in Section 2. Solving Eq. (5.1) numerically in Matlab© provided internal wave periods (T) of 5.5, 15, and 25 hours for wave modes V1H1-V3H1, respectively. The derived along-stream flow profiles of these modes (Fig. 5.11) provide strong evidence for the existence of a V3H1 seiche in the outer estuary. The velocity profile for the second variance mode at A4 is strongly correlated ($r = 0.90$, $N = 10$, $p < .001$) with the profile predicted for a V3H1

seiche. The predicted 25-hour oscillation period is also very similar to the ~24 hour diurnal period of the variance mode.

Neither variance mode at site B4 shows any resemblance to the predicted seiche current profiles, which suggests that these mechanisms play a negligible role in advancing the salt front in the inner estuary. This evidence is compounded by the lack of any lag between the time series of this mode and that of the second mode at the outer estuary site. If a V3H1 seiche were indeed to translate along the pycnocline for the 5 km distance between sites A4 and B3, its celerity of $c = 2LT^{-1} = 0.084 \text{ ms}^{-1}$ would require a travel time of over 16 hours. No such lag was observed in the ADCP or sonde data. Also, while the CTD casts provided some anecdotal evidence of V1H1 or V2H1 seiches existing near the mouth (e.g. Fig. 5.4b), additional measurements show that these do not translate into the inner estuary. This may be a result of the shallow sill depths located 2 km and 4 km from the mouth (e.g. Fig. 5.4) which typically exceed the critical minimum depth required to cause these types of waves to transfer their energy to higher modes or to turbulent mixing (Horn et al., 2001).

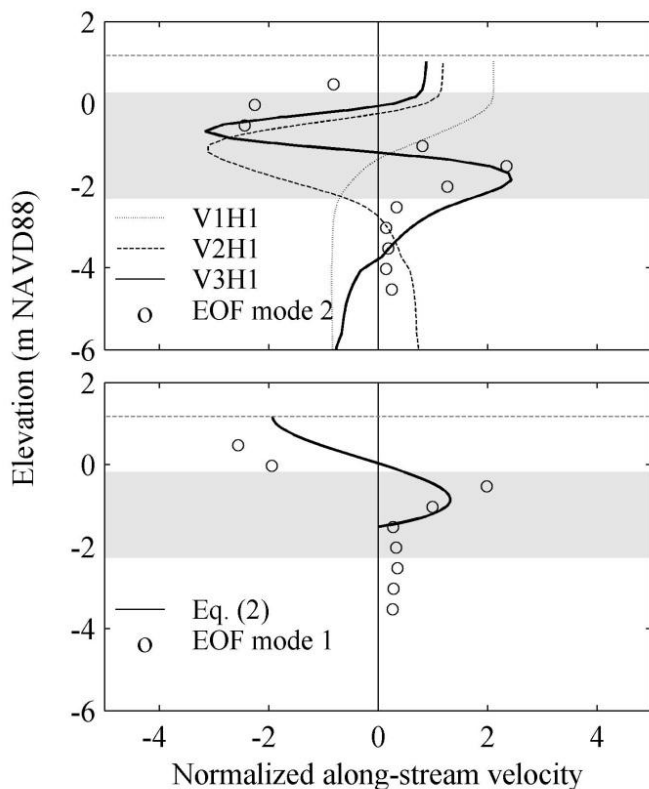


Figure 5.11. Comparison of EOF modes against predicted flow structures. Upper plot compares along-stream velocity vector given for predicted seiche modes against EOF mode 2 at site A4. Lower plot compares gravitational current profile against EOF mode 1 at site B3. Horizontal gray band represents the pycnocline location. At the outer estuary site (A4), the predicted V3H1 seiche is strongly correlated with the second EOF mode (shown). At the inner estuary site (B3), the first EOF mode more closely matches a gravitational current, but there are too few available data points to provide statistical certainty.

Since long wave influence in the inner estuary is doubtful, we investigate buoyancy driving as the primary source of variability in the measured inner estuary currents. This type of forcing is manifested in gravitational currents, which, like seiches, are also common features in basins with longitudinal density gradients and are commonly associated with subtidal motion of tracers in tidal estuaries (e.g. Bombardelli et al., 2009;

MacCready and Geyer, 2010). Solving Eq. (5.2) with a horizontal density gradient measured on 28 September 2010 indeed provides a current profile that compares favorably with the first variance mode at the inner estuary site (Fig. 5.11b). However, since the velocity structure at B3 was confined to the upper 2-3 meters of the water column, there were not enough data with the 0.5 m velocity bins to provide a statistically significant correlation.

5.3.4. Salt front advance in the inner estuary

We investigated the role of buoyancy driving further, using concepts derived from existing laboratory experiments with similar forcing conditions, keeping in mind potential scale effects. Except during upwelling at the mouth, the epilimnion behind the salt front resembles the tanks used in many of the classical laboratory experiments used for understanding gravitational circulation (e.g. Simpson and Britter, 1979). These tests usually consisted of a flat-bottomed rectangular chamber with a vertical partition in the center separating two water bodies of different density. When the partition is removed (lock-exchange problem), the pressure gradient between the water bodies fuels a buoyancy-driven current which leads to eventual vertical stratification. Linden and Simpson (1986) showed that when turbulence is introduced, the gravity current dissipates and the water column mixes vertically, although the horizontal density gradient remains. The gradient still dissipates with time due to turbulent stirring and relatively weak buoyancy-driven circulation, but it is clear from this study that gravitational circulation during times of weak turbulence is a much more efficient mechanism for distributing the

density than the stirring that ensues when turbulence is stronger. They also found that the dispersion of salt along the tank was well described by relating it to a bulk horizontal Richardson Number which they defined as:

$$Ri = \left(\frac{g' h}{q^2} \right) \quad (5.6)$$

where q is the root mean squared (r.m.s.) turbulent velocity fluctuation present in the water column, h is the tank depth and g' is defined above. As Ri trends towards infinity, gravity-driven currents dominate, whereas when it trends toward zero, turbulence prevents frontogenesis and dissipates any existing currents. A subsequent study by Linden and Simpson (1988) showed that alternating periods of turbulent and quiescent conditions allowed frontogenesis to occur: the gravitational current formed again each time turbulence subsided and was dissipated each time it was reintroduced.

We estimated g' from the vertically averaged salt field in the epilimnion, using the peak density gradient measured between any adjacent stations to define the density gradient $\Delta\rho$. This is based on the observation of Linden and Simpson (1986) that the local gradient has more influence on the strength of the gravitational circulation than the total end-to-end density difference in the tank. Lastly, we obtained an estimate for q^2 using an ensemble mean of the turbulent velocity fluctuations from all four ADCP beams within the epilimnion.

We applied this concept to the RRE by examining the epilimnion as an analogy to the described experimental tank. Here, the relatively flat metalimnion acts as a virtual tank floor on which currents driven by the persistent salinity gradient in the epilimnion transport salt upstream (e.g. Figs. 5.4) between intermittent periods of turbulence

production. A key difference is that bathymetric traps lie ahead of the salt front in the natural setting, constraining its motion by inundating negatively buoyant advancing salt water (Fig. 5.4). To study this further, we derive a representative measure of inundation capacity using measures of the estuary bathymetry and density field. Looking upstream from the mouth of the estuary, if we define the front position (x_f) as the first location where the middle of the pycnocline intersects the bathymetry and the pycnocline center elevation (z_f) as an ensemble mean of the centerline elevations measured at each CTD cast location behind x_f , we can estimate the available inundation volume ahead (farther upstream) of the salt front as

$$V_u = \int_{z_{\min}}^{z_f} \int_{y_{\min}}^{y_{\max}} \int_{x_f}^{x_{\max}} 1 dx dy dz \quad (5.7)$$

for which

$$\rho(x, y, z) < \rho_f$$

where x , y and z are the along, across and vertical dimensions in the estuary and ρ_f is a representative measure of the salt front density which we take as an average of the density behind x_f and above z_f . Using Figure 5.3b for illustration of these concepts, z_f is approximately 0.5 m NAVD88 when measurements were taken on 28 September 2010, and x_f is located approximately 7.5 km upstream of the inlet. Therefore, V_u at this time accounts for all of the estuary volume more than 7.5 km upstream of the inlet and below an elevation of 0.5 m NAVD88, which is comparatively small by inspection of conditions on 19 July 2010 (Fig. 5.3a). Eq (7) requires the assumption that z_f is a virtual ceiling for inundation in each pool, which seems reasonable based on the observations, which show a common pycnocline elevation (z_f) between the mouth and x_f (e.g. Fig. 5.4). ρ_f is an

important parameter because remnants of saline tidal water having higher density than the salt front may remain in parts of the inner estuary from tidal motions prior to closure, effectively limiting the available inundation space. We postulate the existence of a variable C , denoted as the dimensionless capacity and defined as a ratio of V_u and the total water volume of the estuary $V_{estuary}$, which is easily derived using the bathymetry and mean water level. Fig. 12 provides a visual example of x_f , z_f and C , within the context of the first and second phases of salt field evolution after closure, which are described above.

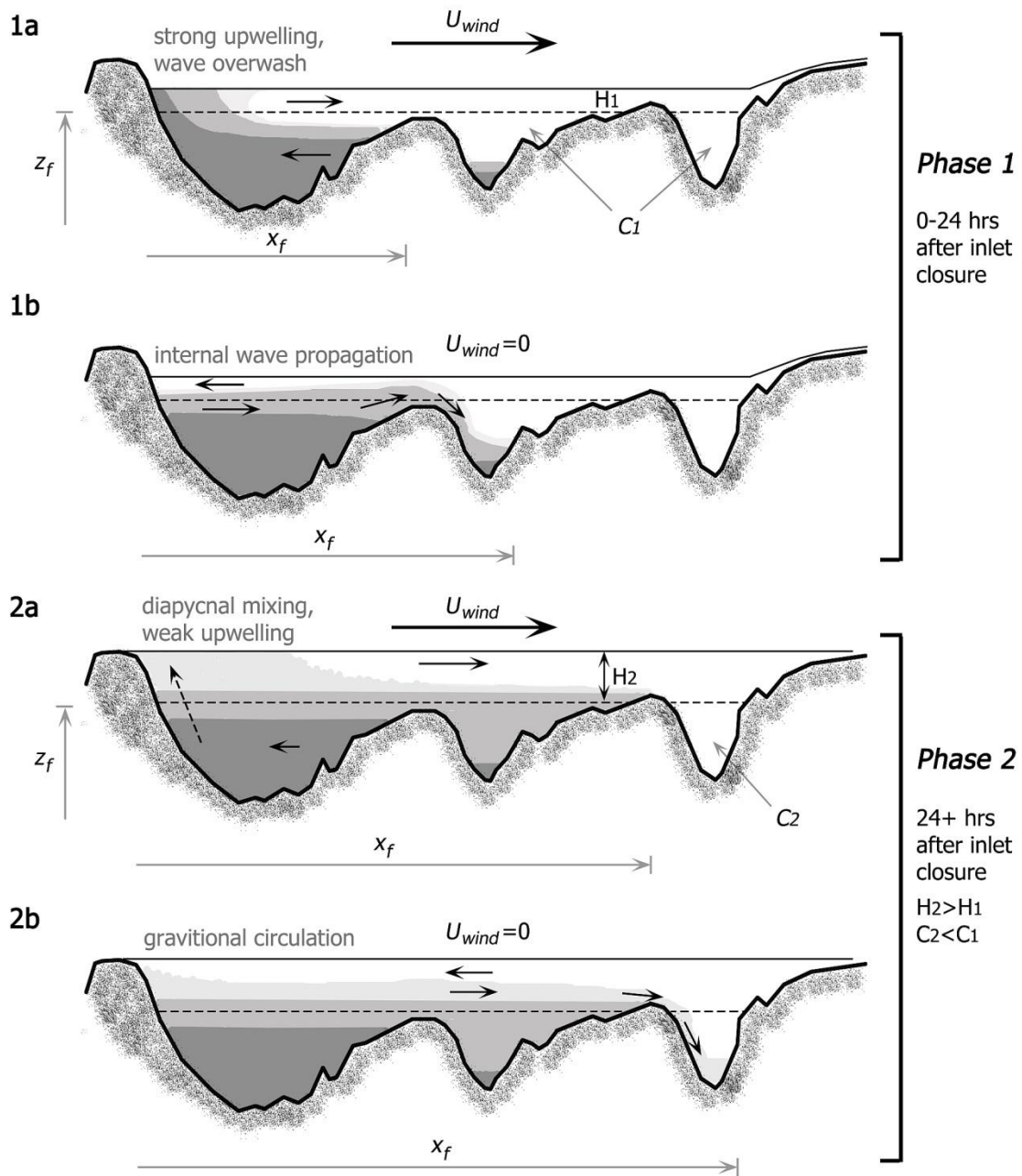


Figure 5.12. Conceptual drawing of the first (1a,b) and second (2a,b) phases of salt field redistribution after closure. H and C are a representative depth of the epilimnion and the dimensionless inundation capacity, respectively. Darker shading represents higher salinity water. The Wedderburn number is sometimes supercritical in the first phase (leading to strong upwelling) and subcritical afterwards, due to change in depth, H .

We compare Ri against the time series of the first variance mode at site B3 (which we have associated with buoyancy driving) during events E4 and E5, when the ADCPs were operated in mode 12. We also examine separate influences individually, namely the buoyancy forcing (via g') and turbulent kinetic energy production (P). To estimate Ri continuously we linearly interpolate values of g' , using the assumption that the salt field is slowly varying. The validity of this assumption is confirmed by Figure 5.6 and the time series of sonde measurements.

Fig. 5.13d shows that the time series of the variance mode associated with buoyancy driving indeed varies in concert with the Ri time series (Fig. 5.13c). Although not perfect, the correlation between the two parameters ($r = 0.46$, $p < 0.0001$, $N = 353$) is strong enough to conclude that gravitational circulation is an important driver of the observed salt migration. The time series of Ri (Fig. 5.13c) is largely controlled by the diurnal pattern in turbulence production (Fig. 5.13b). Large values of P associated with winds force Ri towards zero during the daytime. When P decays at night, the buoyancy forcing contributes to the magnitude of Ri . For example, the initially high values of g' on 4-5 October match the relatively high nighttime values of Ri . Wind stress associated with reverse (seaward) winds at night may also contribute to salt front movement, as indicated by negative phases of EOF variance mode 2 (Fig. 5.13d) which are at times coincident with the positive phases of the mode 1 series. However, nightly winds can presumably impede the salt front advance if they generate enough turbulence to dissipate the front.

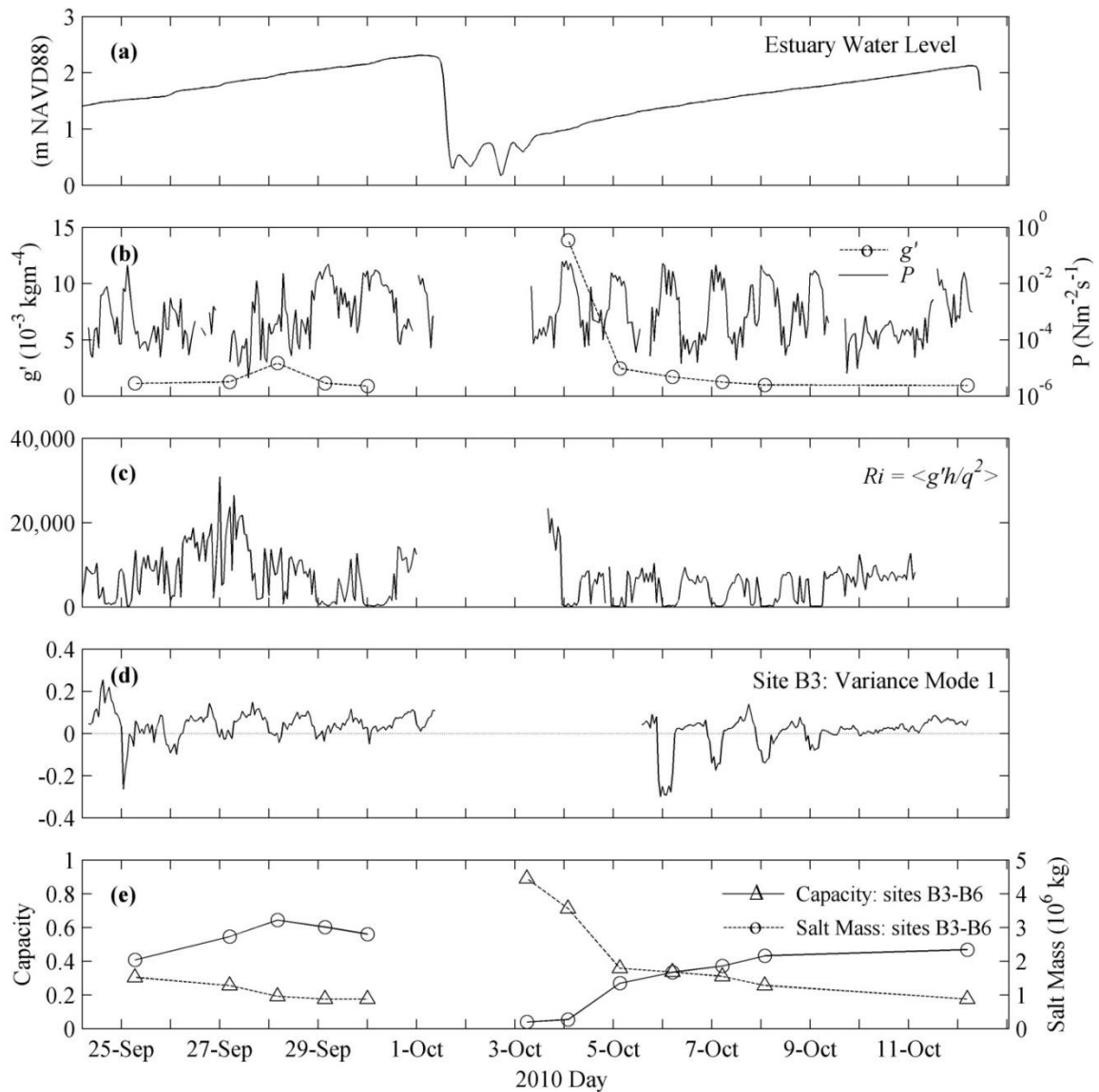


Figure 5.13. (a) Estuary water level from 25 September – 12 October 2010, compared with time series of (b) reduced gravity and TKE production, (c) horizontal Richardson Number (brackets denote vertical average in the epilimnion), (d) the primary variance mode at site B3 and (e) total salt mass and inundation capacity from sites B3-B6. The first variance mode at site B3 is most likely tied to gravitational circulation.

We also compare these measures against the total salt mass measured between site B3 and the upstream boundary. This was estimated using the bathymetry and the salinity values measured from the CTD profiles at stations B3-B6. The salt mass (Fig. 5.13e) is well described by the combination of Ri and C , although neither can describe it individually. Despite the limited amount of data, Ri appears to be a good indicator of periods when the salt front is mobile. This is visible during two bursts in salt mass in the inner estuary from 25-28 September and 4-5 October. In contrast, C acts as a constraint on the salt front movement. The salt mass asymptotes toward a peak value as C approaches zero at the end of both closure events. Salt may be added to the inner estuary when C is low, but it is limited to the elevations above the local sills where it can be redistributed freely by the diurnal winds, so its residence time is extremely limited compared with salt trapped in the pools below the pycnocline. Higher frequency data and a larger number of monitored closure events would improve confidence in these measures.

5.4. Discussion

5.4.1. Processes driving salt front excursion

The dense saline inflows and strong horizontal density gradients set up by tidal currents provide the initial potential for salt intrusion into the inner estuary after inlet closure. The initial response leads to an internal wave propagating upstream, which seems to extend the pre-existing tidal salt front to as far as 7.4 km from the inlet, but not

further. The relatively slower second phase of salt migration (slower nightly pulses of salt moving upstream along the pycnocline) is likely a response to buoyancy driving in the epilimnion, fueled by the persistent presence of salt in the upper water column near the mouth. Time series of g' (Fig. 5.13b) suggest that persistent diurnal winds and a difference in wind exposure between the inner and outer estuary maintain a baseline density gradient in the epilimnion, so that the second phase continues indefinitely. Pycnocline upwelling events at the mouth contribute to this baseline when the epilimnion is thin or if winds are exceptionally strong (Eq. 5.5). Even if a critical Wedderburn Number is not achieved, Okely and Imberger (2007) have shown that diapycnal mixing may occur as a result of upwelling bringing the interface closer to the wind-sheared currents at the surface, thereby increasing the likelihood that a critical gradient Richardson Number (e.g. Monismith, 2010) is achieved. The combination of the two salt migration phases resulted in the salt front advancing to the farthest upstream extent of the estuary during five of the six closure events that were studied.

The EOF analysis provided strong evidence that a V3H1 seiche dominates the outer estuary flow field at night, but there was no evidence that this influenced flows in the inner estuary. This type of mode is not commonly studied, but has been observed in similar systems (Vidal and Casamitjana, 2008). Propagation of this predicted seiche mode into the inner estuary is limited by its weak celerity (0.084 ms^{-1}) compared with the length of the estuary and frequent of winds, which are expected to arrest any remnants of this current before it reaches the inner estuary (Linden and Simpson, 1988). Since much of the salt front advance occurs in the inner estuary, internal waves thus do not appear to

have much influence. This may not be the case in similar systems if faster modes (e.g. V1H1) are present.

The sills present in the estuary appear to impede the first phase of salt advance and aid the second. The large-amplitude seiche which appears to be released at the time of closure is limited in its advance upstream by the sill heights: The wave amplitude is usually of the same scale as the epilimnion thickness, so that the shallow depths over sills in the outer- and mid-estuary probably achieve the critical breaking depth (Vlasenko and Hutter, 2002). This is corroborated by the decay in amplitude of the wave observed from sondes near the surface. Also, the sills appear to physically block the pycnocline 4-6 km from the inlet, which would prevent the wave from propagating into the inner estuary. In contrast, bathymetric traps formed by the naturally occurring pools at channel bends arrest migrating salt in pools whenever the front reaches a location where the local pycnocline is blocked by upstream bathymetry. This trapped salt has an indefinitely long residence time, since winds do not appear to be strong enough to erode it out. Additionally, this salt acts as a platform for subsequent loads. The narrow, canyon-like structure of the RRE, which may contribute to its alternating pool-sill bathymetry, is a common feature of bar-built estuaries along active continental margins, where steep gradients are typical (e.g. Cooper, 2001). Many of the bathymetric and topographic features that contribute to the salt field evolution in this case are expected to be present in similar settings, especially in Mediterranean climates.

5.4.2. Limiting factors

The most important limiters of the salt front advance are turbulence, bathymetry and the vertical structure of the density field. Turbulent mixing during daytime winds creates a vertically-homogeneous epilimnion throughout the estuary (Fig. 5.6), presumably destroying any fronts formed during prior calm periods (e.g. Linden and Simpson, 1988). Also, the wind-sheared profile that arises creates a return (seaward) flow at the pycnocline elevation which acts to transport any salt not already trapped in pools towards the mouth. The elevation of the pycnocline (z_f) and the volumetric size of the pools ahead of the salt front limit its advance by constraining the amount of space available for inundation with mobilized saltwater. The front must inundate each pool until the pycnocline is high enough to allow it to pass over the immediate upstream sill. If not enough epilimnetic salt water is available to do this, the front is arrested until additional mixing events at the mouth provide more. If no space is available, salt added to the inner estuary rests above the pycnocline, and is subject to removal by the wind-shear profile during the day. The importance of this space availability is demonstrated by the strong negative relation shown between C and the salt mass upstream of site B3 (Fig. 5.13).

In many similar systems, riverflow may also be an important limiting factor. In some cases, such as the San Francisco Bay Delta Estuary, the location of the 2 psu isohaline is statistically tied to freshwater inflows (Monismith et al., 2002). During closure at this site, freshwater inflows typically contribute less than five m^3s^{-1} which results in currents of less than one cm s^{-1} , so their effects would be minimal in this case. Depending on the internal hydraulics, stronger inflows could lead to a bidirectional flow

over sills that would still allow salt front advancement, or they could arrest the front and prevent its advance (e.g. Largier, 1992).

5.4.3. The Ri approach and future considerations

The EOF and horizontal Richardson Number approaches suggest that gravitational circulation is present but cannot confirm its importance relative to other mechanisms. The latter method seems particularly useful as a measure of when frontogenesis would allow this type of current to form. Comparison of Ri with the first variance mode at site B3 suggests that buoyancy-driven currents appeared when Ri was $O(10^4)$ or higher, although this is probably a rudimentary measure on its own. Where computationally-expensive numerical modeling is not feasible, a combination of Ri and C may provide a useful set of diagnostic tools for predicting evolution of the salt distribution in similar systems. However, because of the differences in wind-exposure and bathymetry along the estuary it is clear that both internal waves and gravitational circulation (and perhaps other processes that we have not discussed) are important to the overall transition. Thus, a unifying theory explaining salt migration after closure in bar-built estuaries is difficult to formulate. Future study in this area should make use of multiple nearby device arrays to estimate the momentum budget, which could increase confidence in the measures that we have discussed here and better isolate the suite of driving mechanisms (e.g. Giddings et al., 2012).

5.5. Uncertainty Analysis

5.5.1. Measurements

Measurement uncertainties are divided here among flow measurements and boat-based tracer measurements. The standard deviation for a single (mode 12) velocity measurement was 2.01 cm s^{-1} [PlanADCP v2.06, Teledyne RD Instruments (2009)] for the ADCP configuration described above. Ensemble averaging gives a standard error smaller than the standard deviation:

$$se = \frac{\sigma}{\sqrt{n}} \quad (5.8)$$

where se is the standard error and n is the number of measurements within an ensemble.

For 10-minute ensembles of 1 Hz measurements, $se = 8 \times 10^{-4} \text{ m s}^{-1}$.

The instrument noise level was calculated after Stacey et al. (1999) and Williams and Simpson (2004). Instrument noise is a lower bound on the certainty of any given stress estimate (Nidzicko, 2006), and is calculated by comparing the standard deviation of the Reynolds against the along-stream mean of the stress. The variance of the stress is defined by Williams and Simpson (2004) as:

$$\sigma_R^2 = \frac{\gamma_R \left[\overline{(b_1')^2} + \overline{(b_2')^2} \right]}{2M \sin^2 2\theta} \quad (5.9)$$

where b_1 and b_2 are velocity fluctuations on opposite beams, M is the sample size (600), and

$$\gamma_R = 1 + 2 \sum_{n=2}^K \rho(1, n) \quad (5.10)$$

is a correction factor which accounts for autocorrelation between measured velocities at different time steps. ρ in this case is the correlation of the series of measurements with itself shifted by n time steps. The upper limit (K) is usually on the order of 20 s (Stacey et al., 1999). We found $\gamma_R \sim 2$, which gave a standard error of $\rho\sigma_R = 0.032$ Pa for turbulent Reynolds stresses and a noise floor of $2.2 \times 10^{-5} \text{ m}^2\text{s}^{-2}$. The noise floor was about 14 percent of the mean stress magnitude.

CTD measurements were accurate to 0.005 °C for temperature and 0.0005 S/m for conductivity. This gives uncertainties of 0.002 psu for salinity 0.002 kg m⁻³ for density. Pressure measurements gave depth measurements accurate to ~ 2 cm.

5.5.2. Calculations

EOF Method

In Section 5.3.3, we showed that a characteristic set of variance modes dominate the flow structure in the outer and inner estuary using flow data at sites A4 and B3, respectively. We used this to show that gravitational circulation dominates the flow structure in the inner estuary and that diurnally-forced vertical mode 3 internal waves dominate the structure in the outer estuary. To test the significance of the variance modes that were used to make this assessment, we use the Rule N approach, which is described in detail by Preisendorfer (1988).

Rule N is a method for testing the significance of the variance modes calculated using data against those generated by random numbers. Variance modes are estimated for a large number of uncorrelated synthetic datasets of the same size as the original data matrix used in the EOF analysis. The synthetic datasets are composed of normally-distributed random numbers generated from Monte Carlo simulations. For example, the present study used the EOF approach on matrices of along-stream flow velocities measured by ADCPs, where the matrix rows represented elevation and matrix columns represented discrete points in time. The number of columns (time steps) was taken as 100, and there were between 9 and 11 rows (depending on measurement station). To use the Rule N approach, 100 matrices are formed in this case, each having 100 columns and either 9 or 11 rows, and every cell value is a pseudo-random number generated by Matlab© from a normal distribution.

The EOF analysis is performed on each of these 100 synthetic datasets, producing a set of variance modes for each dataset. Ordering the variance modes by magnitude (percent of variance explained) and adding a 95 percent confidence interval gives the dashed line shown in Figure 5.14. This is compared against the variance modes calculated from ADCP data at sites A4 and B3. Variance modes that exceed this dashed curve are considered significant at the 95 percent confidence level (Preisendorfer, 1988). In this case, this confirms that the first two variance modes at stations A4 and B3 are significant, while the third mode at Station A4 is marginal.

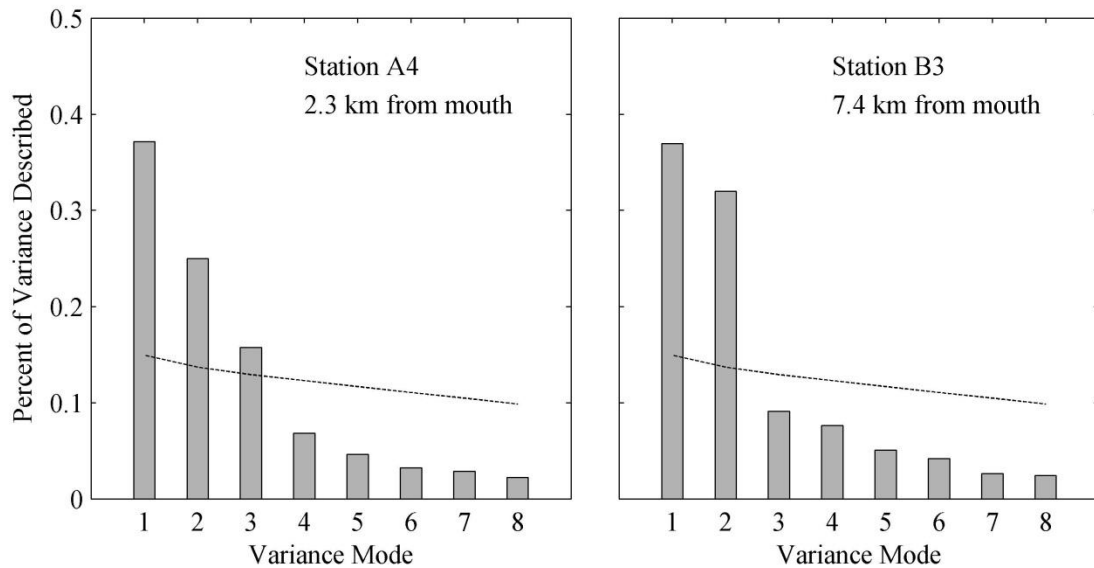


Figure 5.14. The percentage of the total variance captured by the first 8 variance modes for **(left)** Station A4 and **(right)** Station B3. In both plots the 95 percent significance level obtained from a Monte Carlo (Rule N) simulation (Preisendorfer, 1988) are given.

Salt Front Movement

Here we calculate the uncertainties in the terms presented in Figure 5.13, which were used to infer the processes controlling evolution of the salt field during closure. For depth measurements, we consider device error and fluctuations in both density and water level below the measurement intervals. Hourly water levels were obtained at station B3 from pressure measurements taken at two-minute intervals. To get water levels, hydrostatic conditions were assumed:

$$p = \rho gh \quad (5.11)$$

where p is the hydrostatic pressure, and h is the depth in the water column above the sensor. The standard deviation of density in the upper water column is 2.4 kg m^{-3} . For a maximum observed depth of $\sim 3 \text{ m}$ (the depth of the pressure sensor), this gives a maximum error of 0.3 cm due to hourly density fluctuations. The standard deviation of the two-minute time series of water level is 2.5 cm . Both of these estimates, combined with the reported 1 cm maximum error reported for the pressure logger, gives a total uncertainty of 3.8 cm .

Uncertainty in the production of turbulent kinetic energy was found using the methodology of Williams and Simpson (2004), which requires estimation of the standard error of the Reynolds stresses (obtained above) and of the velocity shear:

$$\text{var}\left(\frac{\partial u_n}{\partial z}\right) = \sigma_s^2 = \frac{\gamma_s \left\{ \text{var}[b_{2(n+1)} - b_{1(n+1)} - b_{2(n-1)} + b_{1(n-1)}] \right\}}{4M(\Delta z)^2 \sin^2 \theta} \quad (5.12)$$

γ_s is calculated in the same way as γ_R but represents autocorrelation among velocity shear measurements. We found $\gamma_s \sim 2$ and $\sigma_s = 0.003$. The uncertainty in turbulent energy production is then found from:

$$\sigma_p^2 = \overline{u'w'}^2 \sigma_s^2 + \left(\frac{\partial u}{\partial z}\right)^2 \sigma_R^2 + \sigma_R^2 \sigma_s^2 \quad (5.13)$$

We used the value of shear near the top of the water column rather than at the bottom, since the stratification limits the kinetic energy near the ADCP. Similar studies are usually conducted in an unstratified water column and examine the value 0.75 m above the ADCP face. We found that $\rho\sigma_p = 1.45 \times 10^{-3} \text{ Wm}^{-3}$, which represents roughly 14

percent of the mean value of P measured in the upper water column at Heron Rookery throughout the deployment period.

Buoyancy driving was represented with g' measured from CTD profiles at roughly daily intervals. To account for hourly fluctuations, the standard error of g' was estimated using the hourly SCWA sonde measurements in the outer estuary, at stations A1 and A4. Hourly variations between these two sites are assumed to be representative of others in the estuary. Both sondes are located in the epilimnion, about 1 m below the surface, where salinity and density are well-mixed in the vertical. The standard error for the periods of inlet closure discussed herein is $2.3 \times 10^{-3} \text{ m s}^{-2}$, or about 10 percent of the mean value of g' for the entire dataset.

Uncertainty can be attributed to our estimate of Ri by assuming a worst-case scenario (maximum uncertainty of all variables) with the uncertainties of g' , q' and h . Using the uncertainties for all three terms, as calculated above in Eq. 5.6, gives an uncertainty of roughly 0.22 for Ri .

Uncertainty in the total estuary salt mass and salt inundation capacity (C) are assumed to be dominated by several factors: (1) pycnocline tilt during CTD profiles, (2) errors in estuary water surface estimates, and (3) estuary section uniformity. The first refers to measurements taken when shear in the water column displaces the density interface, artificially inflating or deflating the salinity profile used to estimate total salt mass. Errors in water surface estimates would cause the salinity profile to misalign with the elevation profile. Lastly, our use of 12 CTD profiles to characterize the total salt mass in the estuary requires the assumption that each section of the estuary has a homogeneous

salt field in the horizontal (x and y) directions. Instrument precision and bathymetry resolution are assumed to have only a minor influence.

The uncertainty due to pycnocline tilting was found by applying a tilt of 1 m, which is approximately the maximum observed, which only occurred during BML winds higher than 10 ms^{-1} . The salinity and elevation vectors at each of the 12 CTD profile sites were displaced by 1m and the total estuary salt mass was re-calculated as described above. This produced errors of ~6 percent of the estuary salt mass, which can be considered a maximum error, since winds were typically smaller than 10 m s^{-1} . We estimated the uncertainty due to errors in water surface elevation measurement by performing the same task with a displacement of 4 cm, the approximate error found for water surface measurements. The error in this case is ~ 1.5 percent of the total salt mass. Lastly, the uncertainty in salt mass introduced by sectioning the estuary into 12 parts (rather than an infinite amount) was estimated by finding the total estuary salt mass using 1, 2, 4, 6 and 12 representative sections. The total salt mass asymptoted toward a constant value with increasing amounts of sections. The uncertainty was approximated as the difference between salt mass estimates using 6 and 12 representative sections. This was ~ 2.5 percent of the total salt mass, giving a total error from all sources of roughly 8 percent of the estuary salt mass.

6. The Effects of Several Inlet Management Practices on Water Column Stability in an Intermittently Closed Bar-Built Estuary

Dane K. Behrens, Fabián A. Bombardelli and John L. Largier

6.1. Introduction

As discussed in Chapters 2 and 5, sharp salt-stratification, salt retention and saline-layer hypoxia are common features of bar-built estuaries, with the RRE providing a good example. When closure occurs, a number of management options exist, which are constrained by the habitat requirements of estuarine species and by water quality concerns, flooding concerns, and other issues (see Chapter 2). Both the vertical structure of the salt field and its extent into the estuary are important limiters of habitat space for aquatic species. In the vertical, the density gradient between fresher upper and saltier lower layers inhibits vertical exchange of oxygen, contributing to the hypoxia often observed in bottom waters (Borsuk et al., 2001). The interface (metalimnion/pycnocline) separating the epilimnion and hypolimnion creates a habitat constraint on species that cannot survive in the low-oxygen conditions (Figs. 5.1-2). In the horizontal, the leading edge of the salt front, sometimes measured as the first location having a minimum salinity, is statistically tied to survival of many pelagic and benthic organisms (Jassby et al., 2005).

When the inlet closes, continuing freshwater inflows pond behind the beach, and the resulting hydrostatic pressure gradient that forms between the estuary and the ocean may either (1) eventually balance with seepage and other water losses, (2) destroy the barrier and erode a new inlet (Kraus et al., 2008), or (3) create a small supra-tidal spillover channel that is too weak to erode a new inlet. These conditions are summarized in Figure 6.1. These represent the three most clear management options available. As discussed in Chapter 2, the first is common in rural areas with few stakeholders, while the second is more common where flooding is more of a concern and where agricultural and municipal development are present along the estuary margins. The third is less common, but is currently being adopted as a management approach in the RRE (NMFS, 2008)

Even though the perched overflow and closed states prevent tides and the turbulence that they generate from entering the estuary, the existing salt-stratification may still change, as the salt field is not necessarily stationary during any of these management states (Chapter 5). Since inflows are typically low in these types of systems, wind usually supplies the majority of the kinetic energy to the lagoon (Gale et al., 2006), which may alter the salinity field by directly mixing the epilimnion or by exciting internal wave modes which transfer the energy to the lower layers (Vidal and Casamitjana, 2008).

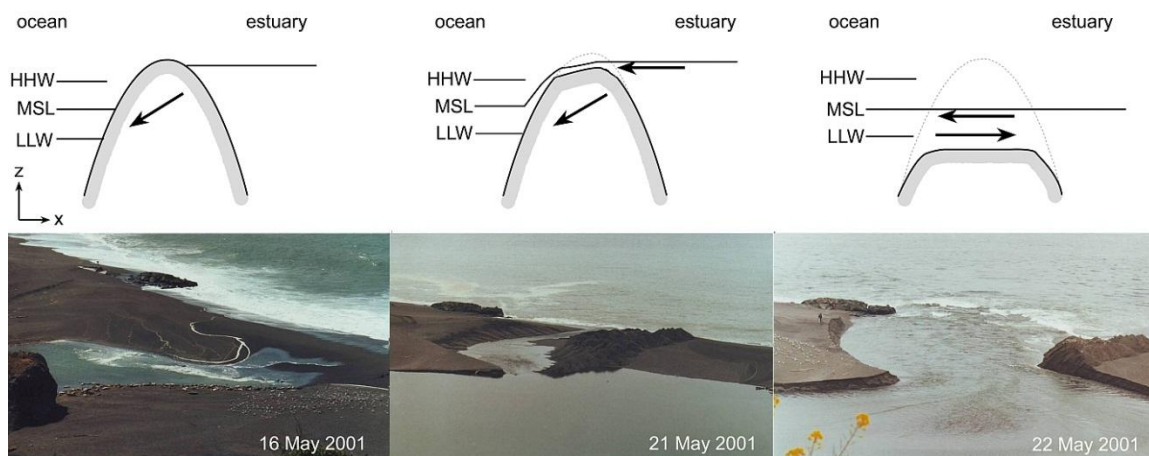


Figure 6.1. Summary of the typical inlet states observed at the Russian River Estuary. From left to right, the states are **(left)** the inlet after closure, **(middle)** the inlet during perched overflow and **(right)** the inlet during open, fully tidal conditions. The modeling effort herein focuses on the closed and perched overflow states. Photographs are courtesy of Elinor Twohy.

Export of estuary waters through the perched overflow channel or through the porous beach may also contribute to the long-term salinity conditions, but there are few existing studies to demonstrate the importance of these factors. While several studies confirm the existence of a perched overflow state (Hayes et al., 2008; Crane and Solomon, 2010; Stretch and Parkinson, 2006), it remains uncertain how a small outflow channel could affect the salt content or structure at the basin-wide scale. The same is true of barrier seepage during closure, although a wealth of studies (e.g. Cable et al., 1997), point to its extreme variability, and in some cases (e.g. de Sieyes, 2008), its effect on scalar transport from lagoons to the ocean.

Though it is well understood that stratification dominates scalar transport in bar-built estuaries (Borsuk et al., 2001; Cousins et al., 2010), the distribution of scalar fields throughout the lagoon is rarely studied when a perched overflow channel is present.

Studies addressing this behavior thus far have focused on the physics of the beach-channel system (Stretch and Parkinson, 2006) or the estuary habitat that it provides for anadromous fish (Hayes et al., 2008; Perissinoto et al., 2010). As a result, little is known about the differences in water column stability that results from the presence or lack of an overflow channel in an already-closed system, even though this has strong implications for the residence time and dissolved oxygen content of bottom waters.

The purpose of this Chapter is to determine how much water column stability would vary in the RRE as a response to implementation of two of the three management actions described above: either the inlet is left closed or altered to have a supra-tidal perched overflow channel following the onset of inlet closure. We also wish to determine how varying wind and beach porosity contribute to the consequences of these states. We achieve these goals with a two-dimensional (2D) numerical model of a real system, and compare its results with existing field data at the site. The results of this study are expected to have important implications for management in these systems, since the habitat requirements of myriad aquatic species are directly tied to the salt field as well as to the temperature and dissolved oxygen fields which are often controlled by it.

6.2. Methods

6.2.1. Field Observations

Since this chapter focuses on typical estuarine conditions during extended closure and perched overflow, it relies heavily on boat-based salinity measurements taken during

events E1 (September-October 2009) and E3 (Jul 2010) for comparison with model results. These are described along with the methods of field data collection in Chapter 3, and maps of the estuary salt field during these periods are provided in Appendix C. Special attention is given to the conditions in the 5 km wind-exposed reach closest to the mouth (Fig. 6.2). This is because the recent bathymetric survey (EDS, 2009) indicates that the outer basin contains the majority of the estuary volume. The majority of the changes in estuary salt structure and mass are thus assumed to take place in this region.

Model inputs draw on empirical estimates of beach berm seepage. These flows are discussed in Appendix A, which shows that the total water losses from the system are significant during closure. Data from 1999-2009 show a strong empirical relation between the estuary-ocean head difference and water losses, suggesting that seepage losses are of primary importance, presumably through the sandy beach. Peak losses rise from $0\text{-}0.5\text{ m}^3\text{s}^{-1}$ at a head-difference of 0.5 m to $1.75\text{-}2.75\text{ m}^3\text{s}^{-1}$ when the head difference approaches two meters.

Winds were also a necessary model input, but since no direct wind measurements were taken in the estuary, winds were assessed qualitatively by examining gradients in along-estuary water level, obtained from the pressure transducers placed in the estuary. Records at the nearby Bodega Marine Laboratory (BML) and pressure measurements in the estuary show a dominant diurnal signal with relatively strong landward winds during the day and negligible or seaward-directed winds at night.

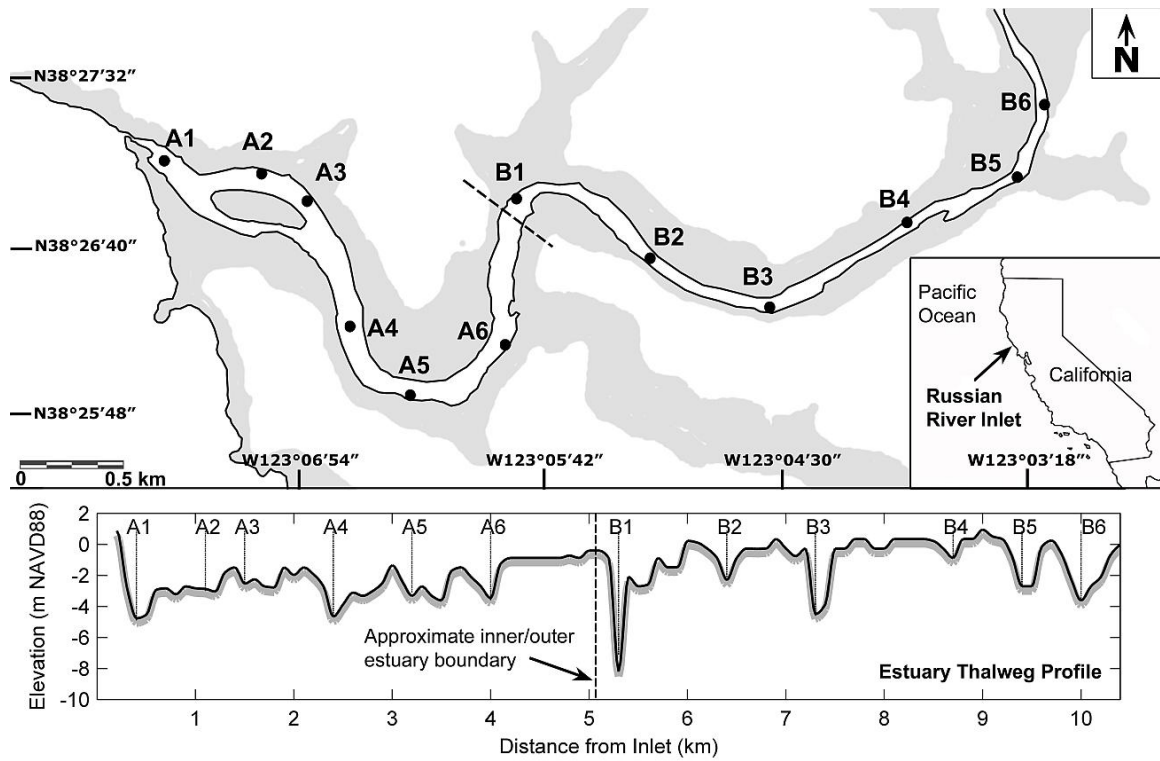


Figure 6.2. (top) Aerial view of Russian River Estuary, showing boat-based CTD measurements sites and (bottom) side view using the estuary thalweg profile to mark the channel bottom. The approximate boundary between the inner and outer estuary (pictured) represents the departure between the relative deep and wind exposed outer estuary and the relatively shallow and wind shielded inner estuary.

6.2.2. Theoretical Model

The theoretical model is based on the Reynolds-Averaged Navier-Stokes (RANS) equations for mass and momentum for an incompressible flow, as follows:

$$\frac{\partial \bar{u}_j}{\partial x_j} = 0 \quad (6.1)$$

$$\frac{\partial \bar{u}_i}{\partial t} + \bar{u}_j \frac{\partial \bar{u}_i}{\partial x_j} = -\frac{1}{\rho_0} \frac{\partial \bar{p}}{\partial x_i} + G_i + \frac{1}{\rho} \frac{\partial \tau_{ij}}{\partial x_j} + SM_i \quad (6.2)$$

where u_i is the velocity component in the i -th direction (i varies from 1 to 3, and the Einstein convention has been employed), t is the time coordinate, x_i is the spatial

coordinate in the i -th direction, p is the pressure, ρ_0 is the reference density, G_i are the body accelerations in the i -th direction (including gravitational forces per unit mass), and τ_{ij} are the shear stresses, including the stresses coming from purely viscous origin and turbulence, and the shear stresses at wall volumes (Flow Science, 2012). SM_i denotes sources/sinks of momentum i -th direction. In the analysis, the Boussinesq assumption has been adopted, whereby the density is only considered in the gravitational terms (Cushman-Roisin, 1994; Bombardelli et al., 2009). This approximation is valid in most estuarine flows, usually when temperature differences are smaller than 20° C. In the Russian River Estuary, the density differences are driven mainly by salinity, since the differences in temperature are smaller than 5° C and, thus, relatively minor (See Appendix B).

Another equation is solved for the transport of density (see Bombardelli et al., 2009; Kundu and Cohen, 2008) as follows:

$$\frac{\partial \rho}{\partial t} + \frac{\partial (\rho \bar{u}_j)}{\partial x_j} = \frac{\partial}{\partial x_i} \left(D_{ij} \frac{\partial \rho}{\partial x_j} \right) \quad (6.3)$$

where D_{ij} is a tensor adding the eddy diffusivity (due to turbulence) and the diffusion due to molecular origin, of salt, i.e., the “effective” diffusivity of salt. This equation is *not* the mass conservation equation; rather, it is a simplified version of the energy equation (Kundu and Cohen, 2008, page 128).

For the porous portion of the domain, i.e., the beach, the theoretical model assumes a momentum loss via a drag-like law, as follows:

$$SM_i = - K u_i \quad (6.4)$$

where K depends on the soil porosity. The code allows the user to define K as a function of the Reynolds Number and porosity. We choose the simplest model embedded in the code, with $K = a$ where a is an empirical coefficient set by the user. To solve for u_i in porous media, the code uses a Darcian approach (Bear, 1988).

The effect of wind is included via a momentum loss at the cells located near the free surface, as follows:

$$SM_i(\text{free surface cells}) = C_w UW_i / (\rho V_F \delta z) \quad (6.5)$$

where C_w is a wind drag coefficient, UW_i is the wind velocity in the i -th direction, V_F is the volume fraction at the volume of the free surface of size δz . The value of the drag coefficient was obtained via calibration, as discussed in Appendix B.

Free surface boundaries and fluid interfaces are treated using the Volume-of-Fluid (VOF) technique (Hirt & Nichols, 1981). The free surface is not only a priori unknown in 3D computations, but it also acts as a boundary for the problem, where adequate boundary conditions need to be specified.

For the present study, we close the RANS equations with the use of the Smagorinsky (1963) model. Eddies below a length scale, L , defined by the product of the sizes of the volume are treated by approximating their effect using a local eddy viscosity that is dependent on the fluid velocity strain rate:

$$\nu_T = (cL)^2 \sqrt{e_{ij} e_{ij}} \quad (6.6)$$

where c is a constant between 0.1 and 0.2, e_{ij} is the strain rate tensor and ν_T is the eddy viscosity.

Since we resolve the entire 11-km extent of the estuary, we choose a mesh which captures the largest eddies ($O(1\text{ m})$) and resolves the majority of the turbulent energy with the Smagorinsky sub-grid-scale (SGS) model. Although Smagorinsky closure is used, this use is of course *not* a formally Large Eddy Simulation (LES); it is a simulation rooted in a RANS framework, with a closure of LES. In some literature, methods referred to as a Coherent Structure Capturing (CSC) or Very Large Eddy Simulation (VLES) models (Ilicak et al. 2007) can be found; in this study, *no* turbulent fluctuations are obtained, a feature which is typical of RANS solutions, not of LES.

6.2.3. Numerical Model

Simulations were performed using FLOW-3D 9.2.5 (Flow Science, Inc., Santa Fe, New Mexico) - a computational fluid dynamics (CFD) code that solves the three-dimensional (3D) transient flow equations by a finite-volume/finite-differences method. The grid is rectangular and staggered, which means that velocities are evaluated at the faces of the volumes, facilitating the imposition of boundary conditions. Although not originally devised for estuarine problems, the model possesses features that are useful for the simulation of stratified flows in natural basins (Bombardelli and García, 2001), river and estuarine circulation (Rodríguez et al., 2004; Abad et al., 2008), gravity currents (Bombardelli et al., 2009), and mixing, and allows for accurate treatment of turbulence, water surface elevations and solid boundaries (Hirt and Nichols 1981; Hirt and Sicilian 1985).

In FLOW-3D, the objects are built in independent fashion with respect to the mesh. The code employs the Fractional-Area-Volume-Obstacle-Representation (FAVOR) technique (Hirt & Sicilian, 1985), which allows for the definition of solid boundaries within the grid. FAVOR computes fractions of areas and volumes open to flow in partially blocked volumes, for the determination of fluxes nearby those boundaries. In this way, the process of defining boundaries and obstacles is independent from the grid generation. Once the geometry has been defined, the computational mesh is constructed separately, facilitating densification in zones of the domain of particular interest.

We have chosen to model a unit-width 2D planar representation of the estuary, emphasizing variation in the x - and z - directions, and neglecting lateral variability. This is because the canyon-like shape of the estuary leaves a narrow and relatively-invariant channel width (Fig. 6.2), so we assume that variation in the lateral direction is relatively minor compared with variation in the vertical and along-stream directions (e.g. Fischer et al., 1979). While LES requires a fully 3D grid to resolve turbulent eddies with full accuracy (Sagaut, 2005), several studies have shown that a 2D approach captures much of the planar components of flows associated with eddies, as long as the mesh is fine enough to properly resolve flow boundaries (e.g. Smith and Foster, 2005). This type of modeling approach has been used before with some success, both at small (Smith and Foster 2005) and large scales (Laatar et al., 2002).

6.2.4. Grid and Boundary Conditions

The modeled planar estuary includes a porous beach at the seaward (left) side of the domain (Fig. 6.1), a rigid bottom boundary representing the channel thalweg, and a free surface with an open air boundary at the vertical extent of the domain, and an upstream (right) boundary with variable freshwater inflows. The beach that separates the ocean from the estuary at the downstream boundary is given a uniform width of 300 m and we assume isotropic porosity. The thalweg profile characterizing the estuary bottom was estimated from a raster of the estuary bathymetry. To fully resolve the salt stratification, our mesh prioritizes the vertical resolution of the density field, with grid cells that are 0.1 m long in the vertical direction and 100 m long in the horizontal. We found that improvements in accuracy imparted from using a finer horizontal resolution were relatively minor compared with the high computational cost.

A constant freshwater ($\rho \sim 998 \text{ kgm}^3$) inflow rate of $0.012 \text{ m}^3\text{s}^{-1}$ is enforced at the upstream boundary, which represents a typical dry-season flow of $2.4 \text{ m}^3\text{s}^{-1}$ divided by the $\sim 200 \text{ m}$ width of the channel at this boundary. A constant sea elevation of 0.25 NGVD is enforced at the ocean boundary, which represents a typical long-term average value of the mean sea level (MSL) measured by the National Oceanic and Atmospheric Administration (NOAA) at Pt. Reyes (http://tidesandcurrents.noaa.gov/station_info.shtml?stn=9415020).

At the beach boundary, variable beach width and soil permeability were taken into account by calibrating the seepage drag coefficient a in Eq. (6.5) with field data from 26 September – 5 October 2009 (Appendix B). The total seepage rate through the beach was adjusted so that seepage losses balanced with freshwater inflows to match the

observed water level changes during this time. At the same time, the vertical profile of permeability was adjusted to allow for the correct prediction of vertical salinity profiles near the mouth (Appendix B). For the present study, we assume that these estimates of the average beach permeability and its vertical profile are reasonable for use with other closure events.

To model closure events, the top of the beach is positioned much higher than the initial estuary water level, allowing the water level to increase behind the beach as freshwater inflows are trapped. For perched overflow, the top of the beach is placed 0.1 m below the height of the estuary water level at the initial time step, allowing the estuary waters to spill over the beach freely.

The vertical boundary (the estuary free surface) is forced with a diurnal wind stress represented in three stages: a high-wind case, a low-wind case and a case with nonexistent wind. We use a repeating 24-hour sinusoidal signal with landward winds that peak at 15:00 h during the day and relatively weaker seaward winds that peak at 3:00 h in the early morning (Fig. 6.3).

The initial salinity field was constructed from observations at the beginning of a typical closure event that began on 4 October 2010 (Fig. 6.3). At the initial time step, the estuary is already stratified in the vertical and most of the estuary salt is concentrated in the outer estuary. The analysis focuses on sites in the outer estuary, since this contains the majority of the volume, salt and habitat space in the estuary. We neglect the effects of temperature and consider density as being controlled exclusively by salinity, since we found that salt had a much greater influence on the density field.

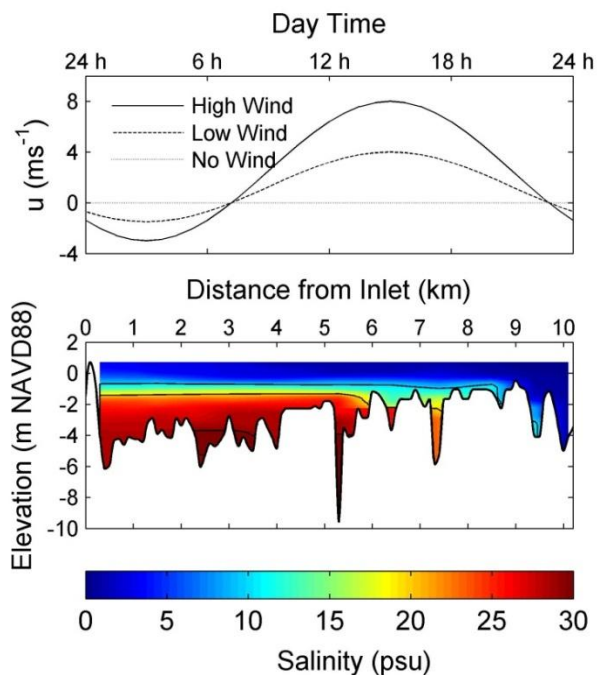


Figure 6.3. Summary of **(top)** wind forcing conditions used in the model runs and **(bottom)** the initial salinity profile enforced at the initial time step. The wind signal is repeated diurnally for the two-week model duration. The initial density field mirrors the salt field.

6.2.5. Validation

Full details of the model validation are provided in Appendix B, where the model is tested in a number of canonical situations and also compared against observations in the RRE from 26 September to 5 October 2009, during closure event E1 (Table 3.2). The model was found to be an excellent descriptor of pycnocline upwelling, vertically-sheared flow structure and density field evolution when compared with the field data, despite the 2D approximation. The grid resolution and our choice of a VLES turbulence model provides limitations to resolving the viscous boundary layer, but this is mitigated by the relative depth of the estuary: With the present specifications, the model fits the

law-of-the-wall profile (Pope, 2000) for all depth values except within ten percent of the total depth from the boundary. The estuary bathymetry and density structure typically relegates this to the hypolimnion, which is well below both the surface and the density interface for most of the outer estuary (Appendix C), so we assume that its effect is minimal.

6.2.6. Model Simulations

Twelve total scenarios were modeled, which are intended to explore the differences between closure and overflow for different beach seepage and wind conditions (Table 6.1). Runs consist of 14-day management periods, all starting from the same initial condition, with the estuary water level resting at a typical higher high water (HHW) tide level of 0.25 m NGVD88. As time passes, the hydrodynamics of these two management choices are expected to diverge, since the estuary will fill during closure and remain the same level during overflow. The forcing conditions used here are intended to reflect typical conditions both at the RRE and at similar bar-built estuaries in semiarid climates (e.g. Cooper, 2001; Roy et al., 2001). In the remaining sections we focus on the current structure, evolution in salinity field, water column stability and total salt mass in the estuary during the model runs.

Table 6.1. Summary of model runs.

Run	Wind	Inlet	Beach
1a	High	Closed	Non-porous
1b	High	Closed	Porous
1c	High	Perched	Non-porous
1d	High	Perched	Porous
2a	Low	Closed	Non-porous
2b	Low	Closed	Porous
2c	Low	Perched	Non-porous
2d	Low	Perched	Porous
3a	None	Closed	Non-porous
3b	None	Closed	Porous
3c	None	Perched	Non-porous
4c	None	Perched	Porous

6.3. Results

6.3.1. Current structure and residual circulation

The stratified salt field used as an initial condition had a strong effect on the current structure in the lagoon. For all model runs, the majority of the shear and kinetic energy resulting from combined wind and river forcing was confined to the upper one meter of the water column (Fig. 6.4). The river currents ($\sim 10^{-2} \text{ m s}^{-1}$) were additive with wind currents ($\sim 10^{-1} \text{ m s}^{-1}$) at night, but were otherwise overpowered by landward winds during daytime. These winds caused the pycnocline to upwell at the mouth and to downwell approximately 4-5 km upstream, forcing the interface to interact with the rigid bathymetry at both sites at a 24 hour interval. Since the system is mostly enclosed, the net currents enforced by the combined wind and river inputs also produced a return flow at depth, with the sharp pycnocline often acting as the dividing boundary between the bi-directional flows (Fig. 6.5).

To examine differences between the closure and overflow cases in detail, we obtained residual flow profiles for both after first non-dimensionalizing elevations by scaling with the total depth, after Giddings et al. (2012). At a site in the middle of the outer estuary (A4; Fig. 6.2), the residual profiles have similar features during both inlet states (Fig. 6.5), but currents were clearly amplified when an overflow channel was present. The high wind scenarios produced a classical residual wind-sheared profile with landward flows at the surface and return flows beneath it, similar to the profile discussed by Mathieu et al. (2002). For the low- and no-wind scenarios this profile increasingly reverted to a typical riverflow-dominated profile with surface flows toward the inlet and a weaker return flow in the pycnocline. Residual surface flows were approximately 0.5 cm s^{-1} faster with an overflow channel than with a closed beach, while upstream-directed return flows just above the pycnocline were about 0.2 cm s^{-1} faster. The flows were not strongly influenced by the inclusion of beach seepage.

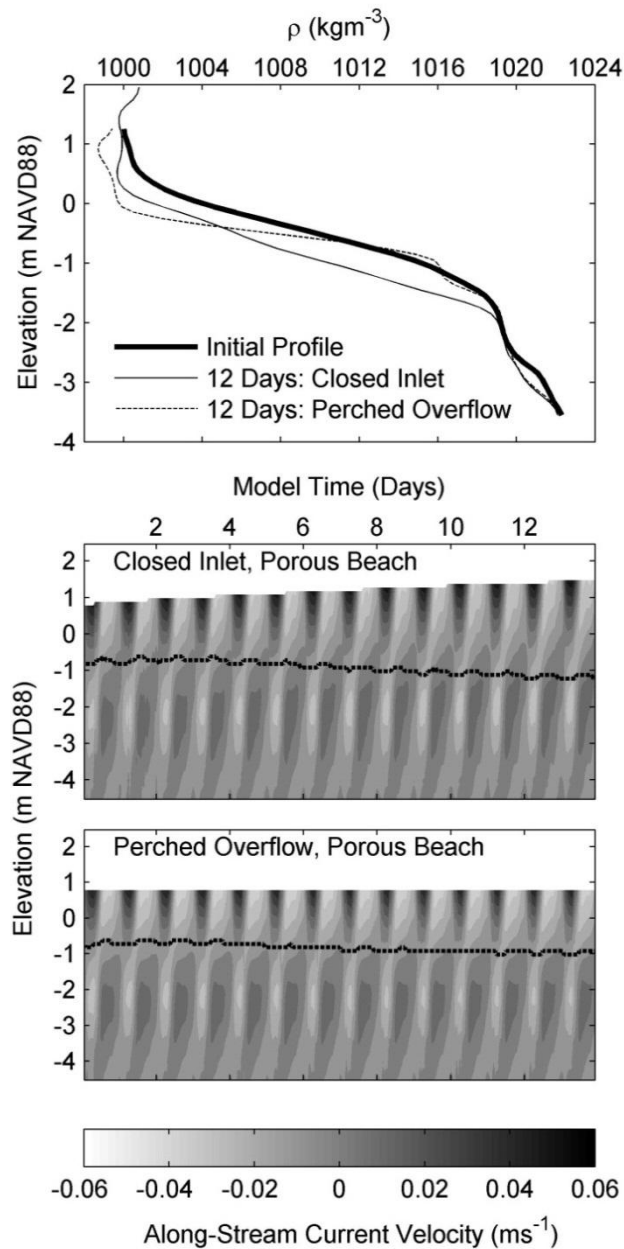


Figure 6.4. (top) Vertical density profiles after 12 days at site A4 during the closed and overflow cases with high-wind and a porous beach, compared with the initial density profile. Along-stream current velocities are also shown at site A4 for the high-wind and porous beach simulations with (middle) a closed beach and (bottom) a porous overflow channel. Positive values are directed upstream. The dashed line represents the vertical location of the mean density, which is the center of the pycnocline.

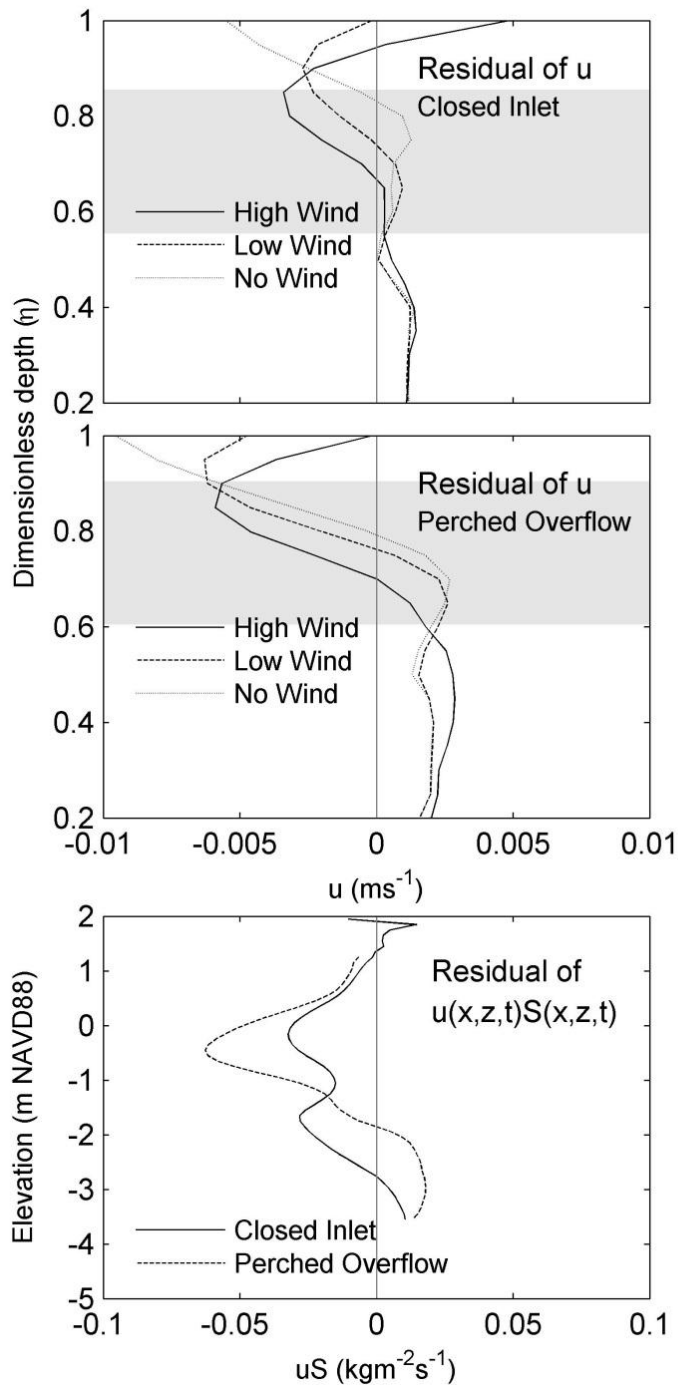


Figure 6.5. Residual current profiles at site A4 for simulations with a porous beach and (top) full inlet closure and (middle) a perched overflow channel. Elevations are normalized by the total depth to account for the change in depth during closure. The grey band represents the pycnocline elevation. (bottom) The residual profile of the product of x-velocity and local salinity, representing the net along-stream salt transport at site A4.

Because of its effect on the current structure, the presence of an overflow channel also dramatically increased the residual salt transport in the outer estuary when compared with inlet closure. Figure 6.4 shows that for overflow, the pycnocline at A4 was close enough to the surface to be subjected to the relatively fast surface currents for the entire simulation period, while during closure, trapped freshwater inflows lifted this high-shear region away from the pycnocline with time. As a result the peak salt transport rates for overflow were markedly stronger than for closure in the vicinity of the pycnocline, indicated in Figure 6.5c for the high wind case. The structure is also mostly bi-directional for overflow and mostly directed toward the mouth during closure. For the low- and no-wind cases, the differences in transport near the pycnocline became much smaller.

6.3.2. Salt field evolution

The net transports shown in Figure 6.5c corresponded to basin-wide salt redistribution, which we trace using image subtraction with the 2D (x - z plane) interpolated salt field (Figs. 6.6-6.7) in the outer estuary. For runs with a closed inlet and a non-porous beach (Fig. 6.6a-c), increasing amounts of salt were accumulated above the pycnocline near the mouth for increasing wind speed. This was partially balanced by a return flow at the pycnocline elevation that transported salt upstream, although the overall net transport was toward the mouth, reflecting the result in Figure 6.5c. When no wind is applied, the riverflow-dominated residual currents gave similar results, although their effects were much weaker (Fig. 6.6c).

While the coloration of Figure 6.6a-f indicates that much of the salt accumulated at the mouth arrives from upstream, the loss of salt below 0 m NAVD88 shows that vertical diffusion at the basin edges during upwelling may also be an important source (e.g. Imberger and Ivey, 1993). For decreasing amounts of wind, this change in salinity at the edges diminished. When a porous beach was used (Figs. 6.6d-f), the salt carried to the mouth was exported through the beach, made visible by a net decrease in the salt throughout the outer estuary and by a lowering of the pycnocline. This export increased for higher winds, with the highest amounts of salt lost in the basin nearest to the mouth.

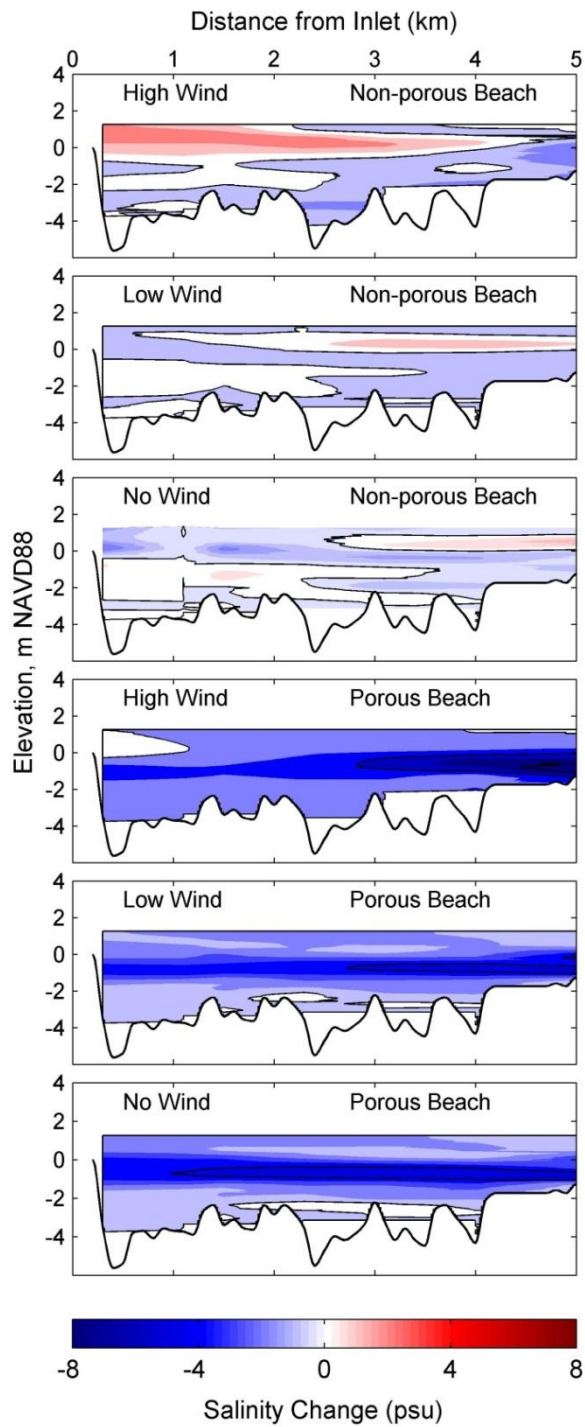


Figure 6.6. Image subtraction of the salt field in the outer estuary between the initial and final time steps, representing a two-week net change in the salinity field. (a-c) Image subtraction for closure with a nonporous beach. (d-f) Image subtraction for closure with a porous beach.

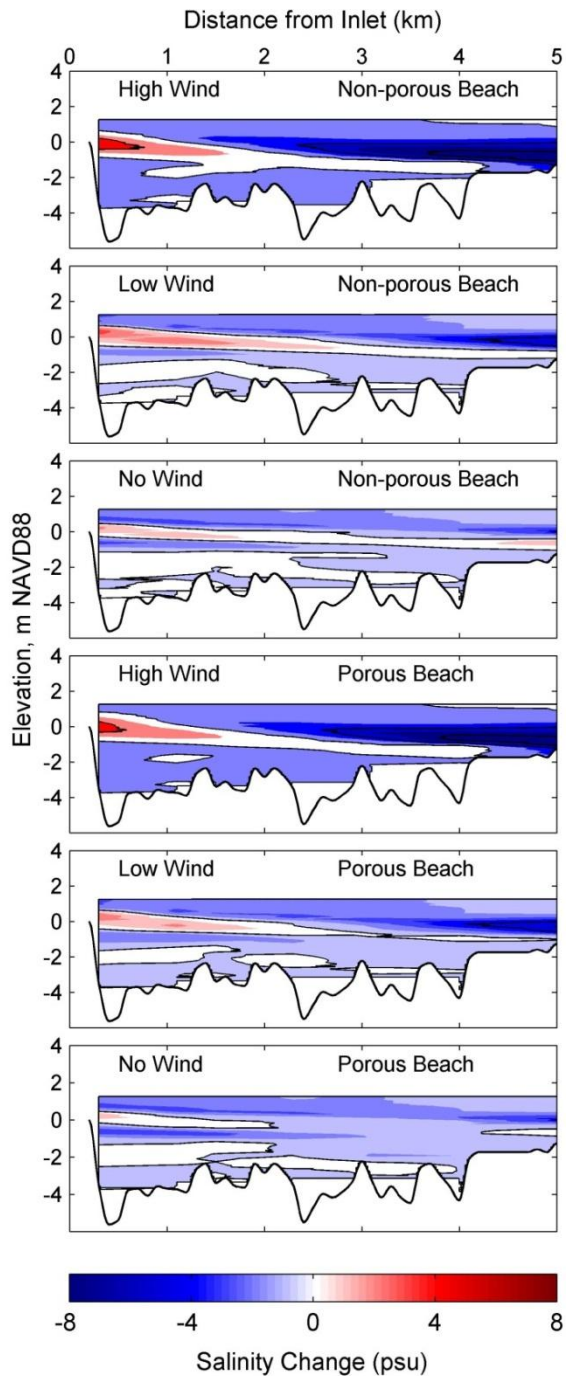


Figure 6.7. Image subtraction of the salt field in the outer estuary between the initial and final time steps, representing a two-week net change in the salinity field. **(a-c)** Image subtraction for perched overflow with a nonporous beach. **(d-f)** Image subtraction for perched overflow with a porous beach.

For the model runs with perched overflow, horizontal transfer of salt in the vicinity of the pycnocline was much stronger than for closure. There was almost no visible difference between the porous and nonporous beach cases, but salt movement was strong for both, and there is again a positive relation between the strength of wind forcing and the amount of horizontal transfer. Again, the basin nearest the mouth was the region where much of the salt was lost, corresponding to observations of stronger upwelling than during closure. The coloration of the high-wind cases in Figure 6.7a-f looks similar to the result of modeled closure without seepage (Fig. 6.6a-c) but with amplified effects: Salinity increased by about 6 psu at the mouth and decreased by roughly 8 psu upstream, compared with changes of 3 and -3 psu observed during the equivalent closure case.

6.3.3. *Water Column Stability*

The difference in salt redistribution between closure and overflow cases also translated to changes in the water column stability, which affected long-term potential for mixing to occur. Without thermal influences, this stability is solely the result of the buoyant freshwater inflows, salt export from seepage and overflow and changes to the strength of stratification (e.g. Simpson et al., 1990). We examine sites at the basin edge (A1) and in open water (A4) using two stability measures, the Brunt Vaisälä frequency (Fischer et al., 1979) and the potential energy anomaly (Simpson et al., 1990). The former is defined as:

$$N^2 = \frac{g}{\rho} \frac{\partial \rho}{\partial z} \quad (6.7)$$

where all variables are defined as above. The potential energy anomaly is defined as:

$$\phi = \frac{1}{h} \int_{-h}^0 (\hat{\rho} - \rho) g z dz \quad (6.8)$$

$$\hat{\rho} = \frac{1}{h} \int_{-h}^0 \rho dz \quad (6.9)$$

Eq. (6.7) provides a measure of the strength of stratification while Eq. (6.8) represents the total mixing energy required to make the vertical density distribution homogeneous in the water column. We estimate N^2 for all cells in the vertical direction, using forward-difference operators to represent the derivative in Eq. (6.7). For analysis, we use the peak value measured in the pycnocline, as this represents the limiting condition for scalar transfer between vertical layers (Borsuk et al., 2001).

Fig. 6.8 shows that peak N^2 values are strongly tied to wind speed both at the basin edge and in open water. When a closed inlet was used, N^2 was generally smaller for stronger winds, regardless of whether seepage was present. However, most of the change occurred within the first week, with N^2 varying between 0.1 s^{-2} and 0.14 s^{-2} near the mouth and between 0.08 s^{-2} and 0.14 s^{-2} in open water, followed by a period where it remained relatively constant. The addition of a porous boundary constrained the trajectories of N^2 to a smaller range, but otherwise did not alter the steady-state nature of the outcome after two weeks.

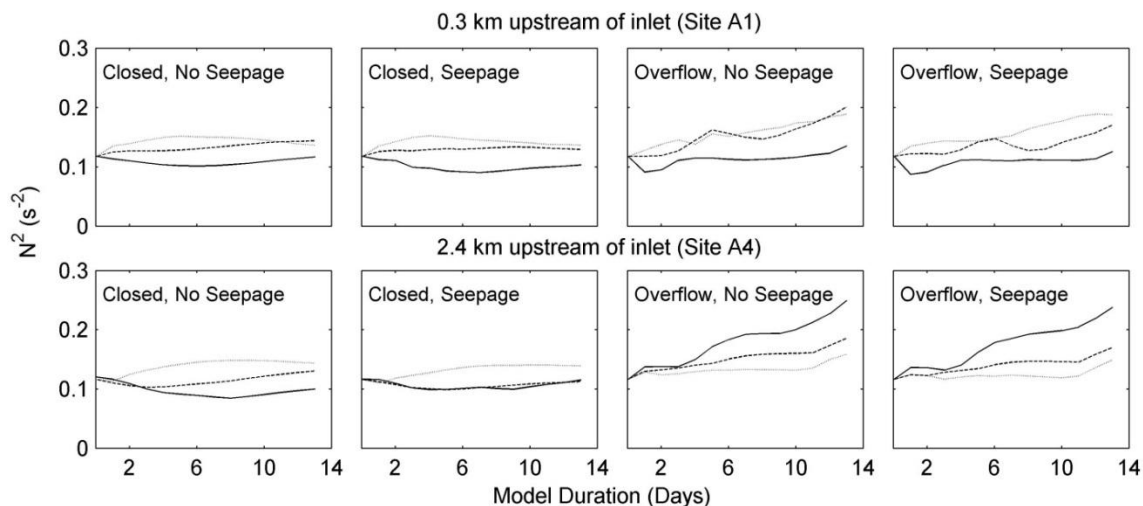


Figure 6.8. Time series of peak N^2 values (a-d) 0.3 km from the inlet and (e-h) 2.4 km from the inlet. Line weights correspond to the (-) high-wind, (--) low wind and (:) no wind cases. Peak N^2 values were generally located at the center of the pycnocline. Values shown here represent a low-pass filter of the raw N^2 time series at each site, using a rectangular filter width of approximately two days. This was used to extract the diurnal variability.

In contrast, changes to N^2 were much larger when an overflow channel was present (Figs. 6.8c,d,g,h). For this case N^2 increased for all wind speeds, both at the mouth and upstream. At the upstream site, stronger winds corresponded to a faster increase in peak N^2 , while near the mouth, the opposite was true, with higher winds causing a slower growth. This may be related to the prior result showing that as winds increase, salt accumulates in the epilimnion near the mouth and is stripped away from the rest of the basin (Fig. 6.7). Unlike with closure, the addition of seepage had an insignificant impact on strength of stratification for the perched overflow cases.

In contrast to N^2 , we found that ϕ (Fig. 6.9) was mostly controlled by the total estuary depth. Trapping of inflows behind the beach during closure led to higher growths of ϕ during the two-week period, despite the fact that stratification was stronger for

perched overflow. During closure, ϕ increased by 20-50 J m^{-3} throughout the estuary, compared with 5-10 J m^{-3} when an overflow channel was present. The spread of the ϕ trajectories differed by location and also by the inlet state: For perched overflow, ϕ approached a steady value near the end of the two-week simulation whereas it showed no signs of stabilizing by this time during closure. The inclusion of beach seepage lowered the growth of ϕ to 20-30 J m^{-3} during closure, but had no noticeable impact during overflow. The sole consistent result across all model runs was that stronger winds led to slower growth rates of ϕ at all sites.

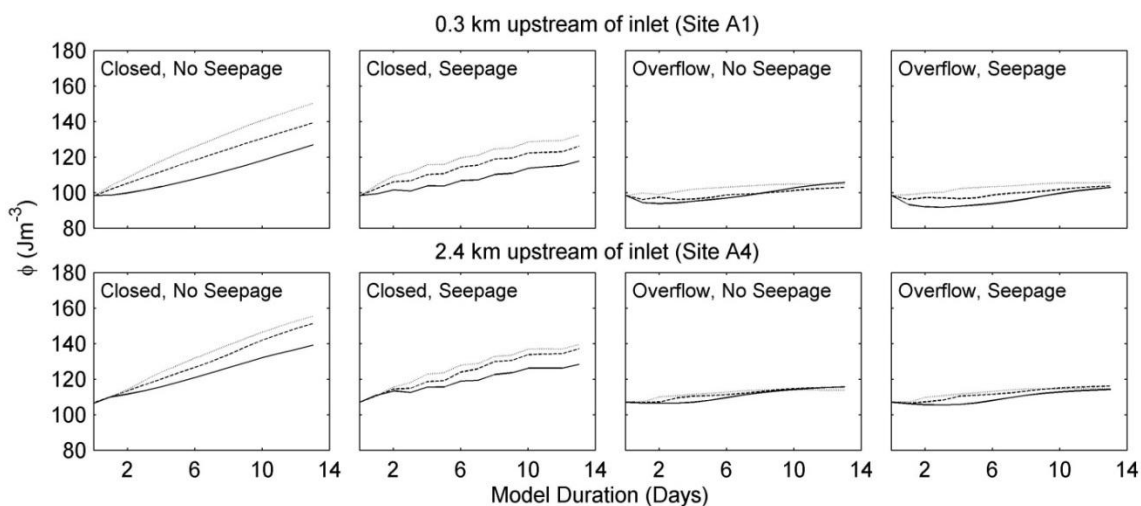


Figure 6.9. Time series of potential energy anomaly (Simpson et al. 1990) measured (**a-d**) 0.3 km from the inlet and (**e-h**) 2.4 km from the inlet. Line weights correspond to the (-) high-wind, (--) low wind and (:) no wind cases. Values shown here represent a low-pass filter of the raw ϕ time series at each site, using a rectangular filter width of approximately two days. This was used to extract the diurnal variability.

6.3.4. Total Salt Mass

We use the time series of the total salt mass in the estuary (SM) to provide a means of forecasting the future water column stability, since salt is the main source of the vertical density difference here. We estimate SM as the sum of the products of the cell volume and cell salinity for the entire domain.

With the inlet closed, SM decayed by a rate that accelerated with time, whereas the presence of an overflow channel limited salt export, leading to SM time series that trended toward constant values (Fig. 6.10b,c). Stronger winds increased the export for both cases. For closure, of the original salt mass (SM_0), 84, 82 and 79 percent remained after 14 days for the no-, low- and high-wind scenarios, respectively. The effect was similar for overflow, but with a much wider range: without seepage, SM reached values of 94, 90 and 81 percent of SM_0 after 14 days for the no-, low- and high-wind cases, respectively. Adding seepage to the perched overflow simulations lowered the final SM values by approximately two percent of SM_0 . For the low- and no-wind cases, having a closed beach consistently led to faster export of salt from the estuary than with an overflow. However, during the first 12 days of the simulation when high winds were used, SM decreased more quickly with an overflow channel. After this time, the difference in the trajectories makes it clear that export during closure would begin to outpace it (Fig. 6.10a,b).

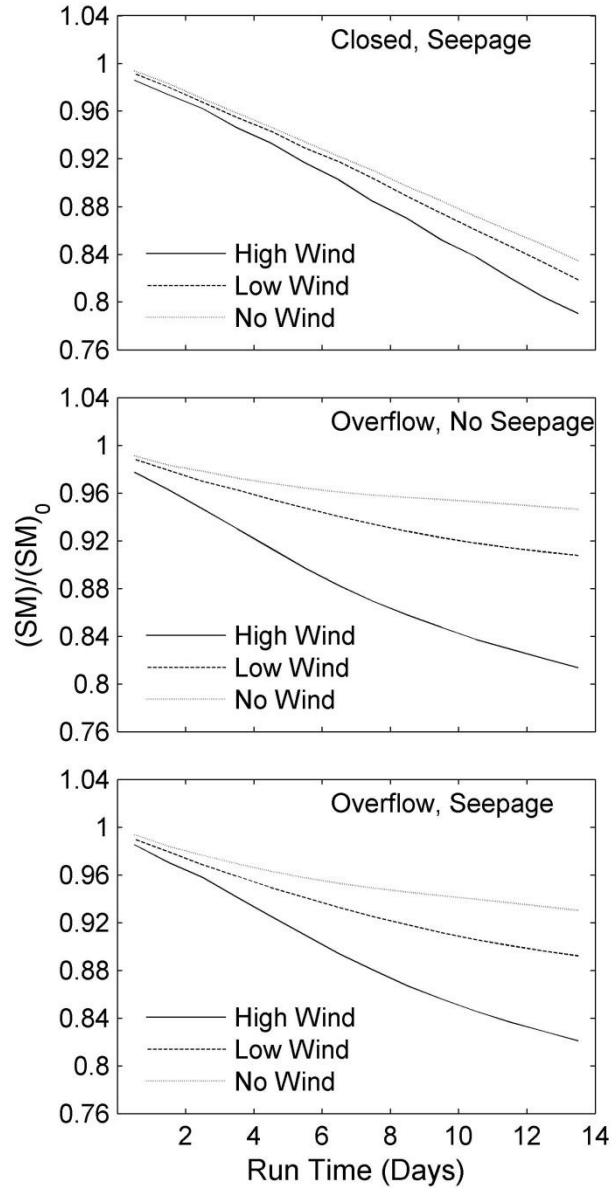


Figure 6.10. Comparison of normalized estuary salt mass during the two-week simulation period for **(top)** inlet closure with a porous beach, **(middle)** perched overflow with a nonporous beach and **(bottom)** perched overflow with a porous beach.

6.4. Discussion

6.4.1. Short-Term Water Column Stability

For the prototypical initial conditions used here, full mixing is impossible within a few weeks whether or not a perched overflow channel is present. This can be explained within the context of typical initial conditions and their effect on the Gradient Richardson Number:

$$Ri_g = \frac{N^2}{\left(\frac{\partial u}{\partial z}\right)^2} \quad (6.10)$$

Many studies have demonstrated the ties between Ri_g and turbulence, with most showing that turbulence is largely dissipated and ineffectual for vertical mixing when $Ri_g < 0.25$ (Monismith, 2010). Peak values of N^2 were above 0.1 s^{-2} for all model runs (Fig. 6.8), a constraint made possible by the inflow of fresh water into the surface layer and by the trapped tidal water having salinity of ~ 20 psu. In response to wind forcing, S^2 profiles are maximal near the surface, having peak values of roughly 0.1 s^{-2} . This translated to peak values smaller than 0.01 s^{-2} near the peak density gradient during closure and even less during overflow. In both cases, this provides Ri_g values above 10, far insufficient to weaken the peak salinity gradient. Thus, a thinner upper layer or much lower salinity difference would be needed for the available wind energy to break up this gradient. In shallower systems, shear at the channel sides and bottom could make mixing easier by

subjecting the pycnocline to regions of high shear (Fischer et al., 1979), so this scaling is assumed to be relevant only for systems with deep basins similar to the RRE.

Even if the surface wind stress is unable to fully mix the water column, any currents that reach the upper pycnocline have the effect of stripping salt away from the middle of the basin and accumulating it at the edges (Fig. 6.5-6.7) in the short term. Figure 6.7 makes it clear that this displacement is strongest for a shallower epilimnion and for sharper stratification, which was earlier shown by Nunes Vaz et al. (1989). Neither of these were present for the closure scenario since inflows were generally larger than seepage losses, allowing the estuary water level to rise and to displace the applied wind energy away from the pycnocline (Fig. 6.4b). This is the probable cause for peak N^2 values becoming stable and invariant after the first week of the simulations (Fig. 6.8a,b,e,f).

The difference in water column stability between the mouth and stations farther upstream (Fig. 6.2) can be attributed to upwelling at the mouth during afternoon winds. Okeley and Imberger (2007) found that upwelling aids vertical diffusion of denser water simply by exposing it to the faster currents near the surface. This was the case here even during partial upwelling. Closer examination of the results indicates that the size of the region with weakened stratification depends on the strength of upwelling at the basin edge and the amount of salt displaced toward it from elsewhere in the estuary. Here it was limited to within 1 km of the beach (Fig. 6.6-6.7). Though the majority of the RRE volume is distant from this region, it is foreseeable that differently-shaped basins could

experience basin-wide destratification from this process if their volume is concentrated next to an up-wind boundary.

6.4.2. Salt Export and Long-Term Stability

Even within a two week period, the results make it clear that the choice of inlet management after closure can dramatically influence water column stability in the long term. Even though the results are partly a reflection of initial conditions, they can also be explained with a simple two-layer mass balance approach that takes into account the dominant salt transfer mechanisms. This provides a means for extending the stability analysis by forecasting the amount of salt remaining in the estuary after some time in the future, based on the forcing conditions present. For a simple estuarine basin with idealized two-layer vertical stratification (Fig. 6.11), the total salt mass export rate can be described as the sum of the rate of changes of salt mass in each layer:

$$\frac{dSM}{dt} = \frac{dSM_1}{dt} + \frac{dSM_2}{dt} \quad (6.11)$$

Where the subscripts 1 and 2 correspond to the upper and lower layers, respectively. Each layer has an associated depth (h_1 and h_2) and salinity (S_1 and S_2) which may both vary in time (Fig. 6.11). We assume that both layers are instantaneously mixed and that the stratification and bathymetry prevent freshwater inflows from entering the lower layer. If we assume that no wave overwash or tides intrude into the estuary, that upstream inflows are fresh and that there are no other sources of salt within the estuary, the net change in salt mass will be negative with time.

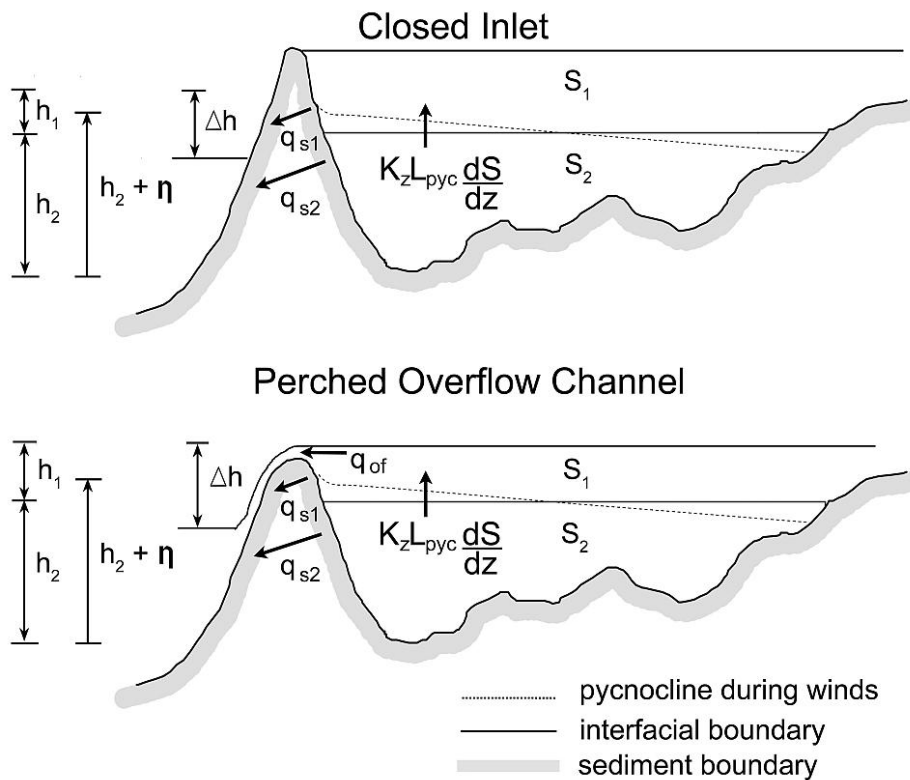


Figure 6.11. Schematic of the inlet during **(top)** inlet closure and **(bottom)** perched overflow, indicating the main components of the salt mass balance. Δh is the head difference between the estuary and mean ocean level adjacent to the beach. η is the displacement of the pycnocline at the upwind (left) boundary. All terms are based on unit widths, corresponding to the x-z planar modeling approach.

Due to increased flow path length, seepage flows should decrease with depth into the beach, so that the amount of salt exported from SM_2 should generally be lower than for SM_1 , unless the base of an overflow channel extends into the lower layer. Wind-induced upwelling of the interface alters the decay of SM_2 by exposing the bottom layer to higher elevations of the beach (Cable et al., 1997). When an overflow channel is present, upwelling also allows direct export of the SM_2 near the surface. The degree of

upwelling can be characterized with the Wedderburn Number (Thompson and Imberger, 1980):

$$W = \frac{g' h_1^2}{u_*^2 L} \quad (6.12)$$

where u_* is the water-side shear velocity, L is the length of the basin and $g' = g(\rho_2 - \rho_1)\rho_1^{-1}$ is the reduced gravity, where ρ_1 and ρ_2 are the upper and lower densities, respectively.

This is incorporated into the prediction of Shintani et al. (2010) for estimating the interface displacement η above its resting position at the upwind boundary:

$$\frac{\eta}{h_1} = 1 - \left\{ \frac{2}{\pi} \tan^{-1} \left[\left(\frac{9}{8} W - 1 \right)^{0.81} \right] \right\}^{0.57} \quad (6.13)$$

Diffusion of salt across the interface into the upper layer is another important source of decay of SM_2 , incited by turbulent eddies which act to vertically displace the lower water in a process which can be treated as Fickian diffusion (Fischer et al., 1979). It can be estimated by first finding the diffusion rate in a homogeneous (unstratified) water column and then accounting for the strength of stratification. The former is defined after Nezu and Nakagawa (1993):

$$K_0 = \beta \kappa u_* z \left(1 - \frac{z}{H} \right) \quad (6.14)$$

where $\beta \sim 1$ is a proportionality coefficient between eddy viscosity and diffusivity (Dyer, 1986), $\kappa = 0.41$ is the von Kármán constant, u_* is the friction velocity, z is elevation above the bed and H is the total water depth. To account for the influence of stratification, we use the diffusion estimate of Munk and Anderson (1948):

$$K_z = K_0 \left(1 + \frac{10}{3} Ri \right)^{-3/2} \quad (6.15)$$

While more sophisticated methods exist for estimating the diffusion, this provides a scale version which is relatively accurate and has been used successfully in the past (Fischer, 1976; Geyer, 1993).

Accounting for both advective and diffusive processes, and taking into account the above assumptions, the mass balances for each layer (Fig. 6.11) can be written as follows:

$$\frac{dSM_1}{dt} = K_z L_{pyc} \frac{dS}{dz} - q_{s1} S_1 - q_{of} S_1 \quad (6.16)$$

$$\frac{dSM_2}{dt} = -K_z L_{pyc} \frac{dS}{dz} - q_{s2} S_2 \quad (6.17)$$

where:

$$q_{s1} = \bar{k}_1 (h_1 - \eta) \frac{dh}{dL}, \quad q_{s2} = \bar{k}_2 (h_2 + \eta) \frac{dh}{dL} \quad (6.18)$$

$$\bar{k}_1 = \frac{1}{h_1} \int_{z1}^{z2} k(z) dz, \quad \bar{k}_2 = \frac{1}{h_2} \int_{z0}^{z1} k(z) dz \quad (6.19)$$

q_s and q_{of} are the outflow rates per unit width of beach from beach seepage and perched overflow, respectively, and L_{pyc} is the unbroken length of the pycnocline. S_1 and S_2 are both functions of the diffusion term.

We propose that the major difference in the salt export observed between the modeled closure and overflow cases can be predicted in part by the relative dominance of the vertical diffusion term relative to the seepage term for the lower layer. This can be found with a simple dimensionless ratio of the two terms:

$$\alpha = \frac{q_{s2} S_2}{K_z L_{pyc} \frac{dS}{dz}} \quad (6.20)$$

For $\alpha \ll 1$, vertical diffusion dominates, and most of the salt export from the estuary occurs from the upper layer. For the converse, diffusion is so small that direct seepage of the trapped saline water through the beach is the only viable export method. Winds enhance the seepage losses in the lower layer through the upwelling mechanism described above but can also increase vertical diffusion in the short-term. If they have the effect of increasing the stratification, they can also have the seemingly paradoxical effect of limiting vertical diffusion in the long-term, as discussed above.

For the low-elevation overflow channel used in this study, seepage losses from the lower layer were relatively unimportant, with α well below one for all six modeled overflow cases. For the closure cases, diffusion was generally larger than the overflow cases, but the difference in seepage was even greater, so that α became larger with time, and was generally above one.

To illustrate the effects of the dichotomy in α between management scenarios, we revisit the prior *SM* trends (Fig. 6.10), replacing time on the *x*-axis with time-integrated measures of Δh and $K_z \frac{dS}{dz}$. These represent the drivers behind the seepage and diffusive fluxes, respectively. Figure 6.12 shows that the previous results now collapse more closely together. For closure, the decay of salt mass is well-described in terms of integrated head difference (Fig. 6.12a) but not by diffusion (Fig. 6.12b). Clearly, stronger diffusion helps export salt more quickly when seepage is important, since it displaces salt upwards toward areas of the beach with faster seepage rates. After two weeks, 78 percent

of SM_0 was left during the high-wind case, compared with 83 and 84 percent for the low- and no-wind cases. The deviation follows from the fact that α was much closer to unity during the high-wind case than during the others. When an overflow channel is present, the trends are reversed: SM decay is described worse by the integration of Δh (Fig. 6.12c) and better by the integrated vertical diffusion (Fig. 6.12d).

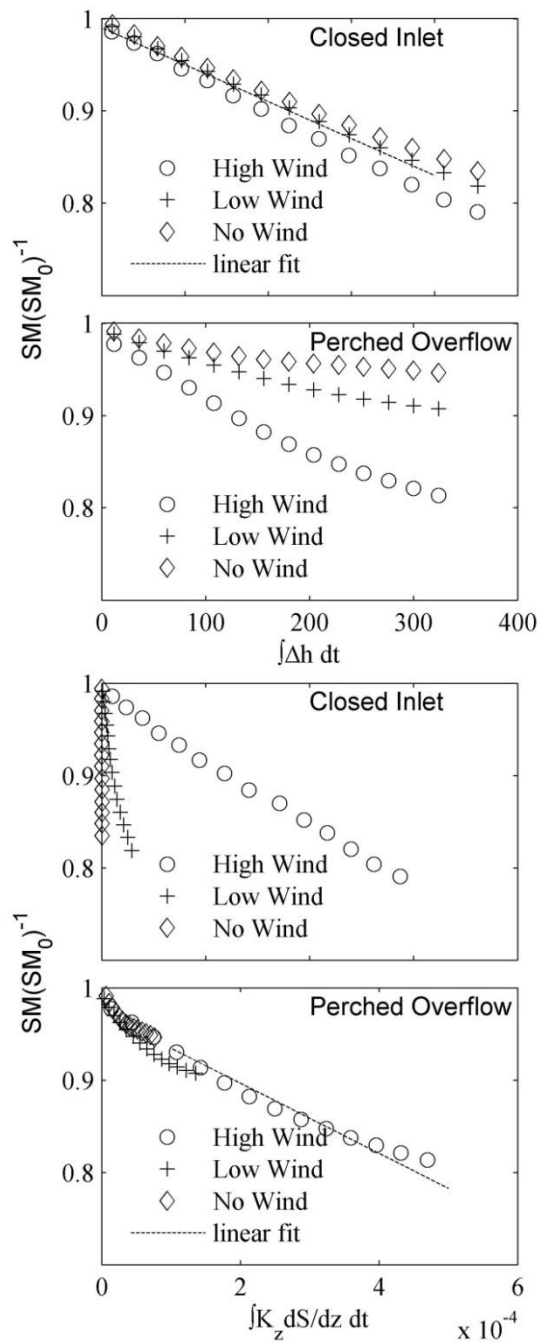


Figure 6.12. Time series of normalized estuary salt mass compared with integrated measures of (a-b) the hourly head difference measured between the estuary and ocean and (c-d) vertical salt diffusion per unit area of the unbroken pycnocline. The data indicate that (a) seepage dominates export during inlet closure and (d) vertical diffusion dominates export during perched overflow, for the conditions used in this study. Linear fits used in (a) and (d) represent least-square fits of the data.

If winds are frequent and strong, the sharpening of the pycnocline observed when an overflow channel is present provides a strong feedback by decreasing the vertical diffusion, and hence, making additional salt export more and more difficult with time. This explains why the high-wind perched overflow case (Fig. 6.10) only briefly allowed faster salt export than for the equivalent closure case: during this short period, diffusion of salt was high, but so were horizontal currents acting to strip salt from the upper pycnocline, enhancing peak values of N^2 . Of course, if seepage is not negligible, as with a perched overflow channel situated at a much higher elevation, salt export may not be so limited by this feedback. It is clear that even if α is well below unity, either the diffusion or the seepage would need to be strong for salt to be actively exported from the lagoon.

6.4.3. Comparison With Observations

Field measurements were taken during seven inlet closure events and one brief period of perched overflow during the 2009 and 2010 dry seasons at the RRE. The overflow event was induced manually with heavy equipment by a local public agency. It succeeded in preventing the water levels from rising in the estuary, but did not have a steady channel elevation. Rather, it slowly eroded over a period of six days from 1-6 July 2010 until the channel was inundated and completely closed by wave-driven sediment. The initial water elevation in the estuary was 1.87 m NAVD88 at the time that overflow was induced and it subsided at an average rate of 0.1 m day^{-1} . During this time estuary inflows were $6.8 \text{ m}^3 \text{ s}^{-1}$, approximately three times higher than the values used here.

Of the closure events, one event lasted longer than two weeks: from 7 September to 5 October 2009. Estuary inflows were between 2 and $2.8 \text{ m}^3 \text{ s}^{-1}$ for most of the event. From an initial water level of 1.0 m NAVD, the estuary infilled to an elevation of 2.7 m NAVD when it was manually breached to prevent flooding of local property. ADCP and pressure logger data indicate a strong diurnal wind influence throughout the event. Wave overwash events occurred 2, 7 and 20 days after the onset of closure, which increased *SM*. Otherwise, the conditions were generally very similar to the those of the modeled closure scenario.

Fig. 6.13 illustrates the development of the peak N^2 , ϕ and during these events. Since we did not collect data at the same time each day, we can assume that diurnal variability alters the overall trends shown here. Nevertheless, these data reaffirm the divergent outcomes for these two separate management states. During the closure event, N^2 decreased from an initial value of 0.2-0.3 s^{-2} and settled at a roughly constant value of $\sim 0.15 \text{ s}^{-2}$ event at both sites A1 and A4, which compares favorably with the model results. While data only exist from three days during the perched overflow event, as expected it is immediately clear that stratification was much stronger, with N^2 well above 0.4 s^{-2} both at the mouth and upstream. The time series of ϕ also compares well with the model results: For both closure and overflow, the energy required for mixing is substantially larger upstream of the mouth.

The time series of *SM* during these events are difficult to analyze within the same context as the model data, since the overflow data are prohibitively short, and since wave overwash disrupted the export of salt during the closure event. However, periods of salt

loss between these influxes confirm that seepage-driven losses from the estuary were indeed real and significant.

Figure 6.14 gives a direct comparison between the modeled and observed salinity fields. Because of the difference in forcing conditions between the natural overflow case and the modeled case, the results cannot be expected to match without error. However, the results demonstrate again that the model is capable of reproducing the differences observed between closure and overflow cases. Aside from the lower flows in the modeled overflow case compared with the observed case, the model enforces higher winds than were observed in the field during July 2010, resulting in a higher amount of diapycnal mixing near the mouth. Otherwise the model results compare favorably with the data.

Diapycnal mixing at the mouth in response to winds is partly the result of upwelling of the density interface near the surface, where surface currents are fastest. Figure 6.15 illustrates how this can occur for both closure and overflow cases, using the modeled salinity field in the estuary. The model data are taken from a day near the end of the simulations, when the difference in water levels between the closure and overflow cases have the largest effect on upwelling.

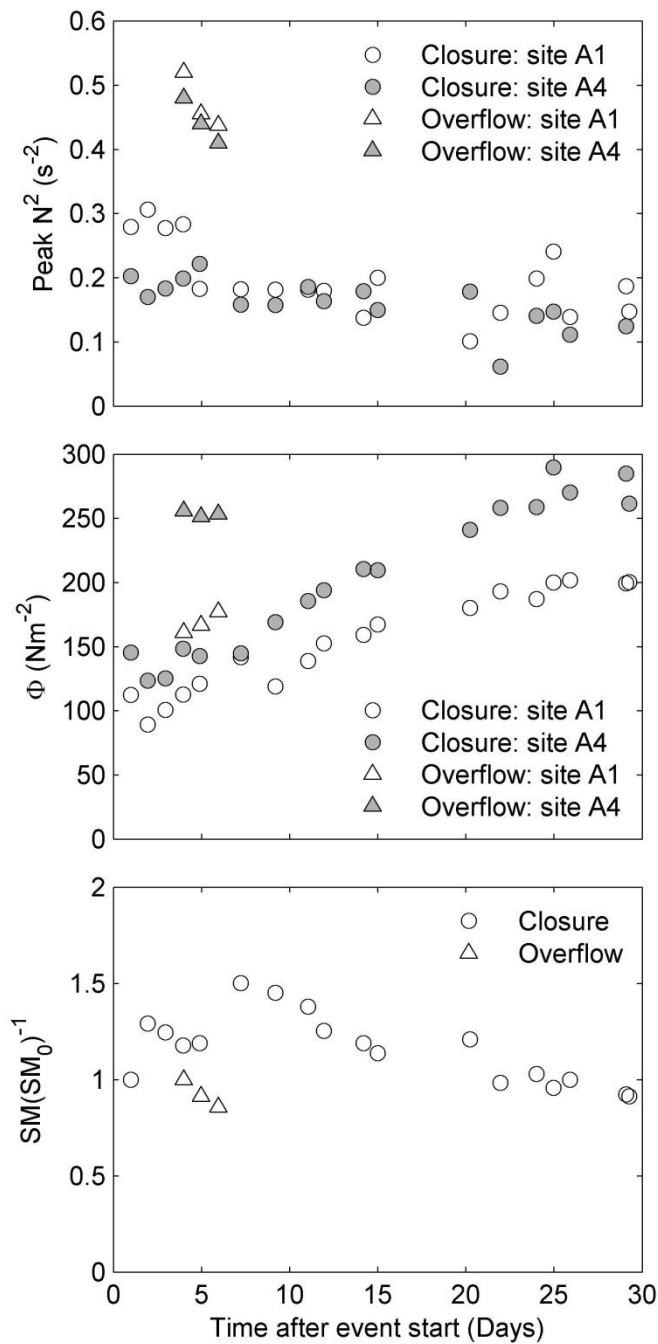


Figure 6.13. Time series of **(top)** peak N^2 , **(middle)** potential energy anomaly and **(bottom)** normalized estuary salt mass during a perched overflow event from 1-7 July 2010 and a closure event from 7 September to 5 October 2009. Values were taken at various times during the days within the field campaign, so that diurnal variability is included in the trends shown here.

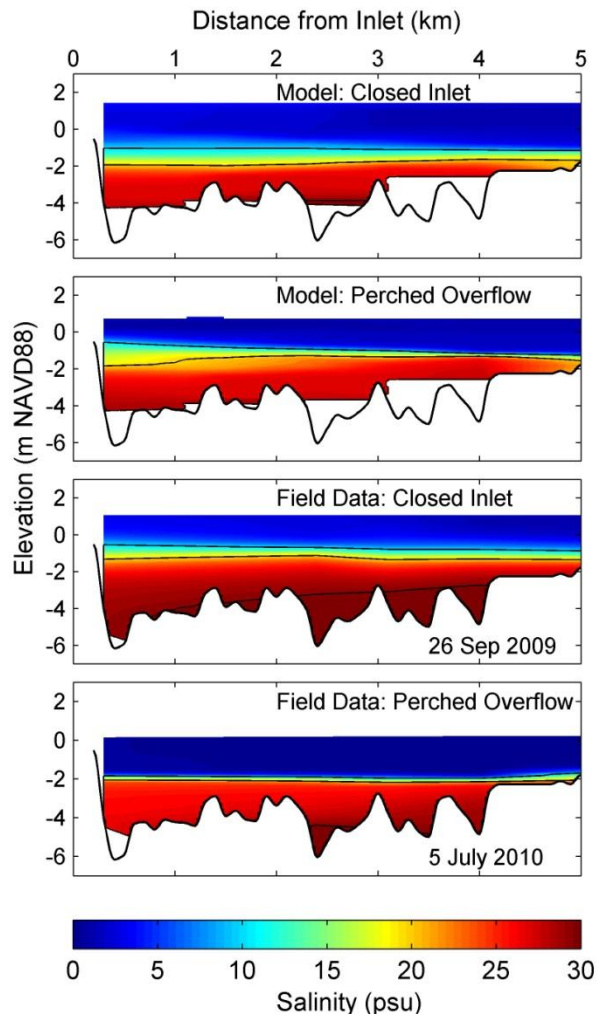


Figure 6.14. Comparison of modeled and observed examples of the estuary salinity field, with using field data from closed-inlet and perched overflow conditions.

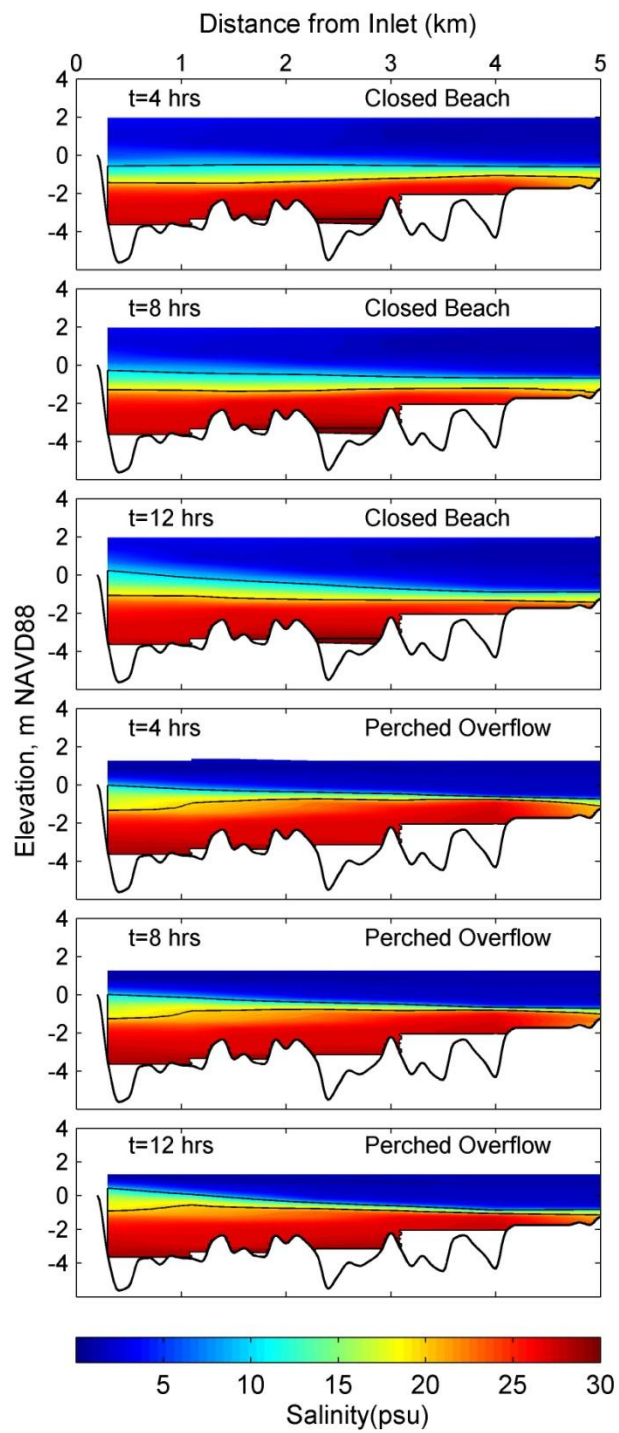


Figure 6.15. Illustration of upwelling for modeled closure and overflow cases. As time advances from 4 to 12 hours, the landward wind increases from 0 to 8 m s^{-1} .

6.5. Conclusions

The results suggest that the long-term state of an estuary after inlet closure is dependent on a number of factors, with the choice of beach management having a significant impact. It is clear that the presence of an overflow channel alone does not imply that the capacity for vertical mixing will increase with time. On the contrary, it appears that as long as river input and applied winds are too weak to dissipate the main density gradient between vertical layers on their own, vertical mixing will become more difficult with time, as the currents reaching the gradient simply export some of the upper salt, increasing the stratification by making the upper layer more fresh. At the same time, even though a completely closed beach may allow the strength of stratification to remain the same by allowing the epilimnion to grow vertically with time, the increased depth also reduces any chance of complete mixing, as shown by the time series of ϕ (Fig. 6.9).

While these results hold true for the conditions of the RRE, shallower systems may produce a different response, since the presence of a hard boundary near the pycnocline could dramatically increase the shear, and thus generate more turbulence (Imberger and Ivey, 1993). In the RRE this happened at the basin edges as a result of upwelling during winds. In a shallower system, similar applied winds could expose the pycnocline to more of the bathymetry and contribute to much more mixing.

While not complete, the results can be used to help understand how beach management in an intermittently open/closed estuary would influence habitat space and vertical scalar transfer, based on the knowledge of the existing bathymetry, typical salinity conditions after closure, and peak wind conditions. The 2D approach used here

also shows promise although it may not be as appropriate when rotational terms are important (Giddings et al., 2012), when lateral variance in salinity is significant, or if rotational internal seiches are present (e.g. Antenucci et al., 2000). Nevertheless, many bar-built estuaries have similar shape and forcing conditions as the RRE (e.g. Cooper, 2001; Roy et al., 2001, Gale et al., 2006). Further work is needed to explore this topic with a wider range of initial and forcing conditions, and to extend the analysis to full seasonal events.

7. Conclusions and Future Work

This dissertation provides a detailed analysis of the dynamics of a bar-built estuary that experiences inlet closure on an intermittent basis. I emphasize three areas: (1) inlet morphology, (2) response of the estuary salt field mechanics to inlet closure, and (3) the impacts of several inlet management strategies on the stratification in the estuary. The structure of this document is intended to emphasize the interrelated nature of beach morphology and estuarine physics, and to introduce a discussion on the impacts of several management choices. In this section, I elaborate on the key findings of the analyses in Chapters 4-6, and suggest a number of future areas in need of additional research.

7.1. Inlet Morphology

Tidal inlets are pathways that connect coastal and estuarine environments. In large systems, they often occupy the open space between barrier islands (US Gulf Coast, Dutch Wadden Sea), or function as the mouth of a perennial river (Mississippi Delta, Hudson River). In bar-built estuaries and small bays, they are narrow passages cut through a beach, and are inherently mobile and unstable, owing to the sandy substrate and variability in flows between the protected bay and the ocean. Since the inlet channel exists within a beach, it is subject to the same wave-building processes as the beach adjacent to it, and can act as a sediment sink during times of heavy sand delivery from waves. Since it also provides a conduit for tidal and fluvial flows, it also localizes erosion and shear stress from flows. Owing to seasonal variations in waves and river flows,

sediment deposition and erosion do not always balance, allowing the inlet to close by filling with sediment until it is indistinguishable from the rest of the beach. The timing, frequency and duration of closure events are highly variable, reflecting the superposition of short-term, seasonal and multi-year processes.

In Chapter 4 we examined several aspects of inlet closure at the RRE using over 60 years of daily records at the site. The records are from two sources, a DWR water level gage operated from 1931 to 1957 analyzed by Rice (1974) and a set of daily written records from 1973 to the present taken by E. Twohy (Behrens et al., 2009). The latter set is complemented by daily photographs of the mouth starting in 1991 also taken by E. Twohy. These were used to characterize inlet width, length and position from 1991 to 2008. Chapter 4 builds on the analysis of Behrens et al. (2009) by providing a comprehensive analysis of the long-term closure signal at the site.

The closure signal from 1973 to 2008 was analyzed with an FFT approach to determine the dominant modes of frequency inherent in the observed closure record. The signal is dominated by a seasonal (~ 365 day) pattern caused by high occurrence of closure in fall and low occurrence in winter months. This frequency and an overtide at 182 days were the only statistically significant frequencies at the 95 percent level. Despite this, a shift in the decay of energy for frequencies smaller than $\sim 1.15 \times 10^{-5}$ Hz (~ 28 days) indicates that the lunar month (i.e. spring-neap frequency) has some significance, and variability for lower frequencies suggest a possible importance of long term (3-5 year) signals. Inspection of the raw closure record shows that the inlet closes in all seasons, but that events are grouped heavily in the months of September-November

and to a lesser degree for April-May. Droughts (e.g. 1967) and floods (1982-1983, 1995) amplify and diminish the seasonal closure signal, respectively.

Analysis of nearshore wave conditions and hydraulic conditions in the inlet and estuary suggest that waves are not typically the limiting factor for closure at the RRE. For the period from 1999 to 2008, the wave conditions (height, period, steepness) immediately prior to closure events are almost indistinguishable from the average conditions for the period of record. In contrast, the tidal prism, peak hourly inlet flow within a 24-hour period and inlet width-to-length ratio are all substantially lower. Since waves are clearly important for causing closure (Fig. 4.5,4.7), this was interpreted to mean that sediment delivery to the inlet is almost always sufficient to cause closure, but that the erosive capacity of the flows in the inlet channel has the power to negate the influence of waves. This is shown by Figure 4.5: While the risk of closure increases for higher waves (moving along the y-axis of the plot), there is no clear cutoff point below which the closure risk drops significantly. In contrast, inlet flows prevent virtually all closure events when the inlet conveys more than $40 \text{ m}^3 \text{ s}^{-1}$ at any hour within a given day. Tidal flows are more than sufficient to provide this threshold amount when the tide range in the estuary is similar to the Pt. Reyes tide range (i.e. when the inlet does not cause muting of the tide range). Hence, closure events occur only after the inlet begins to constrain the tidal flows through the inlet.

The seasonal pattern is tied to the phase difference between seasonal changes in waves and riverflow strength. Figure 4.8. shows that river flows typically increase in November or December, while waves increase some months earlier, creating a window

when flows are typically insufficient to fend off sedimentation in the inlet channel.

Comparison of wave steepness to the Dean Number (Dean and Dalrymple, 2002) suggest that most of the sediment transport in the vicinity of the mouth is due to littoral drift, rather than onshore welding bars (Fig. 4.9).

A parametric model and a metric for analyzing closure risk were presented in Chapter 4 to tie forcing conditions to closure explicitly. The five-day closure risk is a metric that was chosen to account for the fact that closures at the site are not instantaneous, but require extensive sedimentation that sometimes requires days to complete. The parametric model is based on the concept of sediment mass conservation in the inlet channel and builds on previous models from O'Brien (1976) and Battalio et al. (2005). The model compares very well against the five-day closure risk, providing a valuable tool for management which can be used to predict the likelihood of closure in the short-term using wave forecasts and tide conditions in the estuary (Fig. 4.7). The model also performs well at the seasonal scale, predicting the observed seasonal change in closure occurrence. The model is an important addition to the literature because it draws on the strengths of separate modeling approaches: effectively predicting closure likelihood when either tides or fluvial inputs dominate erosion of inlet bed sediments (whereas prior models addressed only one).

At the annual scale, subtracting the long term mean of 48 days of closure per year revealed a cyclical 3-5 year pattern, alternating between sets of years with more-than-average closure and years with less-than-average closure. This alternation is strongly tied to a yearly measure of river flow, indicating that drought and flood periods have a strong

influence on long-term closure patterns at the site, as has been suggested for similar sites (Elwany et al., 1998; Walker, 2003). Annual measures of waves did not correlate with the occurrence of closure. The ENSO and PDO cycles were also compared against the long-term normalized closure pattern, but the data record was too sparse to arrive at conclusive evidence of a connection. However, these large-scale climate shifts are known to influence rainfall and wave conditions in Northern California, so more work is needed to examine the possibility of ties with the RRE and other sites.

The frequency and duration of closure events have shifted dramatically at the RRE from the mid nineteenth century to the present. Anecdotal evidence from early residents suggest that seasonal closure events were common, lasting entire dry-seasons. Drawn-out seasonal closures were mostly absent from the twentieth century records, but a clear shift occurred between the 1931-1955 and 1973-2008 records. Closures occurred every 134 days and lasted for 15 days during the prior period and occurred every 43 days and lasted 6 days during the latter period. These shifts are most likely tied to two major changes in management: (1) artificial increases in dry-season base flows in the mid 1920s, and (2) adoption of a breach protocol for opening the mouth in the 1960s.

Chapter 4 advances the present understanding of inlet closure by showing for the first time how a closure signal can be decomposed into short-term, seasonal and interannual scales. It also provides evidence of how alterations to summer base flows and inlet management can influence a closure pattern. However, more work is needed to address additional questions brought up by this study. Additional issues that need to be addressed are:

- Ties between climate change and inlet closure,
- The role of inlet migration,
- Testing of the generality of the stability model (Eq. 4.9) presented here
- The comparative influence of the tidal prism and fluvial input on inlet stability

The latter two points are important for addressing inlet stability for a broader range of sites. Some sites are similar to the RRE and are dominated by tidal hydraulics for much of the year (i.e. 10 percent or less of inlet flows are attributable to river flows for most of the year). Other sites have an even more confined geometry and rely more heavily on flood events to maintain an open inlet. The model presented here in Eq. (4.9) can be used interchangeably when either tides or flows are the dominant source of erosion in the inlet, but an approach is still needed that addresses both, while providing the same benefits (simplicity, computational efficiency, availability of input parameters at many sites).

7.2. Salt Field Mechanics after closure

Estuaries that are subject to inlet closure undergo extended periods of isolation from the ocean. Due to their tidal nature, saline ocean water is usually trapped in the estuary after the tidal interactions have been blocked by the inlet. This has two primary consequences: (1) Turbulent mixing is vastly reduced, owing to the absence of tidal motions and (2) the trapped saltwater causes strong and sharp vertical stratification. The latter directly influences the temperature and dissolved oxygen fields in the closed

estuary, which has implications for salmonids and other aquatic organisms whose habitat space are limited by the change in estuary regime (e.g. Jassby et al., 1995).

In Chapter 5, we studied the evolution of the salt field in the RRE after the inlet becomes blocked with sediment. In particular, we examined the leading edge (front) of the salt field and its movement to the inner estuary. We used along-stream sets of CTD profiles taken at points along the channel thalweg to characterize the scalar fields and upward facing ADCPs at multiple locations to understand the flow structure driving the observed upstream motion of the front. Velocity fluctuations were also used to obtain an approximate representation of the turbulence in the upper water column. Although Chapter 5 focuses primarily on the evolution of the salt field, the evolution of the concurrent temperature and dissolved oxygen fields are also discussed, and examples of their link to the salt field are shown in Appendix C.

Unlike deeper systems, the bathymetry at the RRE exerts a strong control on the evolution of the salt field. The geometry of the RRE is best described as a narrow (200 m wide) channel with a bottom profile consisting of scour pools separated by shallow areas (sills). At the time of closure, the salt field is often composed of a well-mixed and salty area near the mouth and freshwater conditions upstream. Upstream movement of the salt front is driven by the baroclinic pressure gradient fueled by this initial state and later maintained by winds. As the salt front advances upstream, salt below the pycnocline becomes trapped locally in the pools behind the leading edge of the front. Salt trapping in pools increases the overall residence time of the salt field in the estuary because these

saltwater deposits (if sufficiently deep) require strong currents to remove. Sometimes these currents are only achieved during floods with recurrence intervals of ~ 365 days. The salt field evolves in two phases when the connection between the estuary and ocean is lost: (1) an initial settling phase in which the salt field slumps into position in the outer estuary, possibly triggering vertical mode 1 internal waves or strong density currents, and (2) a secondary phase characterized by front formation above the pycnocline and propagation of gravitational circulation currents upstream during periods of low winds. The first phase is driven by the initial density gradient between the salty mouth area and the fresher areas immediately upstream, and involves a rapid shift of the salt field at all depths. The second phase is driven by the salinity gradient in the well-mixed epilimnion, and occurs entirely above the pycnocline. It is episodic and slow at the RRE, but allows the salt field to move an additional 2-3 km upstream after the first phase is complete. This is important because typical winds are not physically capable of destroying the salt stratification, so every pool that the salt field extends to becomes subject to high residence times and hypoxia at depth (e.g. Fig. C.28).

The upstream motion of the salt field can be described in simple terms: since the salt front is negatively buoyant, it cannot move upstream when blocked by high points in the bathymetry directly in front of it. It accounts for this by inundating the local pool until negatively-buoyant salt fills the pool to the crest height of the ridge in front of it. Once this occurs, the front advances to the next pool, which becomes the new position of the salt front. During the first phase, this is a rapid process driven by strong density gradients throughout the water column. During the second phase, diurnal winds cause stirring of

the salt from the upper pycnocline into the epilimnion during the day. Since much of this mixing appears to occur at the basin edges close to the mouth at the RRE, this perpetuates a weak horizontal salinity gradient above the pycnocline between the relatively well-mixed mouth and upstream (Fig. 5.6). When the diurnal winds recede at night, front formation likely occurs, and gravitational currents act on this gradient in the upper water column to move salt farther upstream.

The dominant components of the flow structure in the inner and outer estuary were identified using an EOF analysis with the ADCP measurements during closure events E1, E4 and E5. The same modes were dominant at each site, regardless of the dataset. Because of the shape of the basin, the stratification at the site, and the diurnal wind frequency, the flow structure in the outer estuary is typified by two dominant EOF modes: a wind-sheared profile (e.g. Winant, 2010) that dominates during the day and a vertical mode 3 internal wave that appears to be caused by a resonant frequency with the wind forcing and the shape of the stratification (e.g. Monismith, 1985). In the inner estuary, the structure is also dominated by two modes, a wind-sheared velocity profile active during the day and what appears to be a gravitational current above the pycnocline that is active at night, when winds are weak (Fig. 5.11-13).

The salt front motion is limited by the physical space available for inundation in front of it and by turbulence caused by the diurnal winds, which break up the salt front when active. To summarize these combined influences, the observed upstream transport of salt was related to a capacity factor developed here, and to a horizontal Ri number developed for lock-exchange laboratory experiments. Salt front motion was inferred by

the change in salt mass upstream of station B2, in the inner estuary. The observed salt mass influx to the inner estuary compared well against the horizontal Ri and the inundation capacity C , suggesting that these measures provide a meaningful description of the physics of salt front advance.

The analysis stops short of providing a predictive measure of salt front advance because of the needs for additional data, particularly CTD profiles taken at higher temporal resolution. A closer examination of the turbulence is needed, and an explicit analysis of the along-stream momentum budget, as has been used elsewhere by Nidzieko et al. (2008) and Giddings et al. (2012). This type of behavior is probably common in other estuaries with similar geometry and forcing conditions (e.g. Largier and Taljaard, 1992). However, a comparable study in other bar-built estuaries with similar geometry is needed to determine the generality of these results.

7.3. Effects of Inlet Management Practices on Water Column stability

Inlet closure is treated with a number of different possible management responses. These range from invasive approaches (permanent jetty structures or manual breaching) to non-invasive (allowing the inlet to remain closed and minimizing anthropogenic impacts). Management strategies reflect economics, municipal needs, safety, environmental preservation, and other factors. Since the inlet and estuary are parts of an

interconnected system, management actions can exert a strong influence on the physical characteristics of the estuary.

Chapter 6 examines the potential difference in estuary response to two management approaches. The first approach is to allow the inlet to remain closed. The second is a newer approach: to enforce perched conditions, allowing spilling outflows over the beach. The former was likely the natural response of the inlet prior to disturbance (Chapter 4), while the latter is an adaptive approach intended to improve conditions for salmonids in the estuary while mitigating the potential for flooding of properties adjacent to the RRE (NMFS, 2008).

The impacts of each of these actions are examined in terms of the water column stability in the outer estuary, the region with the majority of the estuary volume and salt. To fully realize the variability of the system, diurnal winds and beach seepage were also included in the analysis.

We emphasized the short-term (two-week) response of the water column stability in this study. 12 two-week cases were run, with varying wind, seepage and management conditions. Water column stability was addressed in terms of (1) the maximum strength of the pycnocline and (2) the potential energy anomaly. The maximum pycnocline strength is the limiting condition for vertical mixing between the lower and upper layers. The potential energy anomaly is a measure of the total energy needed to fully mix the water column. The residual flow structure was examined, and the evolution of the salt field during each of the 12 runs were described in the context of the effect that this structure has on the local salt field. The salt mass of the estuary was also examined, since

seepage and perched overflow allow export of salt, which has implications for the long-term stability of the estuary water column.

Within the two-week time frame, the closed and perched management cases exhibit different residual flow structures and produce divergent outcomes in terms of water column stability and salt mass. Closure allows freshwater inflows to collect behind the beach, essentially thickening the upper layer and increasingly isolating the pycnocline from the effects of wind-stresses applied at the surface by widening the distance between the surface and pycnocline. Seepage losses increased with the increased depth during inlet closure, so that the export of salt through the beach was shown to accelerate. At the same time, upwelling induced by the winds decreased as the upper layer grew, so that the strength of the pycnocline reached an asymptotic steady-state value over time. The residual horizontal salt transport during closure was toward the mouth, and the corresponding loss of salt through the beach was significant when applying seepage rates consistent with the results of Appendix A. The residual transport, and the corresponding salt losses, were greatest for higher winds, and the resting state of the pycnocline was weakest for higher winds as well. The potential energy anomaly increased as water ponded behind the closed beach, to the point where even storm winds would be incapable of mixing the water column.

When a perched overflow channel was present at the beach (the second management scenario considered), the estuary water level and depth remained constant. The overflow channel allowed rapid export of salt, especially when strong diurnal winds were applied. However, this export weakened with time, and overall the loss of salt from

the outer estuary was smaller than for closure (where seepage was the main driver). Upwelling events were more severe during perched conditions, because the upper fresh layer remained very narrow ($\sim 1.5 - 2$ m) leading to critical Wedderburn Numbers on a diurnal basis.

The largest difference between the perched and the closure management scenarios was the difference in water column stability. The strength of stratification grew with time for perched conditions. The peak stratification in the pycnocline intensified from an initial value of 0.12 s^{-2} to a value of 0.22 s^{-2} after two weeks when strong diurnal winds were applied. When weak winds or no winds were applied, the increase was smaller (0.16 s^{-2} and 0.14 s^{-2} , respectively). This difference is a result of the residual transport favoring export of salt from above the pycnocline. The effect of the outflow on limiting the depth severely limited seepage through the beach by mitigating the pressure gradient between the estuary and ocean, so direct losses of salt from the lower layer through the beach were minimal.

An analysis of the long-term impacts of the two management states was formulated by (1) examining the trajectories seen from the short-term results and (2) presenting a conceptual model of changes in salt mass to speculate about the long-term conditions. The model results were then compared against representative results from the estuary observations (Appendix C).

The conceptual model compares the vertical transfer of salt into the upper layer from turbulent diffusion against the transfer of salt out of the estuary through the beach due to seepage. These were seen as the dominant drivers of salt loss in the perched and

closed management cases, respectively. These two flow rates can be used to provide a dimensionless ratio α which determines when either process dominates. For systems having negligible seepage losses or strong vertical turbulent diffusion, salt export (and thus long-term water column stability) is only possible when an outflow channel exists on the beach. When seepage dominates or vertical diffusion is negligible (i.e. systems with narrow beaches or weak winds) seepage losses can dominate the system, and much of the salt water in the estuary may be lost through the beach berm.

Despite the 2D approximation of the estuary, the trends in water column stability observed in the model are consistent with observations in the RRE (Fig. 6.13). Only limited data exist for perched overflow conditions at the site (event E2, Fig. C.32), but stratification was much stronger during this time than for closure events at the site, as suggested by the model results. Data from E1 also support the finding that the strength of stratification becomes stable during closure.

While Chapter 6 greatly helps in understanding the effect of two markedly different approaches to management on estuarine water column stability (and thus, chance of vertical mixing in the long-term), the analyses were based on a limited number of model runs intended to show some of the dominant trends in water column stability, residual flow structure and salt mass export. Perched outflow channels are a common, and under-studied, feature of many coastlines (Perissinotto et al., 2010). Much more data are needed in systems where this feature is present. It would also be useful for future modeling studies to examine a broader range of outlet channel height (in relation to the pycnocline, as well as outlet channel size, and to provide an additional comparison

against the case of fully breaching the inlet (as opposed to leaving the inlet closed or perched), which was not discussed here, but is more common (see Chapter 2).

References

- Abad, J. D., B.L. Rhoads, I. Güneralp, and M.H. García. 2008. Flow structure at different stages in a meander-bend with bendway weirs. *Journal of Hydraulic Engineering*, 134(8): 1052-1063.
- Alegria-Arzaburu, A.R. and G. Masselink. 2010. Storm response and beach rotation on a gravel beach, Slapton Sands, U.K. *Marine Geology* 278: 77-99. doi: 10.1016/j.margeo. 2010.09.004.
- Allan, J. and P. Komar. 2006. Climate controls on US West Coast erosion processes. *Journal of Coastal Research* 22(3): 511-529. doi: 10.2112/03-0108.1.
- Amein, A., and N. Kraus. 1991. DYNLET1: Dynamic implicit numerical model of one-dimensional tidal flow through inlets. Technical Report CERC-91-10. U.S. Army Engineer Waterways Experiment Station, Vicksburg, MS.
- Antenucci, J.P., J. Imberger, and A. Saggio. 2000. Seasonal evolution of the basin-scale internal wave field in a large stratified lake. *Limnology and Oceanography* 45(7): 1621-1638.
- Aubrey, D.G. and P.E. Speer. 1984. Updrift migration of tidal inlets. *Geology* 92(5): 531-545.
- Bagnold, R.A. 1966. An approach to the sediment transport problem from general physics. Professional Paper 422-I. U.S. Geological Survey, Washington D.C.
- Battalio, B., D. Danmeier, and P. Williams. 2006. Predicting closure and breaching frequencies of small tidal inlets - a quantified conceptual model. Proceedings of the 30th Conference on Coastal Engineering, ASCE, San Diego, pp. 3937-3950.
- Bear, J. 1988. *Dynamics of fluids in porous media*. Dover publications.
- Becker, A., L. Laurenson, and K. Bishop. 2009. Artificial mouth opening fosters anoxic conditions that kill small estuarine fish. *Estuarine, Coastal and Shelf Science* 82: 566-572. doi: 10.1016/j.ecss.2009.02.016.

- Behrens, D.K. 2008. Inlet closure and morphological behavior in a Northern California estuary: the case of the Russian River. M.S. Thesis. University of California, Davis. 160 p.
- Behrens, D.K., F.A. Bombardelli, J.L. Largier, E. Twohy. 2009. Characterization of time and spatial scales of a migrating rivermouth. *Geophysical Research Letters* 36: L09402, doi: 10.1029/2008GL037025
- Biswas, G., and V. Eswaran (Eds.). 2002. *Turbulent flows: fundamentals, experiments and modeling*. Narosa.
- Blake, M. C., R.W. Graymer, and R.E. Stamski. 2002. Geologic map and map database of western Sonoma, northernmost Marin, and southernmost Mendocino Counties, California. US Geological Survey.
- Bloomfield, P. 2000. *Fourier Analysis of Time Series: An Introduction, 2nd ed.* John Wiley and Sons, Inc., New York, 261 pp.
- Bombardelli, F. A., and M.H. García. 2001. Three-dimensional hydrodynamic modeling of density currents in the Chicago River, Illinois. *Civil Engineering Studies, Hydraulic Engineering Series No. 68*.
- Bombardelli, F.A., M.I. Cantero, M.H. García, and G.C. Buscaglia. 2009. Numerical aspects of the simulation of discontinuous saline underflows: the lock-exchange problem. *Journal of Hydraulic Research* 47(6): 777-789.
- Borsuk, M., C. Stow, R. Luettich, H. Paerl, and J. Pinckney. 2001. Modelling oxygen dynamics in an intermittently stratified estuary: estimation of process rates using field data. *Estuarine, Coastal and Shelf Science* 52: 33-49. doi: 10.1006/ecss.2000.0726.
- Brown, E.I. 1928. Inlets on sandy coasts. *Proceedings of the American Society of Civil Engineers*, Vol. LIV, pp. 505-553.
- Brown, D. and A. Comrie. 2004. A winter precipitation 'dipole' in the western United States associated with multidecadal ENSO variability. *Geophysical Research Letters*, 31: L09203. doi: 10.1029/2003GL018726.
- Bruun, P. and F. Gerritsen. 1960. *Stability of Coastal Inlets*. North Holland, Amsterdam, 140 pp.

- Byrne, R., R. Gammisch, and G. Thomas. 1980. Tidal prism-inlet area relations for small tidal inlets. Proceedings of the 21st International Conference on Coastal Engineering, ASCE, New York, pp. 2517-2533.
- Cable, J., W. Burnett, and J. Chanton. 1997. Magnitude and variations of groundwater seepage along a Florida marine shoreline. *Biogeochemistry* 38: 189-205.
- Chant., R.J. 2010. Estuarine secondary circulation. In Valle-Levinson (Ed.), *Contemporary Issues in Estuarine Physics* (pp. 145-185). New York, NY: Cambridge University Press.
- Chikita, A.C., W. Iwasaka, A. Al Mamun, K. Ohmori, and Y. Itoh. 2012. The role of groundwater outflow in the water cycle of a coastal lagoon sporadically opening to the ocean. *Hydrology* 464-465: 423-430. doi: 10.1016/j.jhydrol.2012.07.035.
- Chung, E. G., F. A. Bombardelli, S. G. Schladow. 2009. Modeling linkages between sediment resuspension and water quality in a shallow, eutrophic, wind-exposed lake. *Ecological Modelling* 220: 1251-1265, doi: 10.1016/j.ecolmodel.2009.01.038
- Cooper, J.A.G. 2001. Geomorphological variability among microtidal estuaries from the wave-dominated South African coast. *Geomorphology* 40: 99-122.
- Cousins, M., M. Stacey, and J. Drake. 2010. Effects of seasonal stratification on turbulent mixing in a hypereutrophic coastal lagoon. *Limnology and Oceanography* 55: 172-186.
- Crane, J., and A. Solomon. (Eds.). 2010. *Estuaries: Types, Movement Patterns and Climatological Impacts*. Hauppauge: Nova Science Publishers.
- Csanady, G.T. 1973. Wind-induced barotropic motions in long lakes. *Journal of Physical Oceanography* 3: 429-438.
- Cushman-Roisin, B. 1994. *Introduction to Geophysical Fluid Dynamics*. Prentice-Hall.
- Davidson, G. 1869. Coast Pilot of California, Oregon, and Washington Territory. United States Coast Survey. Government Printing Office, Washington, 341 pp.
- Davis, R., M. Hayes. 1984. What is a wave-dominated coast? *Marine Geology* 60: 313-329.

- De Sieyes, N., K. Yamahara, B. Layton, E. Joyce, and A. Boehm. 2008. Submarine discharge of nutrient-enriched fresh groundwater at Stinson Beach, California is enhanced during neap tides. *Limnology and Oceanography* 53(4): 1434-1445.
- Dean, R. G., R.A. Dalrymple. 2002. *Coastal processes: with engineering applications*. Cambridge University Press, New York, 488 pp.
- Dean, R. and T. Walton. 1973. Sediment transport processes in the vicinity of inlets with special reference to sand trapping. In: Cronin, J.L. (Ed.), 1975. *Estuarine Research, 2, Geology and Engineering*. Academic Press, New York, pp. 129-149.
- Department of Water Resources (DWR), 2006. Progress on Incorporating Climate Change into Planning and Management of California's Water Resources. Technical Memorandum Report. Sacramento, California.
- Donnelly, C., N. Kraus, N., and M. Larson. 2006. State of knowledge on measurement and modeling of coastal overwash. *Journal of Coastal Research* 22(4): 965-991.
- Duong, T., R. Ranasinghe, A. Luijendijk, A. Dastgheib, and D. Roelvink. 2012. Climate change impacts on the stability of small tidal inlets. *Proceedings of COPEDEC VIII, Chennai, India*, pp. 594-602.
- Dussailant, A., P., Galdames, C. Sun. 2009. Water level fluctuations in a coastal lagoon: El Yali Ramsar wetland, Chile. *Desalination* 246: 202-214. doi: 10.1016/j.desal.2008.03.053.
- Dyer, K. 1986. The salt balance in stratified estuaries. *Estuarine and Coastal Marine Science* 2: 273-281.
- Elwany, M. H. S., R.E. Flick, and S. Aijaz. 1998. Opening and closure of a marginal southern California lagoon inlet. *Estuaries* 21: 246-254.
- Environmental Data Solutions (EDS), 2009. Unpublished sidescan sonar bathymetry data and LiDaR topography data for the Russian River from the mouth to Duncan Mills. Environmental Data Solutions, conducted for Sonoma County Water Agency.
- Escoffier, F.F. The stability of tidal inlets. *Shore and Beach* 8(4): 114-115.
- Escoffier, F.F. 1977. Hydraulics and stability of tidal inlets. US Army Coastal Engineering Research Center, GITI report 13, 75 pp.

- Fenton, J., and W. McKee. 1990. On calculating the lengths of water waves. *Coastal Engineering* 14: 499-513.
- Finley, E.L., 1937. *History of Sonoma County, California: its people and its resources*. Press Democrat Publishing Company, Santa Rosa, 453 pp.
- Fischer, H. 1976. Mixing and dispersion in estuaries. *Annual Reviews in Fluid Mechanics* 1976.8: 107-133.
- Fischer, H., J. List, R. Koh, J. Imberger, and N. Brooks. 1979. *Mixing in Inland and Coastal Waters*. London: Academic Press.
- FitzGerald, D.A., 1996. Geomorphic variability and morphologic and sedimentologic controls on tidal inlets. *Journal of Coastal Research*, 23: 47-71.
- FitzGerald, D.A., I.V. Buynevich, R.A. Davis, Jr., and M.S. Fenster. 2002. New England tidal inlets with special reference to riverine-associated inlet systems. *Geomorphology* 48: 179-208.
- Florsheim, J.L., P. Goodwin. 1993. Geomorphic and hydrologic conditions in the Russian River, California: historic trends and existing conditions. Prepared for California State Coastal Conservancy, Oakland.
- Flow Science, Inc. 2012. FLOW-3D version 9.2.5. <<http://www.flow3d.com>> (June 10, 2011).
- Ford, M., J. Wang, and R.T. Cheng. 1990. Predicting the vertical structure of tidal current and salinity in San Francisco Bay, California. *Water Resources Research* 26(5): 1027-1045.
- Friedrichs, C.T., and D.G. Aubrey. 1988. Non-linear tidal distortion in shallow well-mixed estuaries: a synthesis. *Estuarine, Coastal and Shelf Science* 27: 521-545.
- Gale, E., C. Pattiaratchi, and R. Ranasinghe. 2006. Vertical mixing processes in Intermittently Closed and Open Lakes and Lagoons, and the dissolved oxygen response. *Estuarine, Coastal and Shelf Science* 69: 205-216. doi: 10.1016/j.ecss.2006.04.013.
- Gale, E., C. Pattiaratchi, R. Ranasinghe. 2007. Processes driving circulation, exchange and flushing within Intermittently Closing and Opening Lakes and Lagoons. *Marine and Freshwater Research* 58(8): 709-719. doi: 10.1071/MF06121.

- Galgano, F., 2009. Beach erosion adjacent to stabilized microtidal inlets. *Middle States Geographer* 42: 18-32.
- Garcia, M.H. (Ed.), 2008. *Sedimentation Engineering: Processes, Measurements, Modeling, and Practice*. ASCE Manual and Reports on Engineering Practice, vol. 110. American Society of Civil Engineers, New York.
- Geyer, W.R. 1993. The importance of suppression of turbulence by stratification on the estuarine turbidity maximum. *Estuaries* 16(1): 113-125.
- Geyer, W.R. 2010. Estuarine salinity structure and circulation. In Valle-Levinson (Ed.), *Contemporary Issues in Estuarine Physics* (pp. 145-185). New York, NY: Cambridge University Press.
- Giddings, S. N., D. Fong, S. Monismith, C. Chickadel, K. Edwards, W. Plant, B. Wang, O. Fringer, A. Horner-Devine, and A. Jessup. 2012. Frontogenesis and frontal progression of a trapping-generated estuarine convergence front and its influence on mixing and stratification. *Estuaries and Coasts* 35: 665-681, doi: 10.1007/s12237-011-9453-z
- Goodwin, P. and K. Cuffe, K. 1994. Russian River estuary study: hydrologic aspects of an estuary management plan. Technical report for Sonoma County Dept. of Planning, 194 pp.
- Goodwin, P. 1996. Predicting the stability of tidal Inlets for wetland and estuary management. *Journal of Coastal Research Special Issue* 23: 83-101.
- Griggs, G. (Ed.). 2005. *Living with the changing California coast*. University of California Press.
- Hansen, D.V., and M. Rattray. 1965. Gravitational circulation in straits and estuaries. *Journal of Marine Research* 23: 104-122.
- Harley, M. D., I.L. Turner, A.D. Short, and R. Ranasinghe. 2010. Assessment and integration of conventional, RTK-GPS and image-derived beach survey methods for daily to decadal coastal monitoring. *Coastal Engineering* 58: 194-205.
- Hayes, S., M. Bond, C. Hanson, E. Freund, J. Smith, E. Anderson, A. Ammann, and B. MacFarlane. 2008. Steelhead growth in a small Central California watershed: upstream and estuarine rearing patterns. *Transactions of the American Fisheries Society* 137: 114-128. doi: 10.1577/T07-043.1.

- Hirt, C. and J. Sicilian. 1985. A porosity technique for the definition of obstacles in rectangular cell meshes. Proceedings of the International Conference on Ship Hydrodynamics. National Academy of Science, Washington, D.C.
- Hirt, C., and B. Nichols. 1981. Volume of Fluid (VOF) method for the dynamics of free boundaries. *Journal of Computational Physics* 39: 201-225.
- Hughes, S.A. 2002. Equilibrium cross sectional area at tidal inlets. *Journal of Coastal Research* 18(1): 160-174.
- Hume, T. M., and C.E. Herdendorf. 1992. Factors controlling tidal inlet characteristics on low drift coasts. *Journal of Coastal Research* 8(2): 355-375.
- Ilicak, M., T. Özgökmen, H. Peters, H. Baumert, and M. Iskandarani. 2008. Very large eddy simulation of the Red Sea overflow. *Ocean Modelling* 20: 183-206.
- Imberger, J. and G. Parker. 1985. Mixed layer dynamics in a lake exposed to a spatially variable wind field. *Limnology & Oceanography* 30(3): 473-488.
- Imberger, J., and G.N. Ivey. 1993. Boundary mixing in stratified reservoirs. *Journal of Fluid Mechanics* 248: 477-491.
- James, N.C., P.D. Cowley, A. K. Whitfield, and H. Kaiser. 2008. Choice chamber experiments to test the attraction of postflexion *Rhabdosargus holubi* larvae to water of estuarine and riverine origin. *Estuarine, Coastal and Shelf Science* 77: 143-149.
- Jarrett, J.T., 1976. Tidal prism-inlet area relationships. US Army Coastal Engineering Research Center, GITI report 3.
- Jassby, A. D., W. J. Kimmerer, S. G. Monismith, C. Armor, J. E. Cloern, J. R. Schubel, and T. J. Vendlinski. 1995. Isohaline position as a habitat indicator for estuarine populations. *Ecological Applications* 5(1): 272-289.
- Jimenez, J.A., O.S. Madsen. 2003. A simple formula to estimate settling velocity of natural sediments. *Journal of Waterway, Port, Coastal and Ocean Engineering*, ASCE, March/April 2003: 70-78. doi: 10.1061/(ASCE)0733-950X(2003)129:2(70).
- Johnson, J.W., 1973. Characteristics and behavior of Pacific coast tidal inlets. *Journal of Waterways, Harbors and Coastal Engineering Division* 99: 325-339.

- Julien, P.Y.,1998. *Erosion and Sedimentation*. Cambridge University Press, New York.
- Keulegan, G.H. 1967. Tidal flow in entrances: water-level fluctuations of basins in communications with seas. Committee on Tidal Hydraulics, Technical Bulletin No. 14, US Army Engineer Waterways Experimental Station, Vicksburg, MS.
- Khlebnikov, K.T. 1990. The Khlebnikov Archive: Unpublished Journal (1800-1837) and Travel Notes (1820, 1822 and 1824). Translated by John Bisk and Leon Shur. University of Alaska Press, Fairbanks, 60 pp.
- Kjerfve, B., C.A.F. Schettini, B. Knoppers, G. Lessa, and H.O. Ferreira. 1995. Hydrology and salt balance in a large, hypersaline coastal lagoon: Logoa de Araruama, Brazil. *Estuarine, Coastal and Shelf Science* 42: 701-725.
- Kraus, N. 1998. Inlet cross-section area calculated by process-based model. *Proceedings of the International Conference of Coastal Engineering*, Vol. 3, pp. 3265-3278.
- Kraus, N., S. Munger, and K. Patsch. 2008. Barrier beach breaching from the lagoon side, with reference to northern California. *Shore and Beach* 76: 33-43.
- Kundu, P.K. and Cohen, I.M. 2002. *Fluid Mechanics*. Academic Press. San Diego.
- Laatar, A., M. Benahmed, A. Belghith, and P. Le Quéré. 2002. 2D large eddy simulation of pollutant dispersion around a covered roadway. *Journal of Wind Engineering and Industrial Aerodynamics* 90: 617-637.
- Large, W.G. and Pond, S. 1980. Open ocean momentum flux measurements in moderate to strong winds. *Journal of Physical Oceanography* 11: 324-337.
- Largier, J.L., 1992. Tidal intrusion fronts. *Estuaries* 15: 26-39.
- Largier, J. L., and S. Taljaard. 1991. The dynamics of tidal intrusion, retention, and removal of seawater in a bar-built estuary. *Estuarine, Coastal and Shelf Science* 33(4): 325-338.
- Largier, J.L., B.A. Magnell, and C.D. Winant. 1993. Subtidal circulation over the northern California shelf. *Journal of Geophysical Research* 98(18), 18: 147-18,179.
- Laudier, N. A., E.B. Thornton, and J. MacMahan. 2011. Measured and modeled wave overtopping on a natural beach. *Coastal Engineering* 58(9): 815-825.

- LaZerte, B. D. 1980. The dominating higher order vertical modes of the internal seiche in a small lake. *Limnology and Oceanography* 25(5): 846-854.
- Linacre, E. T. 1993. Data-sparse estimation of lake evaporation, using a simplified Penman equation. *Agricultural and Forest Meteorology* 64(3): 237-256.
- Linden, P. F., and J. E. Simpson. 1986. Gravity-driven flows in a turbulent fluid. *Journal of Fluid Mechanics* 172: 481-497.
- Linden, P. F., and J. E. Simpson. 1988. Modulated mixing and frontogenesis in shallow seas and estuaries. *Continental Shelf Research* 8(10): 1107-1127.
- MacCready, P., and W. R. Geyer. 2010. Advances in estuarine physics. *Annual Reviews in Marine Science* 2(1): 35-58, doi: 10.1146/annurev-marine-120308-081015
- Magoon, O.T., D.D. Treadwell, P.S. Atwood, B.L. Edge. 2008. Lost jetty of California's Russian River. *Proceedings of the 31st International Conference of Coastal Engineering, Hamburg*, pp. 3487-3495.
- Mantua, N.J., S.R. Hare. 2002. The Pacific-Decadal Oscillation. *Journal of Oceanography* 58: 35-44.
- Mathieu, P., E. Deleersnijder, B. Cushman-Roisin, J-M. Beckers, and K. Bolding. 2002. The role of topography in small well-mixed bays, with application to the lagoon of Mururoa. *Continental Shelf Research*, 22: 1379-1395.
- Mayor-Mora, R.E., 1977. Laboratory investigation of tidal inlets on sandy coasts. US Army Coastal Engineering Research Center, GITI report 11, 106 pp.
- Mehta, A.J., 1996. A perspective on process related research needs for sandy inlets. *Journal of Coastal Research Special Issue* 23: 3-21.
- Mehta, A.J. and E. Ozsoy. 1978. Inlet hydraulics: flow dynamics and nearshore transport. In: Bruun, P. (ed.), *Stability of Tidal Inlets: Theory and Engineering*, Amsterdam, Elsevier Scientific Publishing Co. pp. 83-161.
- Monismith, S. G. 1985. Wind-forced motions in stratified lakes and their effect on mixed-layer shear. *Limnology and Oceanography* 30(4): 771-783.

- Monismith, S. G. 2010. Mixing in estuaries. In Valle-Levinson (Ed.), *Contemporary Issues in Estuarine Physics* (pp. 145-185). New York, NY: Cambridge University Press.
- Monismith, S. G., W. Kimmerer, J. R. Burau, and M. T. Stacey. 2002. Structure and flow-induced variability of the subtidal salinity field in northern San Francisco Bay. *Journal of Physical Oceanography* 32: 3003-3019.
- Morris, B. D., and I.L. Turner. 2010. Morphodynamics of intermittently open-closed coastal lagoon entrances: New insights and a conceptual model. *Marine Geology* 271(1): 55-66.
- Mount, J.F., 1995. *California Rivers and Streams: The Conflict Between Fluvial Processes and Land Use*. University of California Press, Berkeley, California, 376 pp.
- Moyle, P.B. 2002. *Inland fishes of California*. University of California Press, Berkeley and Los Angeles, California.
- Munk, W. and E. Anderson. 1948. Notes on the theory of the thermocline. *Journal of Marine Research* 7: 276-295.
- Münnich, M., A. Wuest, and D.M. Imboden. 1992. Observations of the second vertical mode of the internal seiche in an alpine lake. *Limnology & Oceanography* 37(8): 1705-1719.
- Nelson, B. W., A. Sasekumar, and Z. Z. Ibrahim. 1994. Neap-spring tidal effects on dissolved oxygen in two Malaysian estuaries. *Hydrobiologia* 285: 7-17.
- Nezu, I. and H. Nakagawa. 1993. *Turbulence in open-channel flow*. IAHR monograph, A.A. Balkema, Rotterdam.
- Nidzieko, N. J., J.L. Hench, and S.G. Monismith. 2009. Lateral circulation in well-mixed and stratified estuarine flows with curvature. *Journal of Physical Oceanography* 39(4): 831-851.
- National Oceanic and Atmospheric Administration (NOAA). 2012. Metadata from 2009-2011 Coastal LiDAR Project. Coastal Services Center.
http://csc.noaa.gov/dataviewer/webfiles/metadata/ca2010_coastal_dem.html.

- Nunes Vaz, R.A., G.W. Lennon, and J.R. de Silva Samarasinghe. 1989. The negative role of turbulence in estuarine mass transport. *Estuarine, Coastal and Shelf Science* 28: 361-377.
- National Marine Fisheries Service (NMFS). 2008. Russian River Biological Opinion. <http://www.scwa.ca.gov/rrifr/>.
- O'Brien, M.P., 1969. Equilibrium flow areas of tidal inlets on sandy coasts. *Proceedings of 10th International Conference on Coastal Engineering, ASCE, Tokyo*, pp. 676-686.
- O'Brien, M.P., 1976. Notes on tidal inlets on sandy shores. US Army Coastal Engineering Research Center, GITI report 5, 27 pp.
- Oceanographic Instruments. 2012. Datawell Waverider Reference Manual. October 10, 2009. http://cdip.ucsd.edu/documents/index/gauge_docs/mk3.pdf.
- O'Callaghan, J., C. Pattiaratchi, and D. Hamilton. 2007. The response of circulation and salinity in a micro-tidal estuary to sub-tidal oscillations in coastal sea surface elevation. *Continental Shelf Research* 27: 1947-1965, doi: 10.1016/j.csr.2007.04.004
- Officer, C. B. 1976. *Physical Oceanography of Estuaries*. Wiley & Sons, New York.
- Okely, P., and J. Imberger. 2007. Horizontal transport induced by upwelling in a canyon-shaped reservoir. *Hydrobiologia* 586: 343-355, doi: 10.1007/s10750-007-0706-6.
- Opperman, J.J., K.A. Lohse, C. Brooks, N.M. Kelly, and A.M. Merenlender. 2005. Influence of land use on fine sediment in salmonid spawning gravels within the Russian River Basin, California. *Canadian Journal of Fisheries and Aquatic Science* 62, 2740-2751. doi: 10.1139/FO5-187.
- Özgökmen, T. M., T. Iliescu, P.F. Fischer, A. Srinivasan, and J. Duan. 2007. Large eddy simulation of stratified mixing in two-dimensional dam-break problem in a rectangular enclosed domain. *Ocean Modelling* 16(1): 106-140.
- Perissinotto, R., D.D. Stretch, A.K. Whitfield, J. B. Adams, A.T. Forbes, and N.T. Demetriades. 2010. Ecosystem functioning of temporarily open/closed estuaries in South Africa. In: *Estuaries: Types, Movement Patterns and Climatic Impacts*, Nova Science Publishers Inc, New York.

- Pritchard, D.W. 1954. A study of the salt balance in a coastal plain estuary. *Journal of Marine Research* 15:33-42.
- Pope, S.B. 2000. *Turbulent Flows*. Cambridge: Cambridge University Press.
- Preisendorfer, R.W. 1988. *Principle Component Analysis in Meteorology and Oceanography*. Elsevier, New York.
- Ranasinghe, R., and C. Pattiaratchi. 2003. The seasonal closure of tidal inlets: causes and effects. *Coastal Engineering* 45(4): 601-627.
- Ranasinghe, R. and C. Pattiaratchi. 1998. Flushing characteristics of a seasonally – open tidal inlet: a numerical study. *Journal of Coastal Research* 14(4): 1405-1421.
- Ranasinghe, R., and C. Pattiaratchi. 1999a. Circulation and mixing characteristics of a seasonally – open tidal inlet: a field study. *Journal of Marine and Freshwater Research* 50(4): 281-290.
- Ranasinghe, R., and C. Pattiaratchi. 1999b. The seasonal closure of tidal inlets: Wilson Inlet - a case study. *Coastal Engineering* 37: 37-56.
- Ranasinghe, R., and C. Pattiaratchi. 2000. Tidal velocity asymmetry at inlets located in diurnal tidal regimes. *Continental Shelf Research* 20(2000): 2347-2366.
- Ranasinghe, R., and C. Pattiaratchi. 2003. The seasonal closure of tidal inlets: causes and effects. *Coastal Engineering* 45: 601-627.
- Ranasinghe, R., C. Pattiaratchi, and G. Masselink. 1999. A morphodynamic model to simulate the seasonal closure of tidal inlets. *Coastal Engineering* 37(1): 1-36.
- Rice, M.P., 1974. The mouth of the Russian River. Unpublished M.S. Thesis. University of California Berkeley, 102 pp.
- Rodriguez, J.F., F.A. Bombardelli, F.A., M.H. Garcia, K.F. Frothingham, B.L. Rhoads, and J.D. Abad. 2004. High-resolution numerical simulation of flow through a highly sinuous river reach. *Water Resources Management* 18: 177-199.
- Rosati, J. D., and N.C. Kraus. 1999. Formulation of sediment budgets at inlets. *Coastal Engineering Technical Note CETN-IV*, 15.

- Roy, P. S., R. J. Williams, A. R. Jones, I. Yassini, P. J. Gibbs, B. Coates, R. J. West, P. R. Scanes, J. P. Hudson, and S. Nichol. 2001. Structure and function of south-east Australian estuaries. *Estuarine, Coastal and Shelf Science* 53: 351-384. doi: 10.1006/ecss.2001.0796
- Rustomji, P., 2007. Flood and drought impacts on the opening regime of a wave-dominated estuary. *Marine and Freshwater Research* 58: 1108-1119. doi: 10.1071/MF07079.
- Sagaut, P. 2005. *Large Eddy Simulation for Incompressible Flows, Scientific Computation, An Introduction*, third ed. Berlin: Springer-Verlag.
- Schrad, J.I., 1992. History of opening Russian River and Salmon Creek. Sonoma County Department of Public Works Road, Maintenance Division, 12 pp.
- Schwing, F.B., T. Murphree, and P.M. Green. 2002. The Northern Oscillation Index (NOI): a new climate index for the northeast Pacific. *Progress in Oceanography* 53(2-4): 115-139.
- Shintani, T., A. de la Fuente, Y. Niño, and J. Imberger. 2010. Generalizations of the Wedderburn number: Parameterizing upwelling in stratified lakes. *Limnology & Oceanography*, 55(3): 1377-1389. doi:10.4319/lo.2010.55.3.1377.
- Simpson, J., and R. E. Britter. 1979. The dynamics of the head of a gravity current advancing along a horizontal surface. *Journal of Fluid Mechanics* 94: 477-495.
- Simpson, J., J. Brown, J. Matthews, and G. Allen. 1990. Tidal straining, density currents, and stirring in the control of estuarine stratification. *Estuaries* 13(2): 125-132.
- Simpson, J., E. Williams, L. H. Brasseur, and J. M. Brubaker. 2005. The impact of tidal straining on the cycle of turbulence in a partially stratified estuary. *Continental Shelf Research* 25: 51-64, doi: 10.1016/j.csr.2004.08.003
- Smagorinsky, J. 1963. General circulation experiments with the primitive equations: I. The basic experiment. *Monthly Weather Review* 91(3): 99-165.
- Smith, H., and D. Foster. 2005. Modeling of flow around a cylinder over a scoured bed. *Journal of Waterway, Port, Coastal, and Ocean Engineering* 131(1): 14-24. doi: 10.1061/(ASCE)0733-950X(2005)131:1(14).

- Sonoma County Water Agency (SCWA). 2010. Unpublished monitoring surveys of Goat Rock State Beach collected in 2009 and 2010.
- Stacey, M. T., J. R. Burau, and S. G. Monismith. 2001. Creation of residual flows in a partially stratified estuary. *Journal of Geophysical Research* 106(C8): 17,013-17,037.
- Stacey, M. T., S. G. Monismith, and J. R. Burau. 1999. Measurements of Reynolds stress profiles in unstratified tidal flow. *Journal of Geophysical Research* 104(C5): 10,933-10,949.
- Steiner Environmental Consultants (SEC), 1996. A history of the salmonid decline in the Russian River. 86 pp.
- Stevens, C.L. and G.A. Lawrence. 1997. Estimation of wind-forced internal seiche amplitudes in lakes and reservoirs, with data from British Columbia, Canada. *Aquatic Science* 59: 115-134.
- Stockdon, H. F., R. A. Holman, P.A. Howd, and A.H. Sallenger. 2006. Empirical parameterization of setup, swash, and runup. *Coastal Engineering* 53(7): 573-588.
- Stretch, D., Parkinson, M., 2006. The breaching of sand barriers at perched temporary open/closed estuaries – a model study. *Coastal Engineering* 48(1): 13-30.
- Syvitski, J., S. Peckham, R. Hilberman, and T. Mulder. 2003. Predicting the terrestrial flux of sediment to the global ocean: a planetary perspective. *Sedimentary Geology* 162: 5-24. doi: 10.1016/S0037-0738(03)00232-X.
- Thompson, R., and J. Imberger. 1980. Response of a numerical model of a stratified lake to wind stress. *Proceedings of the International Symposium on Stratified Flows* 2: 562-570.
- Townend, I. 2005. An examination of empirical stability relationships for UK estuaries. *Journal of Coastal Research* 21(5): 1042-1053.
- Trenberth, K. and J. Hurrell. 1994. Decadal atmosphere-ocean variations in the Pacific. *Climate Dynamics* 9: 303-319.
- Tsuruya, H., S. Nakamo, and H. Kato. 1983. Experimental study on wind driven current in a wind-wave tank - effect of return flow on wind driven current. *Port and Harbour Research Institute*, in Japanese, 22(2): 127-174.

- UNESCO. 1981. Tenth report of the joint panel on oceanographic tables and standards (UNESCO technical papers in marine science, no. 36). Retrieved from: <http://unesdoc.unesco.org/images/0004/000461/046148eb.pdf>
- US Army Corps of Engineers (USACE), 1965. Technical report on cooperative beach erosion study of coast of northern California - Pt Delgada to Pt Año Nuevo: Appendix 8. Contract No. W-04-193-ENG 5196.
- US Army Corps of Engineers, 1984. Shore Protection Manual. Coastal Engineering Research Center.
- US Army Corps of Engineers (USACE). 2002. Coastal Engineering Manual: Chapter 3: Estimation of nearshore waves. Coastal Engineering Research Center.
- Van de Kreeke, J., 1985. Stability of tidal inlets - Pass Cavallo, Texas. *Estuarine, Coastal and Shelf Science* 21, 33-43.
- Van de Kreeke, J., 2004. Equilibrium and cross-sectional stability of tidal inlets: application to the Frisian Inlet before and after basin reduction. *Coastal Engineering* 51: 337-350. doi: 10.1016/j.coastaleng.2004.05.002.
- Vidal, J., and X. Casamitjana. 2008. Forced resonant oscillations as a response to periodic winds in a stratified reservoir. *Journal of Hydraulic Engineering* 134(4): 416-425, doi: 10.1061/(ASCE)0733-9429(2008)134:4(416).
- Vijith, V., D. Sundar, and S.R. Shetye. 2009. Time-dependence of salinity in monsoonal estuaries. *Estuarine, Coastal and Shelf Science* 85(4): 601-608.
- Vlasenko, V. I., and K. Hutter. 2002. Transformation and disintegration of strongly nonlinear internal waves by topography in stratified lakes. *Annales Geophysicae* 20: 2087-2103.
- Walker, D., 2003. Assessing environmental flow requirements for a river-dominated tidal inlet. *Journal of Coastal Research* 19(1), 171-179.
- Webb, C.K., D.A. Stow, and H. Chang. 1991. Morphodynamics of southern California inlets. *Journal of Coastal Research* 7, 167-187.
- Whitfield, A.K., J.B. Adams, G.C. Bate, K. Bezuidenhout, T.G. Bornman, P.D. Cowley, P.W. Froneman, P.T. Gama, N.C. James, B. Mackenzie, T. Riddin, G.C. Snow, N.A. Strydom, S. Taljaard, A.I. Terörde, A.K. Theron, J.K. Turpie, L. van

- Niekerk, P.D. Vorwerk, and T.H. Wooldridge. 2008. A multidisciplinary study of a small, temporarily open/closed South African estuary, with particular emphasis on the influence of the mouth state on the ecology of the system. *African Journal of Marine Science* 30: 453-473.
- Wiegand, R. C., and V. Chamberlain. 1987. Internal waves of the second vertical mode in a stratified lake. *Limnology and Oceanography* 32(1): 29-42.
- Williams, E., and J. H. Simpson. 2004. Uncertainties in estimates of Reynolds stress and TKE production rate using the ADCP variance method. *Journal of Atmospheric and Oceanic Technology* 21: 347-357.
- Winant, 2010. Wind and tidally-driven flows in a semi-enclosed basin. In Valle-Levinson (Ed.), *Contemporary Issues in Estuarine Physics* (pp. 145-185). New York, NY: Cambridge University Press.
- Wingfield, D. and C. Storlazzi. 2007. Spatial and temporal variability in oceanographic and meteorologic forcing along Central California and its implications on nearshore processes. *Journal of Marine Systems* 68(3-4): 457-472. doi: 10.1016/j.jmarsys. 2007.02.008.
- Wolter, K., M.S. Timlin. 1998. Measuring the strength of ENSO events: How does 1997/98 rank? *Weather* 53: 315-324.
- Zoulas, J. and A. Orme. 2007. Multidecadal-scale beach changes in the Zuma littoral cell, California. *Physical Geography* 28(4): 277-300. doi: 10.2747/0272-3646.28.4.277.

Appendix A. Estuary Water Balance and Berm Seepage

This section outlines the procedures used to characterize seepage losses from the RRE during inlet closure. Flow losses are estimated on a daily basis using data taken from inlet closure events between 19 June 1999 and 10 October 2009. Given the limited data on the characteristics of the water table adjacent to the RRE, aquifer exchange and beach seepage are not distinguished here, but rather referred to jointly as flow losses.

A.1. Importance of Flow Losses

Flow losses through porous media, whether from the estuary to the ocean or from the estuary to the adjacent aquifer, are an important component of the water budget in systems subject to closure (Chikita et al., 2012). In many systems, porous flow losses are negligible, owing to wide beach barriers or fine sediments in the beach and at the boundaries of the estuary (Dusaillant, et al., 2009). When these conditions are not the case, flow losses can potentially have several important impacts:

- Reduction of flows through the inlet
- Prolonged inlet closure events (see Section 4.11)
- Discharge of tracers from the estuary to the aquifer or coastal zone (Perissinotto et al., 2010)

Although seepage losses from permanently closed coastal lagoons (sometimes referred to as coastal lakes) have been studied in the past, little research exists to explain its

importance in perched or intermittently closed coastal lagoons. In these systems, the setup of water levels behind the beach produces heightened pressure gradients between the lagoon and ocean, or between the lagoon and the local aquifer. If the resulting seepage flows have the same order of magnitude as inflows or precipitation, closure events may be extended indefinitely since this condition would prevent the estuary water levels from filling to the critical height required for overtopping the beach (e.g. Kraus et al., 2008).

The transport of conservative tracers between the closed estuary and the adjacent aquifer or ocean is also of high importance, and is poorly understood. Recent work in Northern California has suggested that porous discharge to the ocean through the beach can be a prominent source of pollutants in the coastal zone (de Sieyes et al., 2008). This type of transport is also known to influence the habits of migrating salmonids, which must return to their (sometimes closed) native estuary to spawn after migrating to the ocean. This involves an olfactory response caused by sediment discharged through the porous berm (James et al., 2008). In the RRE, losses of estuary salt at depth near the mouth (see Sections 5 and 6) indicate that seepage through the porous beach is an important process. This process is examined more closely in this appendix.

A.2. Methods

Flow losses are estimated here by treating the estuary as a control volume. By applying the concept of conservation of mass, the change in estuary water volume with time can be tied to the net sum of inflows and outflows to the closed estuary:

$$\frac{dV}{dt} = Q_{river} + Q_{overwash} + P - E - (Q_{seep} + Q_{aquifer}) - Q_{extract} \quad (\text{A.1})$$

where V is the estuary volume, t is time, Q_{river} is the river inflow, $Q_{overwash}$ is the volume of water contributed by waves spilling over the beach, P and E are precipitation and evaporation, respectively, Q_{seep} is the flow loss due to seepage through the beach, $Q_{aquifer}$ is the exchange flow between the estuary and adjacent aquifer and $Q_{extract}$ is a flow loss term accounting for direct extraction of water from wells or pumps. These terms are illustrated in Figure A.1. and the methods for estimating them are described below.

Similar approaches have been used in the past (e.g. Kjerve et al., 1996)

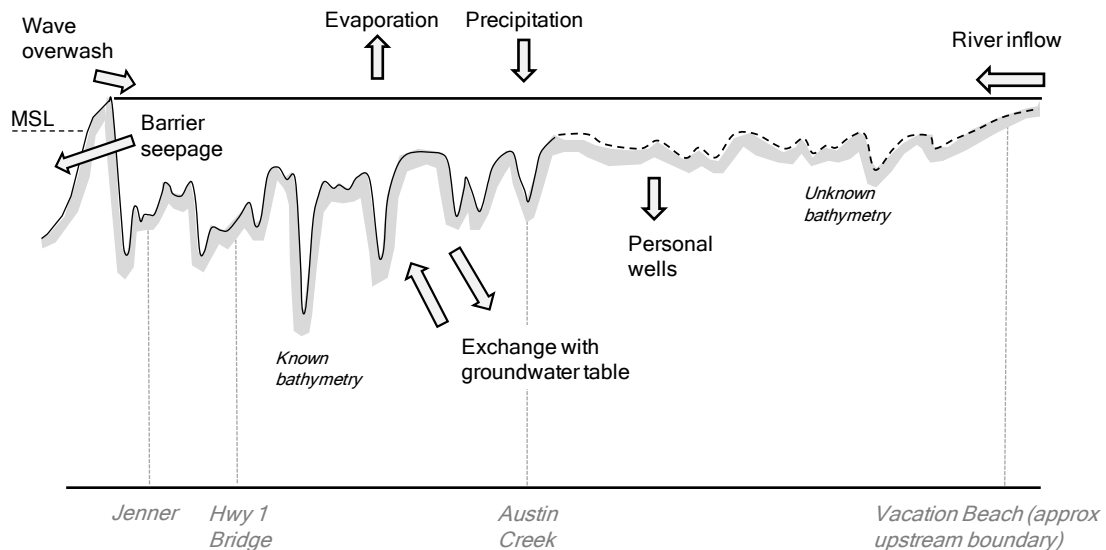


Figure A.1. Estuary schematic detailing processes relevant to changes in water volume during closure.

A.2.1. Mass Balance Components

Estuary Volume

During most tidal conditions, the upstream extent of the estuary is between 10 and 12 km from the estuary, as this is the maximum extent of salt intrusion into the estuary (Appendix C). During closure, trapped inflows pond behind the closed beach to a maximum height of 8 ft NGVD, and the water surface inundates areas farther upstream. The maximum upstream extent of this inundation is at Vacation Beach, where a temporary dam is placed during the dry months (pers. comm. C. Delaney). The entire 23 km extent from the mouth to Vacation beach was considered when characterizing the estuary volume, which was estimated from the following:

- The existing 10 m x 10 m raster of the bathymetry (EDS, 2009),
- The water level time series measured at the Jenner boat ramp, and
- A limited number of cross-channel survey profiles taken between the confluence with Austin Creek (Figure 3.1) and Vacation Beach, 23 km from the inlet (Goodwin and Cuffe, 1994).

These three sets of data were used to derive an approximate stage-storage relation (hypsoetric curve) for the estuary. An hourly record of estuary volume was obtained using the hypsoetric curve in concert with the hourly readings of water surface elevation at Jenner. This required the assumption that the estuary water surface was flat at all times (i.e. that the surface measurement at Jenner is representative of the surface throughout the estuary).

The available high-resolution bathymetry does not include the region between Austin Creek and Vacation Beach. This region was accounted for in the hypsometric curve by delineating an approximate water surface area using the channel cross-sections provided by Goodwin and Cuffe (1994) and by assuming that this area is not hydraulically connected to the estuary until it reaches a water level of 5 ft NGVD (~7.5 ft NAVD88). This assumption is based on the maximum sill heights present near Austin Creek in the EDS (2009) bathymetry. The volume contributed to the hypsometric curve from this region was calculated by multiplying its approximate surface area (which was assumed constant) by the height of the water surface above 5 ft NGVD. Since this is a coarse estimate, a sensitivity analysis was conducted by altering this upstream volume by 25 percent. As shown in Figure A.2, this leads to only small changes in the total estuary volume, on the order of one percent at an elevation of 8 ft NGVD. This is because the region nearest to the mouth is significantly deeper relative to mean sea level, so that a significant amount of the estuary volume is contained at elevations lower than 5 ft NGVD from the mouth to Austin Creek.

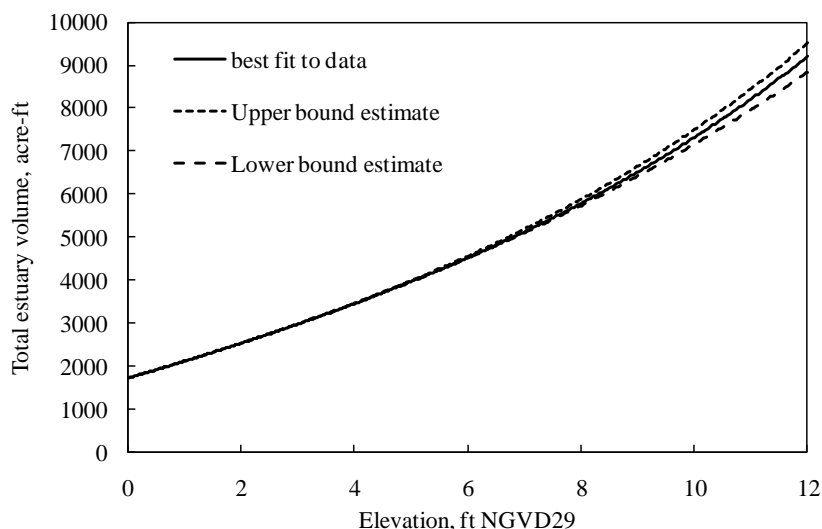


Figure A.2. Estuary stage-volume relation comparing methods of estimating upstream surface area.

Freshwater Inflows

Estuary inflows were characterized using the USGS gages at Guerneville and Austin Creek. The locations of these in relation to the inlet are shown in Figure 3.1. Although many tributaries exist between the mouth and Guerneville, the only perennial tributary is Austin Creek, so the joint contribution of these tributaries is assumed to be small.

When possible, direct measurements from SCWA provided at Vacation Beach were used to compare against the established gage data. Vacation beach is located approximately 7 km downstream of the USGS Guerneville gage. Vacation beach data from 2009 show a close agreement with measurements at the USGS gage but provide the added benefit of measuring flows caused by the removal of the temporary dams below Guerneville during early October each year. For the years when Vacation Beach flow measurements were not available, data taken during the first several days of October are neglected, so the effects of dam removal do not alter the results.

Wave Overwash

Wave overwash into the lagoon can contribute significant amounts of water (Laudier et al. 2011), especially when the beach is newly formed at the onset of closure, because the combination of a low berm and high waves can cause the water level on the ocean side to exceed the beach crest height. As an example, data recorded during the September 2009 closure event show a sudden increase in estuary water level during a period of high waves on 13-14 September (Fig. C.3). A concurrent drop in estuary temperature and increase in the

mass of salt in the estuary (Figs. C.11, C.19) indicate that wave overwash was likely the cause of the water-level change.

Estimation of $Q_{overwash}$ requires an understanding of the nearshore wave climate, as well as tides, wave setup and beach characteristics. Like most beaches, Goat Rock State Beach is subject to substantial seasonal change in shape (i.e. crest height and beach width) as well as incident wave conditions. Wave setup is a change in the time-averaged water surface elevation in front of the beach face caused by breaking waves (Komar, 1998). Wave runup is the maximum height that a wave front reaches on the beach face before receding (Stockdon et al., 2006). These are additive, contributing to the TWL (USACE, 2002). Wave overwash occurs when the TWL is higher than the beach crest (Donnelly et al., 2006), allowing ocean water to spill over the beach and contribute to the estuary water volume.

Since a time series of the beach crest height is not available, uncertainty in $Q_{overwash}$ estimates would probably be of the same order of magnitude as the estimates themselves. Rather than estimating $Q_{overwash}$, the combined water level response to mean tides, wave setup and wave runup on the shoreface were used to provide an estimate of the total water level (TWL) on the ocean side of the berm, and days when this exceeds a threshold elevation are excluded from the dataset, so the impact of $Q_{overwash}$ on the flow loss calculation is minimal.

Data from the Pt. Reyes tide gage (Fig. 3.1) were averaged over 25-hour intervals (representative of a lunar day) and assumed to be representative of tide conditions offshore of Goat Rock State Beach. Wave setup and runup were estimated using the methodology provided by Stockdon et al. (2006) who provide empirical formulations based on an extensive set of field data. These required nearshore estimates of H_s , as well as beach foreshore slope β and wave length L . These were estimated using the methods described in Sections 3 and 4. Hourly setup and runup were added to the smoothed tide data to give an hourly time series of TWL.

Precipitation, Evaporation and Extractions

Because of California's dry climate during late spring, summer and fall, precipitation is assumed to have a minimal impact. Evaporation was estimated from Linacre (1993) using temperature, wind speed and relative humidity data from BML and estimates of estuary water surface area derived from the EDS (2009) bathymetry data. This is used to get a representative daily evaporation rate, E . I assume that the BML measurements are representative of conditions at the RRE. While this may be true of the part of the estuary closest to the beach (where marine influences are presumably strongest), this may not be the case upstream, where hills likely alter the wind and temperature fields. Direct water extractions from wells and pumps below Guerneville and Vacation Beach are assumed to be small, but this needs to be tested as more data become available.

Seepage Losses

Q_{seep} and $Q_{aquifer}$ are driven by pressure gradients caused by the estuary filling with water during closure. As the estuary water level rises one expects the seepage rate to increase (given that ocean water level changes little at time scales longer than tidal). The increase in the combined flow loss due to rising pressure gradients is described by D'Arcy's Law (Bear, 1988), which is discussed in Section 6. There are no data to describe the seasonal change in the water table elevation surrounding the estuary, so the influence of $Q_{aquifer}$ on the total seepage losses is uncertain, and may vary by season. For the purpose of providing an initial estimate of flow losses, this interaction is assumed to be small relative to seepage through the beach. This is suggested by the relatively high losses of salt near the mouth of the RRE during closure. A time series of the

bottom salinity measured at two locations in the RRE is given in Figure A.3, indicating a much higher rate of salt loss near the inlet during the closure event lasting from 7 September to 5 October 2009. This shows that the amount of Q_{loss} attributed to the beach is much higher than that associated with the upstream reaches. This result was evident in all closure events studied, regardless of season.

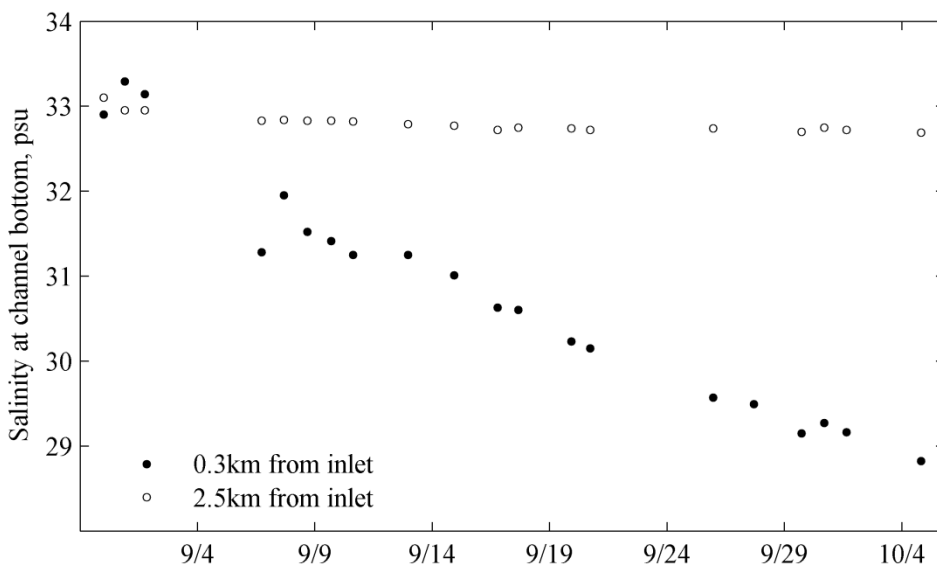


Figure A.3. Salinity measured at the bottom of the pools near the mouth (Station A1) and 2.3 km upstream (Station A4) during closure event E1.

A defining feature that distinguishes the RRE from many other intermittently closed estuaries in the literature is its coarse sediment and the presence of a rock jetty in the beach. Sediment on Goat Rock State Beach has a high fraction of coarse sand, with a median grain size of about 1 mm. While the grain size presumably leads to higher flow losses than systems with fine sediments, the effect of the jetty is presently unknown, and is the subject of ongoing studies funded by SCWA.

A.2.2. Application

To evaluate flow losses, I focus on dates when the Jenner gage indicates that the inlet is closed, and combine Q_{seep} and $Q_{aquifer}$ into a single term. To support the total flow loss estimate, I have also made the following assumptions:

- The terms $Q_{overwash}$, P and $Q_{extract}$ are negligible.
- Uncertainty in the stage-storage relation due to the lack of high-resolution bathymetry in the region upstream of Austin Creek is small
- The water surface in the closed lagoon can be considered horizontal
- Atmospheric conditions measured at BML are representative of conditions at the RRE
- Seasonal changes in $Q_{aquifer}$ are small

To ensure that these assumptions remain valid, data are excluded from the analysis when the following conditions are met:

- Jenner gage below 1.5 m (~ 5 ft NGVD)
- TWL greater than 2.5 m NGVD (~ 8 ft NGVD)
- BML wind speed greater than 10 m s^{-1}
- Q_{inflow} greater than $6 \text{ m}^3\text{s}^{-1}$ (~ $200 \text{ ft}^3\text{s}^{-1}$)

The first point ensures that no data are used during tidal conditions. The maximum tide height is close to 4 ft NGVD, so the estuary only surpasses this level during perched or

closed conditions. The second point is intended to ensure that $Q_{overwash} \sim 0$. The beach surveys conducted from 2009-2011 (see Chapter 3; SCWA, 2010) suggest a typical minimum beach crest height of about 10 ft NGVD after closure. The cutoff of 8 ft is a conservative value which accounts for errors in the TWL estimate. The third condition ensures that the assumption of a horizontal water surface remains valid. Wind causes stresses at the water surface that ultimately cause the water surface to tilt upward in the downwind direction (Winant, 2010). When this happens, the water surface measured at Jenner would give an over- or under-estimate of the lagoon volume. Observations in the estuary suggest a total tilt of roughly 10 cm between Stations A1 and B3 when BML winds exceed 10 m s^{-1} . Lastly, the fourth condition is intended to make sure that the assumption of $P \sim 0$ holds. Although precipitation records are available from BML, precipitation likely varies throughout the watershed between the mouth and Guerneville. Flows below $6 \text{ m}^3\text{s}^{-1}$ are indicative of dry-season baseflow conditions (e.g. Fig. 4.8).

Applying these conditions to Eq. (A.1) gives a simplified version of the mass-balance model:

$$Q_{loss} = (Q_{river} - E) - \frac{\Delta V}{\Delta t} \quad (\text{Eq. A.2})$$

Q_{loss} was calculated for at a daily time step ($\Delta t = 1 \text{ day}$) for closure periods between 19 June 1999 and 10 October 2009. Representative daily values of each of the terms in Eq. 2 were calculated from the hourly time series. TWL was taken as a daily maximum, while all other parameters were taken as daily averages. The term ΔV in Eq. (A.2) was estimated as the difference between the estuary volume at the last and first hour of the

day. After applying the above rules, Q_{loss} was calculated for a total of 158 days within the ten year period from 1999 to 2009.

A.3. Results

Fig. A.4 compares Q_{loss} against Δh , the difference between 25-hour averages Jenner and Pt. Reyes tide gages. Δh produces a better fit with flow loss estimates than the Jenner gage level alone, because the sea level is not constant but varies in response to winds and waves (Largier et al 1993; O'Callahan et al., 2007), which have a different local effect on the beach at the mouth of Russian River than they do on the headland at Point Reyes. A p -test of the result shows that overall, there is a moderate correlation between Q_{loss} and Δh ($r = 0.48$, $p < 0.001$) for the sample size of $N = 158$ days. The spread was characterized by subtracting the linear fit of the data (Fig. A.4) from the sample and then calculating the standard deviation which was found to be $17.5 \text{ ft}^3\text{s}^{-1}$. Evaporative losses were found to be a small component of the water balance, having less than 5 cfs ($0.14 \text{ m}^3\text{s}^{-1}$), even during dry-season conditions.

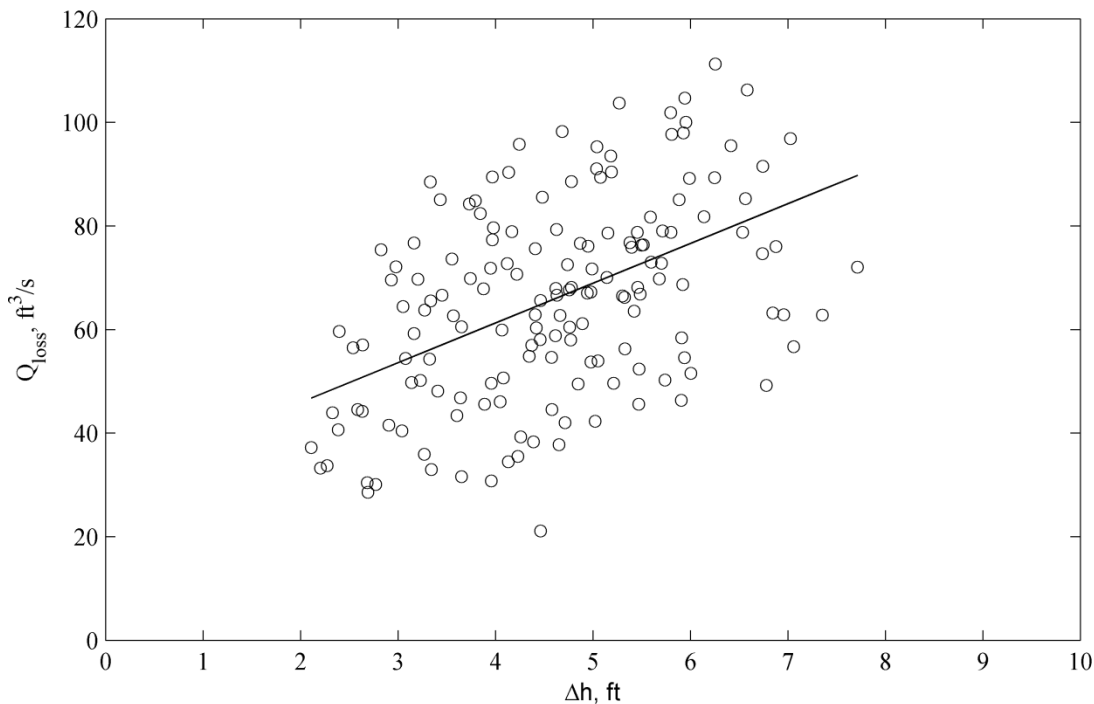


Figure A.4. Q_{loss} compared against Δh for the period from 1999 and 2009. Data were taken out when certain conditions were met (Section A.2.2) which would have invalidated the simplifying assumptions needed for this estimate. Q_{loss} represents the combination of Q_{seep} and $Q_{aquifer}$.

The result suggests that flow losses from the RRE during closure increase linearly with Δh , which is consistent with D’Arcy’s Law (Bear, 1988). Despite the spread of the data, the shape of the data cloud yields another important result: the upper and lower envelopes of Q_{loss} are well-defined, so cutoff Q_{loss} values can be defined with good confidence. To explore this, the correlations for these trends were calculated using the minimum and maximum values of Q_{loss} within 0.1 intervals. Linear fits were then created between the minimum and maximum envelopes (respectively) and Δh . Comparison of the minimum Q_{loss} envelope against Δh gives a linear fit of $Q_{loss} = 8.3\Delta h + 7.5$ and a stronger

correlation than observed for the total data set ($r = 0.74, p < 0.001$). For the maximum Q_{loss} envelope, the linear fit is $Q_{loss} = 6.8\Delta h + 53.2$ and the correlation is weaker ($r = 0.55, p < 0.001$), but still indicates a better fit than for the total dataset. The standard deviations were 12.1 and 16.5 ft^3s^{-1} for the minimum and maximum envelopes, respectively.

The observed linear increase in Q_{loss} for the dataset was also apparent at the event scale. Separate closure events are examined in Figure A.5. As with Figure A.4, the trends of Q_{loss} for these events have a scatter of $\pm 20 \text{ ft}^3\text{s}^{-1}$, commensurate with the scatter for the entire dataset. Nevertheless, they reflect an roughly linear increase in seepage losses with rising head difference between the estuary and ocean, which is expected.

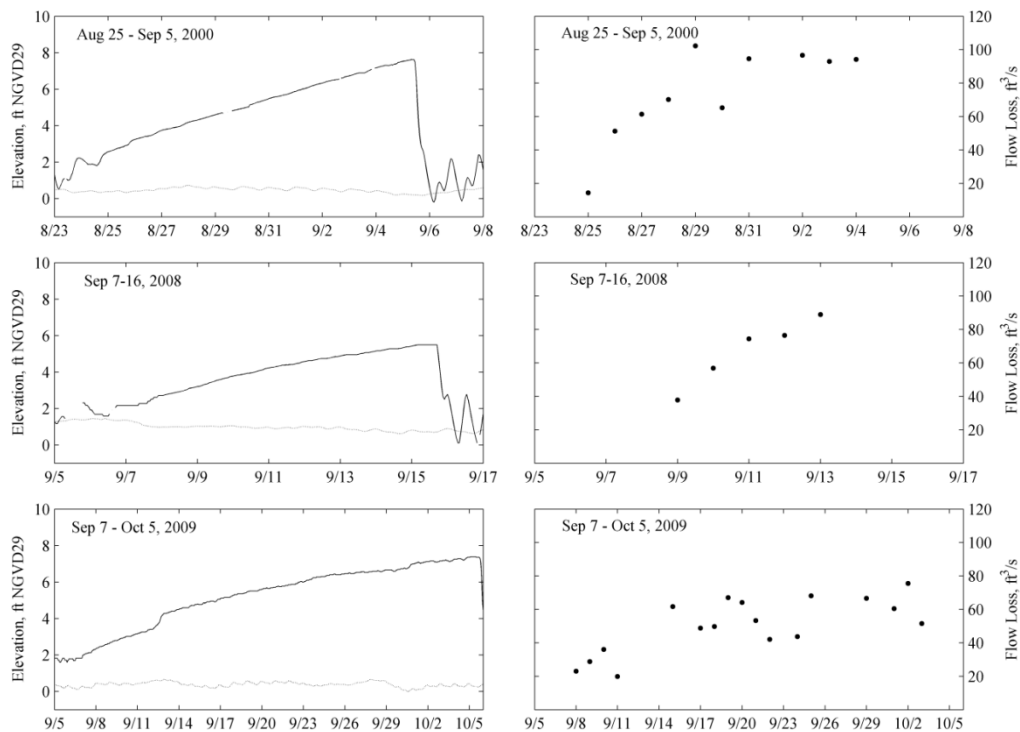


Figure A.5. Q_{loss} vs time during several individual closure events. Plots at left show estuary water surface elevation (-) and 25-hr average Pt. Reyes tide level (--).

A.4. Uncertainty

The uncertainty in the Q_{loss} estimates is high ($\sigma \sim 16 \text{ ft}^3\text{s}^{-1}$), reflecting the coarseness of the mass balance approach at this scale and the lack of information about $Q_{aquifer}$ and $Q_{extract}$. Uncertainties in wave parameters are discussed in Chapter 4, but the conservative value of TWL used for extracting data is assumed to have removed all events when $Q_{overwash} > 0$ and includes a buffer to account for uncertainties in wave estimates. Because of the simplifying assumptions used to formulate Eq. A.2, the only error resulting from the methods is from the estimation of evaporative losses. Linacre (1993) reports a maximum error of 0.8 mm day^{-1} of evaporation, which translates to an error of about $0.4 \text{ ft}^3\text{s}^{-1}$ at the RRE based on a representative surface area during closure. Errors due to uncertainty of the bathymetry upstream of Austin Creek were examined by varying the upstream surface area by 25 percent, which led to a maximum change of $2 \text{ ft}^3\text{s}^{-1}$.

Definitive uncertainty cannot be prescribed to $Q_{extract}$ and $Q_{aquifer}$, given the data limitations. While seasonal changes in the water table adjacent to the estuary are expected to alter the magnitude of Q_{loss} , they are not expected to change the pattern shown in Figure A.4. Since seepage is greatest near the mouth (Fig. A.3), changes to Q_{loss} due to variation in $Q_{aquifer}$ are expected to be small, but future work needs to address this further to reduce uncertainty. Direct measurements of seepage through the beach with wells, tracers or other means would also provide more insight.

Appendix B. Numerical Model Validation

B.1. Basis for Validation Tests

As discussed in Chapter 6, the estuary is modeled as a two-dimensional (x- and z-plane) system, having unit width. The model uses a simple approach to approximate turbulence and tracks the evolution of the estuary density field, which is used to approximate the salinity field. These approximations add computational efficiency, but also provide challenges in properly reproducing the key features of the estuary, including beach seepage, upwelling, and vertical mixing. To resolve these features with the model setup described in Chapter 6, several simplifying assumptions are required:

- Lateral variations in the salinity and density fields are negligible,
- Turbulent mixing in the RRE can be modeled adequately with a simple Smagorinsky approach (Sagaut, 2005), and
- The effects of temperature on the density field are small compared with salinity.

The first point is tested with the boat-based field measurements described in Chapter 3 and relies on the fact that the channel width is much smaller than the channel length. The second point is also tested against field measurements, but relies on the fact that the strong salinity stratification constrains most of the turbulent flows to the thin layer of freshwater above the pycnocline. The third assumption is addressed with a sensitivity test using a typical range of temperature observed in the estuary.

After verifying the simplifying assumptions, model validation is performed with a number of tests:

- The model domain, mesh and resolution are tested for their ability to reproduce the typical density profile in the estuary
- The model is run for several canonical tests with known solutions,
- Model results are tested against observations of the flow structure and density field in the estuary.

Each of these tasks are performed individually below. The canonical tests include simple domains and are intended to show that the model reproduces the analytical solutions of several problems with known outcomes. Each of these tests were chosen to represent different physical aspects of the estuary, such as wind forcing or flows over hard boundaries. Lastly, the model is run for parts of closure events E1 and E3, and the evolution of the density and flow fields are compared against observations.

B.2. Model Domain and Mesh

Two-Dimensional Approximation

The choice of using a simplified 2D estuary was based on computational efficiency and the narrow shape of the RRE. This type of approach has also been applied elsewhere. Vijith et al. (2009) used it to study the time-dependence of salinity in a monsoonal estuary and (Ford et al., 1990) used it to study the position of the salt front in

San Francisco Bay. Both applied the approach to much larger estuaries than the RRE. 2D conceptual models are also sometimes used to explain internal wave motions in lakes and reservoirs (e.g. Horn et al., 2001), or to simulate gravitational circulation resulting from dam-break scenarios (Özgökmen et al., 2007). Thus far, this approach appears to be absent in regards to bar-built estuaries.

The assumption that lateral variations in the density field are small was tested with a set of cross-channel CTD transects. These were taken on 28 September 2010, during closure event E.4. Representative winds and river flows during this time are summarized in Figure C.6. Two locations were chosen, one at station A4, where the channel is straight and oriented in the direction of predominant winds, and another at station A5, where the channel bends sharply (Fig. 3.2). Channel curvature is a concern because in systems with strong curvature, the lateral component of acceleration terms can become important to the overall momentum budget, along with accelerations due to curvature (Nidzieko et al., 2008). This can lead to lateral advection of saltwater and tilting of the pycnocline at the channel bends (Chant, 2010).

Figure B.1. shows that the lateral cross-section observations of density exhibit marked uniformity. These data were taken during relatively quiescent conditions, when along- and cross-stream velocities measured at station A4 near the pycnocline were both less than 10 cm s^{-1} . These were generally limited to 20 cm s^{-1} near the pycnocline, even during strong winds (Fig. 5.9). The magnitude of the baroclinic pressure gradient was estimated after Giddings et al. (2012):

$$BCPG = -\frac{g}{\rho_0} \left(\int_z^0 \frac{\partial \rho}{\partial y} dz' \right) \quad (\text{B.1})$$

where ρ_0 was taken as 998 kg m^{-3} . At both sites, the lateral BCPG was $O(10^{-4})$, or about an order of magnitude lower than values observed by Nidzieko et al. (2008) and Giddings et al. (2012) in tidal estuaries with similar degrees of curvature to the RRE. In the Snohomish River Estuary, Giddings et al. (2012) found that the lateral BCPG was $O(10^{-2} - 10^{-3})$ at a channel bend when along- and cross-stream velocities were roughly 1 and 0.5 m s^{-1} , respectively. During slack tide, when currents fell back to roughly 20 cm s^{-1} , the lateral BCPG was $O(10^{-4})$ (Giddings et al., 2012; Fig. 5). Since the RRE lacks tidal motions during closure, and since most winds at the site are insufficient to generate currents higher than $\sim 20 \text{ cm s}^{-1}$, the assumption of a uniform lateral density field is assumed to remain valid for the present work.

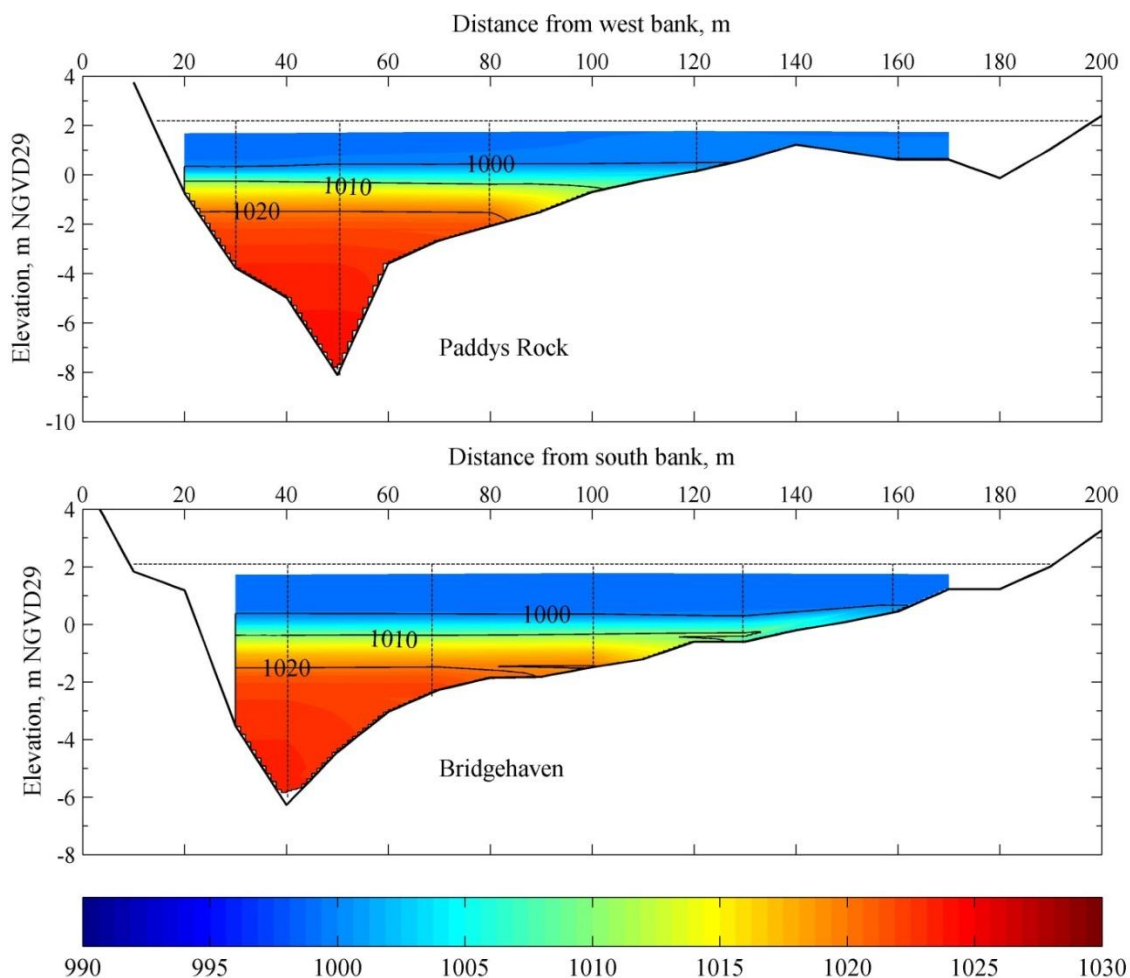


Figure B.1. Cross channel density plots at **(top)** site A4 and **(bottom)** site A5, on 29 September, 2010, during a closure event. At the time of data collection, winds were below 3 ms^{-1} .

Another consequence of the 2D approximation is that channel bifurcations are collapsed into a single representative channel, wherever they occur. The only major channel bifurcation occurs at Penny Island (Fig. 3.2 adjacent to stations A2 and A3). The validity of the 2D assumption was tested in this case by examining the fraction of the total flow attributed to both channels. The 2009 bathymetry indicates that the southern channel has a much smaller depth and volume than the northern channel. Quasi-uniform

flows and representative cross-sections for both channels were used to estimate the relative fraction of discharge carried by each channel. The flows in the south channel were estimated to be less than ten percent of those in the northern channel.

Approximation of turbulence

The RANS-Smagorinsky approach for modeling turbulence was chosen because it provided good initial results and required approximately a tenth of the time required for alternatives, typically both the $k-\varepsilon$ and RNG models for the same mesh. Because of the size of the mesh, much of the energy is resolved at the subgrid scale. Although the results below show that this model compares well against observations, the effects of using this approximation instead of other methods were deemed satisfactory as compared with the use of the alternative closures.

The Smagorinsky (1963) model relates the turbulent stresses used in the Reynolds-Averaged Navier Stokes (RANS) equations to the local velocity strain rate at each depth. In using this approach we rely on the fact that the strong stratification observed in the RRE limits most of the turbulence to the upper water column, where the vertical density structure is nearly homogeneous (e.g. Fig. C.13). Because of this condition, the role of turbulence is limited to diffusion of salt from the lower to upper layers across the pycnocline, which is strongest at the basin edges (Imberger and Ivey, 1993).

Effects of Temperature

In estuaries, the density field is much more heavily influenced by salinity than temperature (Geyer, 2010). This is demonstrated here by showing the typical range of salinity and temperature in the estuary and examining the effect that these have on the density magnitude, using the UNESCO (1981) Equation of State.

The estuary density varies from 998 in fresh water regions to 1026 kg m⁻³ in trapped salt water regions during closure. Changes in temperature were rapid in the upper water column and slower at the depth of the pycnocline and below. Hourly fluctuations measured by the SCWA sonde near the mouth (station A1) were typically ~2°C, while changes in the pycnocline and below drifted by as much as 5°C from the beginning to the end of some closure events. Using the Equation of State, these correspond to density changes of ~0.5 kg m⁻³ for daily fluctuations and ~1.2 kg m⁻³ over the course of closure events. In contrast, the change in salinity of some areas amounts to as much as a 20 psu (Fig. 5.5), which corresponds to a density change of 15.3 kg m⁻³. Thus, it is expected that salt field redistribution by winds and losses of dense bottom waters from seepage flow out of the estuary will have a higher impact on the modeled density than the change in temperature.

Grid Resolution

Typically, when RANS turbulence models are used in representing the flow field, the mesh used in the model needs to be refined (i.e. size of grid cells decreased) until the modeled solution converges, in order to be sure that the choice of mesh size itself is not

affecting the solution. However, when the Smagorinsky turbulence model is implemented in LES, the usual concept of grid independence is absent (Biswas and Eswaran, 2002).

This is because different grid sizes in LES merely change the amount of turbulence that is directly solved (i.e. eddies larger than size of grid cells) and modeled (i.e. sub-grid scale). Because of this, our main constraint in the initial model setup is to ensure that the mesh used with our RANS-Smagorinsky approach is capable of resolving the features of importance in the estuary.

In the present case, one of the most important features to resolve in the estuary is the observed sharp stratification during closure, because the sharpness of the gradient between low density and high density waters has great influence on both vertical and horizontal flows in the estuary (Fischer et al., 1979).

We tested several grid sizes in both the vertical and longitudinal directions. To test their effect on stratification, we ran the model using the approximation of the RRE thalweg and beach used in Chapter 6 to characterize the domain. We used an impervious beach berm and applied wind stress at the water surface and typical dry-season inflows at the upstream boundary. The density distribution observed at 15:00 h on 26 September was applied to the model and it was run until 15:00 h on 5 October. We found that changing the longitudinal (x -direction) grid size did not have much effect on the modeled vertical density profiles for grid sizes below 100 m, while vertical (z -direction) resolution had greater importance. Figure B.2 shows the model results near the mouth (Station A1), 0.3 km upstream of the barrier beach, with vertical cell sizes ranging from 10 to 50 cm. Clearly, as the cell size increases in the vertical, the density profile becomes increasingly

diffused, effectively smoothing the stratification. As expected, the results indicate that the sharpness of the stratification converges with smaller vertical cell size, and that there is relatively little gain from a reducing the cell size below 10 cm.

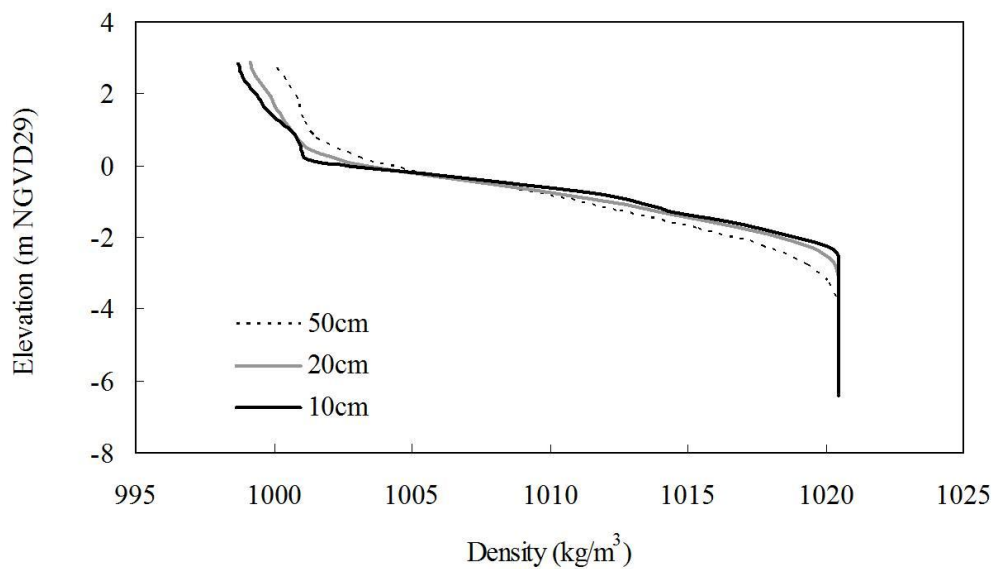


Figure B.2. Comparison of modeled density profiles at the mouth for different vertical grid resolutions.

B.3. Canonical Tests

Several simple canonical tests were used to test the ability of the model to accurately reproduce some of the key elements of estuarine physics relevant to the RRE.

These include:

- The effect that solid boundaries have on the flow structure, via the the classical "Law of the Wall" theory (Pope, 2000).
- Velocity profile produced by wind blowing over a closed freshwater basin (Tsuruya et al., 1983; Mathieu et al., 2002).
- Movement of the density interface in a two-layer enclosed basin with wind stress at the surface (Shintani et al., 2010).

The first case is a classical result for channel flows. The second two cases were chosen because they address two important characteristics of the estuary when closed: namely that strong vertical stratification is present and that the primary source of energy is from winds acting on the surface. These tests are described in more detail in the following subsections.

B.3.1. Effect of rigid boundary on flows

The effects of the bottom and lateral surfaces of the estuary depend on the basin geometry and the degree of turbulence present (Fischer et al., 1979), but in many cases these boundaries have been shown to have a large effect on the flow characteristics in the

basin. In turbulent channel flow, the interaction of a moving fluid with a rough boundary produces a well-known velocity profile, which is described by the so-called "Law of the Wall" (Pope, 2000). This logarithmic increase in velocity away from the boundary is discussed broadly in the literature. It results from the no-slip condition where the fluid touches the boundary and from the vertical diffusion of momentum via eddies, which act to dissipate the existing momentum gradients.

To apply a simple channel flow case to the estuary, a model domain is used that is representative of the shallow flat zones in the Russian River estuary, where the boundaries have the largest effect on the flow structure. Figure B.3 illustrates the model domain for this test: a 4 km - long channel with a depth of one meter. The mesh consists of cells having stream-wise length of 100 m and height of 10 cm, giving a total of 400 computational cells. For simplicity, the water is given a constant density of 1000 kg m^{-3} (freshwater) and the bottom roughness has a height of 0.001 m, corresponding to coarse sand. Vertically-constant incoming and outgoing velocities are enforced at the upstream (left) and downstream (right) edge of the channel. Boundary velocities of 0.2, 1 and 5 cm s^{-1} were applied, to represent the range observed by ADCPs at the depth of the shallow zones.

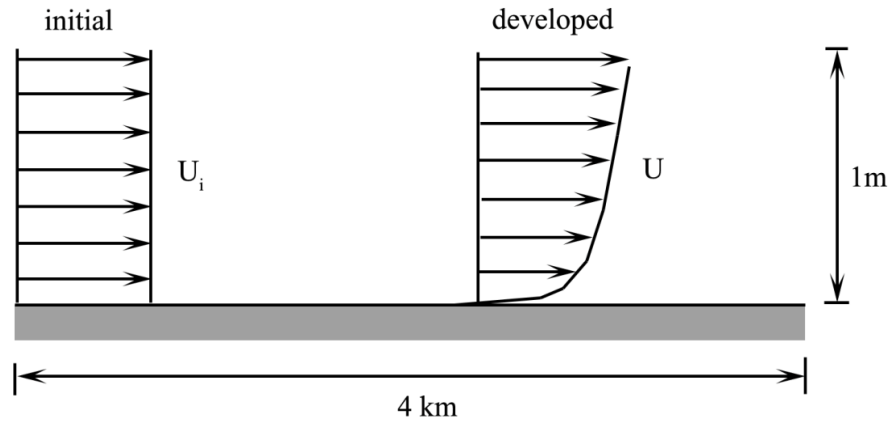


Figure B.3. Model domain for boundary-effect test, with expected result.
Theoretical Basis

To construct the Law-of-the-Wall profile for the given setup, we need to first find the shear velocity which applies to each inflow amount:

$$u_* = \sqrt{\frac{\tau_w}{\rho}} \quad (\text{B.2})$$

where τ_w is the shear stress at the boundary and ρ is the fluid density. We can define the shear stress using the Darcy-Weisbach formulation (Julien, 1998):

$$\tau_w = \left(\frac{f}{8}\right)\rho U^2 \quad (\text{B.3})$$

where U is the incoming fluid velocity (specified at the left-hand side of the model domain) and f is the Darcy-Weisbach friction factor. To determine f , we solve for it implicitly using the Colebrook-White equation (Julien, 1998):

$$\frac{1}{\sqrt{f}} = -2\log_{10}\left(\frac{\varepsilon}{3.7D} + \frac{2.51}{\text{Re}\sqrt{f}}\right) \quad (\text{B.4})$$

where ε is the roughness height (coarse sand), D is the hydraulic diameter (1 m) and Re is the Reynolds number, defined as:

$$Re = \frac{4HU}{\nu} \quad (\text{B.5})$$

After solving for f , we reinsert it into Eq. B.3 to find τ_w and then solve Eq. B.2 for the shear velocity. For a bottom roughness corresponding to coarse sand, we can assume that our flow conditions lead to a "hydraulically smooth" boundary (Julien, 1998), which means that we can solve for the Law-of-the-Wall velocity profile using the following equation:

$$u(z) = 5.75u_* \log\left(\frac{u_*z}{\nu}\right) + 5.5 \quad (\text{B.6})$$

The velocity profile given by Eq. B.6 is valid for a range of distances away from the wall. The term in brackets provides a measure of the distance, termed "wall units":

$$y^+ = \frac{u_*z}{\nu} \quad (\text{B.7})$$

Fewer than about ten wall units (~ 10 cm for the present model domain) from the boundary, the viscous sublayer dominates the flow, and Eq. B.6 is not valid. The relation is valid for 10 - 300 wall units, which encompasses the depth scale of 1 m used for the test.

The RANS Smagorinsky approach is not expected to reproduce the rapid change in velocity within the viscous boundary layer. This requires turbulence modeling with $k-\varepsilon$, $k-\varepsilon$ RNG, or LES approaches. The desired result is for the present model to reproduce the

velocity profile above the viscous boundary layer, but within the region for which the Law of the Wall solution is valid.

Modeled Channel Flow

Figure B.4 compares the modeled velocity profiles against the analytical solution at the center of the basin. As expected, the model accurately captures the velocity profile in the upper 80-90 percent of the water column, but misses the drop in velocity at the boundary. This is true for all boundary velocities tested. The model was also run with the $k-\varepsilon$ and $k-\varepsilon$ RNG approaches, which produced a better fit to the wall (not shown), but required run times that were 10-100 times longer than used here for the RANS Smagorinsky model. The 10-20 cm boundary layer not represented by the present model is expected to have only a minimal impact on the modeled flow structure in the majority of the estuary, since this is much smaller than the typical depth of 4-12 meters.

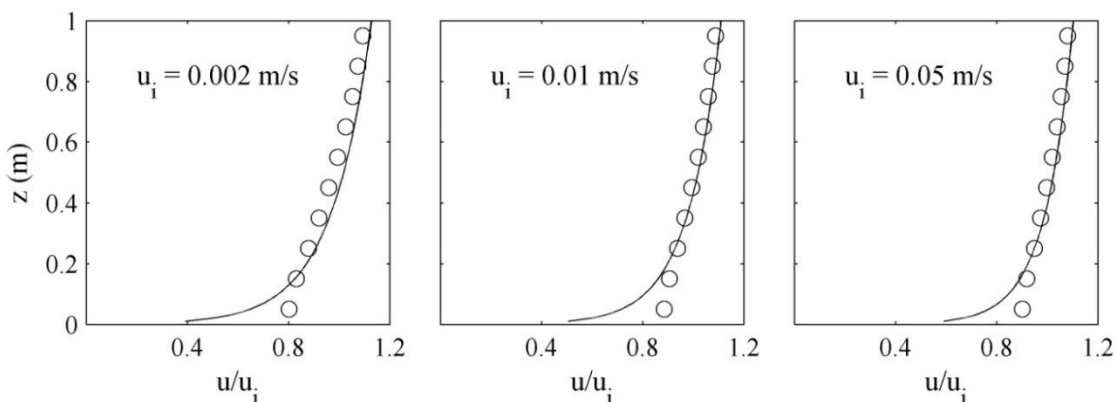


Figure B.4. Comparison of FLOW3D results (o) and the analytical solution (-) for the velocity profile in fully turbulent channel flow. Velocities are normalized by the constant incoming velocity (u_i), and sampled at the center of a 4 km-long basin.

B.3.2. Wind Stress

Wind forcing was shown to be the main source of turbulent kinetic energy in the estuary after closure (Chapter 5), and has been studied extensively in similar systems (Csanady, 1973; Imberger & Parker, 1985; Stevens & Lawrence, 1997; Winant, 2010). In this special case, the vertical velocity profile comprises two separate parts (Figure B.5), a region with velocities in the direction of the wind at the surface and a slower return flow oriented in the opposite direction at depth.

The capacity of the model to reproduce these features is tested using a simple case of wind blowing over an enclosed freshwater basin. Although no analytical solutions exist for this case, the approaches of Tsuruya et al. (1983) and Mathieu et al. (2002) provide approximate solutions.

Tsuruya et al. (1983) combine a Law-of-the-Wall formulation for both the surface and bottom of the channel while Mathieu et al. (2002) provide a solution which assumes uniform eddy viscosity. The latter is used only for qualitative comparison, since several studies have shown that eddy viscosity varies with depth (e.g. Nezu & Nakagawa, 1993). The constructed domain consists of a 4 km - long open-surface channel which has a uniform depth of two meters (Figure B.5). This depth is intended to represent the thickness of the surface freshwater layer during inlet closure (see Appendix C). The same density and bottom roughness conditions are applied here as for Section B.3.1. Cells are 100 m long in the horizontal and 10 cm long in the vertical directions. Wind speeds were varied from 4 to 16 m s⁻¹ to cover the range of low and high winds observed near the estuary at BML.

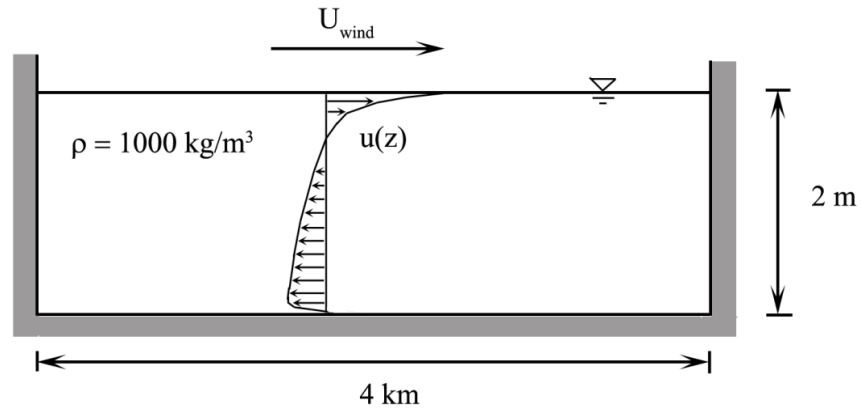


Figure B.5. Model domain for test of wind-driven velocity profile in a freshwater basin.

Theoretical Basis

We first describe the method by Mathieu et al., (2002) which assumes a constant eddy viscosity across the water column depth. We estimate the shear stress applied by the wind to the water surface after Kundu & Cohen (2002):

$$\tau_{wind} = \rho C_D U_{10}^2 \quad (\text{B.8})$$

where ρ is the density of air, C_D is the surface drag coefficient and U_{10} is the wind speed measured ten meters above the water surface. C_D was estimated from the method of Large and Pond (1980). A representative eddy viscosity was obtained by averaging the approximation of Nezu and Nakagawa (1993; Eq. 6.16) in the vertical. The formulation of Mathieu et al., 2002 then gives:

$$u(z) = \frac{\tau_{wind} H}{\rho \nu} \left(\frac{\alpha}{2} \sigma^2 + \sigma(1 - \alpha) \right) \quad (\text{B.9})$$

$$\alpha(x, z) = \frac{\rho g H \frac{\partial \eta}{\partial x}}{\tau_{wind}} \quad (\text{B.10})$$

where σ is the normalized depth above the bed and $\partial \eta / \partial x$ is the slope of the water surface caused by the applied wind stress, which we solve for after Winant (2010) in Section B.4.1. Eq. B.9 is based on the solution of a simplified momentum equation by applying a no-slip boundary condition at the bottom and the kinematic boundary condition at the water surface.

The method by Tsuruya et al. (1983) is simpler to apply and does not explicitly include the eddy viscosity. As discussed above, it describes the velocity response to winds as a combination of a Law-of-the-Wall solution at the bottom and surface boundaries:

$$u(z) = \left(\frac{u_{*s}}{\kappa} \right) \ln \left(\frac{z_{0,s} + H}{z_{0,s} - z} \right) - \left(\frac{u_{*b}}{\kappa} \right) \ln \left(\frac{z_{0,b} + H + z}{z_{0,b}} \right) \quad (\text{B.11})$$

where z_0 is a roughness height and all other variables are as defined above. The subscripts "s" and "b" denote the surface and bottom, respectively. The surface roughness height is a function of wave height (Tsuruya et al., 1983). It did not affect the solution very much, except for large wave heights, which were not present for the RRE. Coarse sand was again used to characterize bottom roughness. The shear velocity at the surface, u_{*s} , was estimated using Eq. B.2. The shear velocity, u_{*b} , becomes an enforcing condition for mass conservation. Since the wind acts over a closed basin, the net flow past a given point in the basin must be zero. After specifying the other variables, $u(z)$ is solved by adjusting u_{*b} iteratively until this condition is met.

Modeled Wind Stress Response

For a uniform vertical resolution of 10 cm, the model matches the result of Tsuruya et al. (1983) well, but decreases in accuracy for higher wind speeds (Figure B.6; Table B.1). At the surface, the modeled velocity increases linearly, fitting the solution of Mathieu et al. (2002) more closely than the logarithmic increase given by Tsuruya et al. (1983). This under-prediction of the latter method increases with wind speed but is always limited to the upper ten percent of the water column, which is analogous to the rigid-boundary result found in Section B.3.1. Due to the quasi-linear shape of the modeled velocity profile at the surface, this under-prediction leads to a slight over-prediction of velocities in the middle of the water column. However, in all cases the model predicts the bottom return-flow very well. Overall, the RMSE is small, ranging from 0.28 to 1.18 cm s⁻¹. These tests were also performed using the $k-\varepsilon$ and $k-\varepsilon$ RNG turbulence models, but this resulted in only slight improvements at a much higher computational cost

Table B.1. Agreement between modeled wind-driven profile and empirical solutions.

Run	Horizontal resolution (m)	Vertical resolution (m)		Wind speed (m/s)	RMSE (cm/s)	Run time (s)
		Lower 90%	Upper 10%			
1	100	0.10	0.10	4	0.28	31
2	100	0.10	0.10	8	0.57	35
3	100	0.10	0.10	12	0.90	38
4	100	0.10	0.10	16	1.18	41
5	100	0.10	0.02	4	0.23	60
6	100	0.10	0.02	8	0.46	62
7	100	0.10	0.02	12	0.70	78
8	100	0.10	0.02	16	0.92	77

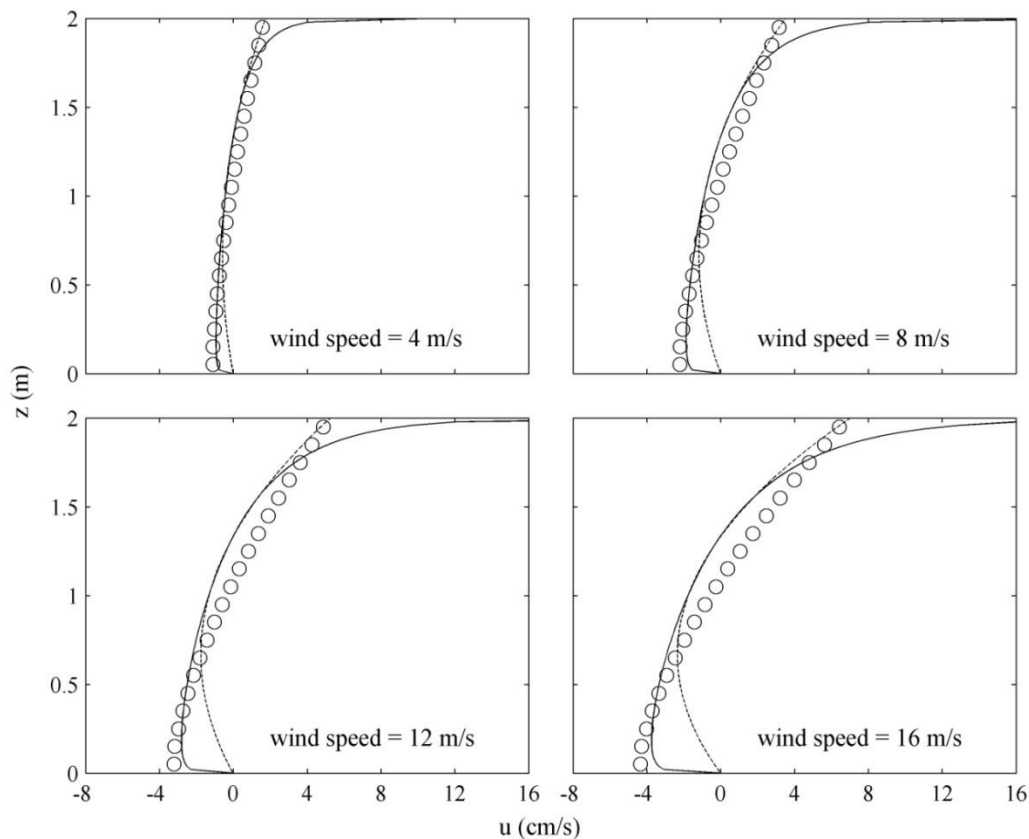


Figure B.6. Modeled velocity profiles (o) compared with solutions of Mathieu et al. (-) and Tsuruya et al. (--), for wind blowing over a 4 km - long basin with water of uniform density. Vertical cell resolution is 10 cm.

B.3.3. Density interface displacement

The effects of wind stress on a stratified basin were tested using a similar setup as Section B.3.2, but with a two-layer density profile. For this simulation, a 4 km long basin is used with a uniform 5 m depth, having an open surface and a roughness corresponding to coarse sand at the bottom (Fig. B.7). The water column is sharply stratified, with a 2 m-thick layer at the surface resting atop a 3 m layer at the bottom. The

upper and lower layers have densities of 1000 kg m^{-3} and 1026 kg m^{-3} , respectively, representing freshwater and tidal saltwater. Winds are varied from 4 to 14 m s^{-1} . The value of 14 m s^{-1} was chosen as an upper bound because it generates the critical Wedderburn value required for the bottom layer to upwell to the surface for this particular setup (see Shintani et al., 2010).

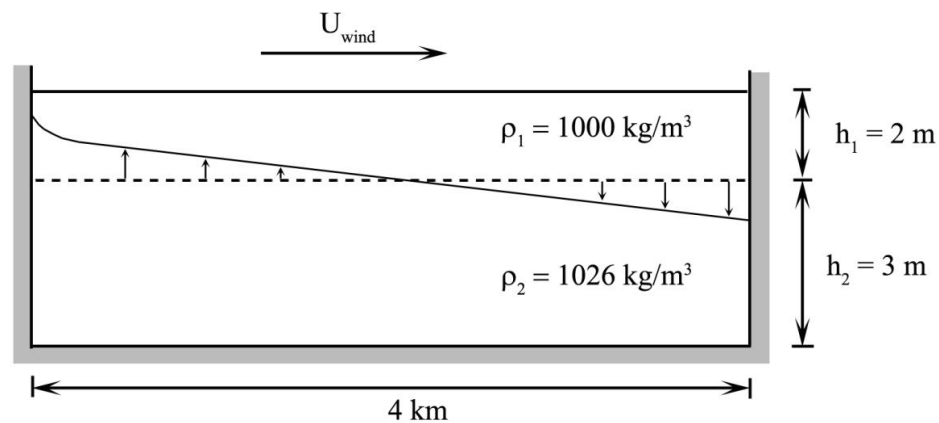


Figure B.7. Model domain for test of interface tilt during winds.

Theoretical Basis

The shape of the interface can be predicted using a mass balance and a parameterization of the basin geometry and wind stress known as the Wedderburn Number (Thompson and Imberger, 1980):

$$W = \frac{g' h_1^2}{u_*^2 L} \quad (\text{B.12})$$

where h_1 is the depth of the upper layer, L is the length of the basin, u_* is the shear velocity caused by winds at the surface and g' is the reduced gravity, defined as:

$$g' = g \frac{(\rho_2 - \rho_1)}{\rho_1} \quad (\text{B.13})$$

The shear velocity is defined as in Section B.3.1. To find the shape of the deformed interface during steady winds, the maximum displacement at the upwind edge of the basin, $H_1(0)$, is first obtained from the approximation of Shintani et al. (2010):

$$H_1(0) = h_1 - h_1 \left\{ \frac{2}{\pi} \tan^{-1} \left[\left(\frac{9}{8} W - 1 \right)^{0.81} \right] \right\}^{0.57} \quad (\text{B.14})$$

Using the displacement at the side of the basin, the position of the interface is approximated at each successive distance away from the edge. This requires solving the following system of equations iteratively:

$$H_1(x) = \sqrt{2 \frac{u_*^2}{g'} x + H_1(0)} \quad (\text{B.15})$$

$$Lh_1 = \int_0^L H_1(x) dx \quad (\text{B.16})$$

After solving for interface displacement at each location, x , using Eq. B.15, the total mass of the upper layer is calculated with Eq. B.16. The total mass of the upper layer is a constant, so the initial value (before winds have had an effect on the interface) can be used as a check on the calculation. The two equations are solved iteratively by adjusting the value of dx .

The model performed very well for all wind speeds used, as summarized in Figure B.8 and Table B.2. The RMSE of the modeled interface positions ranges from 5-11 cm (1-2% of total depth) and does not increase with wind speed. The greatest errors are at the outermost edges of the basin, where the interface is displaced the most, and are on the

order of 5 - 15 cm. The model results are particularly encouraging for the case with the highest winds (Fig. B.8: lower right panel). In this case it accurately reproduces the critical upwelling condition, causing the bottom layer to nearly touch the surface.

Table B.2. Agreement between modeled interface displacement and analytical solution

Run	Horizontal resolution (m)	Vertical resolution (m)	Wind speed (m/s)	Wedderburn No.	RMSE (m)
1	100	0.10	4	11.2	0.05
2	100	0.10	8	2.8	0.09
3	100	0.10	12	1.2	0.03
4	100	0.10	14	0.9	0.11

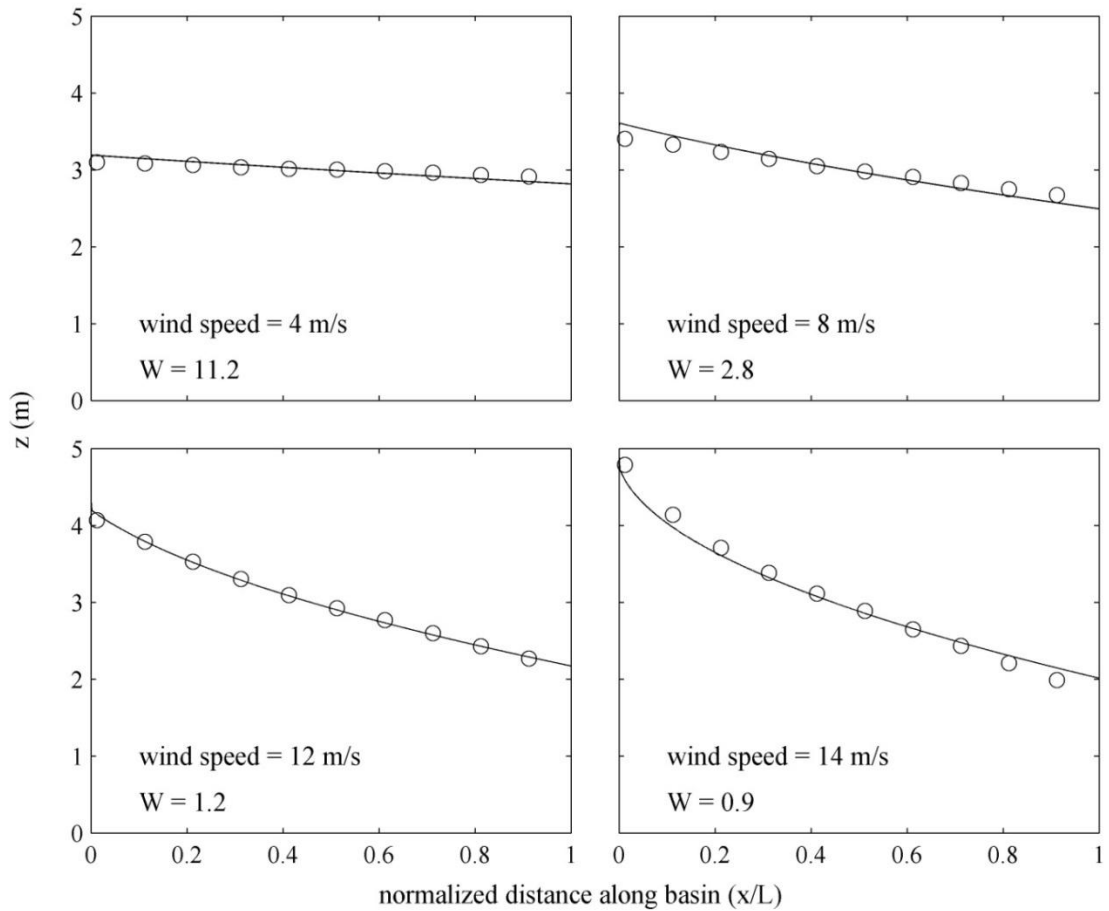


Figure B.8. Modeled (o) and analytical (-) solution for the displacement of the density interface during wind speeds ranging from 4 to 14 m s^{-1} . The Wedderburn number (W) is also indicated.

B.4. Comparison Against Observations

The model was used to simulate parts of closure events E1 and E3, to allow comparison of modeled and observed flow structure and density field evolution in the outer estuary. E1 was chosen as a study case for the density field evolution because it encompassed several severe wind events, a high-flow event following the release of a temporary summer dam, and a large change in the density field in the outer estuary. E3 was chosen to study the flow structure in the outer estuary, because local winds appeared to follow a clear diurnal oscillation in strength. Conditions during these events are illustrated in Figures C.3 and C.5, respectively.

B.4.1. Approximating Surface Wind Stress

Since BML wind speed and direction are measured 13 km away from the site, a more reliable estimate of wind forcing is needed for the estuary. To account for this we chose to use the measurements of the water level at two points in the estuary as a proxy to infer wind speed and direction (landward or seaward). Although this only provides a coarse approximation of wind speed, it is a good indicator of the direction (whether landward or seaward), which is important for accurately representing the flow-structure in the estuary. The water level records taken at the Mouth (site A1) and Heron Rookery (station B3) stations are used to analyze the surface tilt (Fig. B.9). First, the hourly water level records were each de-trended by subtracting a centered running 25-hour mean from each hourly measurement. Next, the difference between the two water levels at each hour

was divided by the distance between stations to produce an approximate mean surface tilt of the estuary:

$$\frac{\overline{\partial\eta}}{\partial x} \sim \frac{(\eta_{B3} - \eta_{A1})}{(x_{B3} - x_{A1})} \quad (\text{B.17})$$

where η is the water surface elevation and x is the along-stream distance upstream of the inlet. The wind stress is found from the surface slope using the formulation of Winant (2010), who provides a solution for a rectangular basin:

$$\frac{\partial\eta}{\partial x} = \frac{\partial\eta^*}{\partial x^*} \frac{\tau}{\rho g H} \quad (\text{B.18})$$

where τ is the surface wind stress, ρ is the mean density of the estuary, g is gravitational acceleration and the term $\partial\eta^*/\partial x^*$ is a dimensionless surface slope defined by the cross-channel geometry, defined as:

$$\frac{\partial\eta^*}{\partial x^*} = \frac{3 \int_{-1}^1 h^2 dy}{2 \int_{-1}^1 h^3 dy} \quad (\text{B.19})$$

Here, h is a dimensionless depth that varies in the lateral direction (y) across the channel. For a rectangular channel cross section, $h = 1$ for all y , giving $\partial\eta^*/\partial x^* = 1$. Using the average depth and density between stations A1 and B3, and inserting the solution for Eq. (B.19) into Eq. (B.18) provides a time series of the surface wind stress. This is then transferred to surface wind speed with Eq. (B.8).

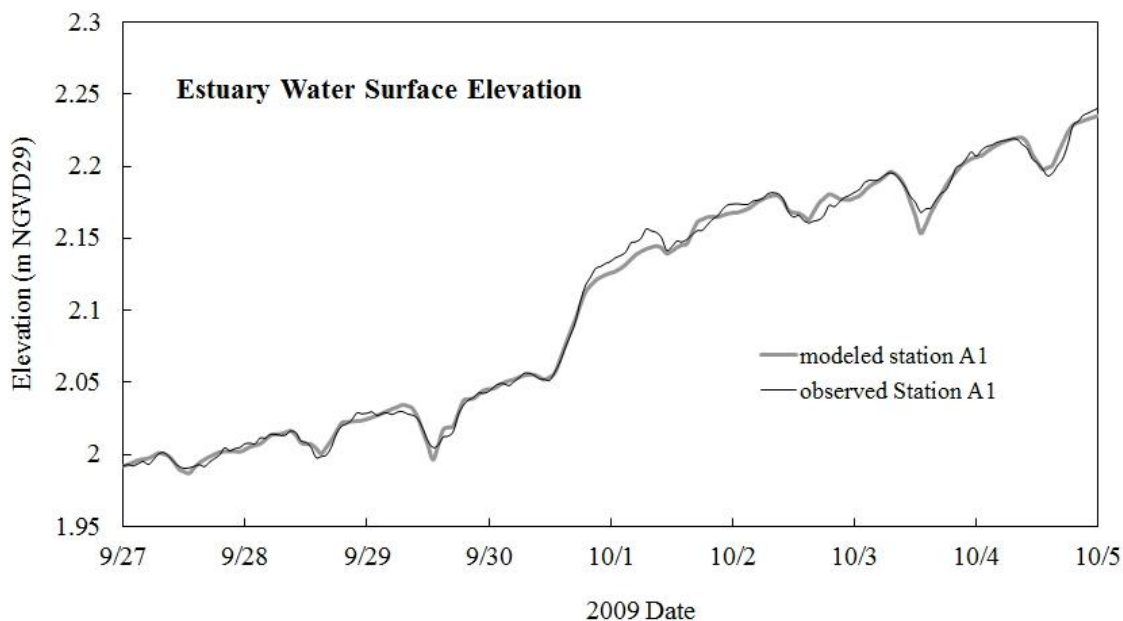


Figure B.9. Modeled (thick grey line) and observed (narrow black line) water surface elevation near the mouth (Station A1) of the RRE during closure event E1.

B.4.2. Flow Structure Comparison

The model was run for the 36-hour period from 28 September 0:00 to 29 September 8:00, 2010. Water level records indicate that the winds followed a diurnal pattern, with landward-directed winds active on the afternoon of 28 September, peaking at approximately 3 m s^{-1} between the hours of 12:00 and 16:00, and dying down at night, leading into a negligible surface tilt ($U \sim 0$) by the early morning hours of 29 September. During the afternoon of 28 September, the velocity near the surface was oriented in the direction of the wind, with a strong seaward-directed return flow developing beneath this. As winds died down after 16:00, the flow structure became dominated by this seaward-directed flow and a landward-directed flow that began to develop beneath it.

As mentioned earlier, the lack of direct wind measurements and the simplifications inherent in the model prevent any complete comparison between modeled and observed velocities resulting from the wind stress. To account for this, the comparison focuses on the dimensionless magnitude of the velocities, emphasizing the shape of the velocity profile rather than the magnitudes.

The run was initialized using the CTD observations to characterize the density stratification and the water surface slope to characterize winds. The observed density field and water level on the night of 27 September was used as a starting point. A time series of wind was then constructed to match the observed change in the water level slope along the estuary during this time following the methodology shown above.

The modeled wind response generally agrees with the data, as summarized in Figure B.10. Correlation (r) values listed in Table B.3 are mostly above 0.7 and have p -values below 0.01, indicating a good fit and high statistical significance. Qualitatively, the model fits the overall shape of the velocity profile well, but misses some of the eccentricities which probably result from the complexity of the real bathymetry and wind conditions. For example, on 28 September 16:00, the model produces the same velocity extrema as the observations, but displaces them slightly, which led to a lower correlation. Despite these small discrepancies the model appears to reproduce the complex flow structure well.

Table B.3. Correlation between modeled and observed wind speeds at Station A4

Date	Time	Wind speed (m/s)	Correlation Coefficient	p-value
9/28/2010	8:00	1	0.88	0.0001
9/28/2010	12:00	3	0.74	0.004
9/28/2010	16:00	3	0.41	0.17
9/28/2010	20:00	2	0.73	0.005
9/29/2010	0:00	0.4	0.77	0.002
9/29/2010	4:00	0.2	0.74	0.004

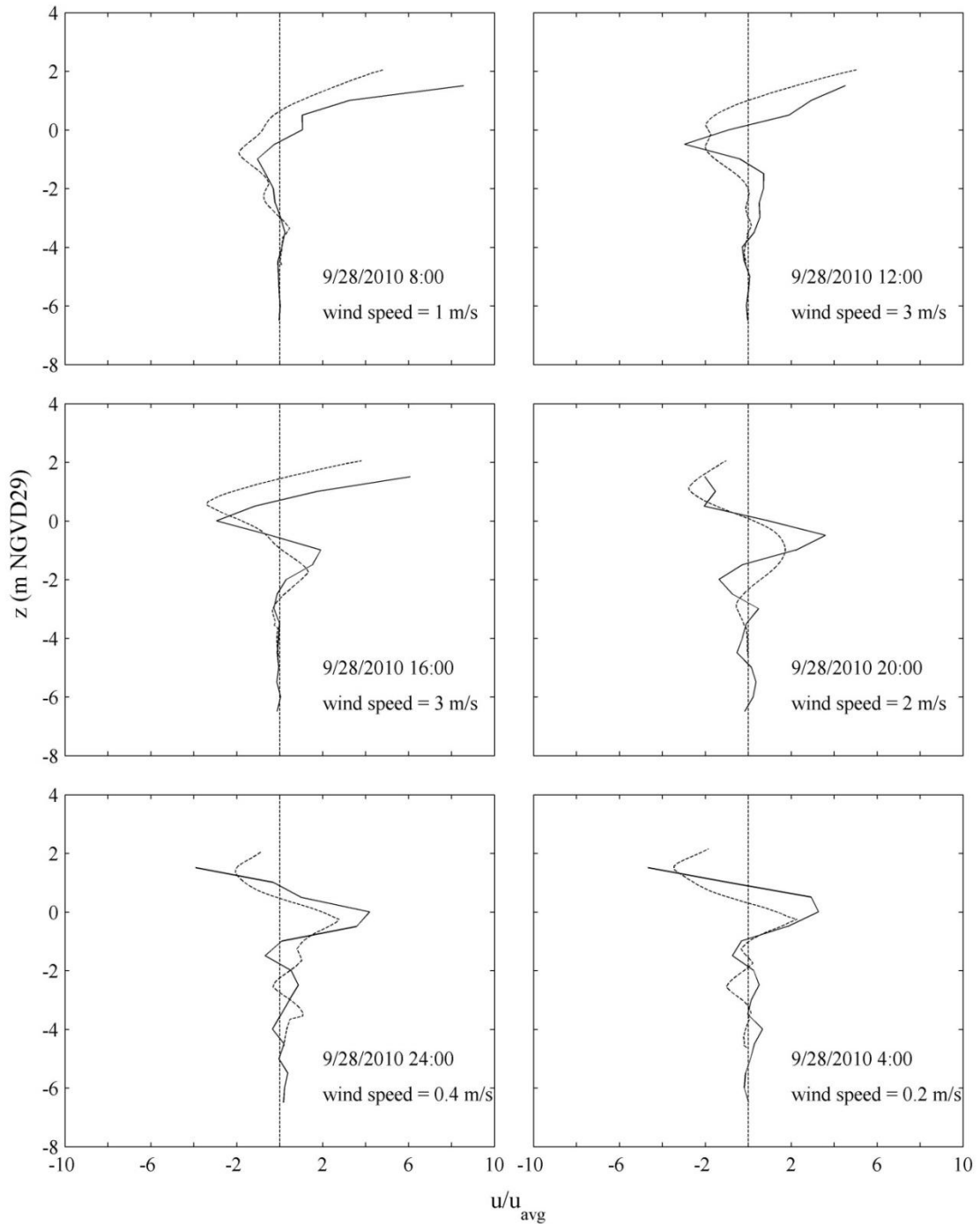


Figure B.10. Modeled (--) and observed (-) streamwise velocity profile at Station A4 (Fig. 3.2) resulting from winds on 28 September 2010. Velocities are normalized by the mean magnitude of velocity in the water column.

B.4.3. Comparison with Observed Density Field Evolution

The model was also used to simulate event E1 from 17:00 on 26 September until 15:00 on 5 October, 2009. Strong diurnal winds were present during this ten day period, and inflows to the estuary temporarily spiked from 3 to 9 m³s⁻¹. Both were visible in the records of the water surface elevation (Fig. B.9). The winds are apparent from a diurnal drop in the water surface in the mouth, and the temporary flood event caused the depth of the estuary to increase by almost 10 cm in less than 8 hours on the evening of 30 September. Both aspects were well-approximated by the model, as shown in Figure B.9. The impact of these events on the density field is shown in Figures C.12-13.

The largest change in the density structure occurred near the mouth, where the high winds caused repeated upwelling, which amplified diapycnal mixing across the pycnocline. The model domain is shown in Figure B.11, indicating the representation of the upwelling density interface. Model results at the mouth for different points during the ten day simulation period are shown in Figure B.12. The model captured the evolution of the interface and the lower profile well. However, the upper 2 m of the profile differed from the observations by roughly 1 kg m⁻³ after the initial time step. The difference does not show any consistent growth or decay, which indicates that it is probably not introduced by model error. This was true of all the runs, and can be explained by our exclusion up to this point of the effects of temperature. Figure C.21 shows that the upper water column cooled over the last ten days of the closure event. Using the Equation of State (UNESCO, 1981) with the observed change in temperatures, the change in density

due to temperature in the upper water column was found to match the discrepancy between the model results and observations.

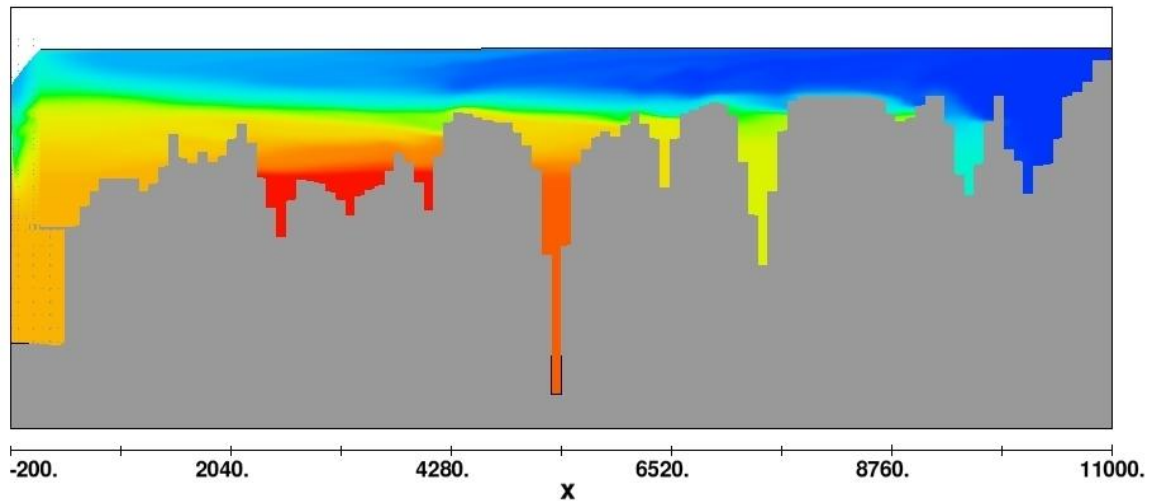


Figure B.11. Model domain, showing wind-induced upwelling of the interface at the mouth (left). The porous beach is at left, shown by the drop in water surface elevation indicating the sloping water table from the estuary to the ocean. Higher density water is indicated by warmer colors. Blue represents $\rho = 998 \text{ kg m}^{-3}$.

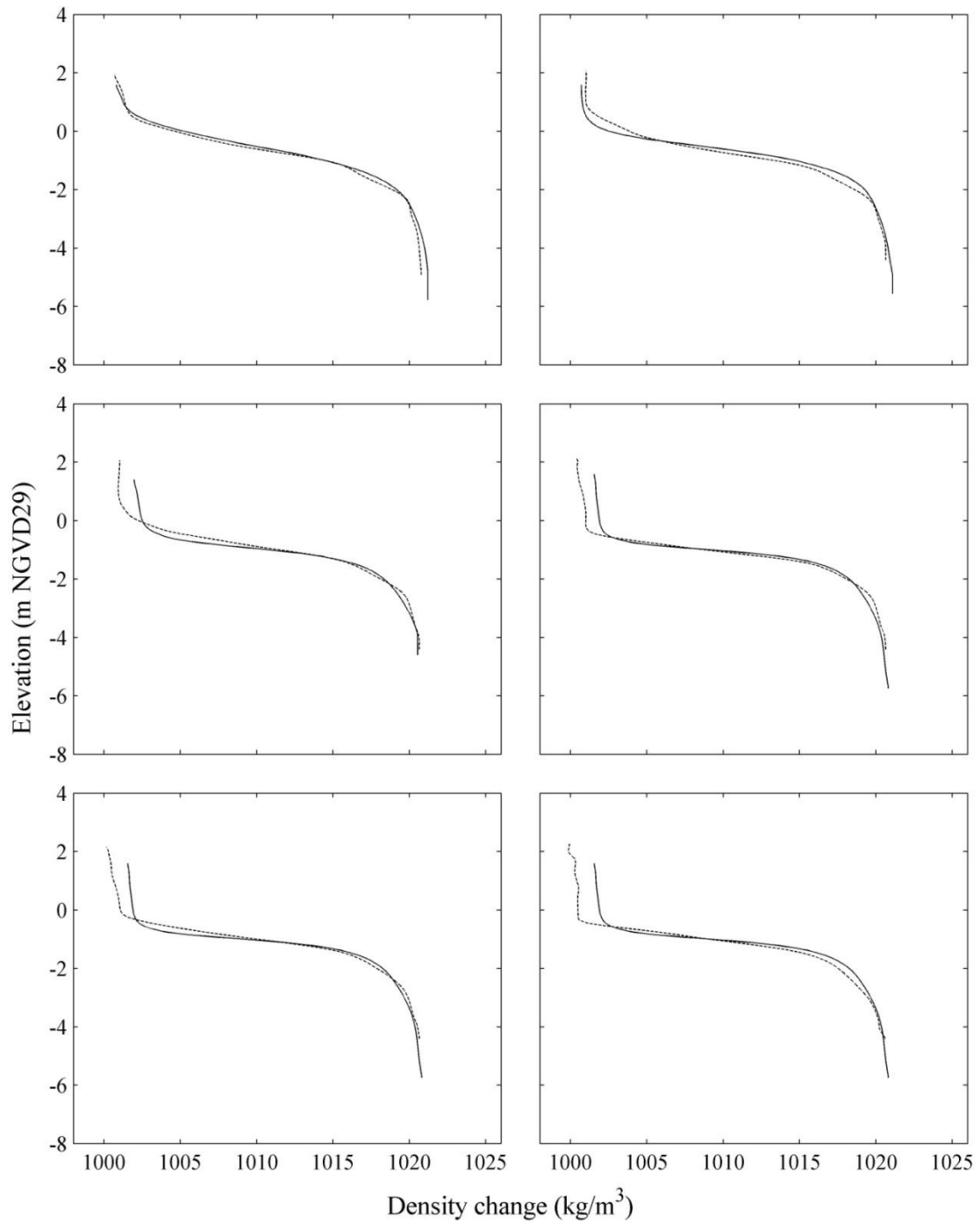


Figure B.12. Modeled (--) and observed (-) density profiles at the Mouth in the final 10 days of the 2009 closure event.

Table B.4 summarizes the RMSE of the modeled density profiles at several sites. Apart from the last day of the closure event, the RMSE appears to fluctuate around a mean value during most of the event. The last day produced the highest error at most sites, most of which is accounted for in the upper 2 m of the water column. We attribute this to the exclusion of temperature from the model and from the fact that data taken on this date were taken during the afternoon, when temperatures are at their peak, whereas the others were taken during the morning. Apart from this, most of the results are in good agreement with the observations.

Table B.4. RMSE (kg m^{-3}) of modeled density profiles during the 2009 closure event.

2009 Day	Mouth (Station A1)	Paddy's Rock (Station A4)	Sheephouse Creek (Station B1)	Heron Rookery (Station B3)	Freezeout Creek (Station B5)
Sep 26	0.45	1.17	1.47	0.78	0.87
Sep 28	0.85	--	0.74	0.90	0.82
Sep 30	0.86	2.06	1.30	0.86	0.95
Oct 1	0.67	--	1.70	0.89	1.04
Oct 2	0.81	1.55	1.49	0.82	1.49
Oct 5	1.02	2.60	2.03	1.57	1.05

Appendix C. Boat-Based Field Data

This section summarizes boat-based field data collected in the RRE during the summer and fall seasons in 2009 and 2010. Data were collected by dropping a continuously-sampling CTD profiler through the water to create a vertical profile of scalar quantities. Collection methods are discussed in more detail in Chapter 3, where reference is also given to the other measurements taken in the estuary at this time. These data complement the existing SCWA sondes, which obtain continuous hourly time series of scalars from fixed positions, and are used to assess changes in key water quality parameters (e.g. temperature, dissolved oxygen, salinity) which affect summer rearing habitat for salmonids in the estuary.

In total, 70 sets of CTD profiles were collected during the 2009 and 2010 seasons. Most sets encompass the span from Stations A1 to B5, but in some cases hourly sets of profiles were taken from A1 to B2 in order to assess rapid change in estuary conditions during periods when the inlet was open. Aside from the limited number of sets taken during tidal conditions, measurements were focused toward opportunistic collection during periods of inlet closure. These were used to support the analyses in Chapters 5 and 6.

Figure C.1 provides an overview of the closure events studied in the 2009 season, which all occurred between the months of September and October. The majority of the measurements at this time focus on event E1 (Table 3.2), which was the longest closure event to occur in over 30 years. Figure C.2 summarizes the 2010 season, which encompassed a brief perched overflow condition in July and several closure events during

the fall months. Measurements ended after the first major rainfall event each year, because conditions became unsafe for small boat operation. Figures C.3-8 summarize the conditions observed during each of the six events included in this study (Table 3.2).

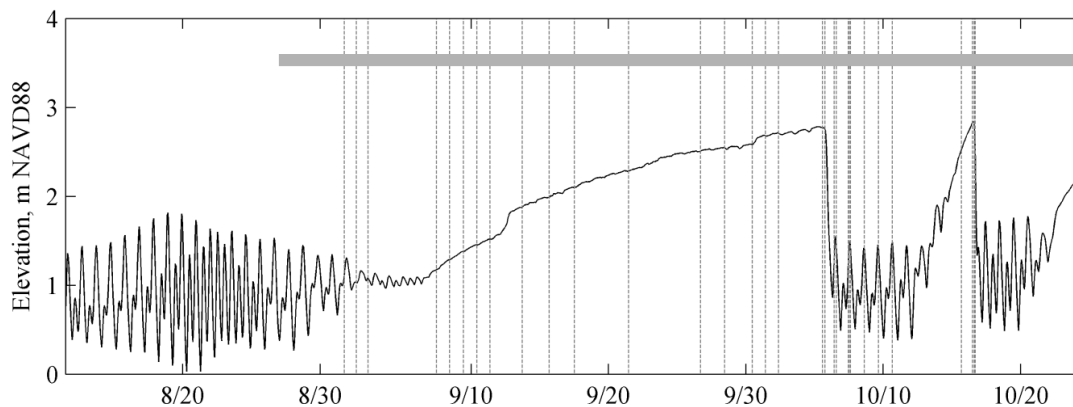


Figure C.1. Time series of water surface elevation measured near the RRE mouth during the 2009 field season. Vertical dashed lines represent times when CTD transects were taken in the estuary. The horizontal grey bar represents the period of the ADCP deployment.

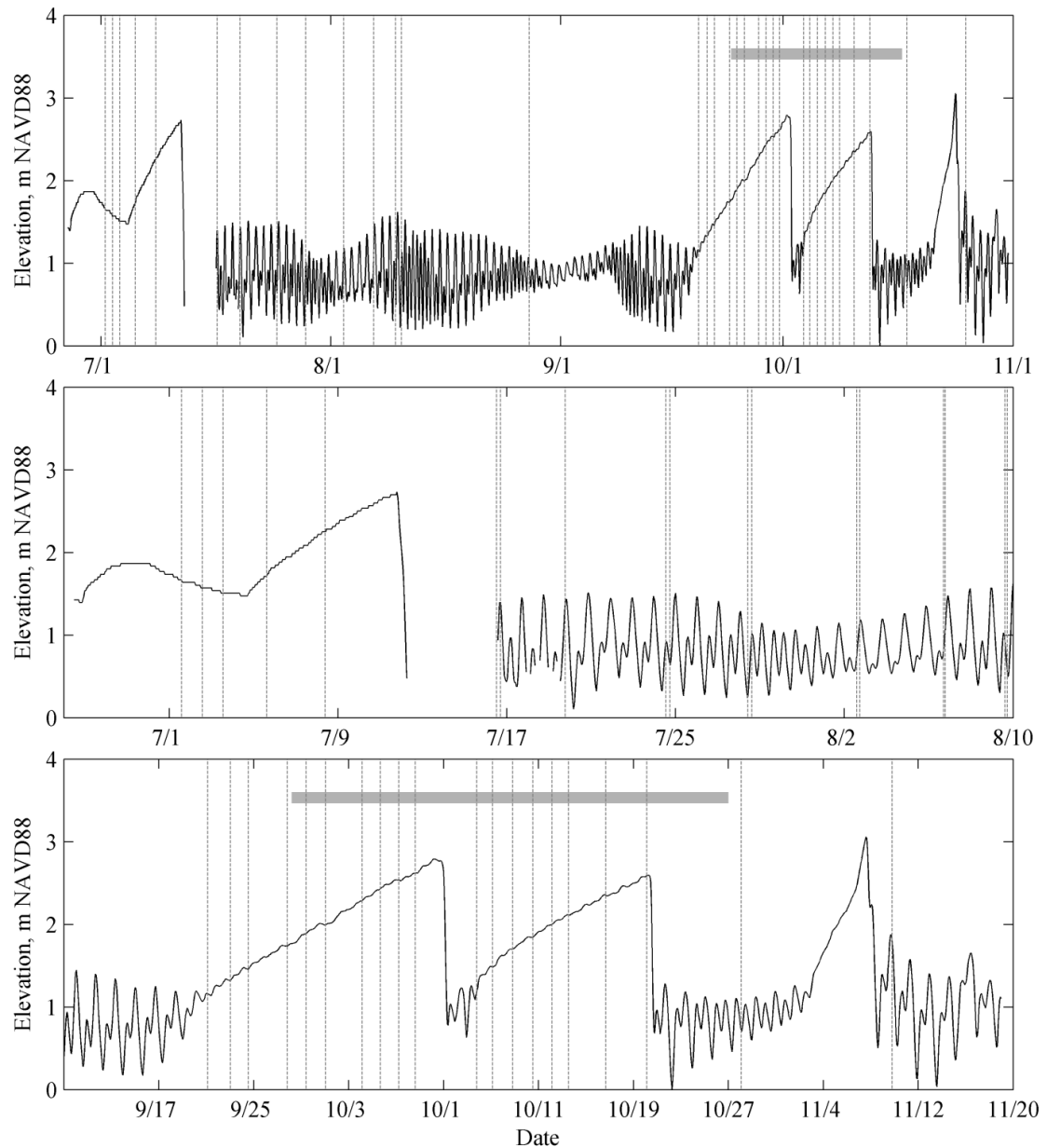


Figure C.2. (top) Time series of water surface elevation measured near the RRE mouth during the 2010 field season. Bottom panels are close-ups of the closure events E3-E6 (see Table 3.x). Vertical dashed lines represent times when CTD transects were taken in the estuary. The horizontal grey bar represents the periods of ADCP deployments.

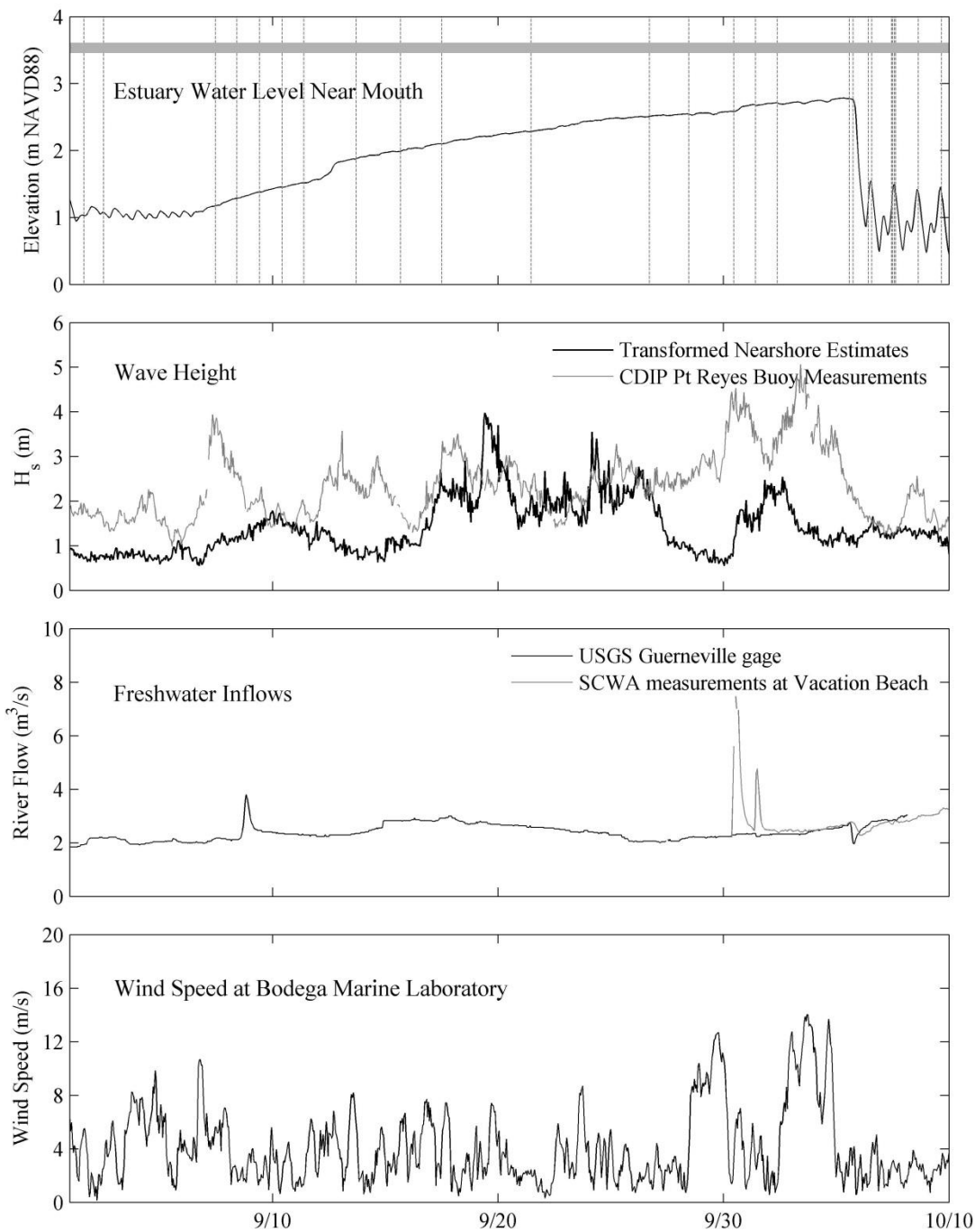


Figure C.3. Summary of (a) water levels, (b) offshore and nearshore waves, (c) freshwater inflows and (d) BML wind speed during closure event E1. Vertical dashed lines represent times when CTD transects were taken in the estuary. The horizontal grey bar represents periods of ADCP deployment.

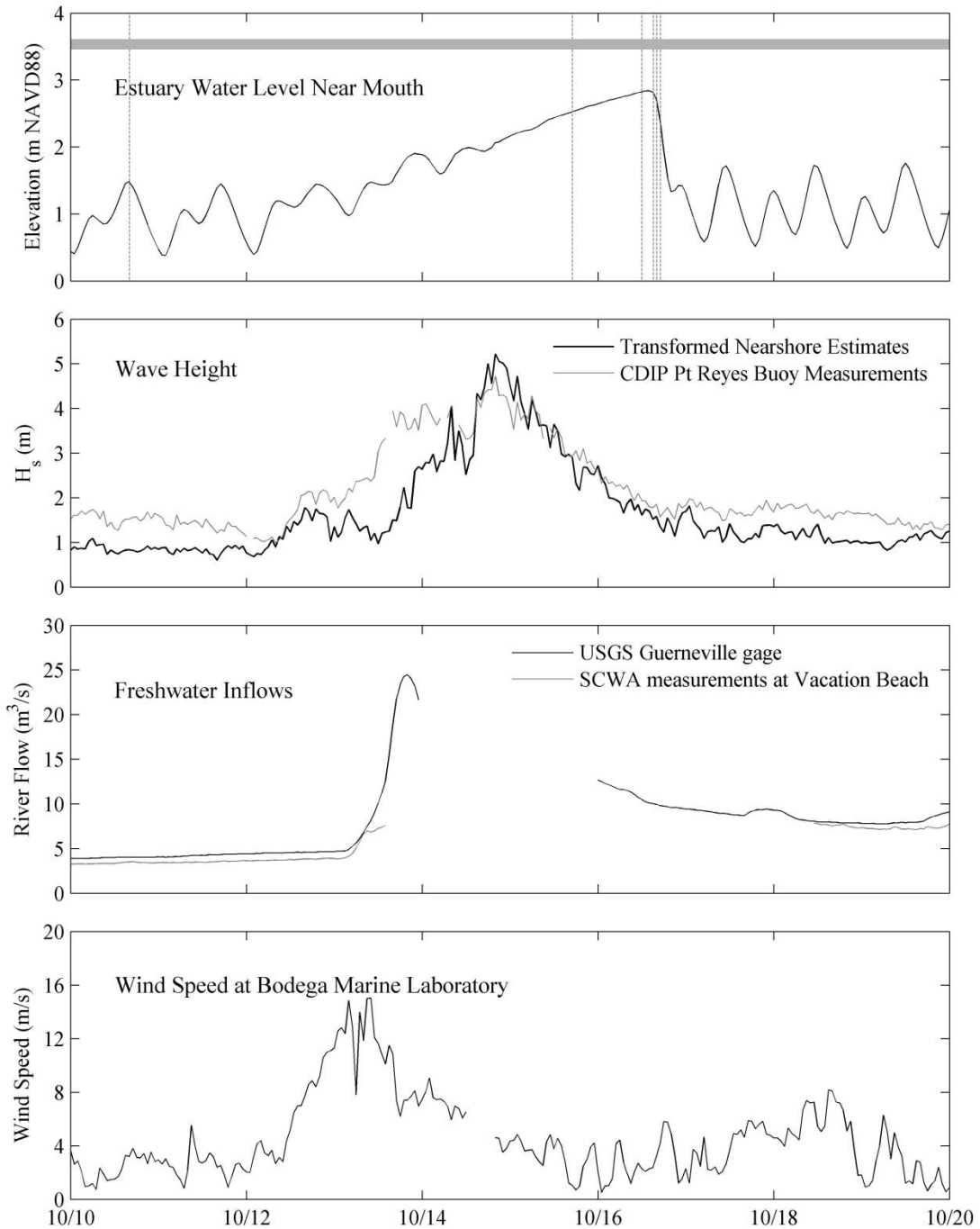


Figure C.4. Summary of (a) water levels, (b) offshore and nearshore waves, (c) freshwater inflows and (d) BML wind speed during closure event E2. Vertical dashed lines represent times when CTD transects were taken in the estuary. The horizontal grey bar represents periods of ADCP deployment.

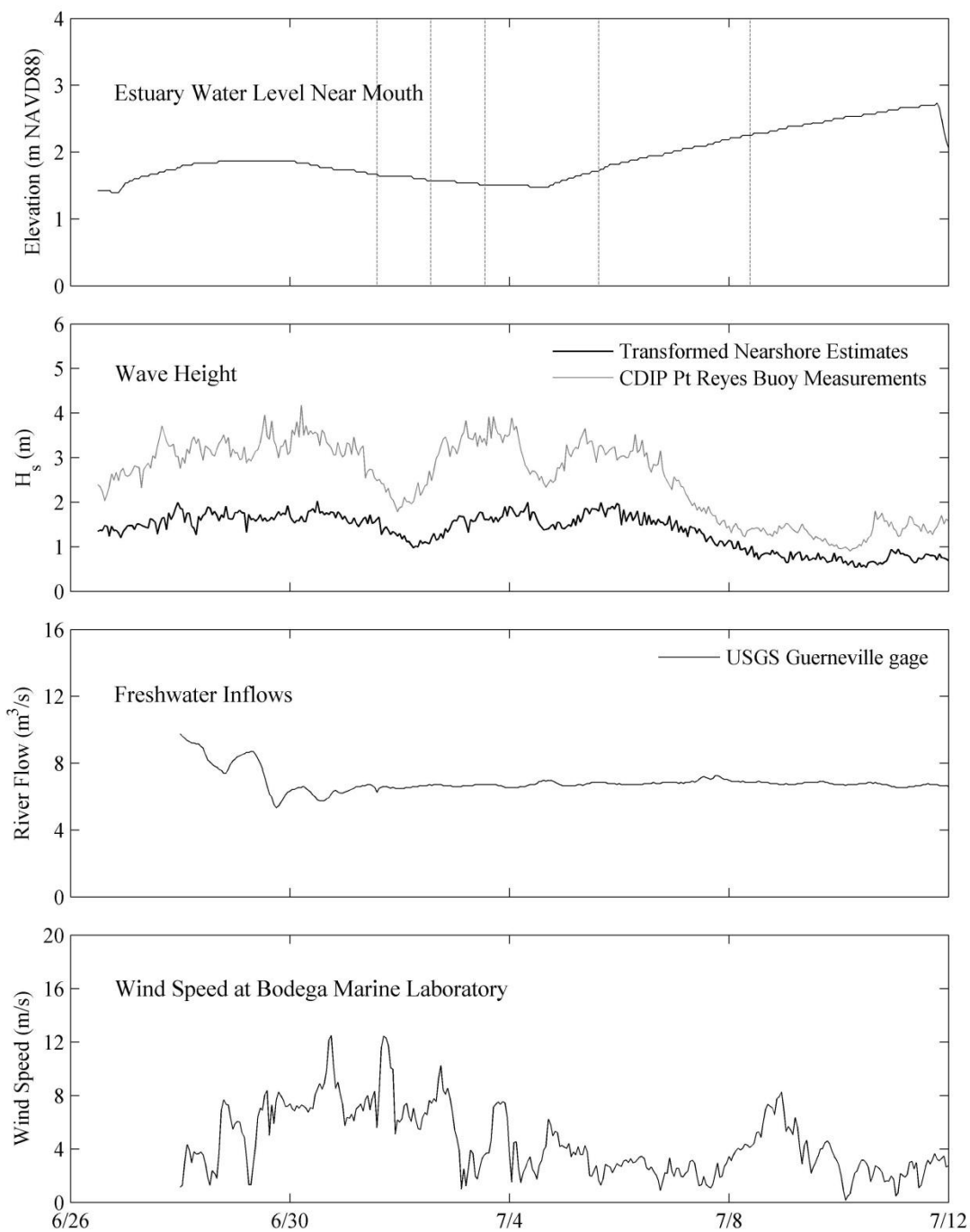


Figure C.5. Summary of (a) water levels, (b) offshore and nearshore waves, (c) freshwater inflows and (d) BML wind speed during closure event E3. Vertical dashed lines represent times when CTD transects were taken in the estuary.

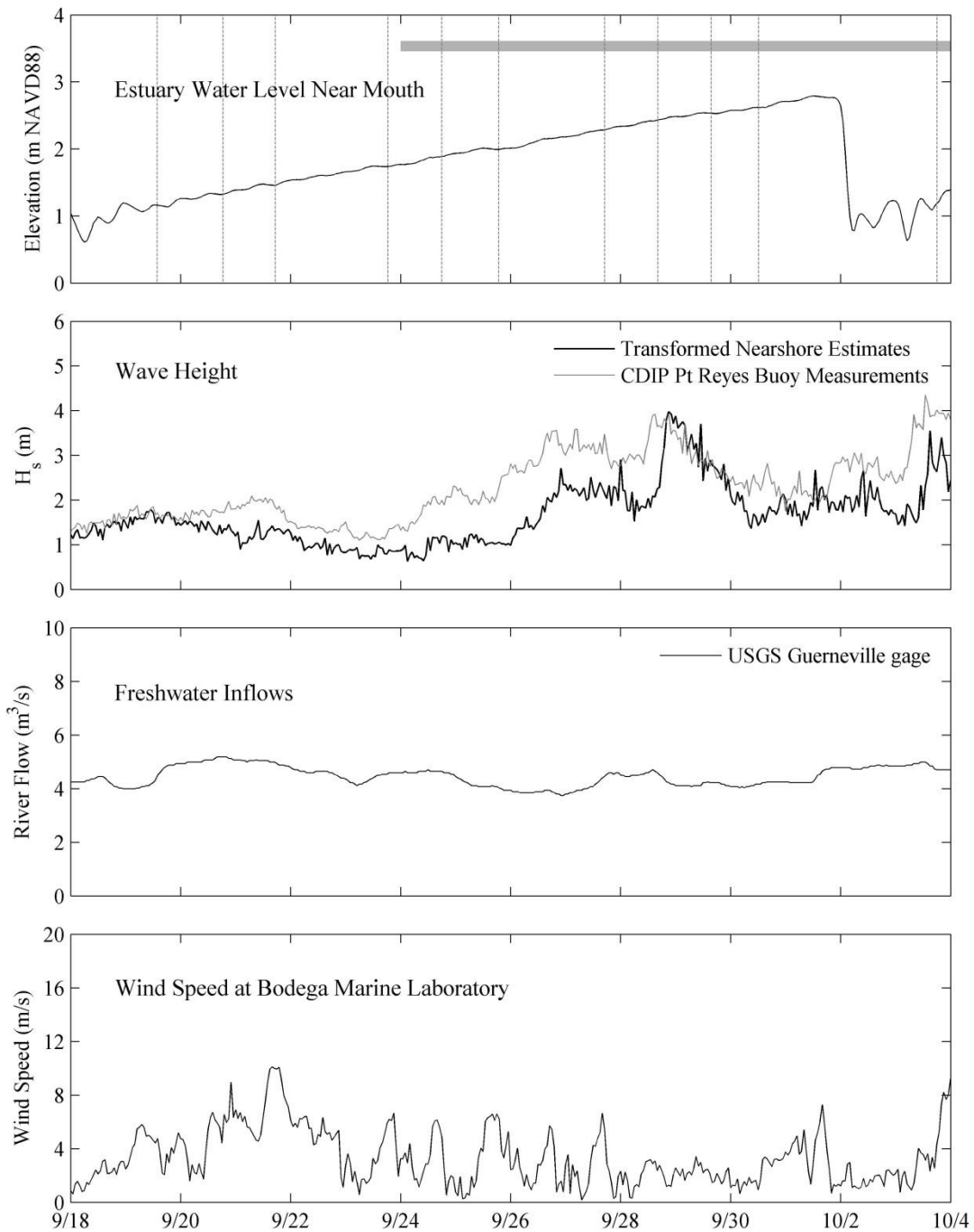


Figure C.6. Summary of (a) water levels, (b) offshore and nearshore waves, (c) freshwater inflows and (d) BML wind speed during closure event E4. Vertical dashed lines represent times when CTD transects were taken in the estuary. The horizontal grey bar represents periods of ADCP deployment.

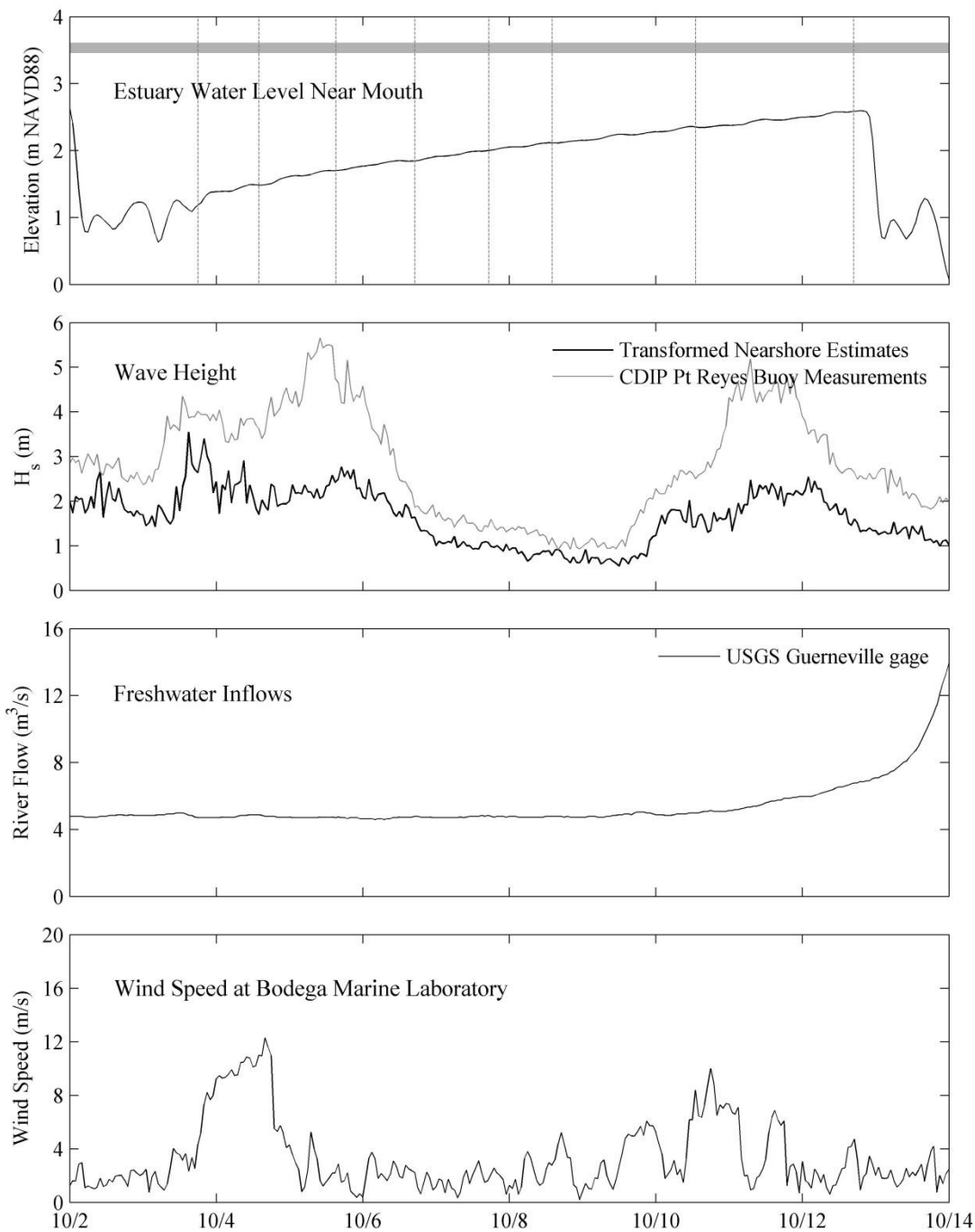


Figure C.7. Summary of (a) water levels, (b) offshore and nearshore waves, (c) freshwater inflows and (d) BML wind speed during closure event E5. Vertical dashed lines represent times when CTD transects were taken in the estuary. The horizontal grey bar represents periods of ADCP deployment.

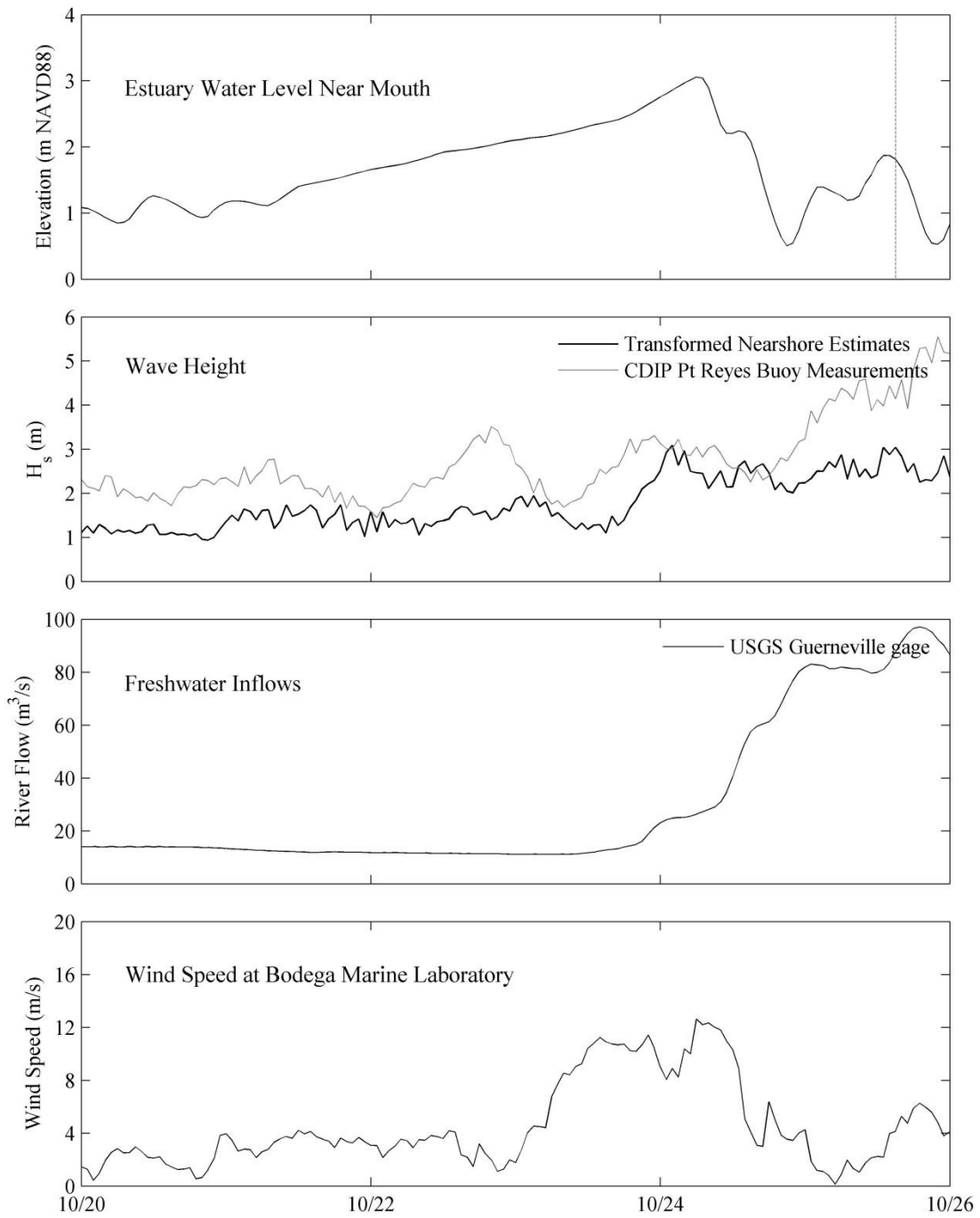


Figure C.8. Summary of (a) water levels, (b) offshore and nearshore waves, (c) freshwater inflows and (d) BML wind speed during closure event E6. Vertical dashed lines represent times when CTD transects were taken in the estuary.

C.1. Lagoon Scalar Fields in 2009

Figures C.9-31 summarize the 2D (x - and z -plane) scalar fields in the RRE during the 2009 season. Results are separated by scalar type: salinity (Figs. C.9-16), temperature (Figs. C.17-24) and dissolved oxygen (Figs. C.25-31). As discussed in Chapters 3 and 5, these estuary plots were created using a 2D nonlinear spline interpolation of the CTD profiles in Matlab ©. Each plot is indexed in Figure C.1 as a vertical dashed line to give context. Additional plots were created using CTD profiles of photosynthetically active radiation (PAR) and fluorescence. These are not shown here, as they were outside the scope of this study. They can be found at the website for the Bodega Ocean Observing Node (<http://bml.ucdavis.edu/boon>).

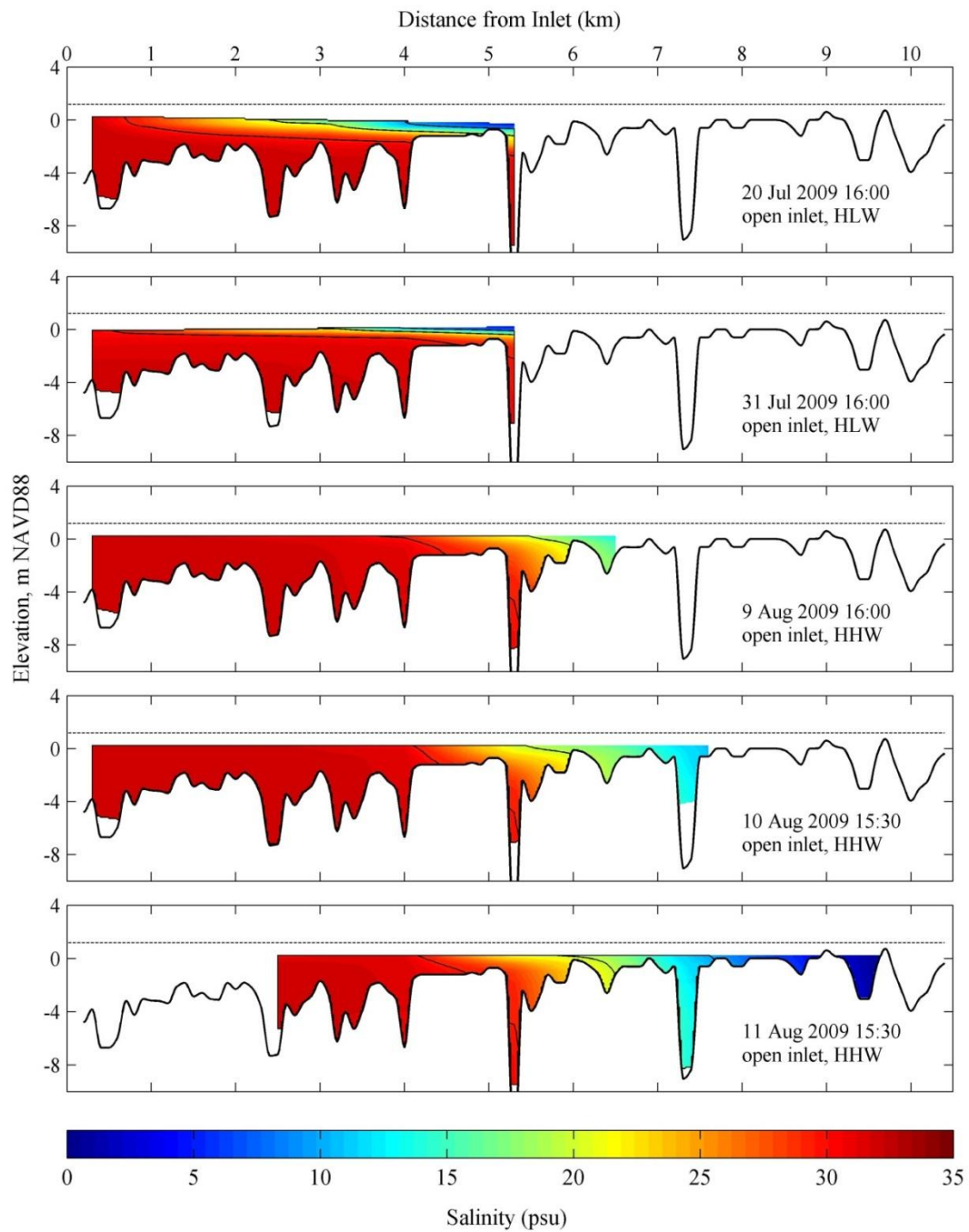


Figure C.9. 2D planar view of the estuary salinity interpolated from CTD transects from 20 July to 11 Aug 2009.

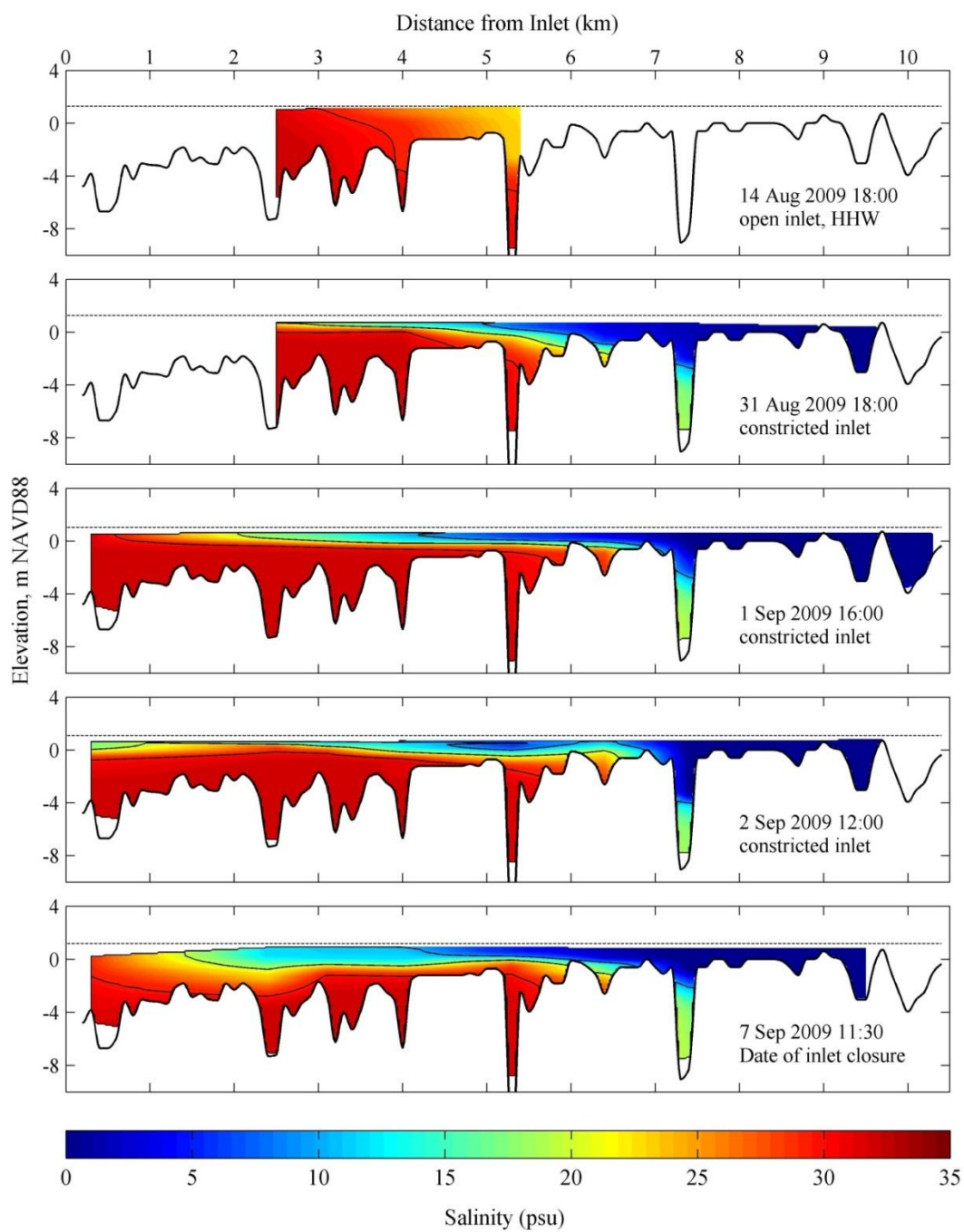


Figure C.10. 2D planar view of the estuary salinity interpolated from CTD transects from 14 Aug 2009 to 7 September 2009.

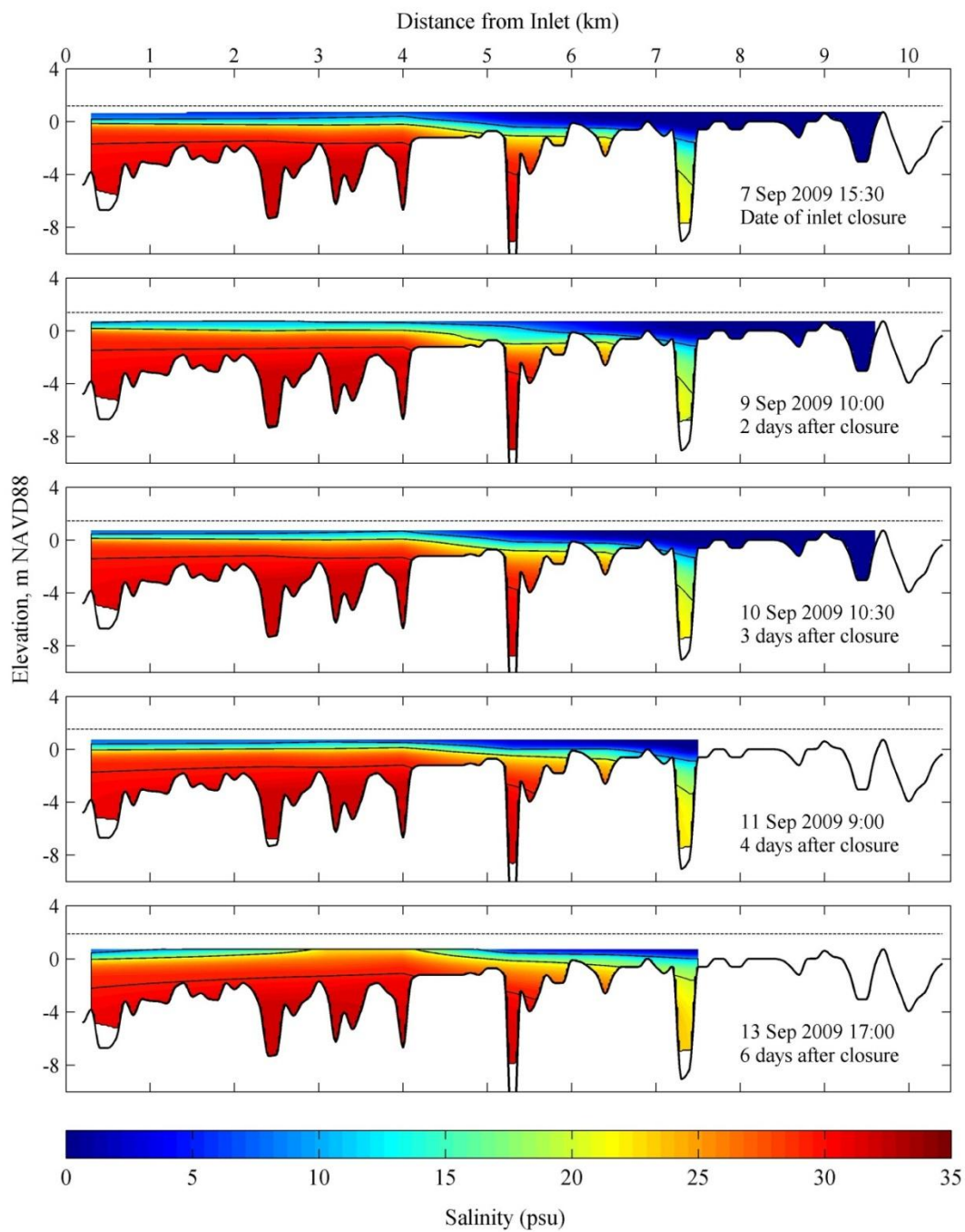


Figure C.11. 2D planar view of the estuary salinity interpolated from CTD transects from 7 September 2009 to 13 September 2009.

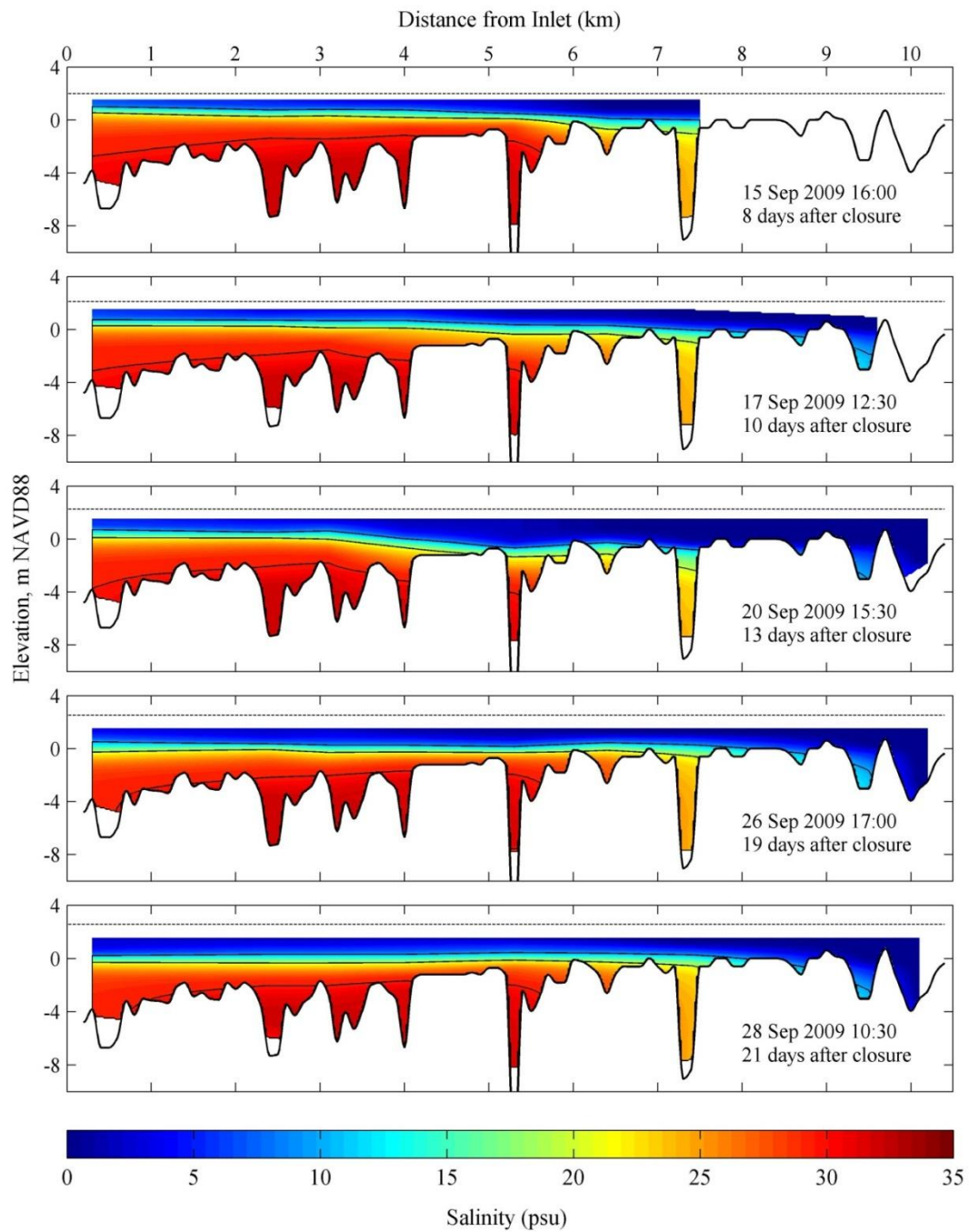


Figure C.12. 2D planar view of the estuary salinity interpolated from CTD transects from 15 September 2009 to 28 September 2009.

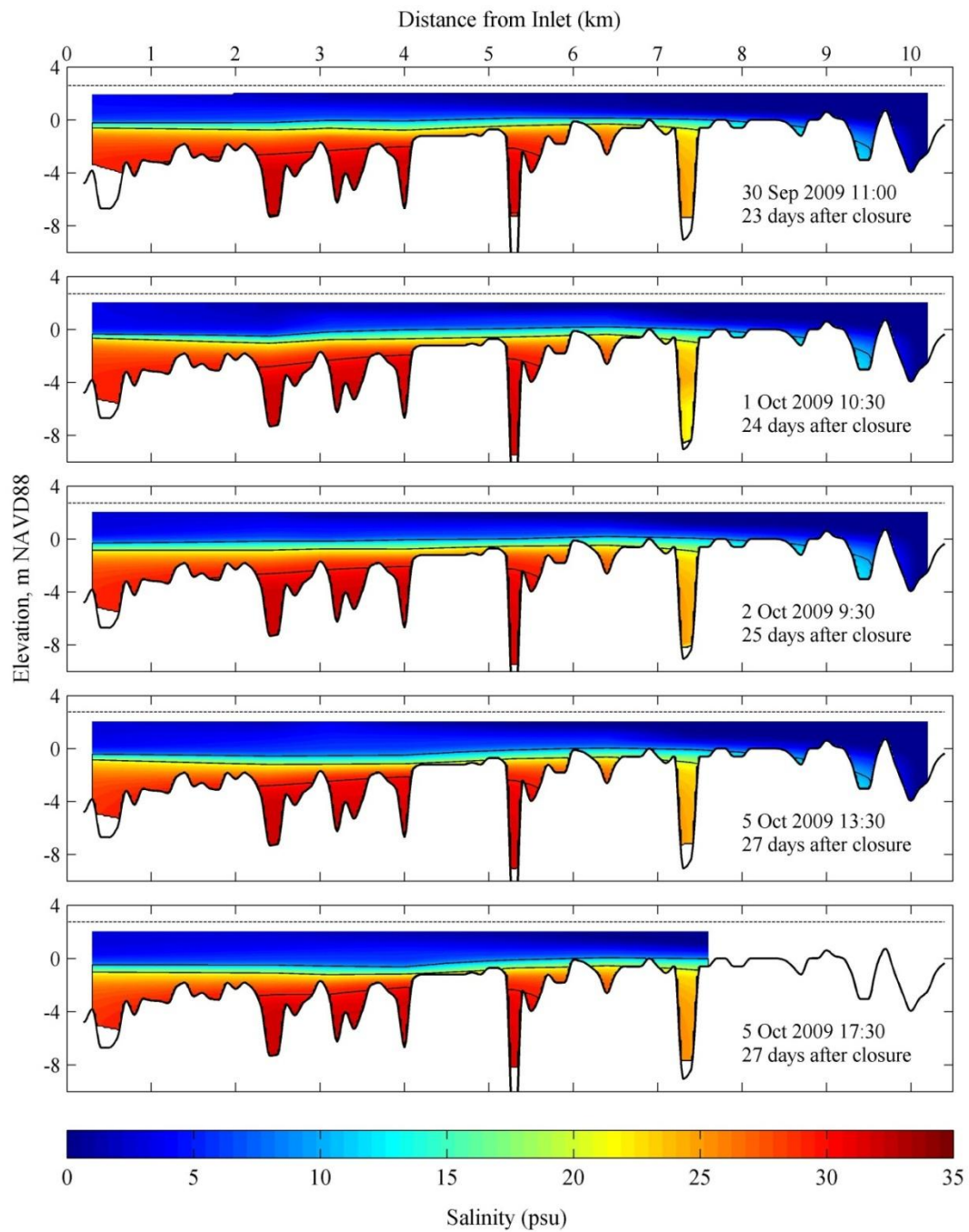


Figure C.13. 2D planar view of the estuary salinity interpolated from CTD transects from 30 September 2009 to 5 October 2009.

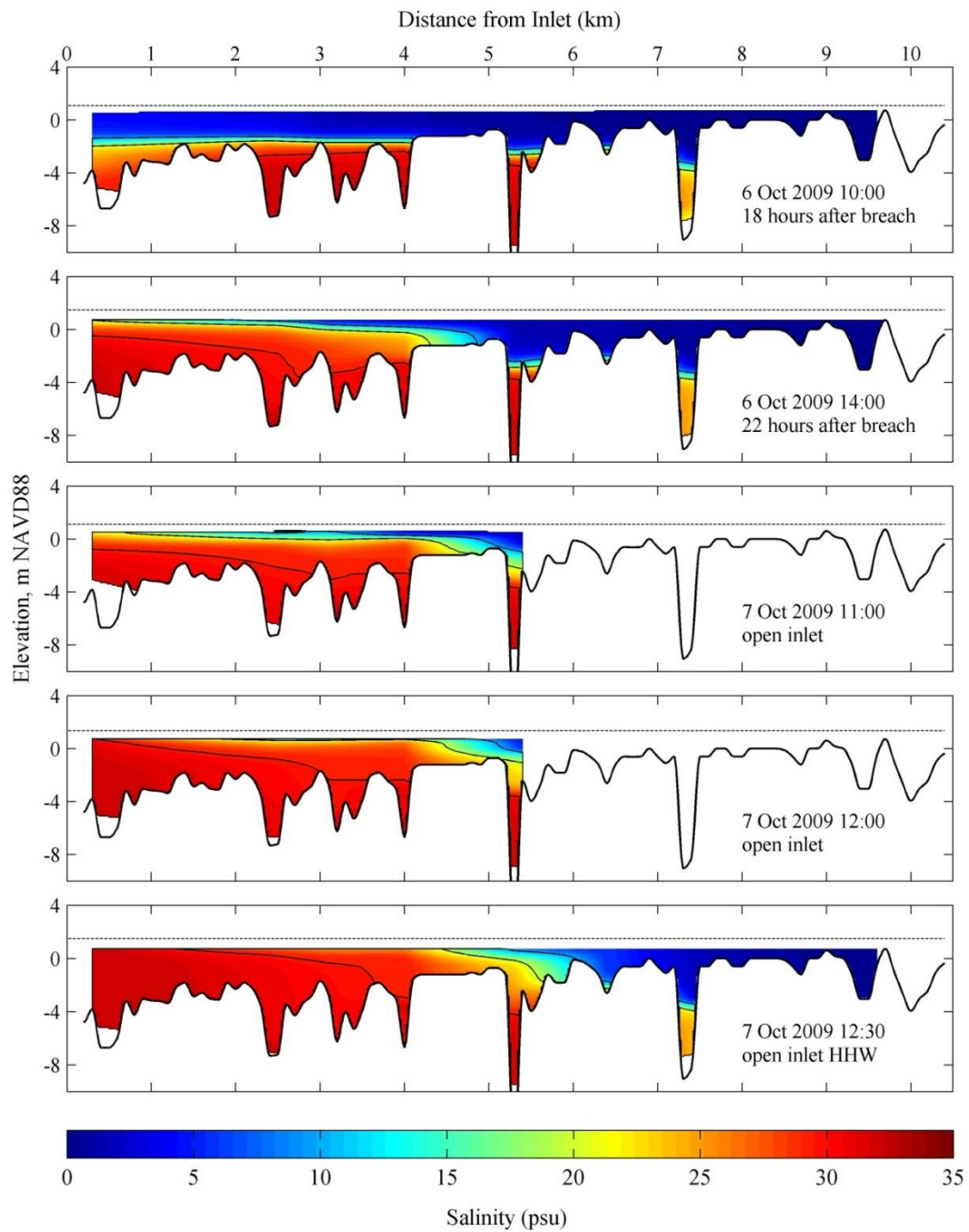


Figure C.14. 2D planar view of the estuary salinity interpolated from CTD transects from 6 October to 7 October 2009.

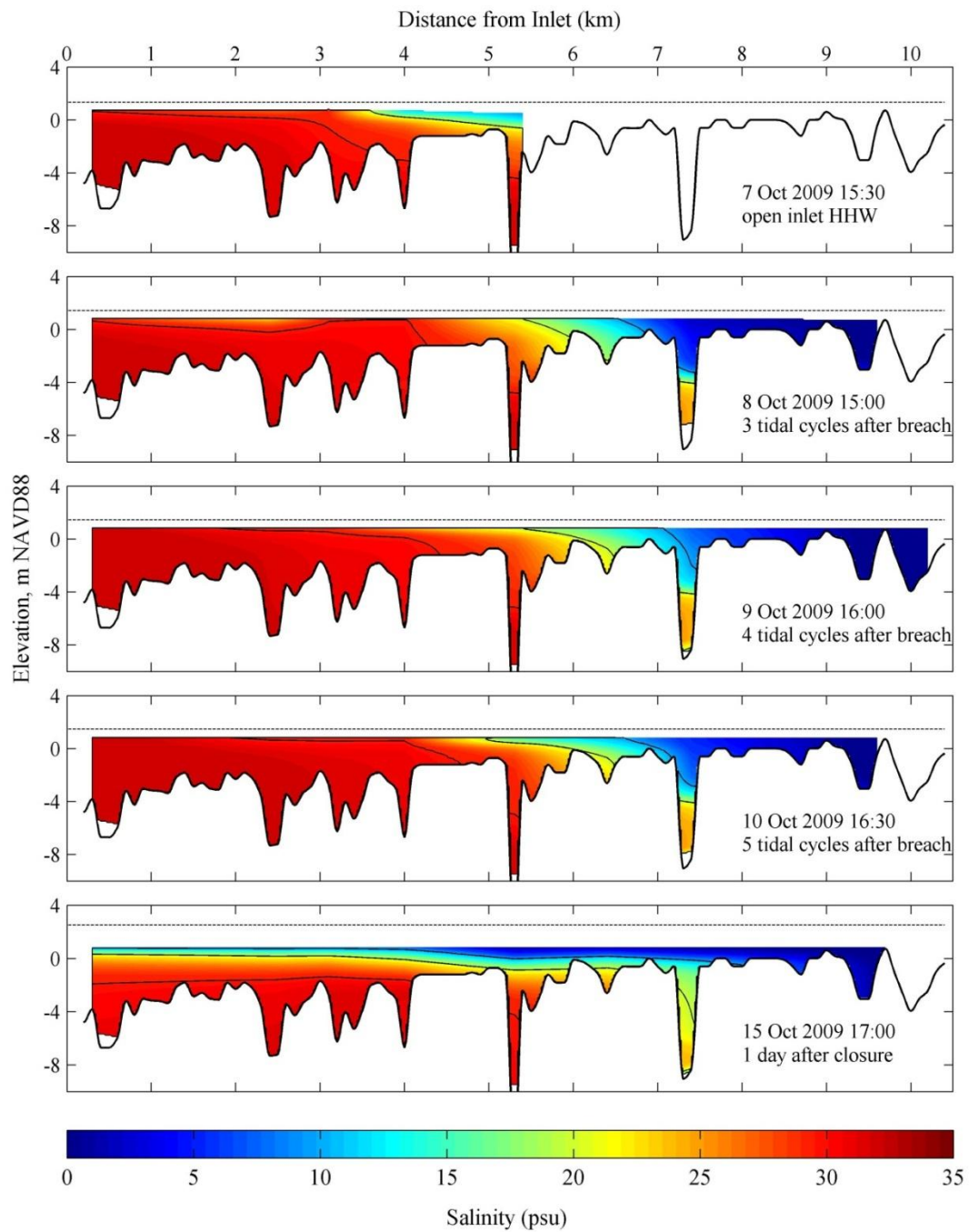


Figure C.15. 2D planar view of the estuary salinity interpolated from CTD transects from 7 October to 15 October 2009.

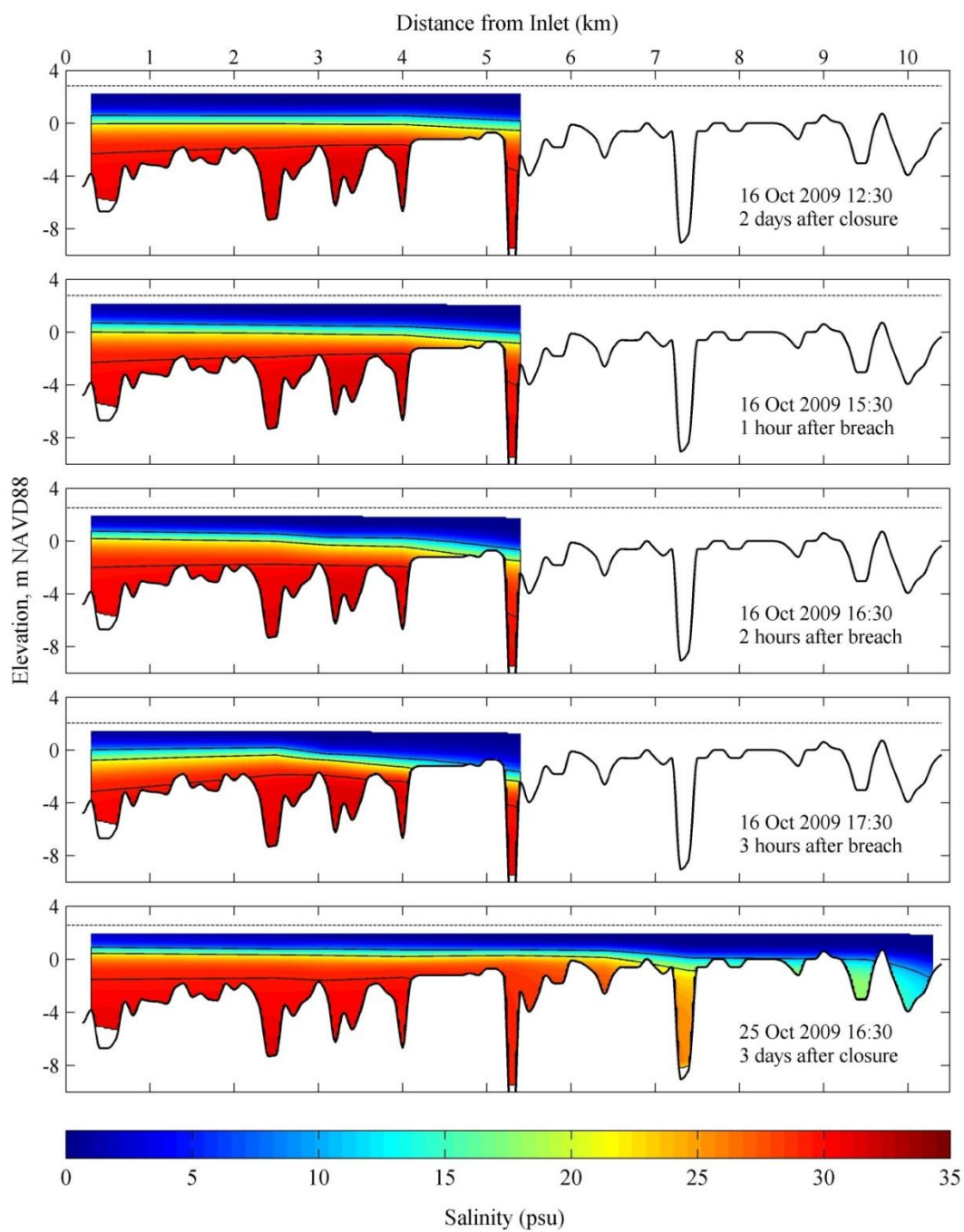


Figure C.16. 2D planar view of the estuary salinity interpolated from CTD transects from 16 October to 25 October 2009.

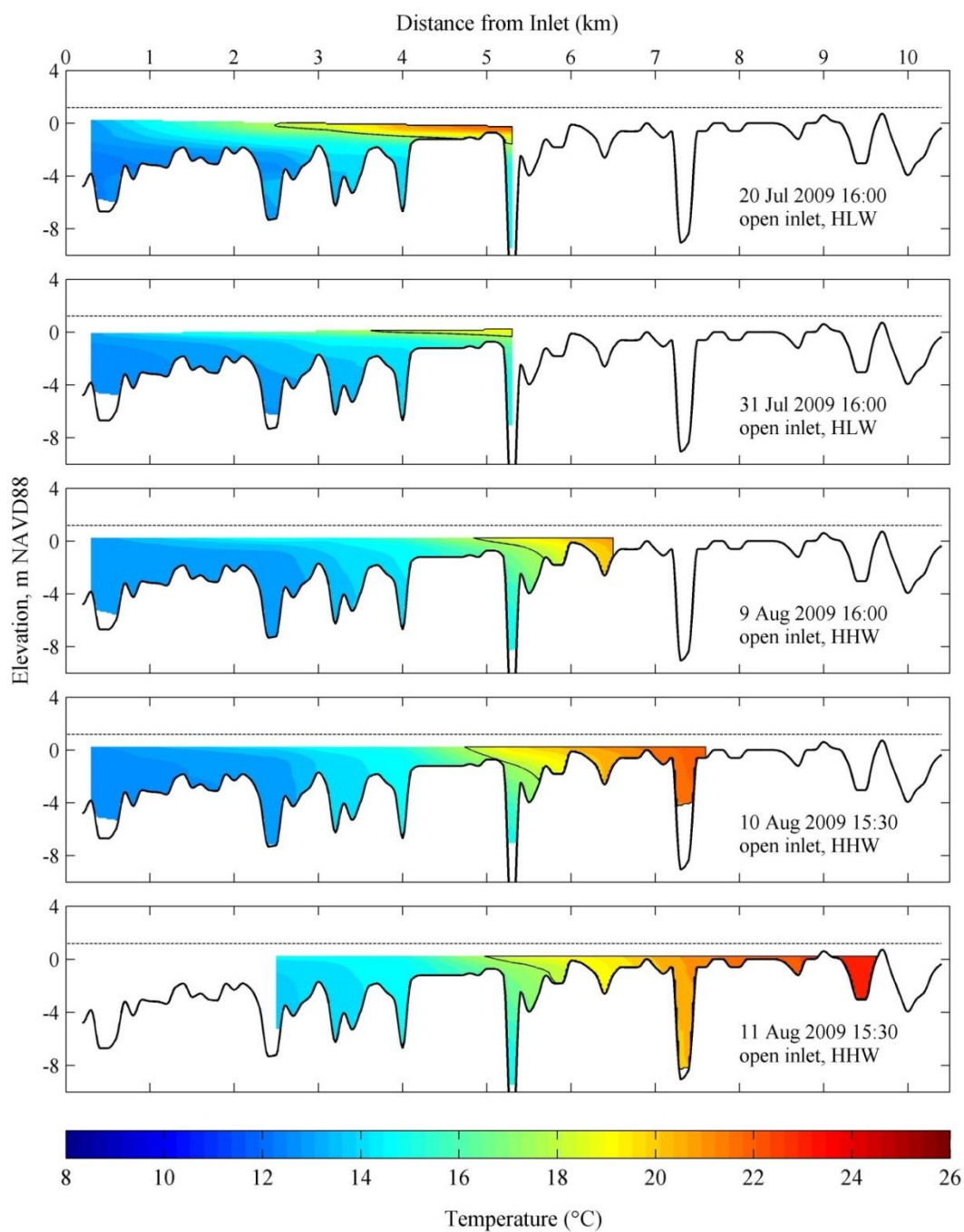


Figure C.17. 2D planar view of the estuary temperature interpolated from CTD transects from 20 July to 11 August 2009.

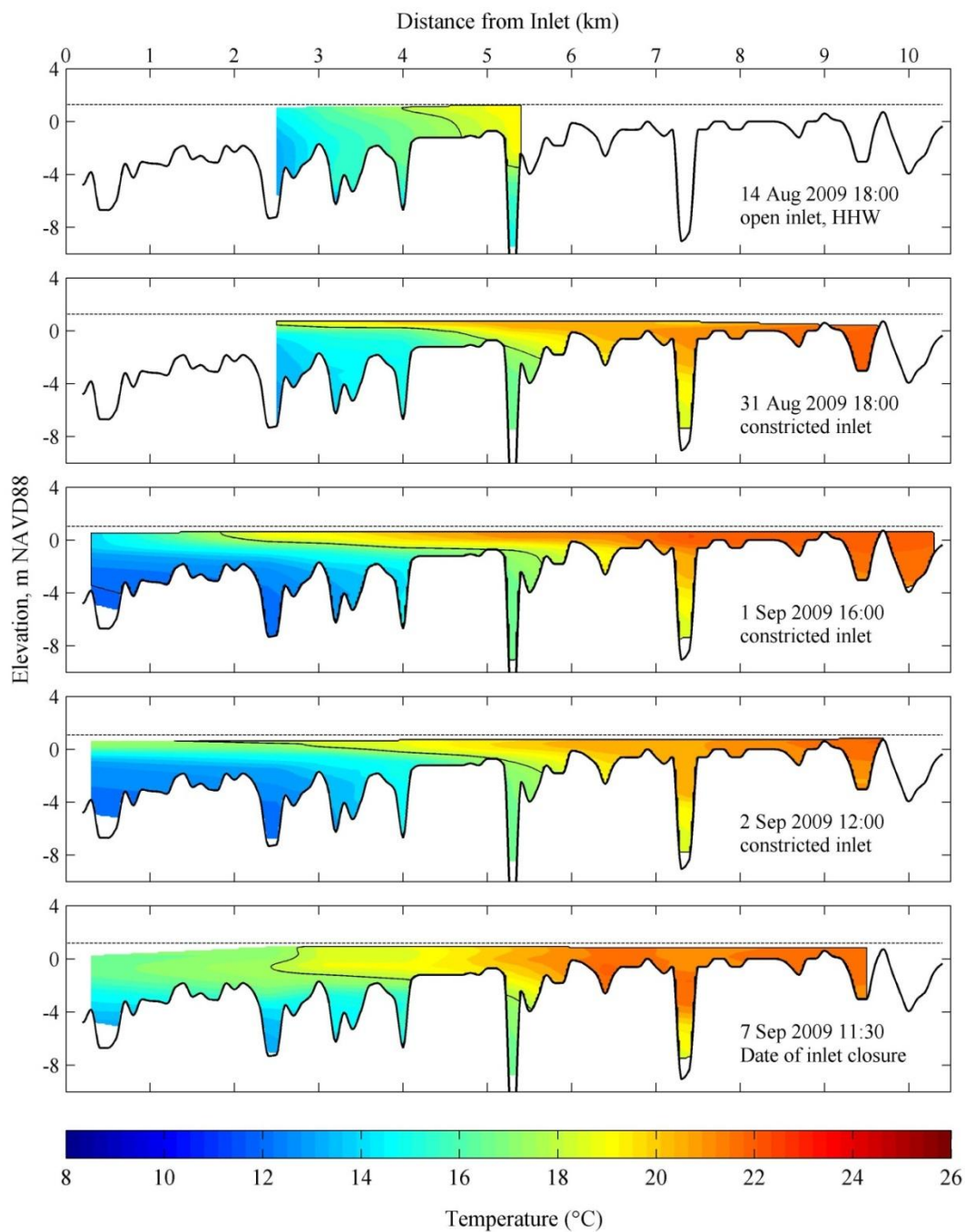


Figure C.18. 2D planar view of the estuary temperature interpolated from CTD transects from 14 August to 7 September 2009.

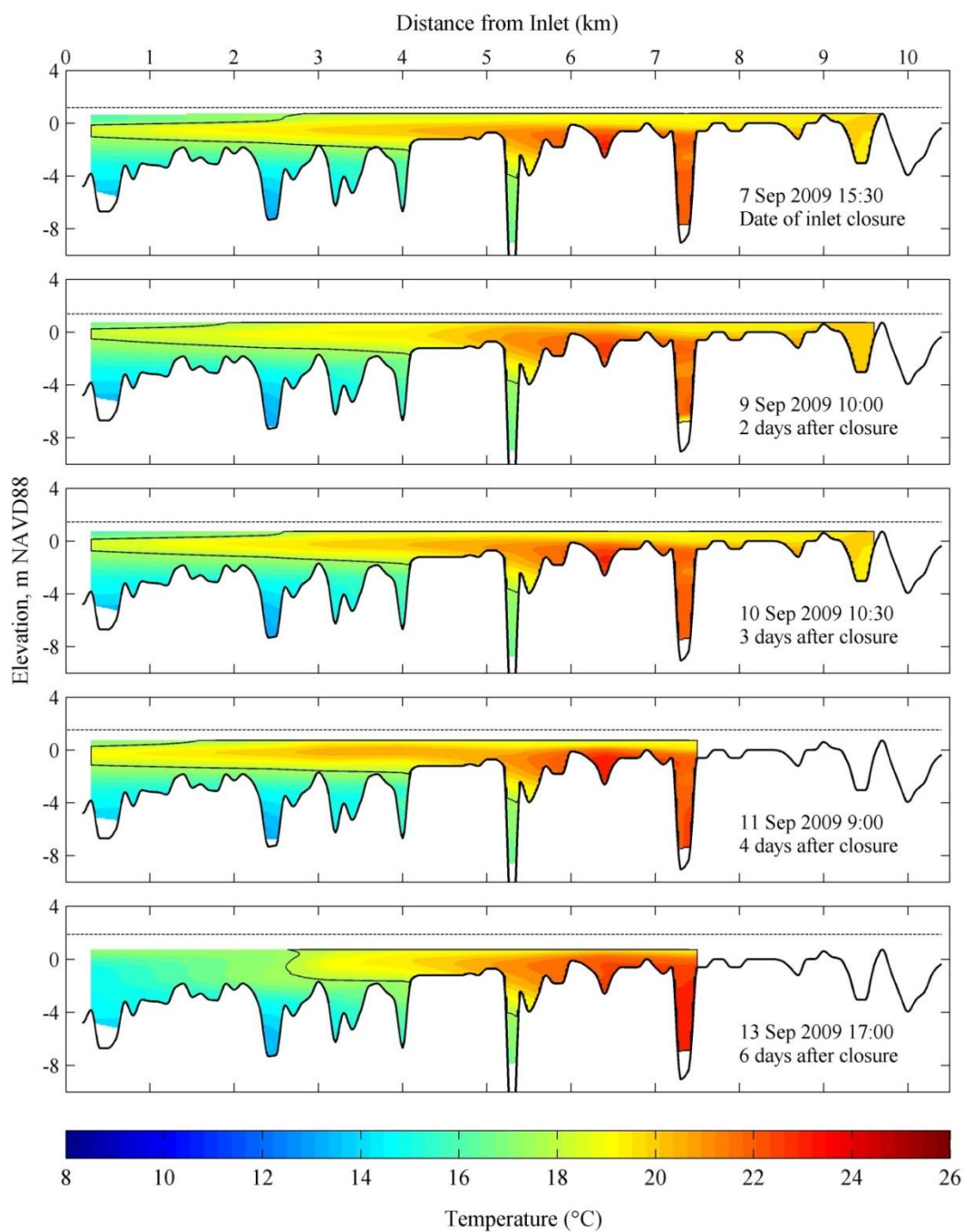


Figure C.19. 2D planar view of the estuary temperature interpolated from CTD transects from 7 September to 13 September 2009.

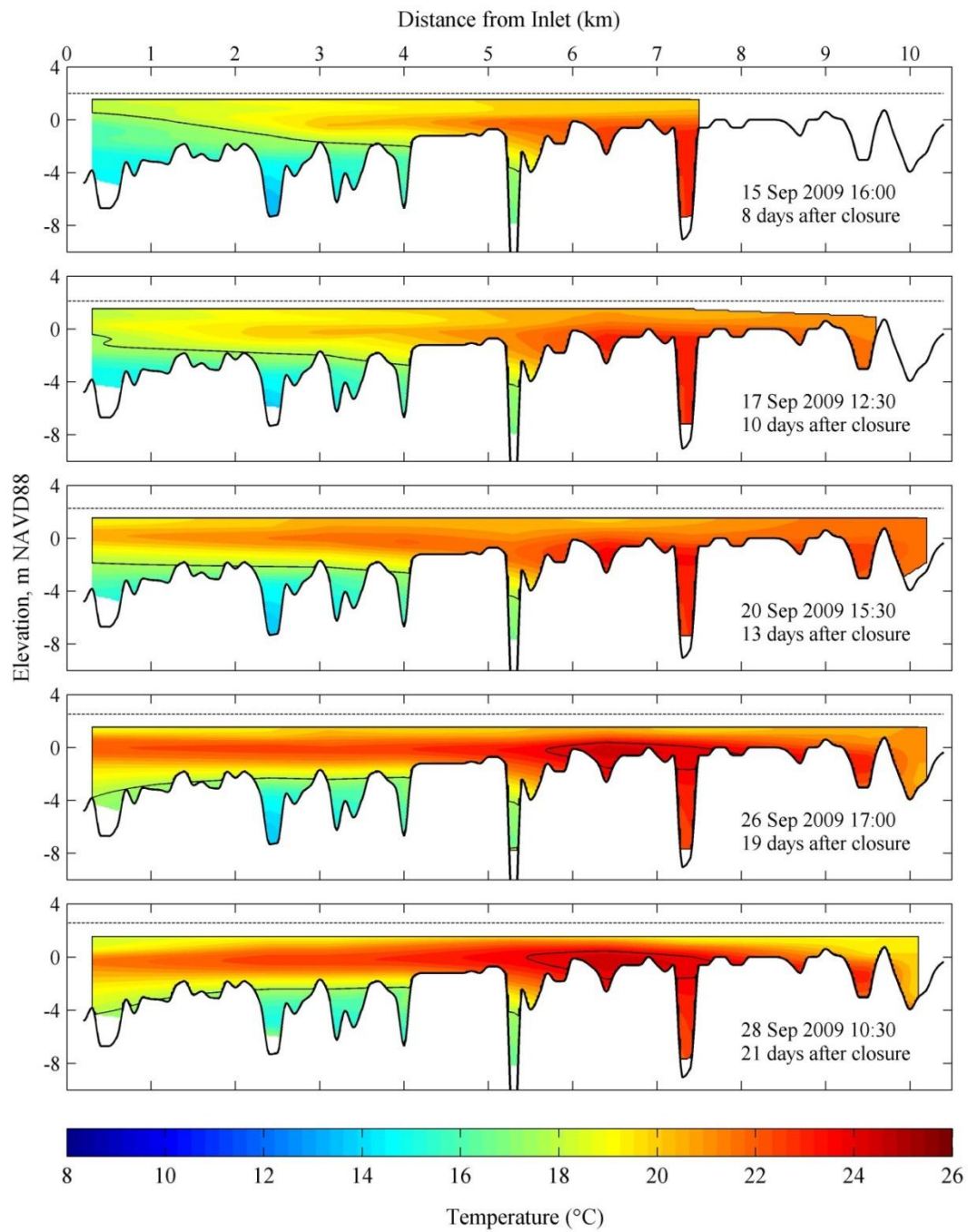


Figure C.20. 2D planar view of the estuary temperature interpolated from CTD transects from 15 September to 28 September 2009.

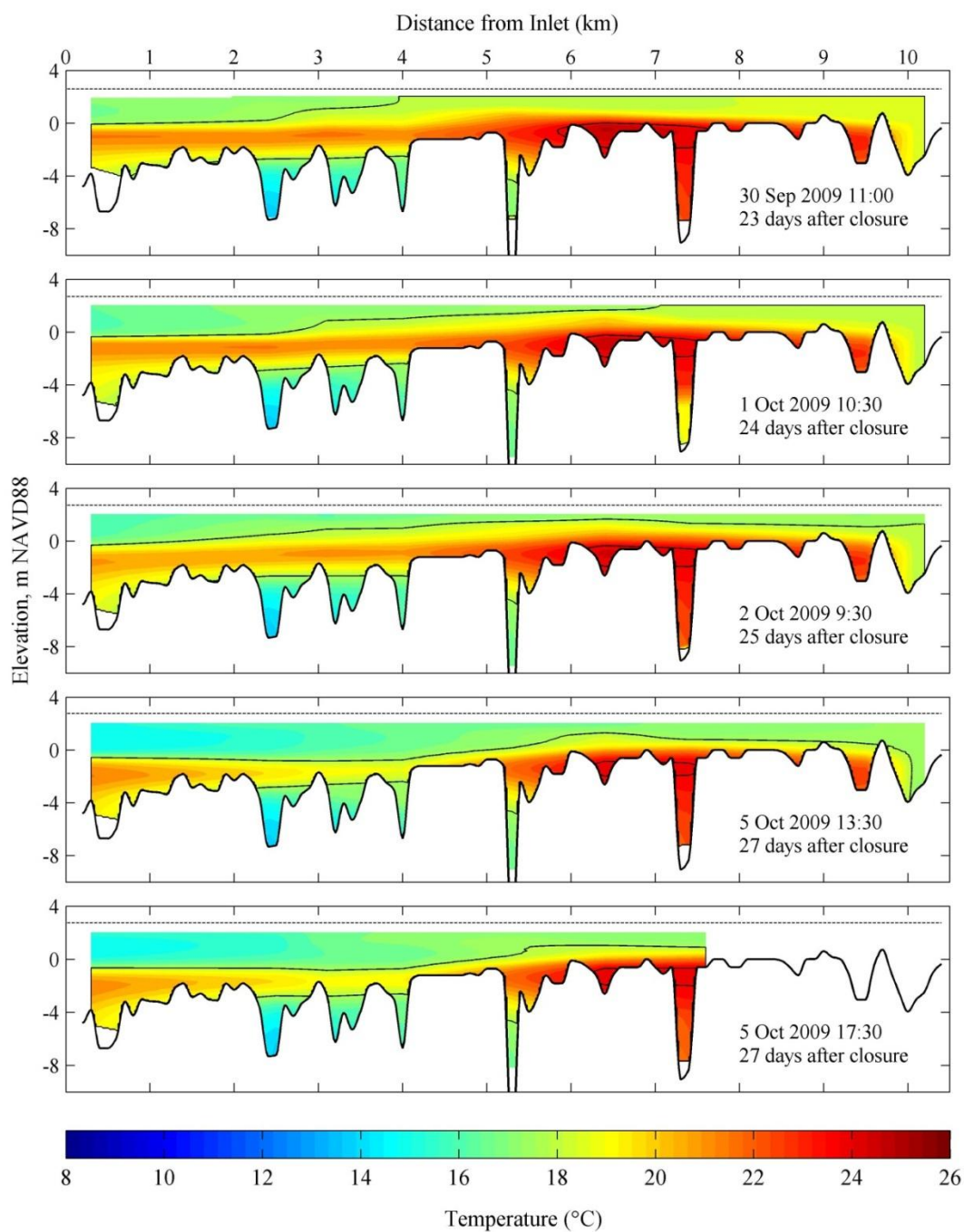


Figure C.21. 2D planar view of the estuary temperature interpolated from CTD transects from 30 September to 5 October 2009.

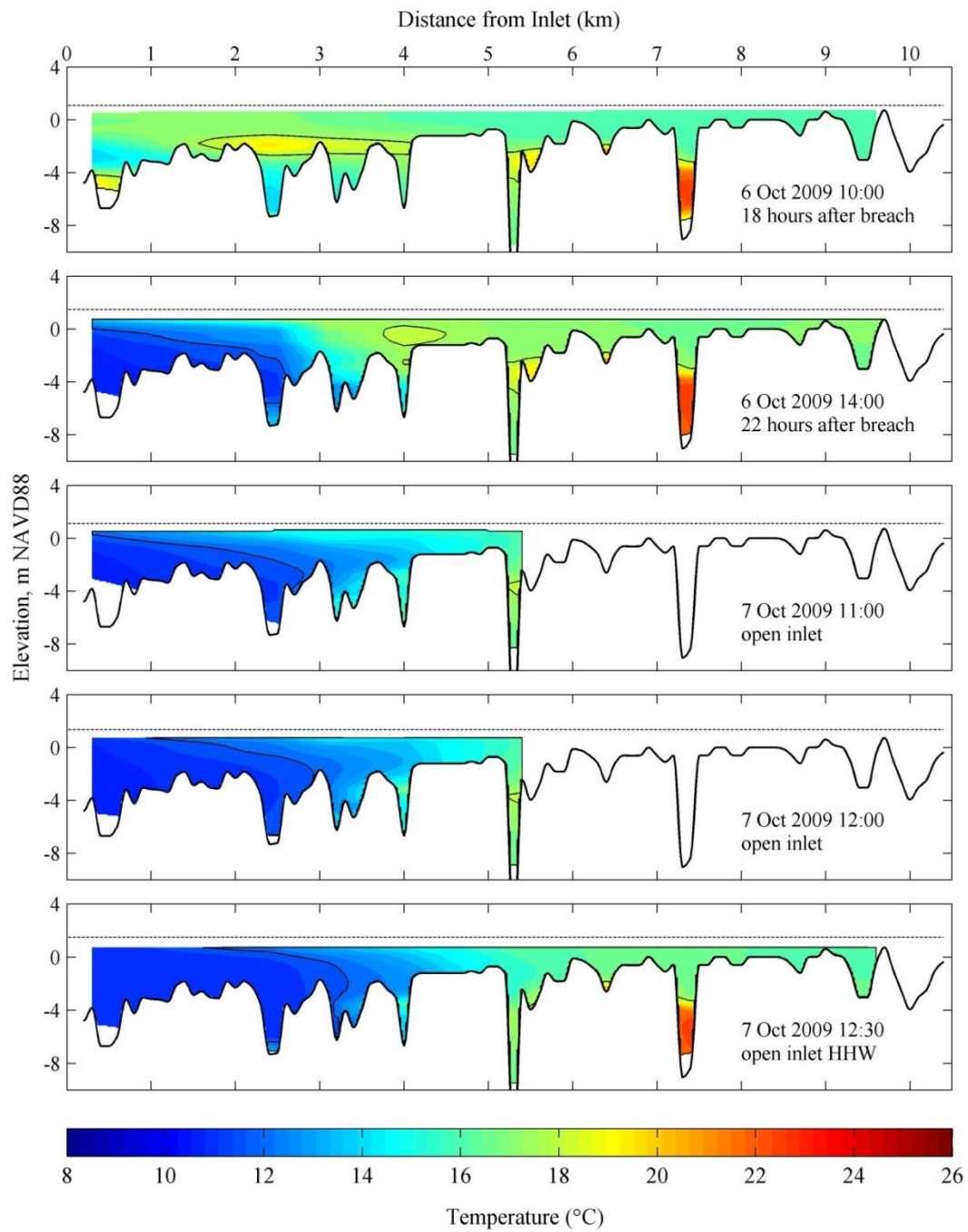


Figure C.22. 2D planar view of the estuary temperature interpolated from CTD transects from 6 October to 7 October 2009.

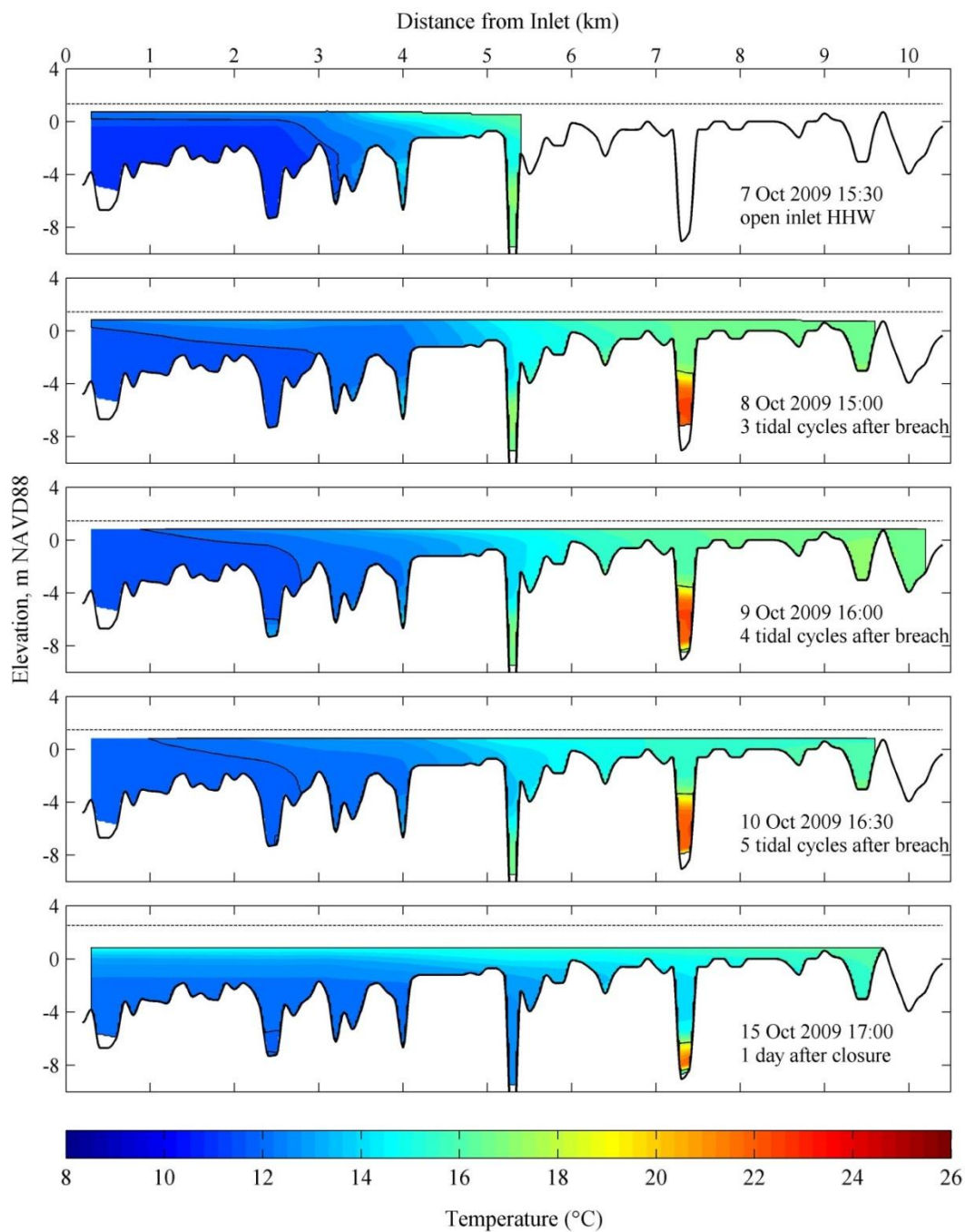


Figure C.23. 2D planar view of the estuary temperature interpolated from CTD transects from 7 October to 15 October 2009.

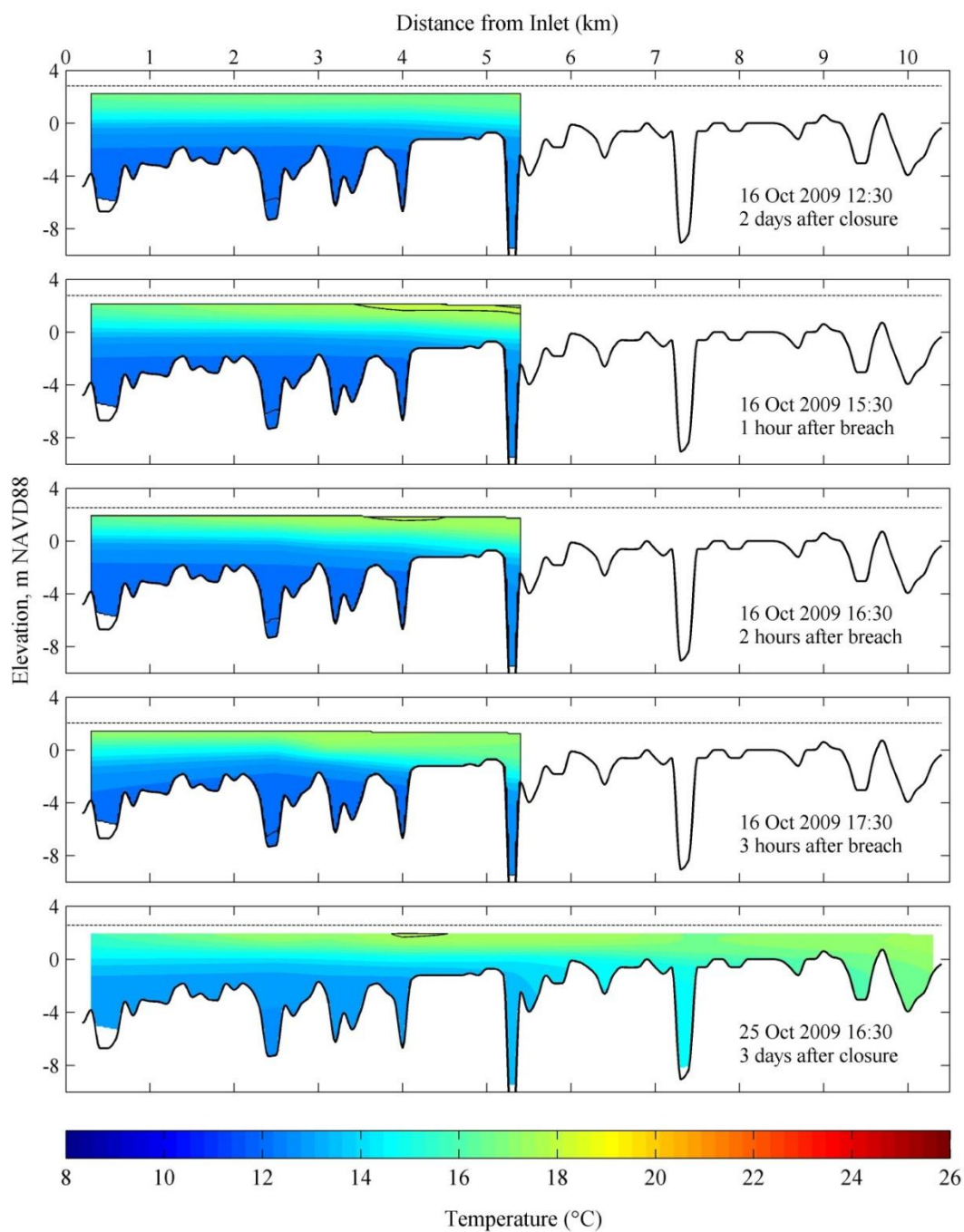


Figure C.24. 2D planar view of the estuary temperature interpolated from CTD transects from 16 October to 25 October 2009.

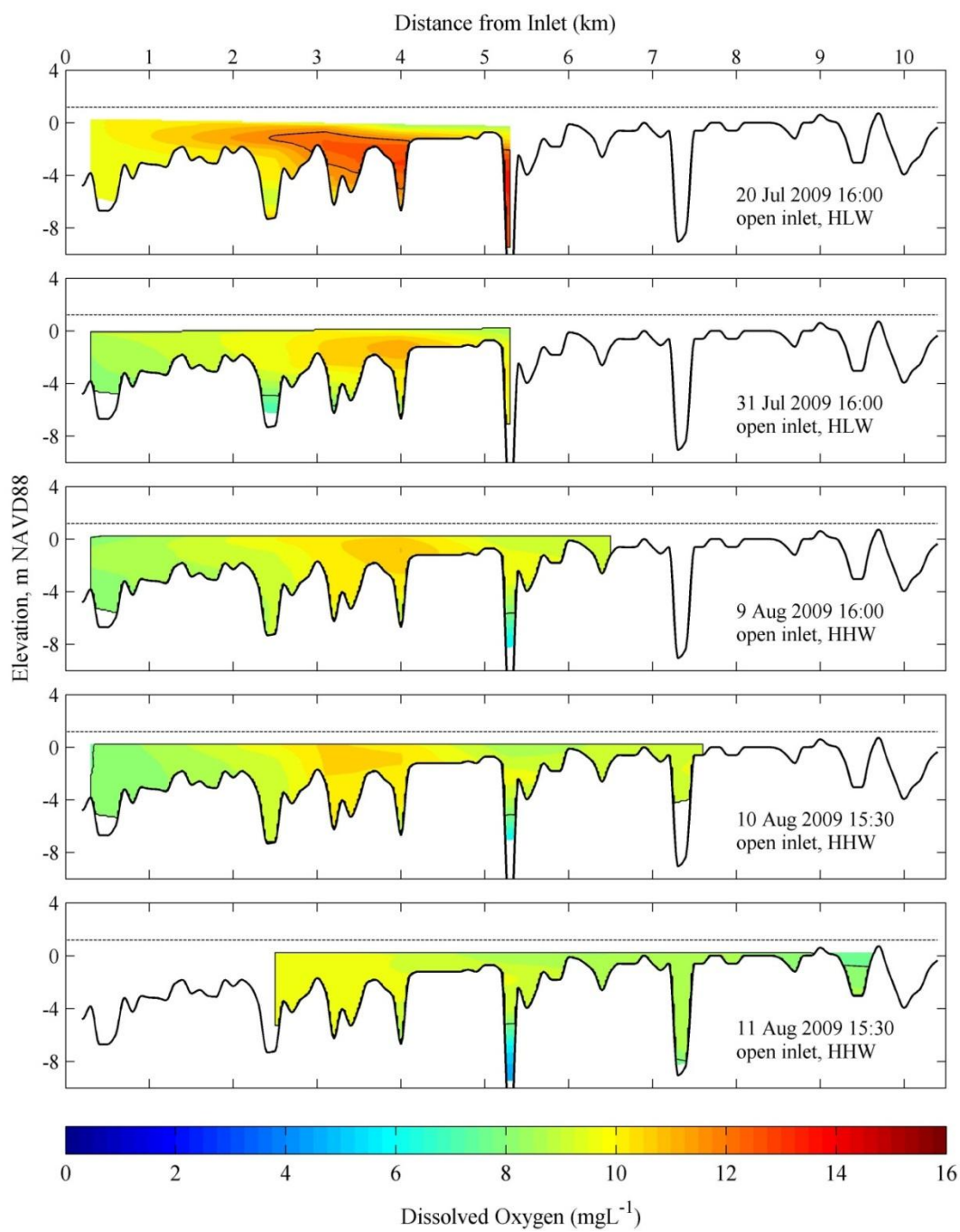


Figure C.25. 2D planar view of the estuary dissolved oxygen interpolated from CTD transects from 20 July to 11 August 2009.

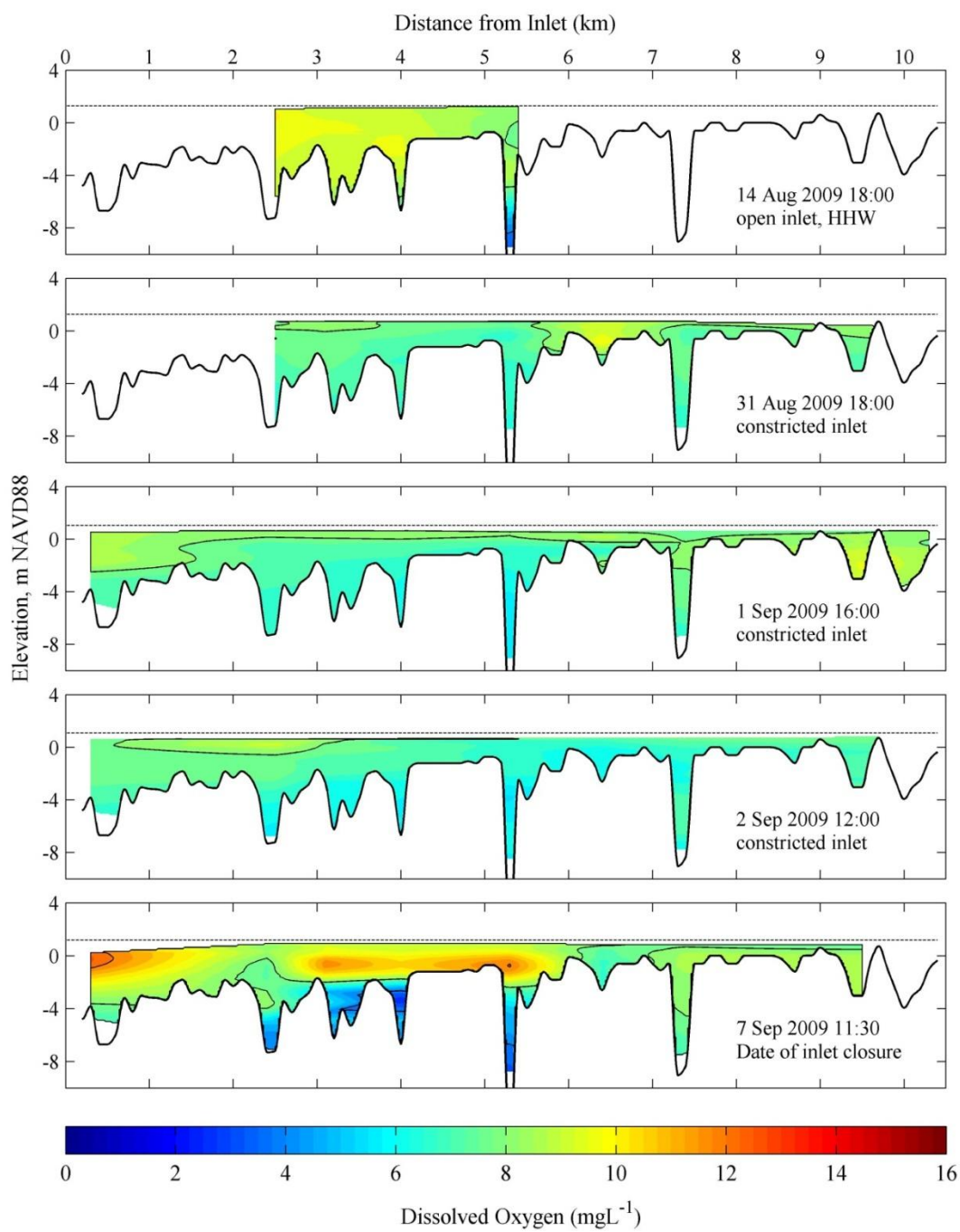


Figure C.26. 2D planar view of the estuary dissolved oxygen interpolated from CTD transects from 14 August to 7 September 2009.

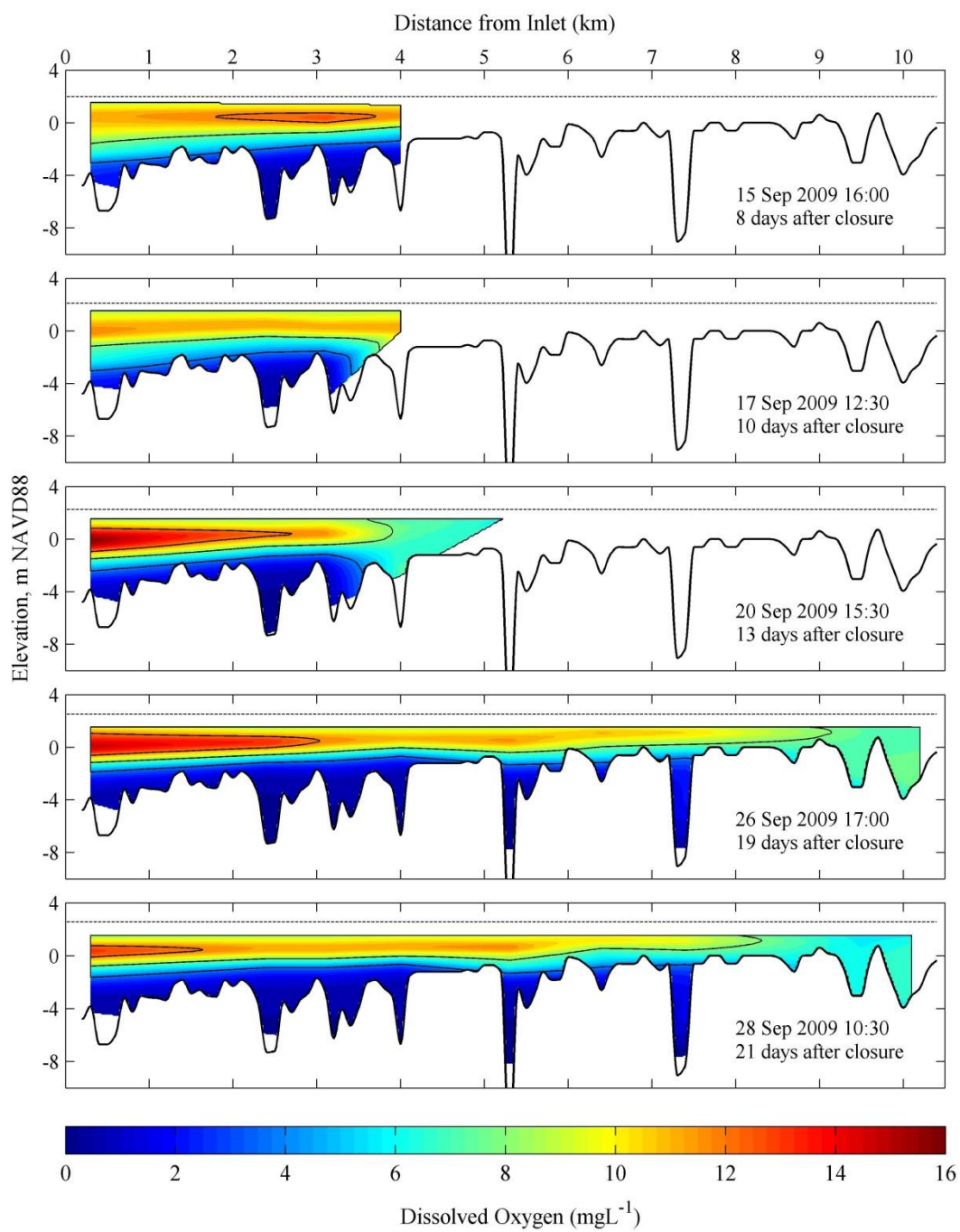


Figure C.27. 2D planar view of the estuary dissolved oxygen interpolated from CTD transects from 15 September to 28 September 2009.

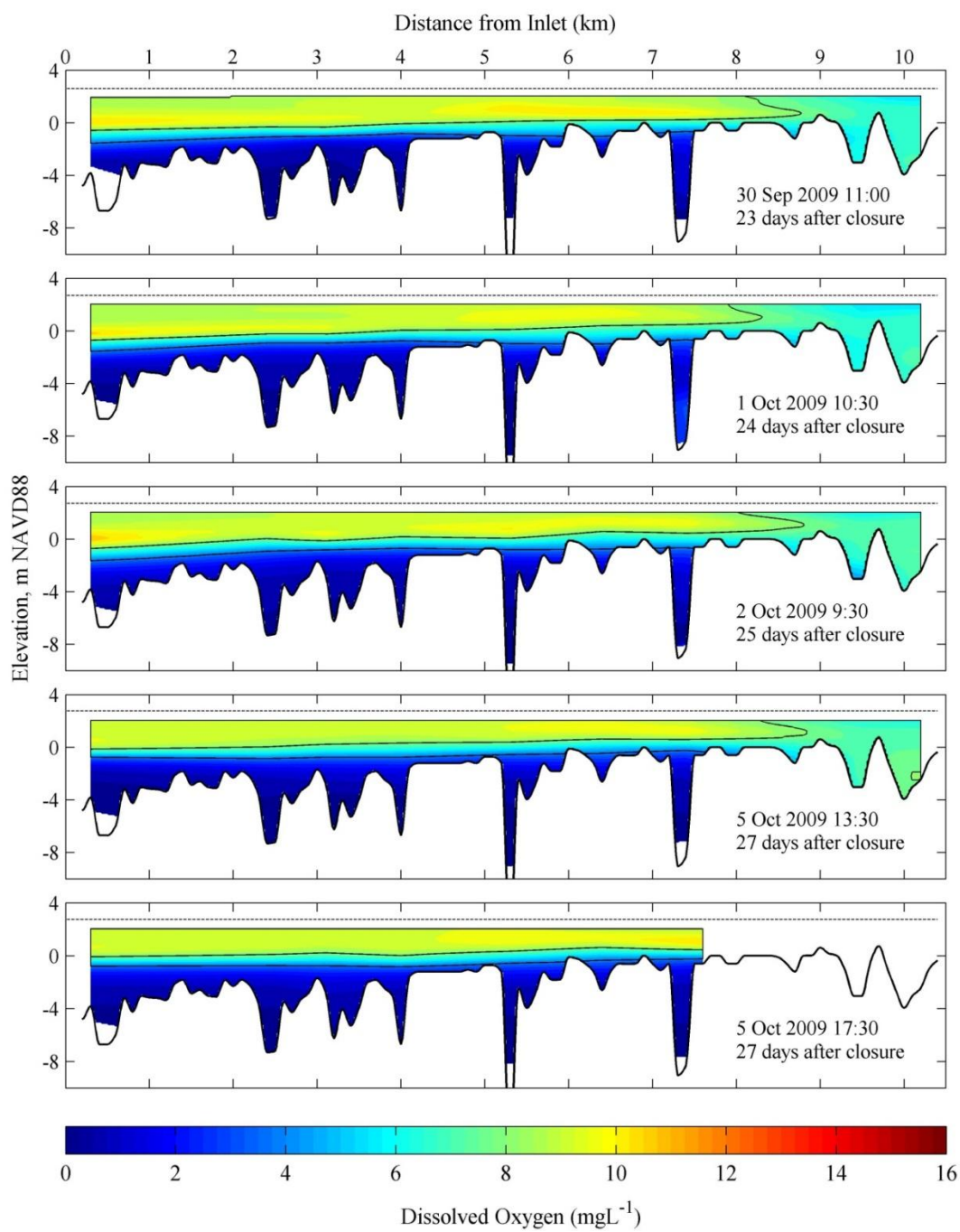


Figure C.28. 2D planar view of the estuary dissolved oxygen interpolated from CTD transects from 30 September to 5 October 2009.

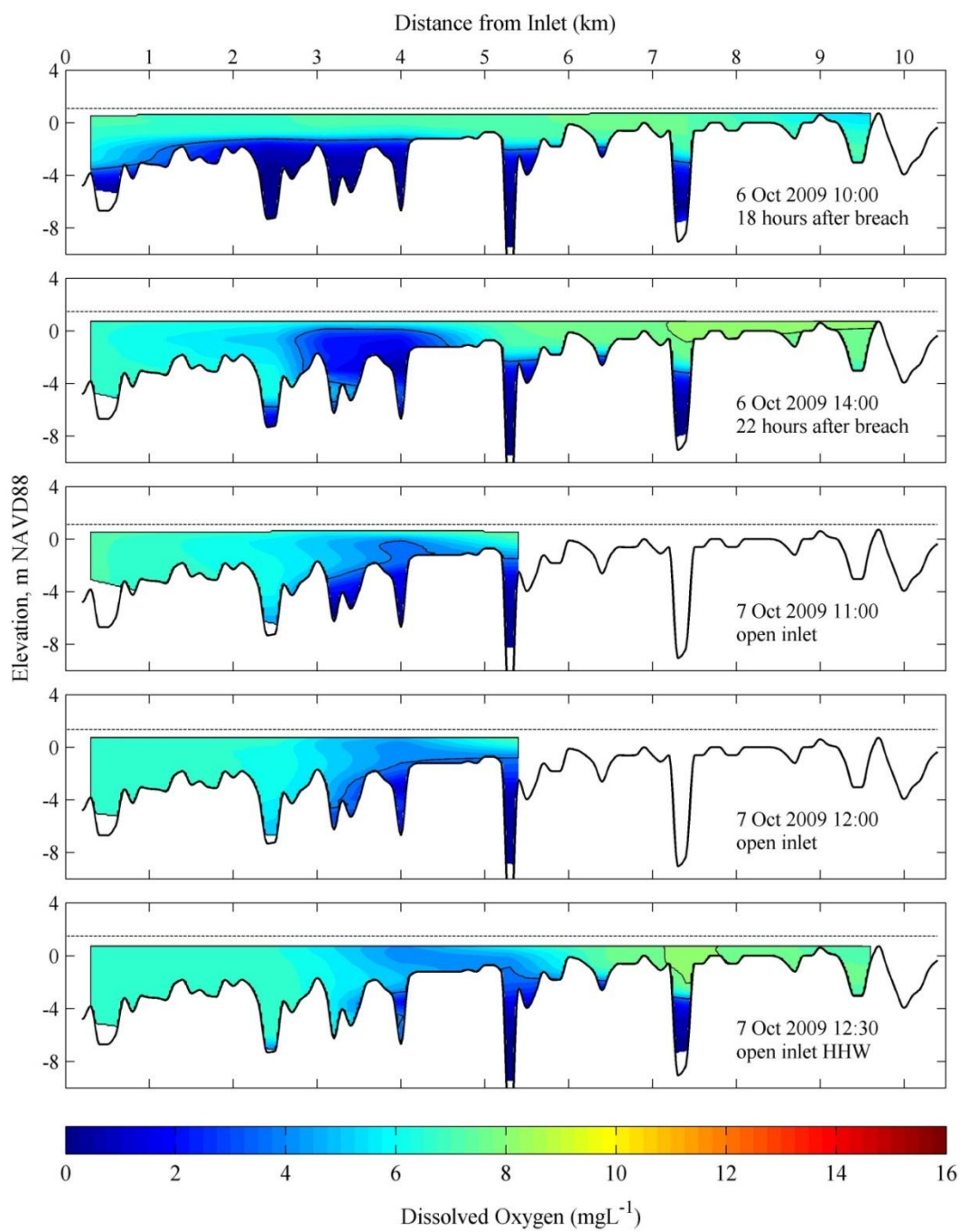


Figure C.29. 2D planar view of the estuary dissolved oxygen interpolated from CTD transects from 6 October to 7 October 2009.

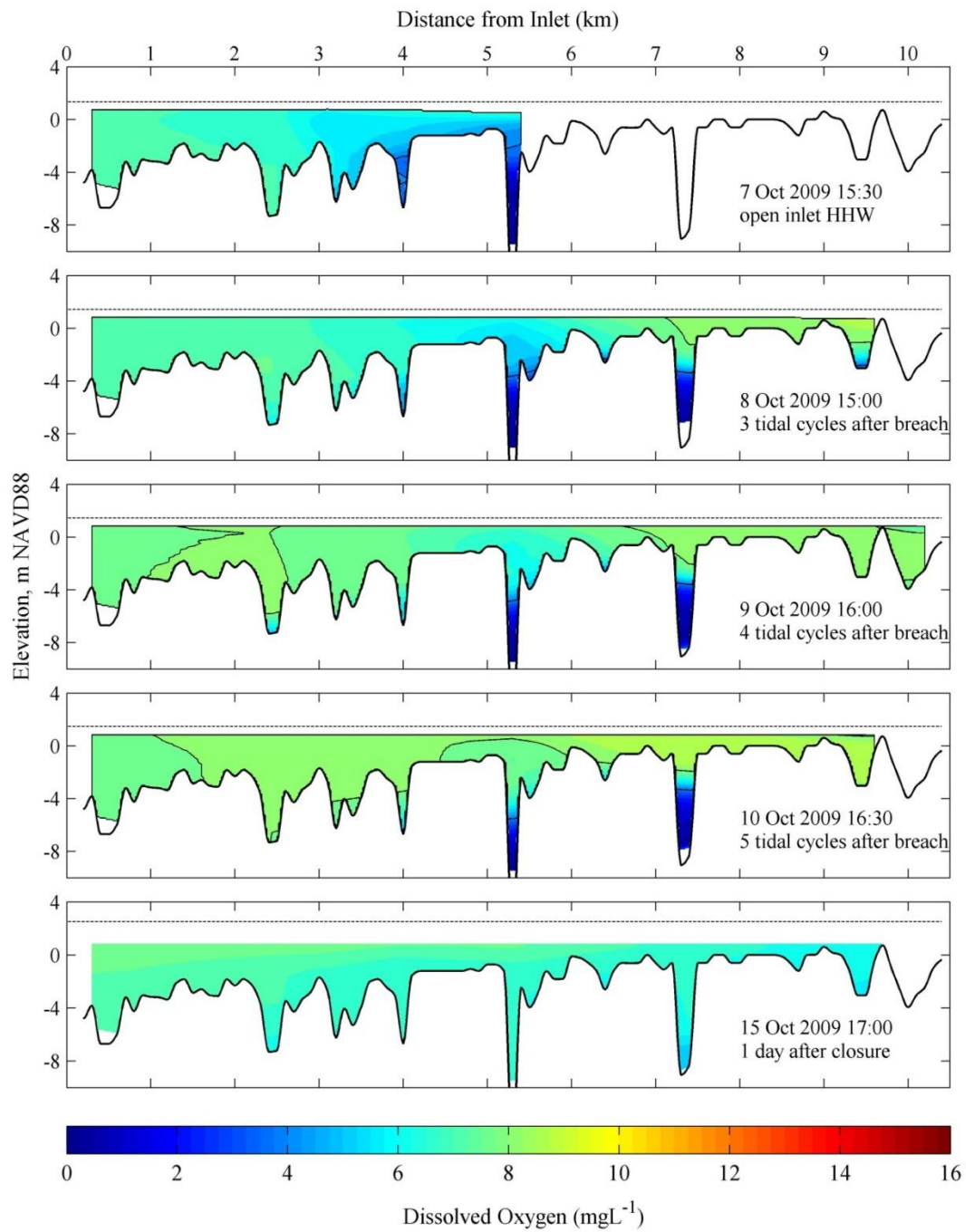


Figure C.30. 2D planar view of the estuary dissolved oxygen interpolated from CTD transects from 7 October to 15 October 2009.

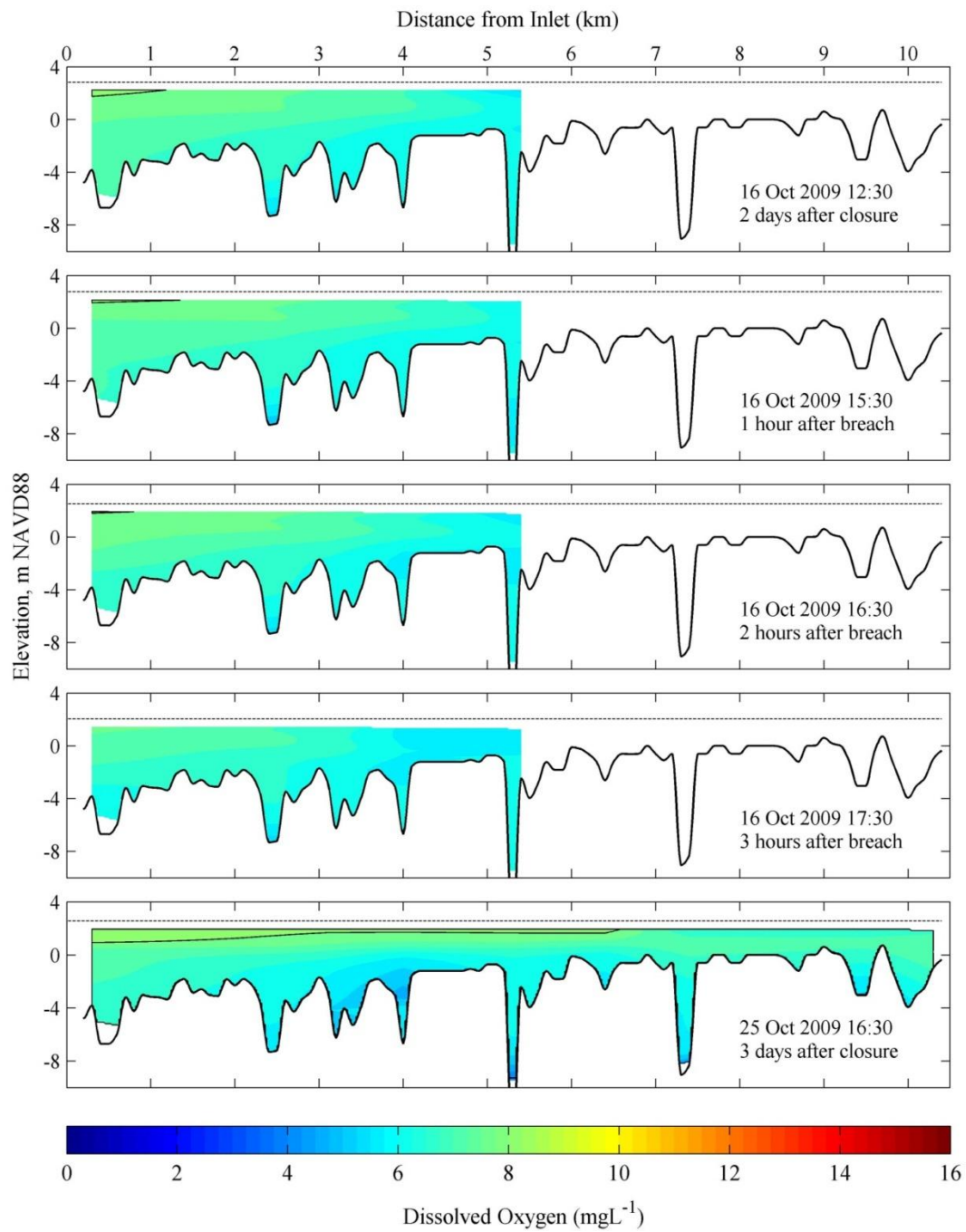


Figure C.31. 2D planar view of the estuary dissolved oxygen interpolated from CTD transects from 16 October to 25 October 2009.

C.2. Lagoon Scalar Fields in 2010

Figures C.32-55 summarize the 2D (x - and z -plane) scalar fields in the RRE during the 2010 season. Results are separated by scalar type: salinity (Figs. C.32-39), temperature (Figs. C.40-47) and dissolved oxygen (Figs. C.48-55). Plots are indexed in Figure C.2 as a vertical dashed line to give context. Additional plots were created using CTD profiles of photosynthetically active radiation (PAR) and fluorescence. These are not shown here, as they were outside the scope of this study. They can be found at the website for the Bodega Ocean Observing Node ([http:// bml.ucdavis.edu/boon](http://bml.ucdavis.edu/boon)).

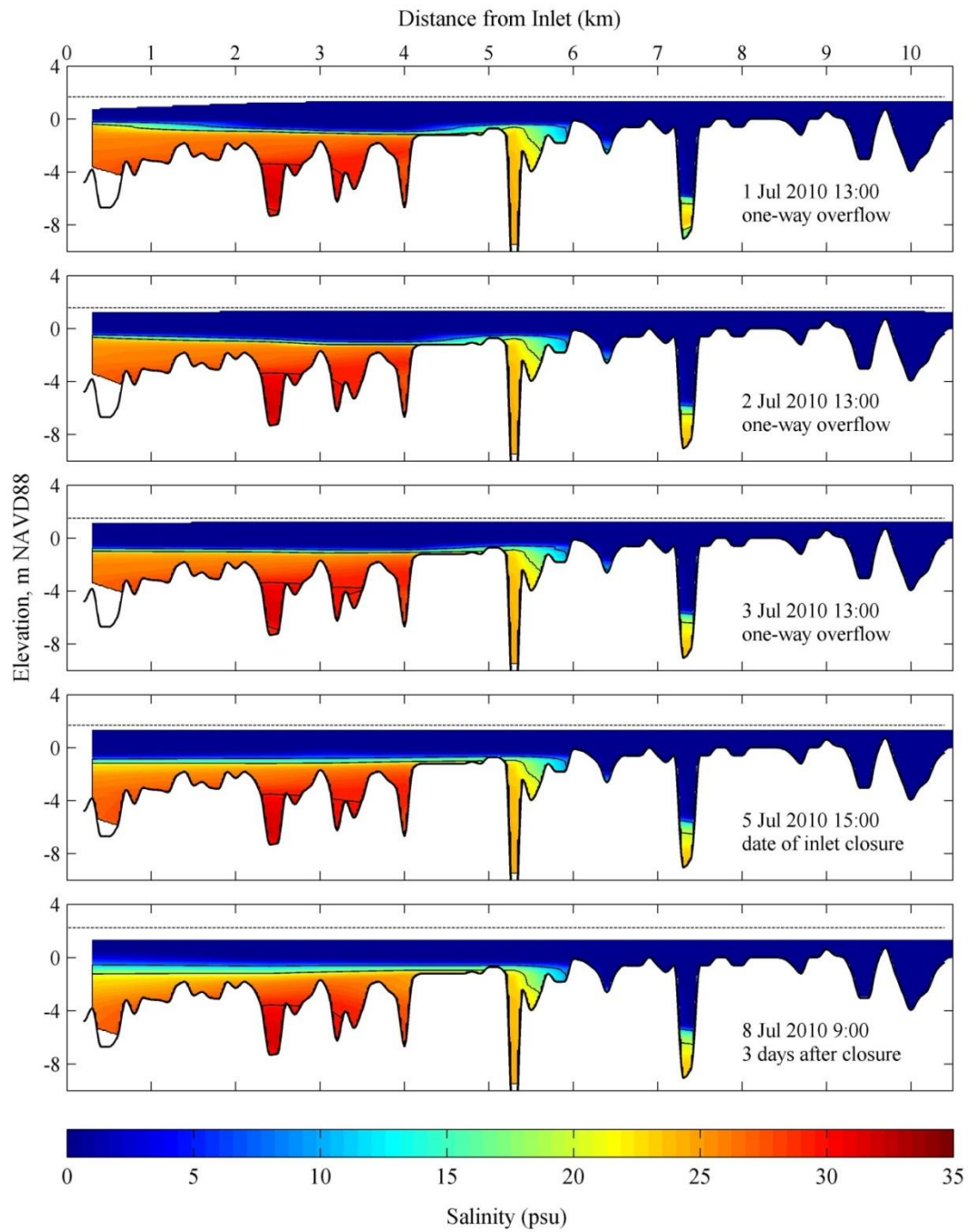


Figure C.32. 2D planar view of the estuary salinity interpolated from CTD transects from 1 July to 8 July 2009.

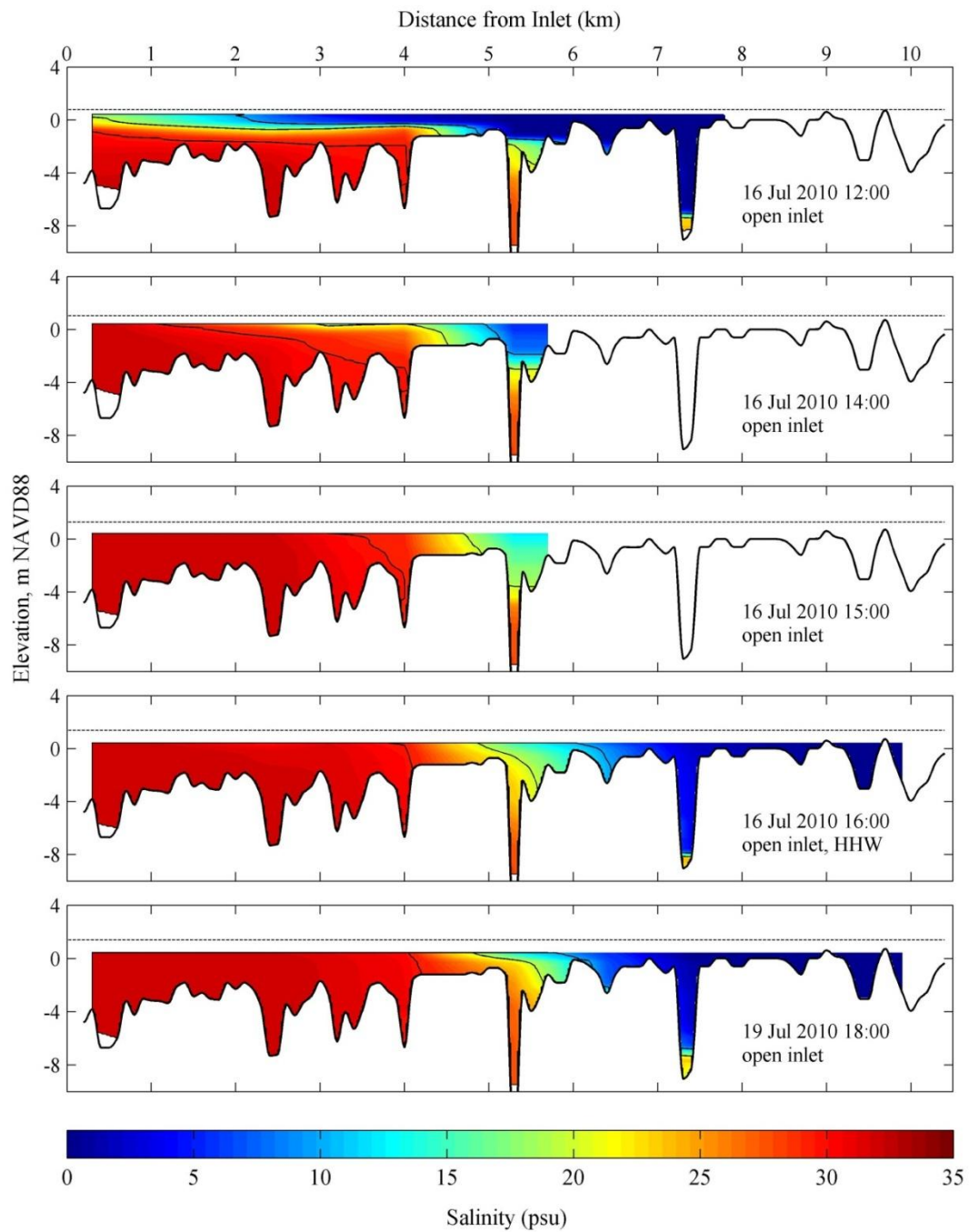


Figure C.33. 2D planar view of the estuary salinity interpolated from CTD transects from 16 July to 19 July 2009.

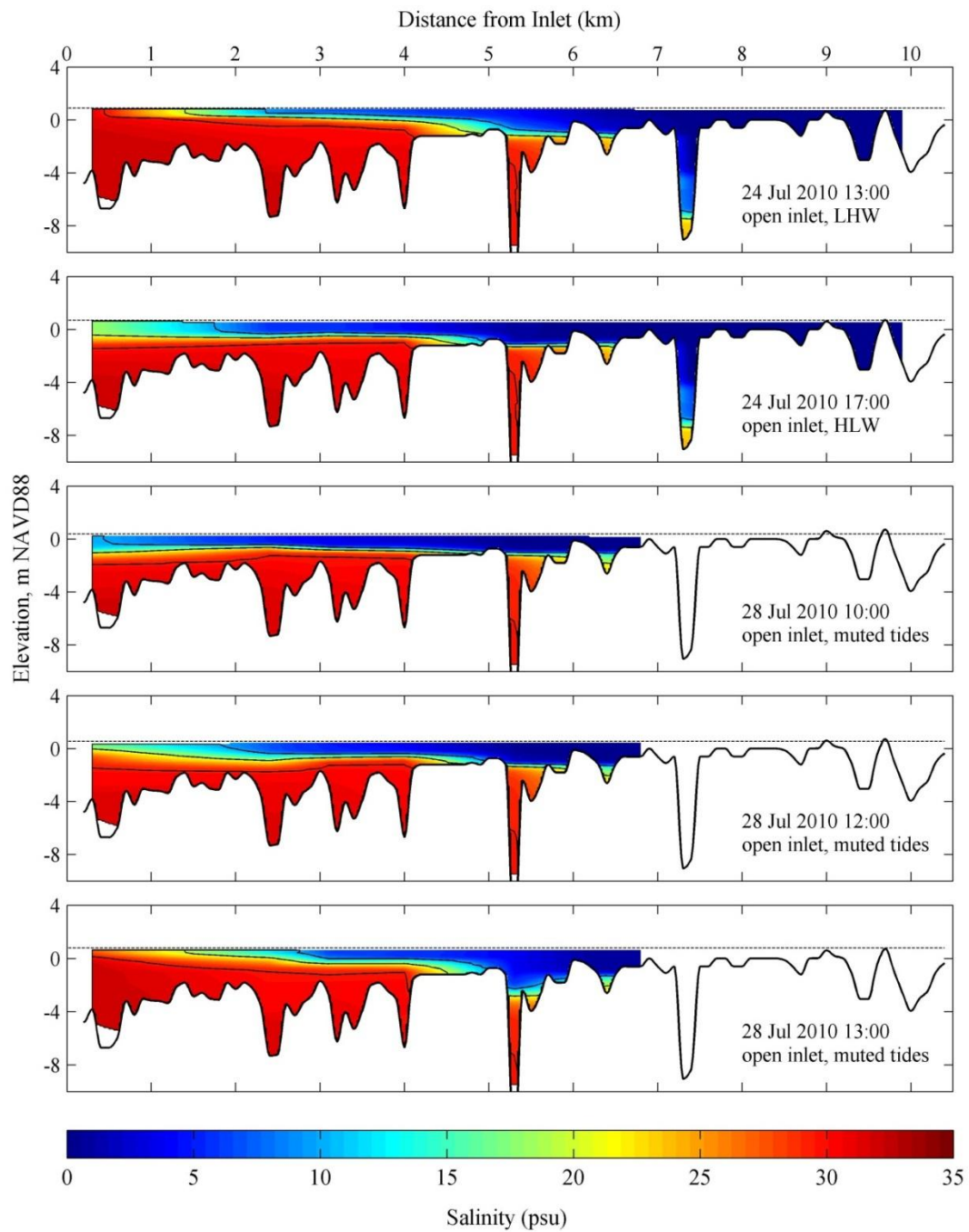


Figure C.34. 2D planar view of the estuary salinity interpolated from CTD transects from 24 July to 28 July 2009.

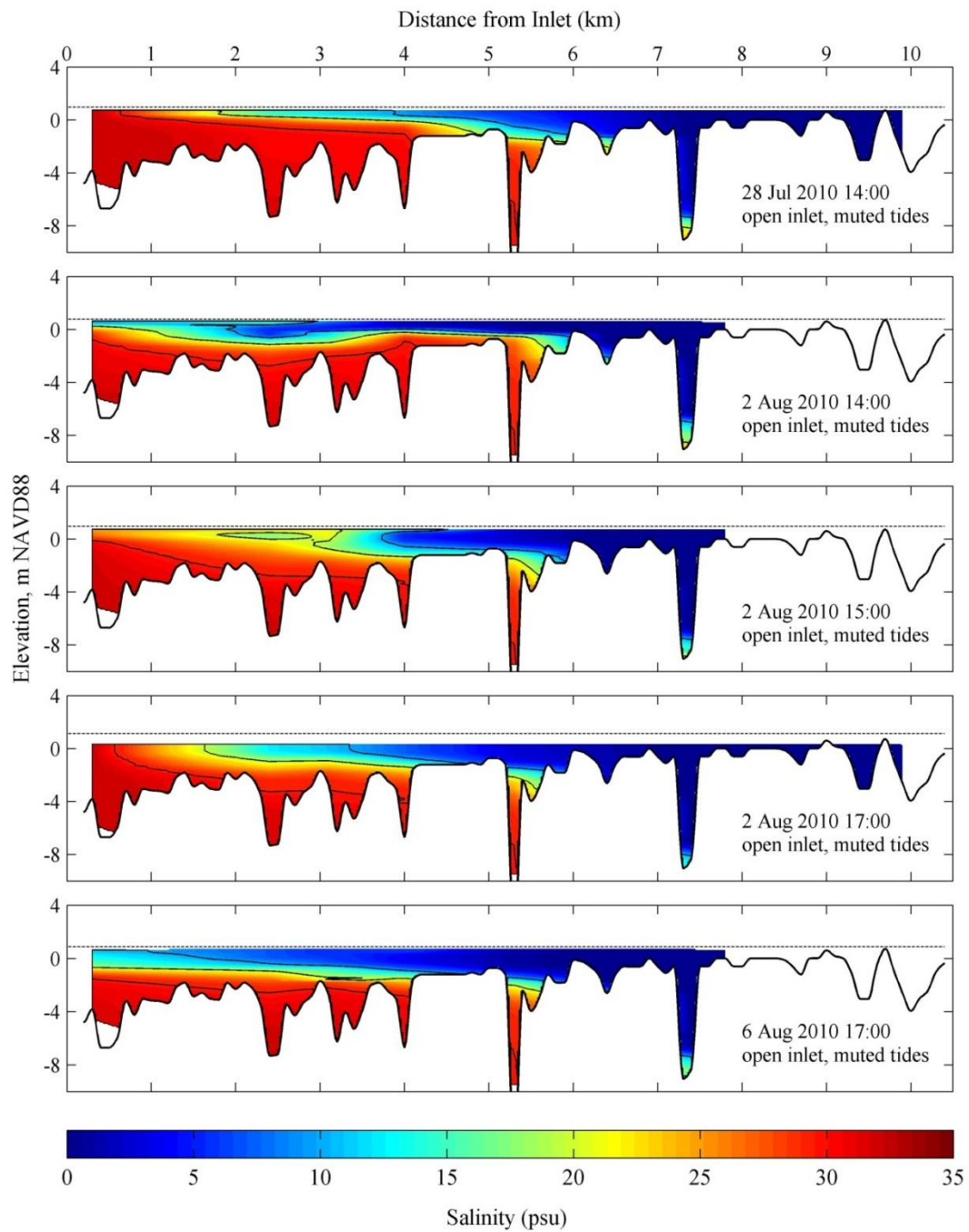


Figure C.35. 2D planar view of the estuary salinity interpolated from CTD transects from 28 July to 6 August 2009.

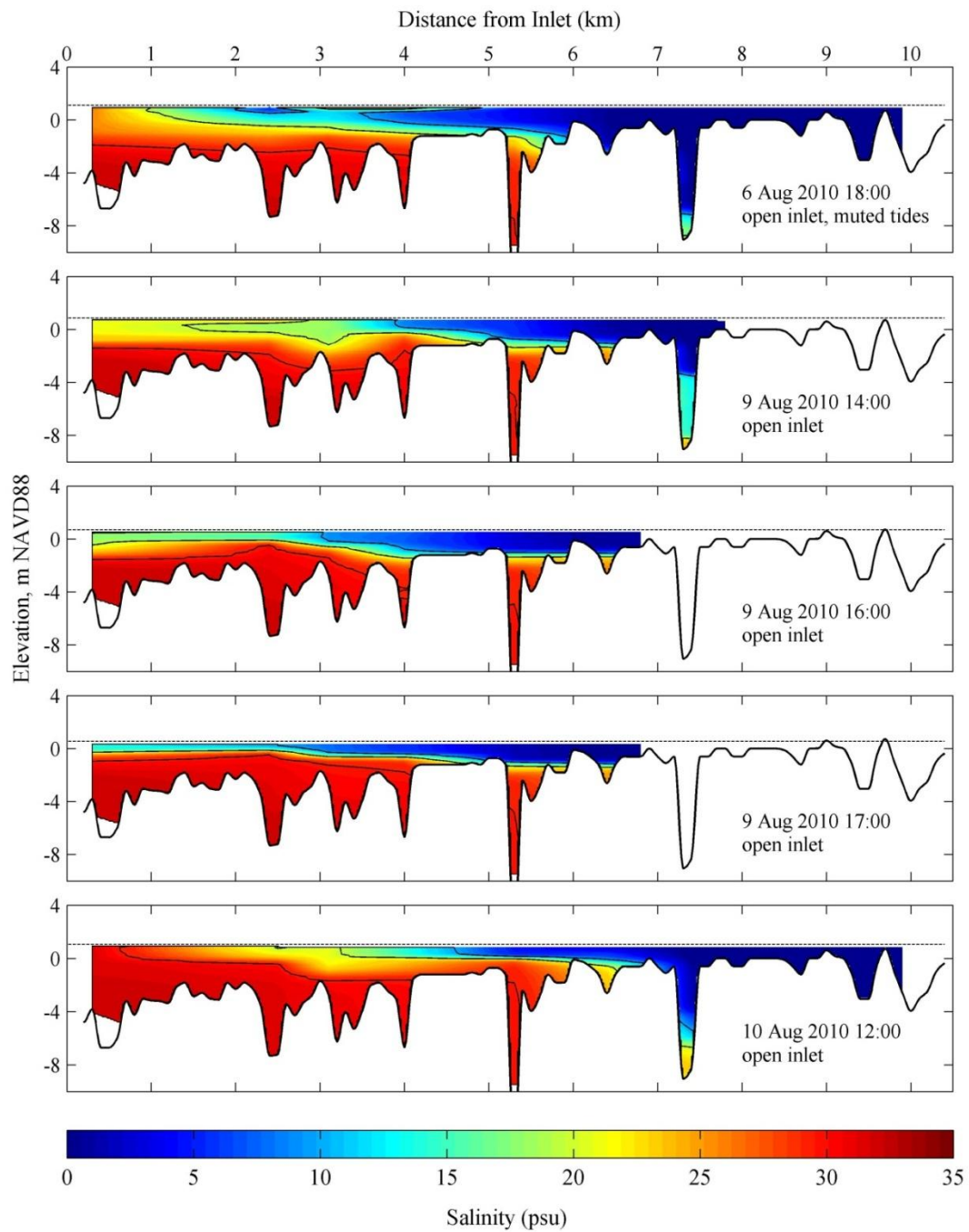


Figure C.36. 2D planar view of the estuary salinity interpolated from CTD transects from 6 August to 10 August 2009.

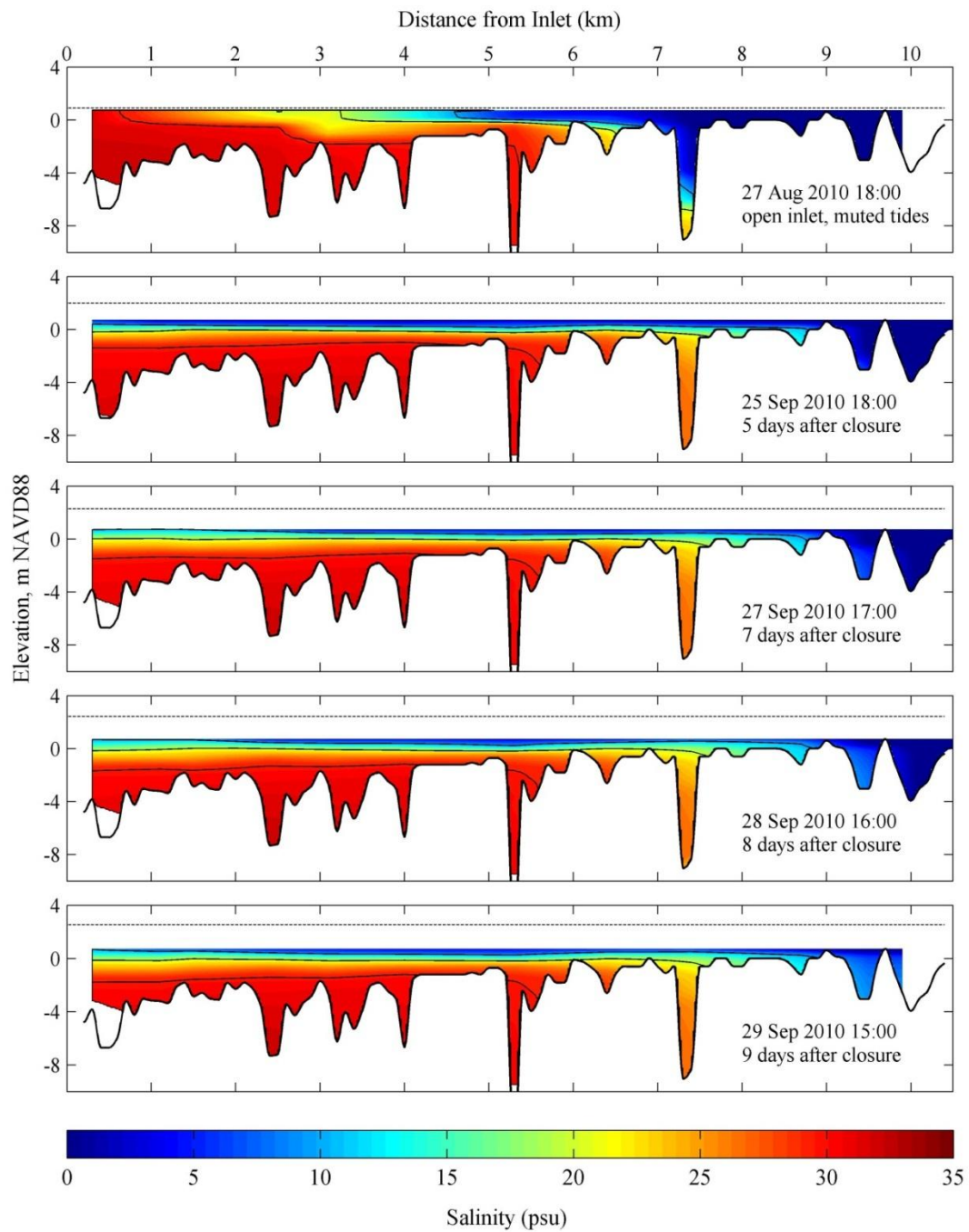


Figure C.37. 2D planar view of the estuary salinity interpolated from CTD transects from 27 September to 29 September 2009.

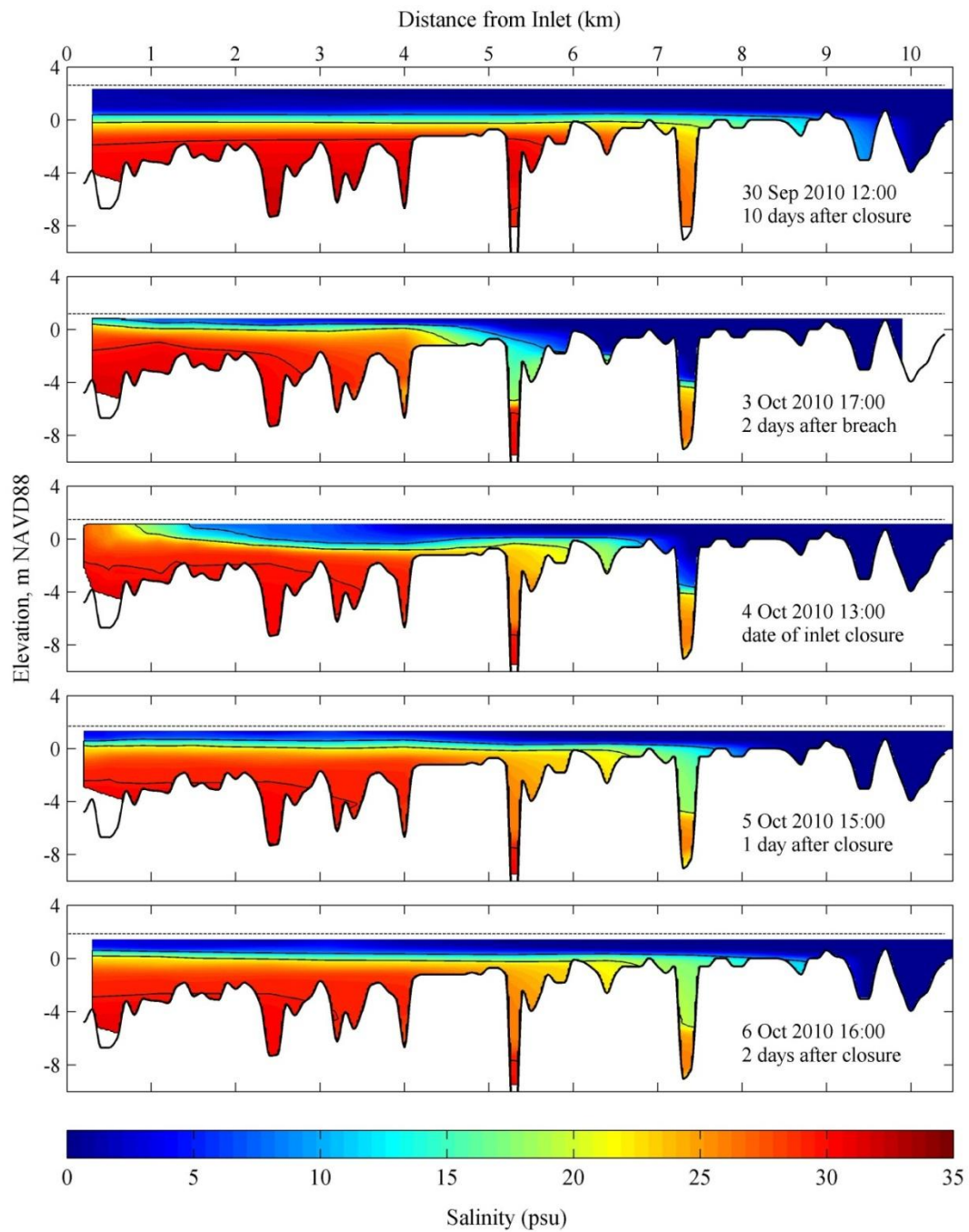


Figure C.38. 2D planar view of the estuary salinity interpolated from CTD transects from 30 September to 6 October 2009.

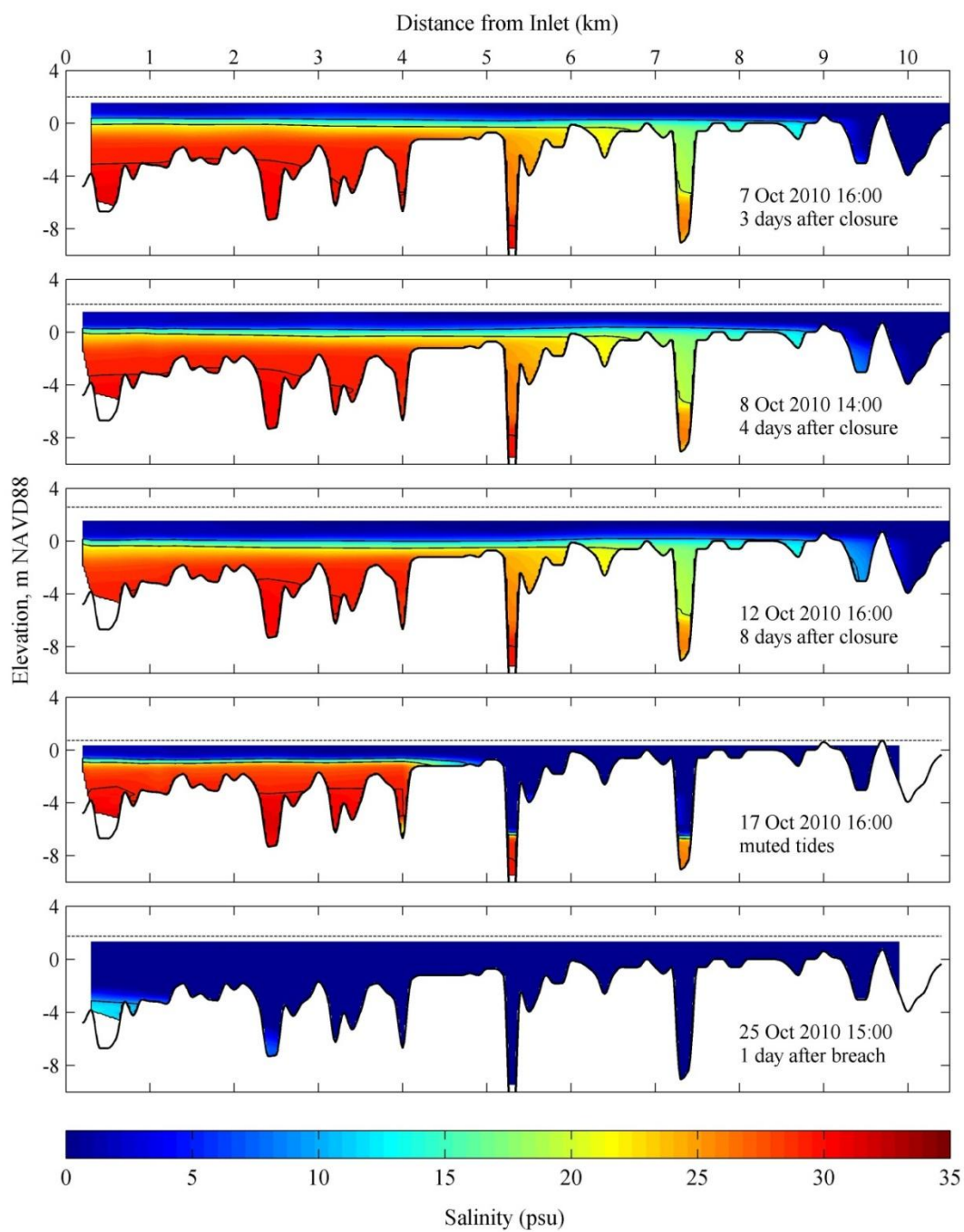


Figure C.39. 2D planar view of the estuary salinity interpolated from CTD transects from 7 October to 25 October 2010.

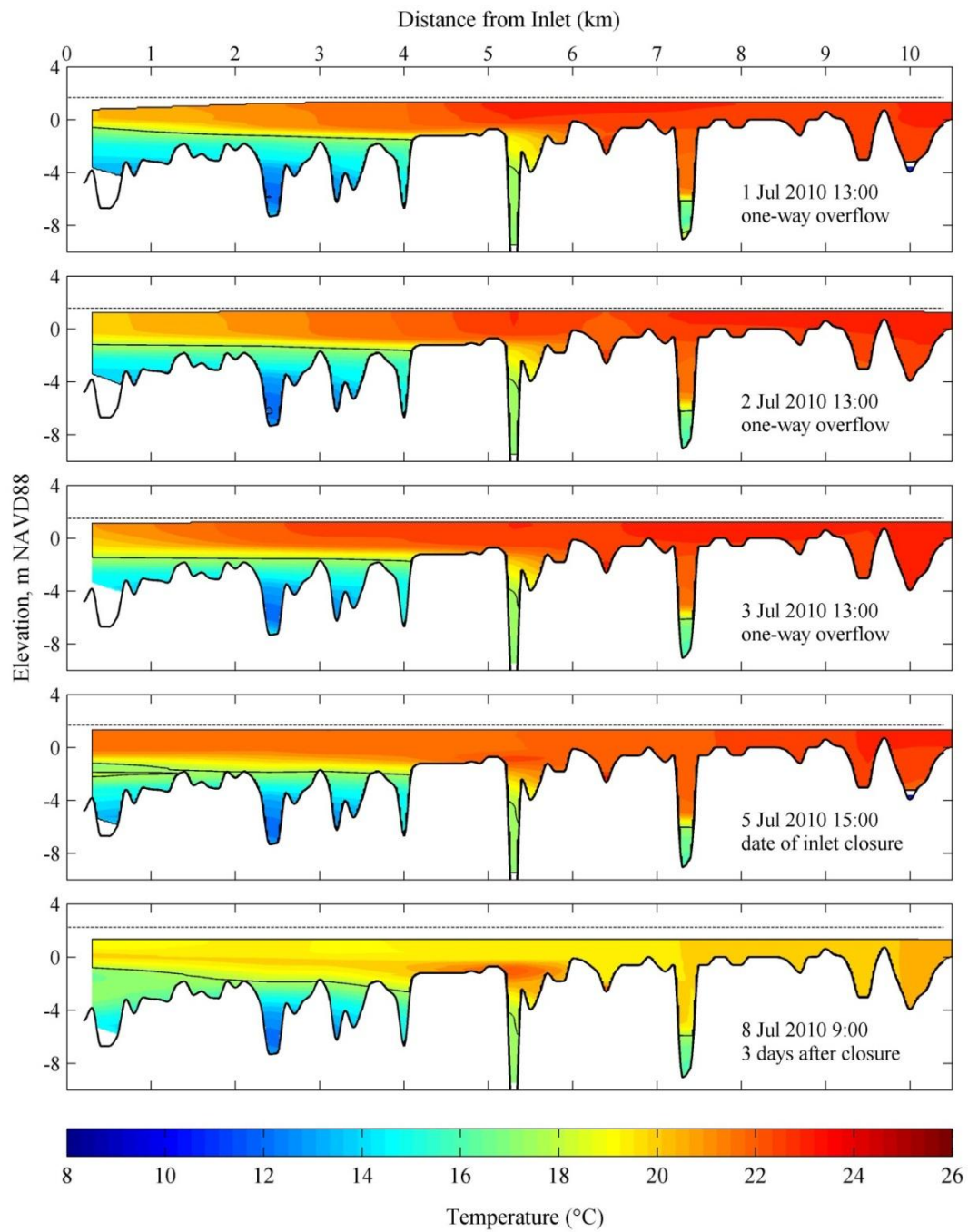


Figure C.40. 2D planar view of the estuary temperature interpolated from CTD transects from 1 July to 8 July 2010.

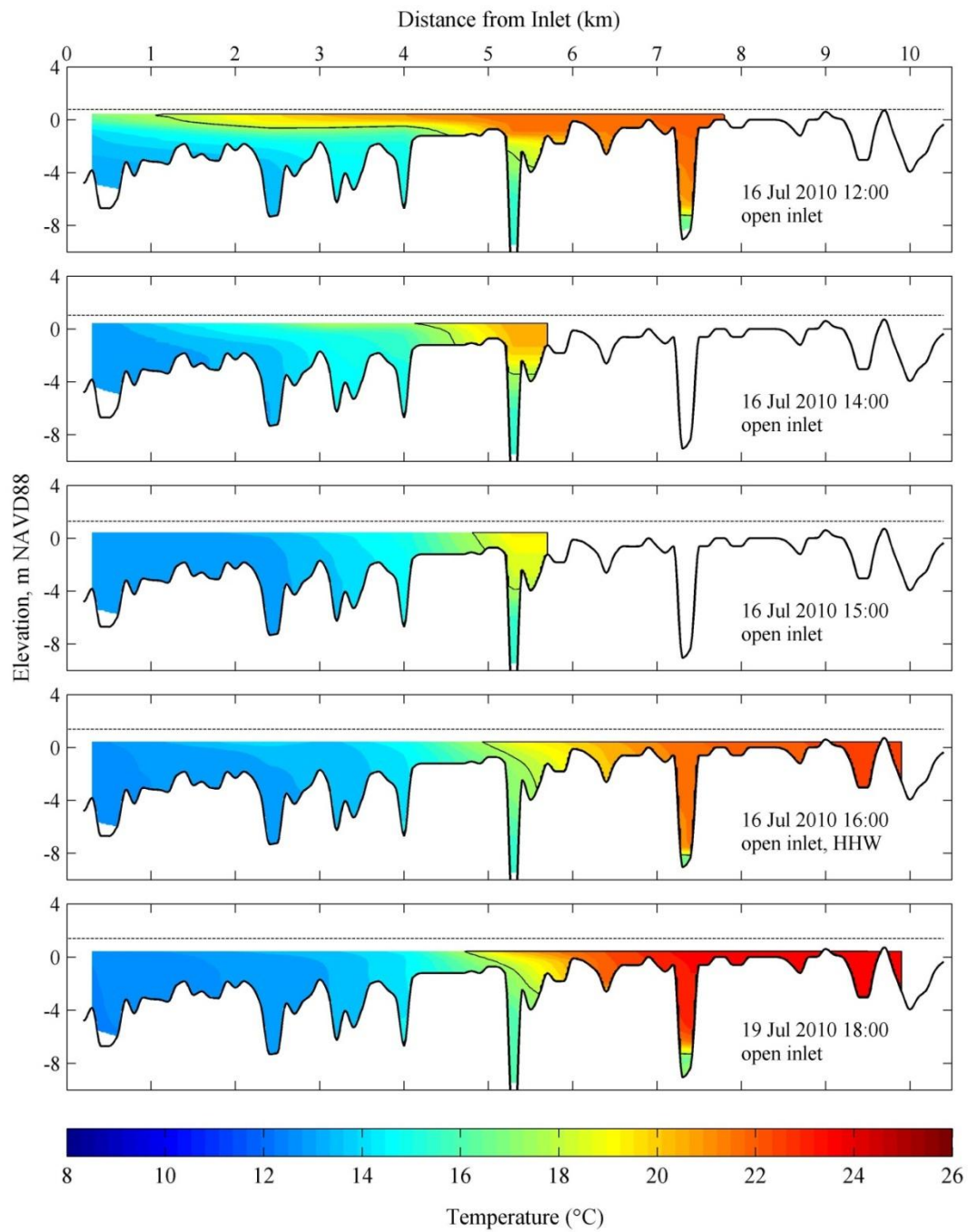


Figure C.41. 2D planar view of the estuary temperature interpolated from CTD transects from 16 July to 19 July 2010.

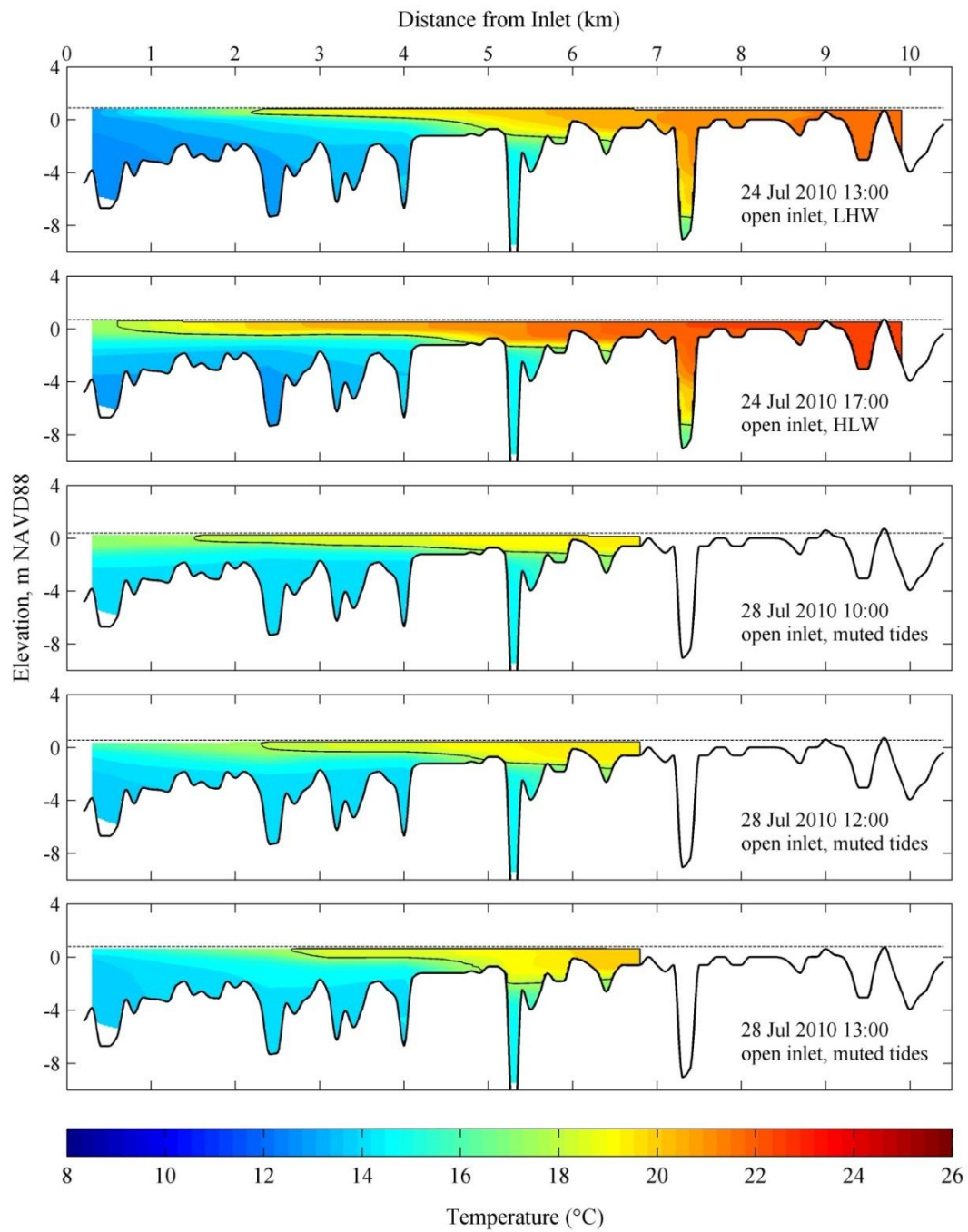


Figure C.42. 2D planar view of the estuary temperature interpolated from CTD transects from 24 July to 28 July 2010.

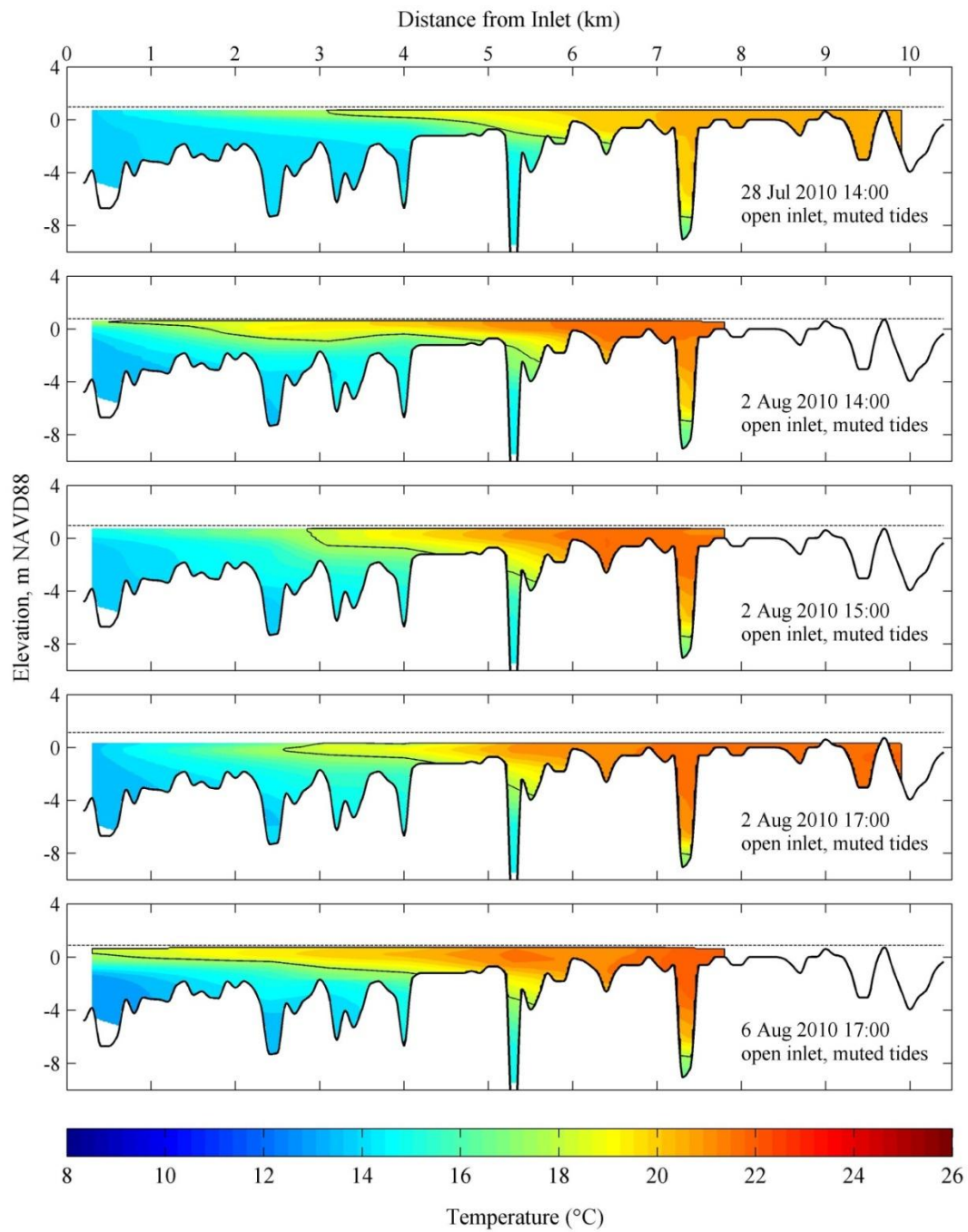


Figure C.43. 2D planar view of the estuary temperature interpolated from CTD transects from 28 July to 6 August 2010.

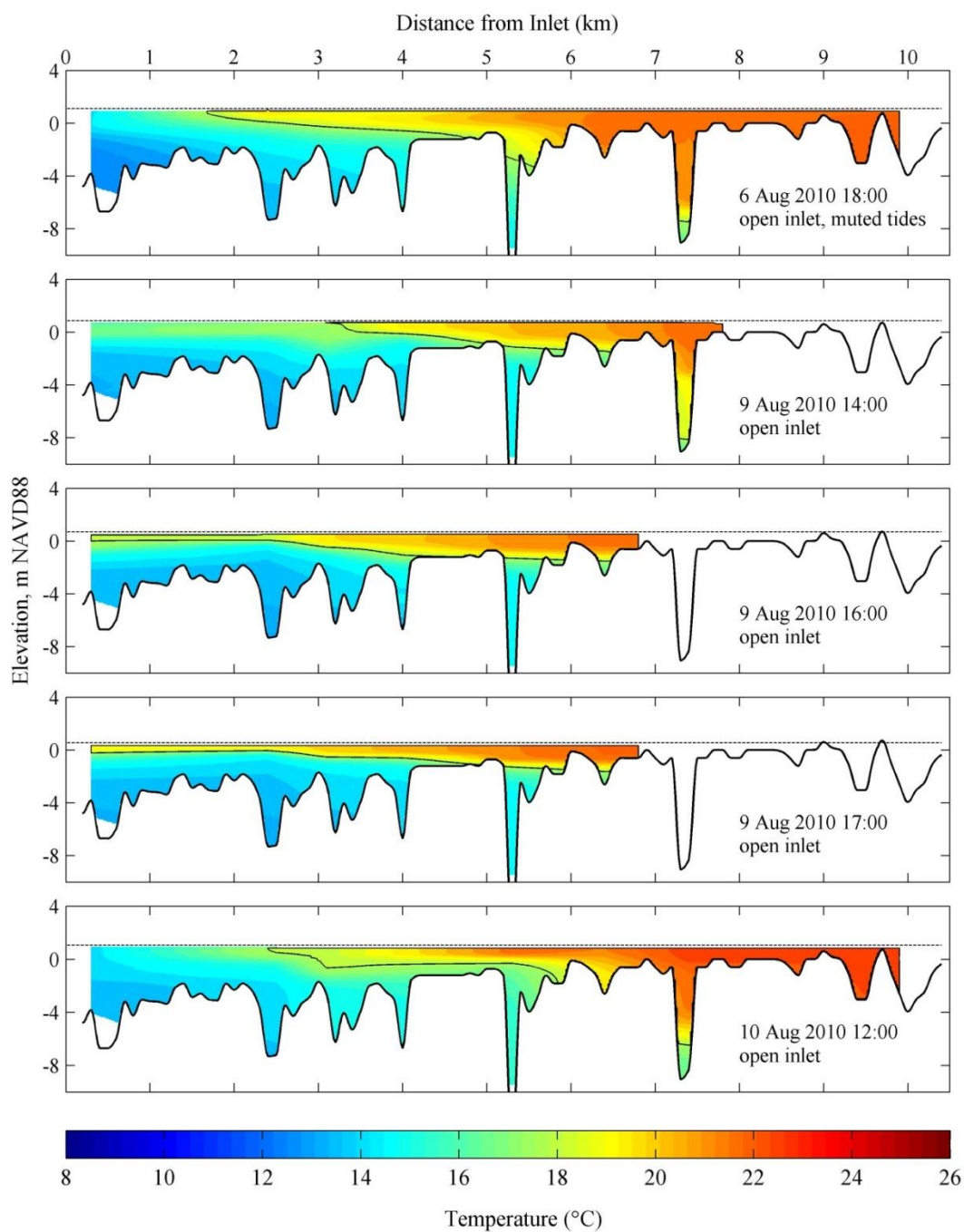


Figure C.44. 2D planar view of the estuary temperature interpolated from CTD transects from 6 August to 10 August 2010.

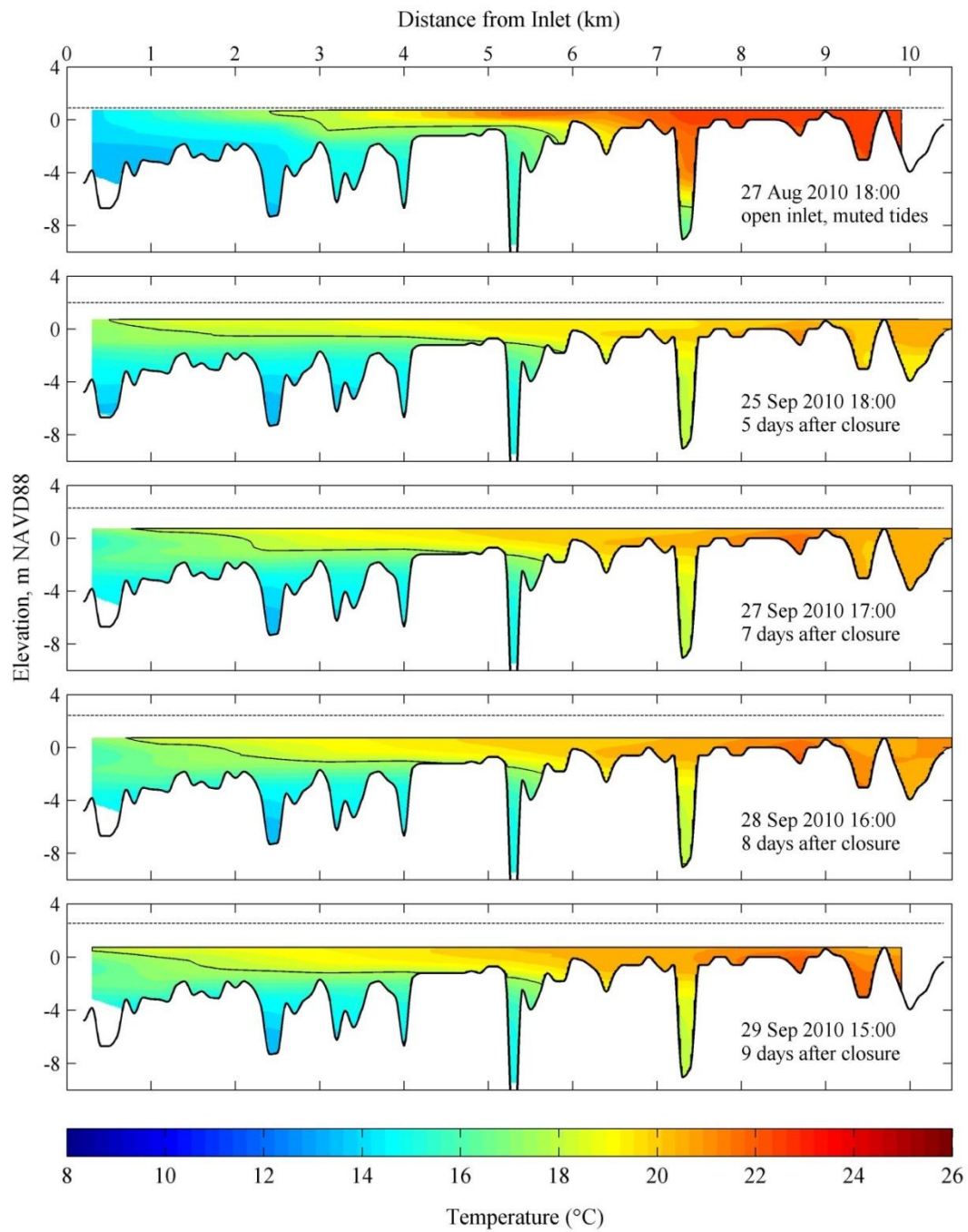


Figure C.45. 2D planar view of the estuary temperature interpolated from CTD transects from 27 August to 29 September 2010.

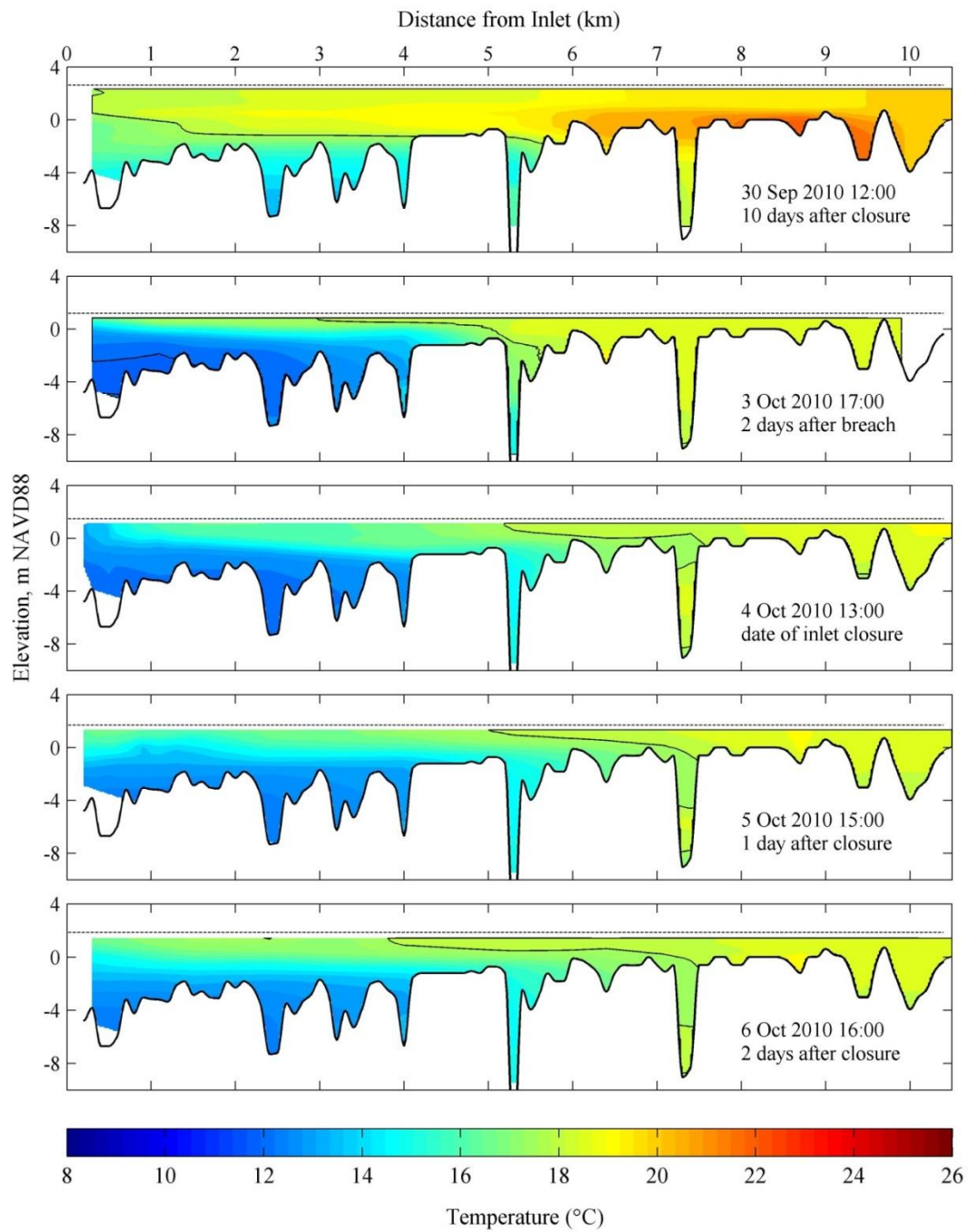


Figure C.46. 2D planar view of the estuary temperature interpolated from CTD transects from 30 September to 6 October 2010.

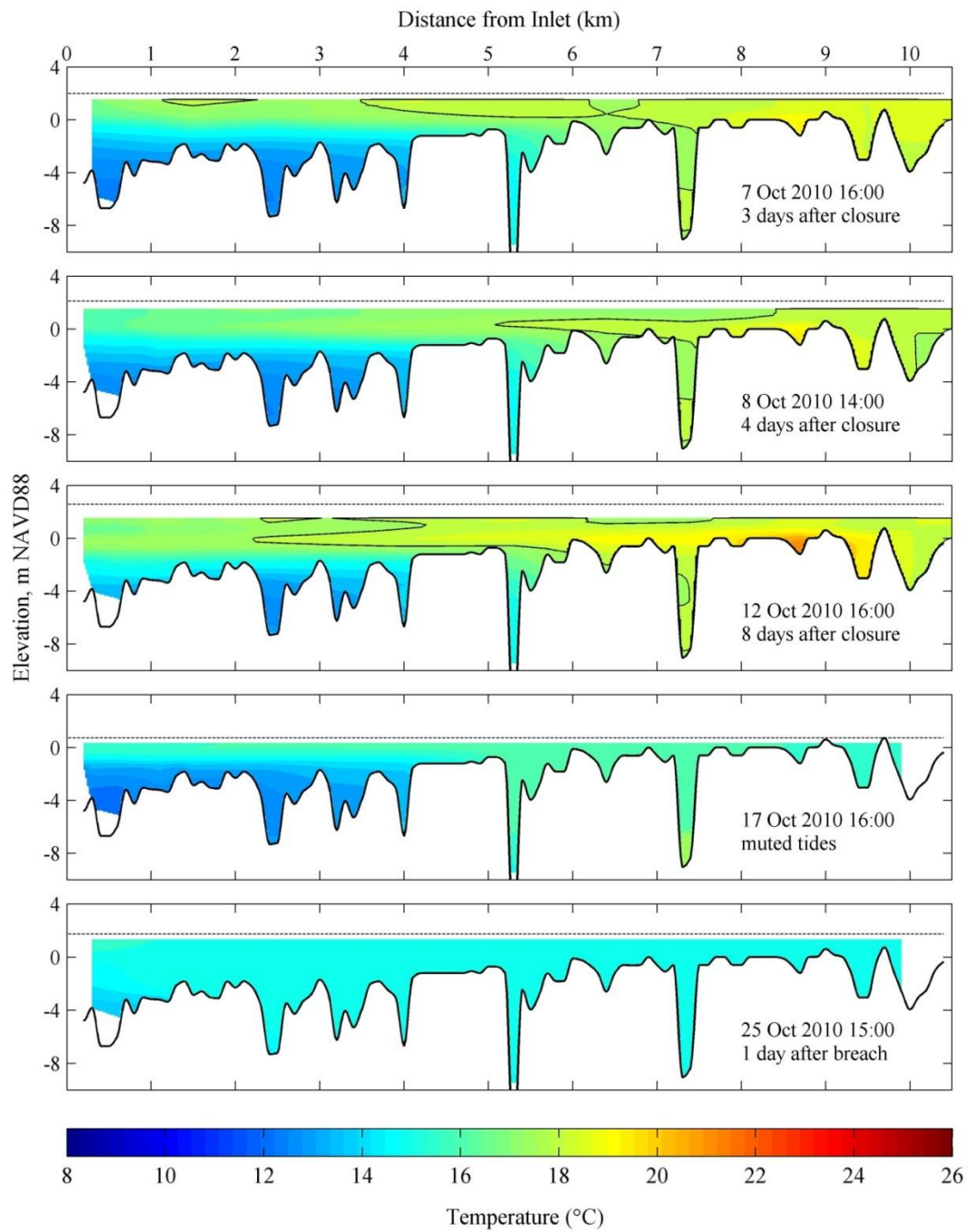


Figure C.47. 2D planar view of the estuary temperature interpolated from CTD transects from 7 October to 25 October 2010.

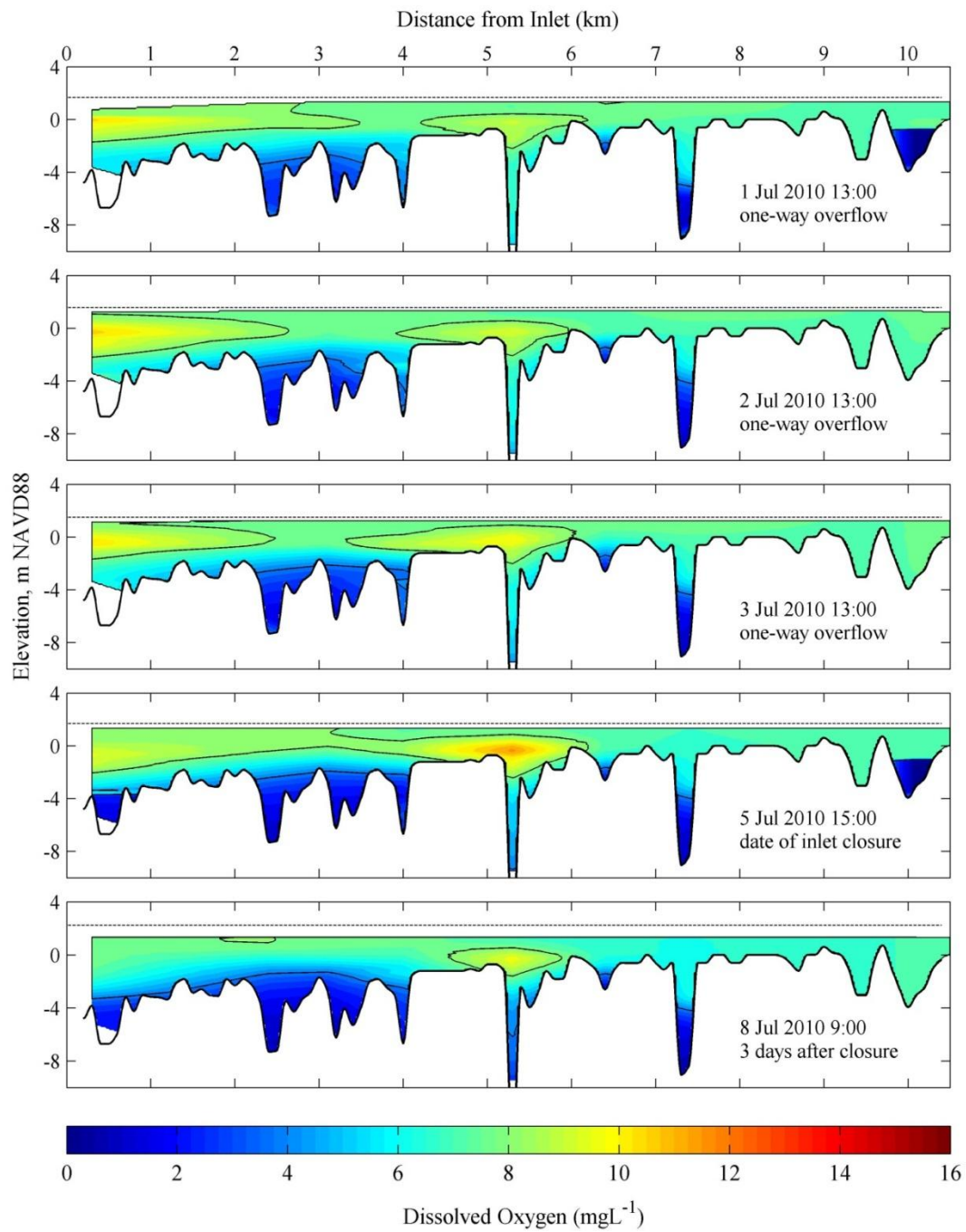


Figure C.48. 2D planar view of the estuary temperature interpolated from CTD transects from 1 July to 8 July 2010.

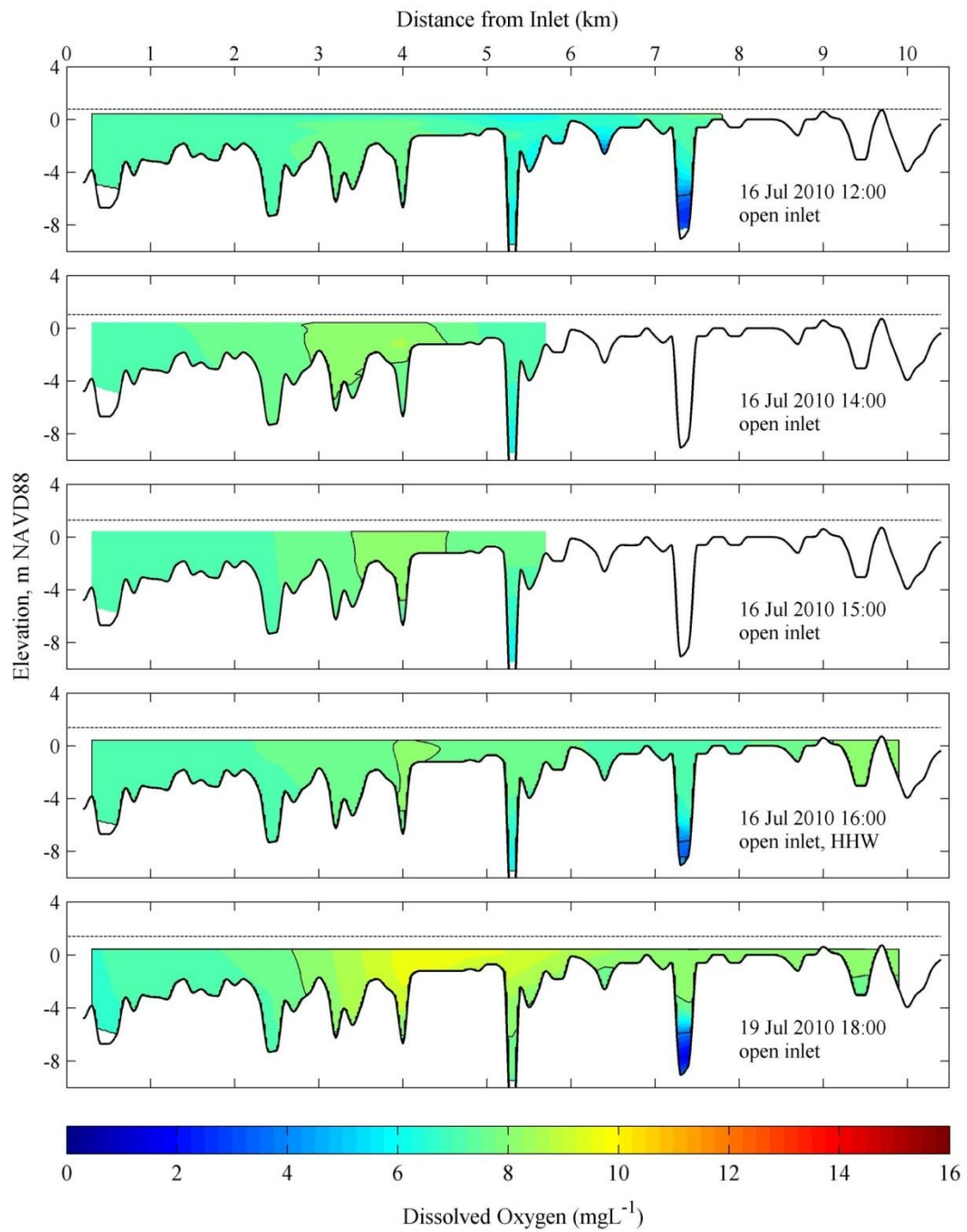


Figure C.49. 2D planar view of the estuary temperature interpolated from CTD transects from 16 July to 19 July 2010.

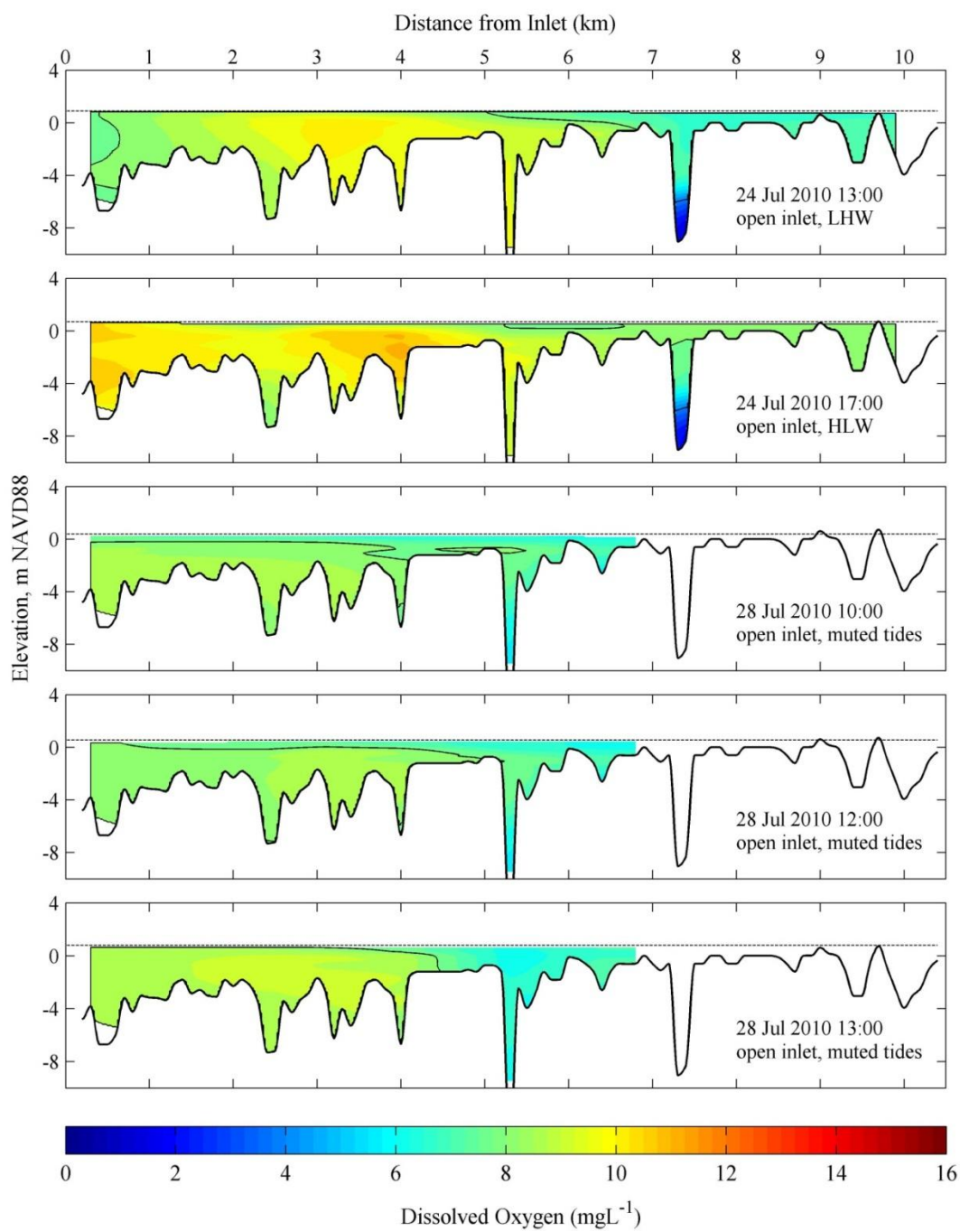


Figure C.50. 2D planar view of the estuary temperature interpolated from CTD transects from 24 July to 28 July 2010.

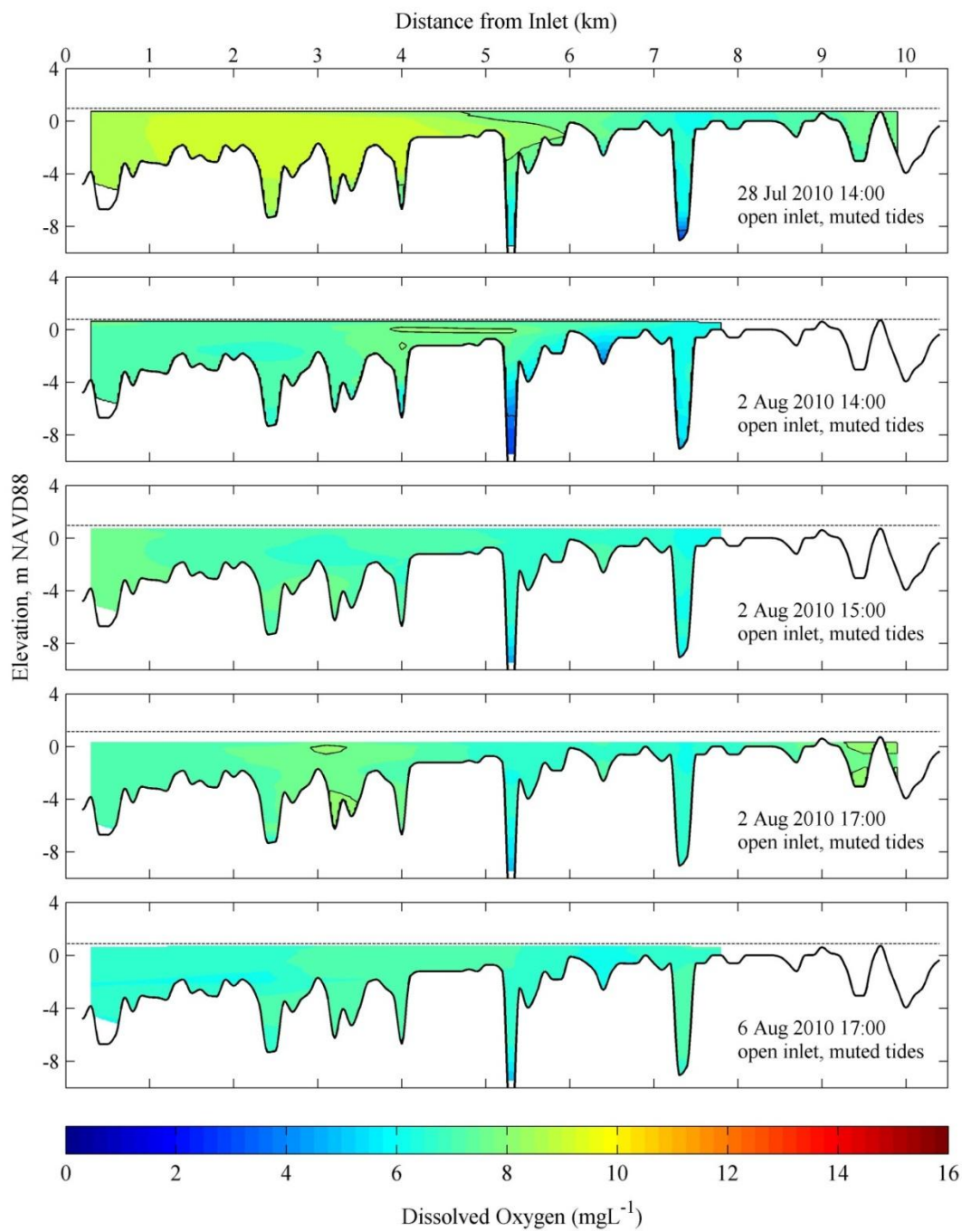


Figure C.51. 2D planar view of the estuary temperature interpolated from CTD transects from 28 July to 6 August 2010.

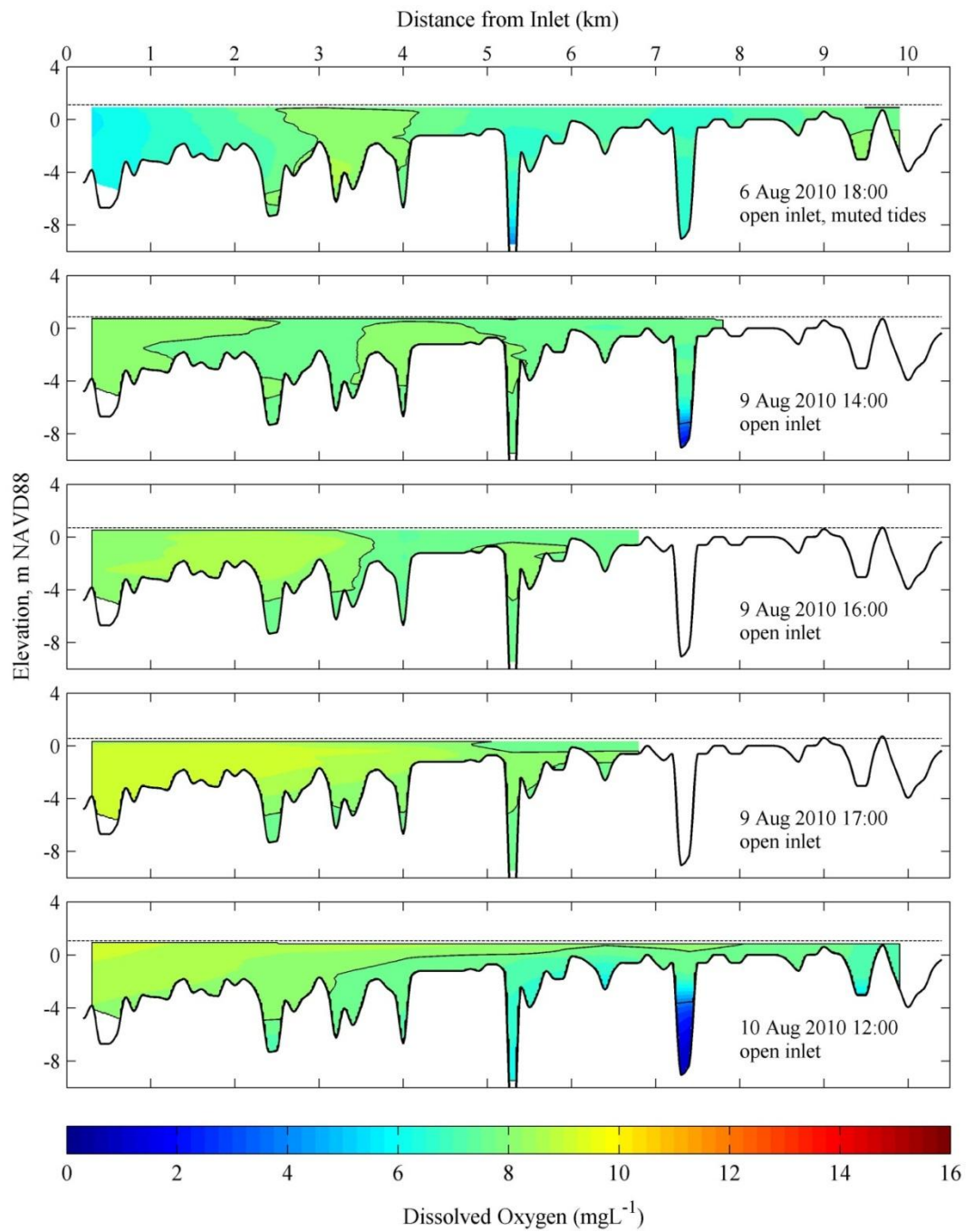


Figure C.52. 2D planar view of the estuary temperature interpolated from CTD transects from 6 August to 10 August 2010.

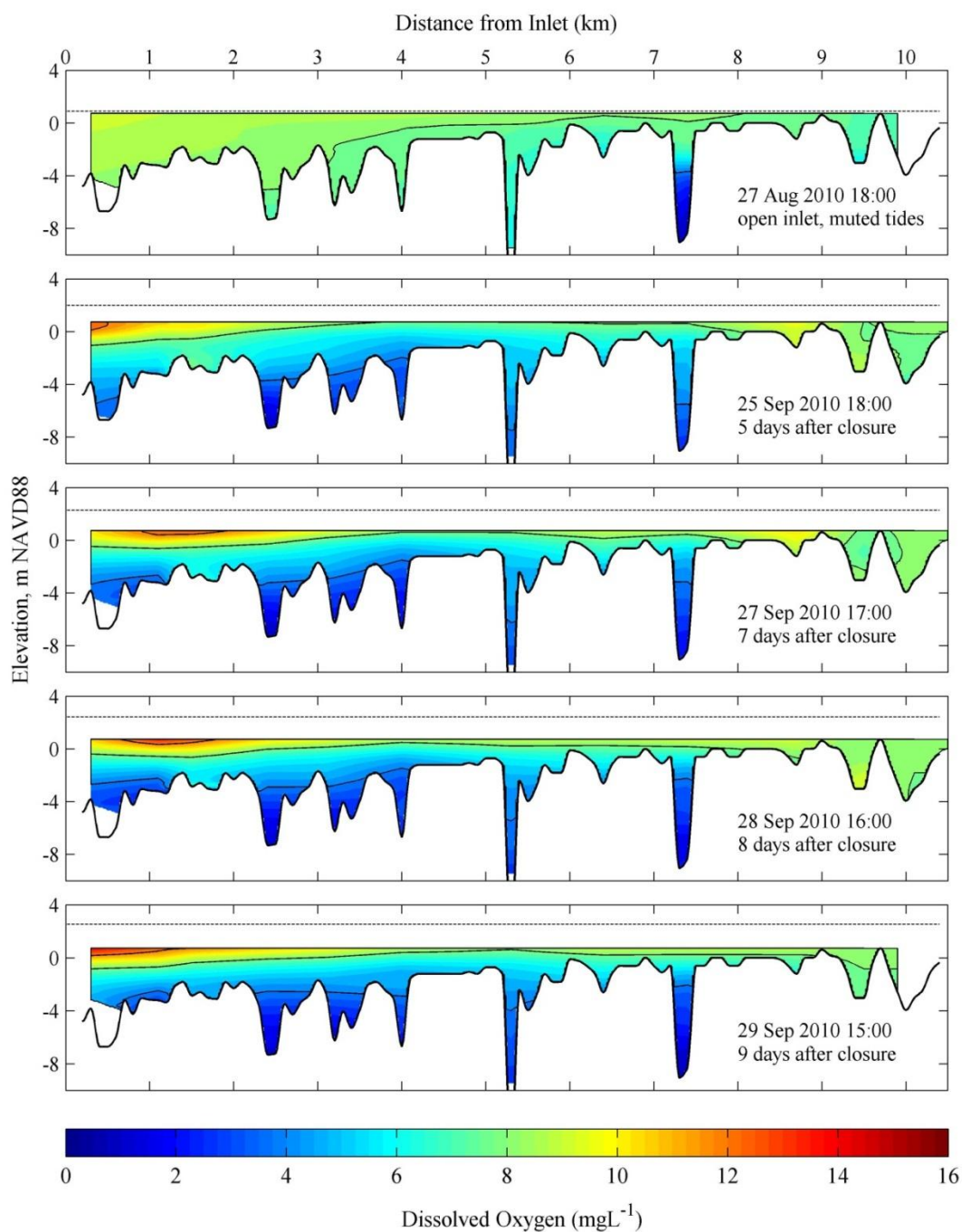


Figure C.53. 2D planar view of the estuary temperature interpolated from CTD transects from 27 August to 29 September 2010.

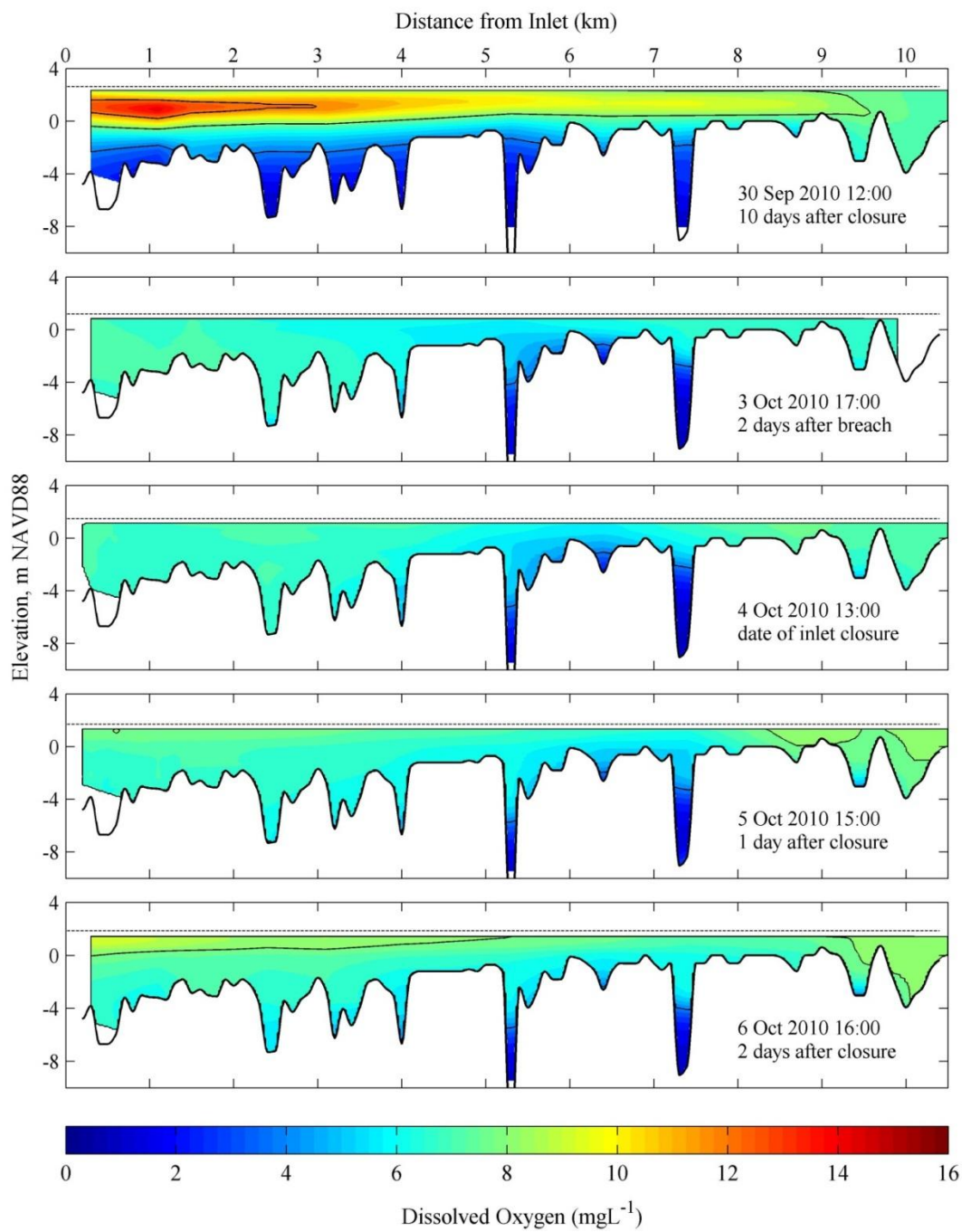


Figure C.54. 2D planar view of the estuary temperature interpolated from CTD transects from 30 September to 6 October 2010.

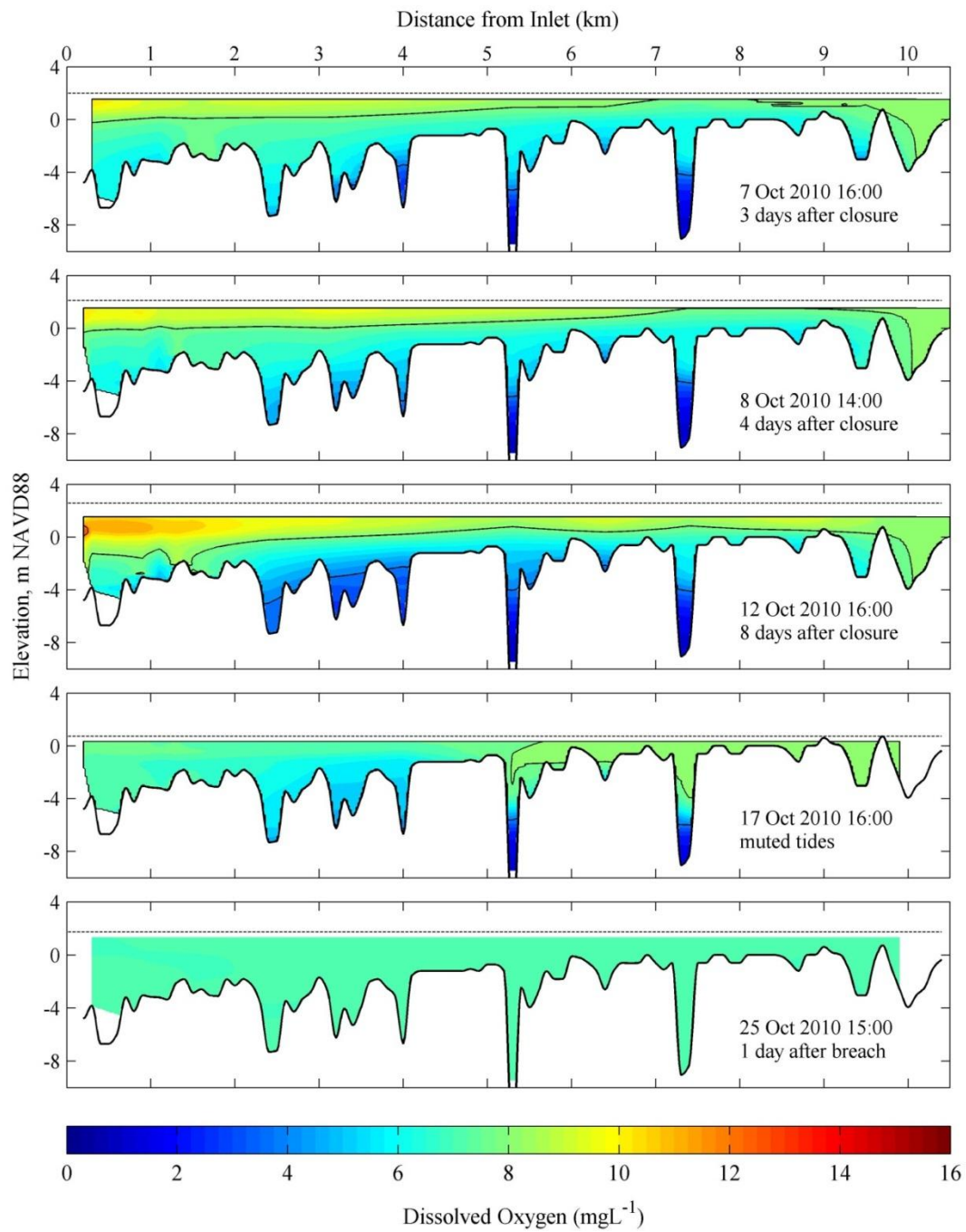


Figure C.55. 2D planar view of the estuary temperature interpolated from CTD transects from 7 October to 25 October 2010.